THE UNIVERSITY OF CHICAGO

STELLAR MASS ASSEMBLY IN GALAXY CLUSTERS AND HIGH-REDSHIFT GRAVITATIONALLY LENSED GALAXIES

A DISSERTATION SUBMITTED TO
THE FACULTY OF THE DIVISION OF THE PHYSICAL SCIENCES
IN CANDIDACY FOR THE DEGREE OF
DOCTOR OF PHILOSOPHY

DEPARTMENT OF ASTRONOMY AND ASTROPHYSICS

BY
GOURAV KHULLAR

CHICAGO, ILLINOIS
AUGUST 2022

Gowtham and Debo — this one is for you.

Table of Contents

List of Figures

List of Tables

ACKNOWLEDGMENTS

I work on studying the properties of galaxies that form, live, and evolve in communities. This thesis, and my work over the last few years could not have happened without my community, that supported me towards a career in astronomy, and supported me while my time here in Chicago.

First, I would like to thank my advisor, Mike Gladders, for being the best teacher, mentor, and collaborator and for all of your support and encouragement throughout my PhD. My thesis committee could not have been a more supportive group of mentors: Brian Nord, Dan Hooper, Rich Kron and Tom Crawford. This thesis is a representation of your belief in my work and vision. I would like to offer my sincerest gratitude to the administrative staff at UChicago — Laticia Rebeles, Jennifer Smith, Brent Barker, Julia Brazas and Val Smith — for supporting me throughout my PhD candidacy. I am also incredible grateful to Mike Mcdonald, Michael Calzadilla and Laurel White for making my time at the Massachusetts Institute of Technology so welcoming, and allowing me to conduct my science in such an enriching environment.

I have been so fortunate to work with many incredible collaborators and mentors. In particular, I would like to thank Matt Bayliss, Keren Sharon, Jane Rigby, Guillaume Mahler, John Chisholm, Brian Nord, Rich Kron, John Carlstrom, Kate Whitaker, Michael Florian, Hakon Dahle, Emil Rivera-Thorsen, Keunho Kim, Brad Benson, Lindsey Bleem, Tom Crawford, Juan Remolina Gonzalez, Kate Napier, Ben Floyd, Mike Brodwin, Tony Stark, Veronica Strazzullo, Alex Saro, Alex Ciprijanovic, Mike Mcdonald, Michael Calzadilla, Rachel Bezanson, David Setton, Florian Ruppin, Steve Allen, Doug Applegate, Sebastian Bocquet, Ezra Bulbul, Jason Poh and Phil Mansfield.

The COOL-LAMPS collaboration has been an integral part of my time here at Chicago; I could not have done this without my students and collaborators — Ezra Sukay, Katya Gozman, Owen Matthews Acuña, Jorge Sanchez, Viraj Manwadkar, Yunchong Zhang, Ben

Levine, Will Cerny, Jason Lin, Michael Martinez, Emily Sisco, Daniel Stein, Kaiya Merz, Kiyan Tavangar, Liz Medina, Dan Mahronic, Erik Zaborowski, Isaac Sierra and Finian Ashmead.

Thank you to all my friends who helped me settle, grow and thrive in Chicago — Jason Poh, Andrew Neil, Phil Mansfield, Amy Tang, Mandy Chen, Rebecca Diesing, Jordan Scherer, Bodhi Vani, Emily Gilbert, James Lasker, Zoheyr Doctor, Celeste Keith, Adina Feinstein, Maya Fishbach, John Hood, Tracy Hood, Grace Chesmore, Jazmine Jefferson, David Zegeye, Kaeli Hughes, Andrea Bryant, Lucas Beaufore, Paul Jerger, Tim Steeves, Gwen Gallagher, Lipi Gupta, Lesya Horyn, Abby Lee, Judit Prat, Jose Maria Ezquiaga, Alex Gonzalez, Christine Simpson, Danielle Norcini, Tad Komacek, Dan Baxter, Ankur Agrawal, Neeti Menon, Bipul Pandey, Khushboo Singh, Shobhit Gupta, Suhail Rehman, William Wagstaff, Zach Loeffler, Breck Radulovic, Freddy Rockwood, Lily Burton, Rania, Ashley, Dominique Walker and Joshua Singh.

Thank you to many members of the UChicago Astronomy community for your support and friendship. Thank you to all the members of IDEA — our own early career researcher group, Inclusion, Diversity, Equity in Astronomy — and the Astrobites collaboration, who have worked tirelessly to build community, support each other, and to make our department and the astronomy community a better and more just place.

I would like to express my sincere gratitude towards the staff and workers at the 6.5m Magellan Telescopes at the Las Campanas Observatory, Chile, Gemini-North telescopes at Mauna Kea, Hawaii, USA, the Nordic Optical Telescopes, Canary Islands, Spain, and Yerkes Observatory, Lake Geneva, USA, for their valuable labor. Here, I wish to recognize and acknowledge the very significant cultural role and reverence that the summit of Mauna Kea has always had within the indigenous Hawaiian community. In my work, I have been most fortunate to have the opportunity to collect data from the NOIRLab-operated Gemini-North facility from this mountain. I urge you, the reader, to read about the impact of astrophysical

observatories and research on this sacred Native Hawaiian land using the following resources — Kahanamoku et al. (2020); Prescod-Weinstein et al. (2020), and references therein.

I began the PhD program at the University of Chicago after years of working towards the goal of conducting astronomy research. Thank you to my high school and university teachers and professors for always believing in me. Thank you to my friends Karan Mitra, Hemant Chaher, Akrisht Pandey, Shibani Santurkar, Murtuza Shergadwala, Deeksha Rawat, Harshita Gangrade, Pawan Lelani, Gowtham Ragavendar, Debabrata Sahoo, Ambrish Rawat, Digvijay Trigathia, Baranidharan Mohan, Nishit Jain — "gouravisation" is not a real thing, but the work in this PhD dissertation most certainly is.

This thesis is a labor of love, hard work, a time of anxiety, uncertainty and confidence, simultaneously. To Chelsea Football Club, the TV show Parks and Recreation, the Marvel Cinematic Universe, singers K.K., Arijit Singh and Diljit Dosanjh, writers Arundhati Roy, Octavia Butler and James S.A. Corey, video games Age of Empires II and Cricket 2022 — I could not have done spent my 20s doing this absolutely wonderful work without you.

I wish all the power and solidarity to my graduate worker union — Graduate Students United. Thank you to my friends Grant Macdonald, Natalia Piland, claudio gómez-gonzáles, Woo Chan Lee, Mathilde Gerbelli-Gauthier and Clara del Junco, who have taught me everything I know about organizing and building community in the spaces one occupies.

Finally, thank you to my family - both in India and the US. Thank you Bill, Ellen and Lily! Mom, Dad, Gouri — I could not have done this without you, and I hope I have made you proud. To Bella, my cat — thank you for being you.

I could not have imagined I would move to the US someday, and find my person here. Thank you for being there for me, Nora. Thank you for introducing me to artisan coffee, The Office, honey badgers, IPAs, and convincing me that cats are lovely creatures and numpy arrays are not monsters. Thank you for your love and patience as we traverse our journey together.

ABSTRACT

A major challenge in the field of extragalactic astrophysics is understanding when the most massive galaxies form the bulk of their stars, and determining the specific pathways they take to assemble mass across a wide range of redshifts and environments. In this thesis, I describe my work to characterize stellar populations in massive galaxies at two epochs — redshifts 0.5 and 5.

I use spectra of galaxies in massive South Pole Telescope galaxy clusters to address the question: on what timescales do galaxies that end up in clusters form their stars, and does the cluster sample matter when studying these properties? This mass-limited cluster sample across redshifts $0.3 < z < 1.5$ allows me to constrain star formation histories and formation redshifts of 900 quiescent galaxies in clusters, as a function of cluster environment and mass. This study explores mass-dependent evolution in cluster quiescent galaxies and characterises galaxy evolution across a descendent-antecedent cluster sample.

On the other 'end' of the redshift scale, I describe the characterization of COOL J1241+2219, a lensed galaxy at $z = 5.04$ that is the brightest galaxy known at $z > 5$ (at AB magnitude $z \sim 20.5$). This galaxy was discovered by COOL-LAMPS — ChicagO Optically-selected strong Lenses - Located At the Margins of Public Surveys — initiated to find strongly lensed systems, consisting primarily of a team of undergraduate students. I characterize the lensed galaxy using ground-based spectrophotometric data to find an intrinsically luminous and massive star-forming galaxy.

In this thesis, I also show first results aimed at comparing CJ1241 and other COOL-LAMPS discovered lensed massive galaxies at $z > 3$ with their potential descendents — quiescent massive lensed galaxies at lower redshifts. With anticipated multi-wavelength spectroscopic data, including from an approved JWST Cycle 1 Program (GO 2566, PI: Khullar), I will help uncover mass assembly pathways in CJ1241 well into the epoch of reionization. Finally, I describe efforts to create efficient machine learning-based frameworks

— specifically using simulation-based inference (SBI) — to calculate posterior distributions of key galaxy parameters, and motivate future efforts to study stellar mass assembly in massive galaxies across different epochs.

CHAPTER 1

INTRODUCTION

1.1 Mass Assembly in Galaxies

Unpacking the life cycle of a galaxy is a long standing problem (and an exciting one) in astrophysics. Galaxies are observed over a range of masses, in varied shapes and sizes, and contain varied amounts of baryonic matter (stellar populations, star-forming gas, dust) and dark matter. A family of prescriptions is desirable to explain the diversity of properties that galaxies exhibit in the Universe.

Historically, galaxies were collectively referred to as "nebulae" as early as the 1700s. Charles Messier (between 1771-1784) led the first effort to conduct a survey of extended objects in the night sky, and catalogued 110 objects (Messier, 1781). The Dreyer Index Catalogue (IC), published in 1888 (and a subsequent new version in 1895), mapped approximately 15000 such objects (Dreyer, 1895). The National Academy of Sciences debate of 1920 between Harlow Shapley and Heber Curtis (Shapley & Curtis, 1921) discussed the possibility that these nebular objects might in fact be extragalactic, as opposed to being gravitationally bound structures within our own galaxy, the Milky Way. Edwin Hubble used the distances estimated from Cepheid variable stars to demonstrate the extragalactic nature of these objects, which were in some cases like our own galaxy in size, mass and chemical properties (Hubble, 1929; Hubble & Humason, 1931; Hubble, 1934). This marked the beginning of observational extragalactic astrophysics.

The last century has seen tremendous advancement in the discovery and characterization of billions of galaxies, with systematic ground based telescope surveys and targeted observations of these interesting systems. Numerical simulations with physical prescriptions for galaxy formation and evolution — from the initial conditions of gravitational instabilities and perturbations to nonlinear evolution of these perturbations to radiative cooling that led

to the initial stars in galaxies — have offered great insights in our quest to understand the inner workings of galaxies across cosmic time.

How and why galaxies accrete and/or form stellar mass, and cease star formation are key questions in the field. Observations have shown that the majority of high-redshift star-forming galaxies (which at later times may have become quiescent systems) have star formation rates (SFRs) correlated with their stellar mass, a scaling relation referred to as the star forming main sequence (SFMS; Noeske et al. (2007a); Daddi et al. (2007); Whitaker et al. (2012)). This gives credence to theories in which continuous modes of cold molecular gas accretion are responsible for supplying the constant fuel of star formation in galaxies, as their stellar mass grows (Bouché et al., 2010; Lilly et al., 2013; Mitchell et al., 2014; Dekel & Mandelker, 2014; Tacchella et al., 2018). As the cosmic star formation rate density peaks at redshifts $z \sim 2$ (see Madau & Dickinson (2014) and references therein), we see the population of massive quiescent systems increasing from $z \sim 3$ to $z \sim 1$. Understanding the mechanisms and timescales related to quenching across cosmic time is a key motivation of the work presented in this thesis. To study these key factors across redshift, we must use the archaeological record of a galaxy's formation history, encoded within photometric and spectroscopic observations. Not only does this path lead us to answers about evolutionary processes that affect star formation in galaxies, but also enlightens us about the dependence of star formation on factors such as environment, epoch of observation, chemical abundances and dynamics.

In this chapter, I introduce the most massive galaxies in the Universe, and describe the environment in which we find these galaxies — galaxy clusters. I also discuss how we build cluster samples, and how we study star formation in cluster members. Finally, I also introduce the studies of early Universe galaxies, and a prominent mechanism to observe these systems — gravitational lensing.

1.1.1 The most massive galaxies in the Universe

Why do we care about the most massive galaxies across cosmic time? Firstly, stellar and dark matter halo masses are key properties of galaxies that are correlated with other interesting parameters; many studies over the last few decades have demonstrated the robustness of stellar mass as a key indicator of the galaxy's evolutionary history (see Brinchmann et al. (2004); Muzzin et al. (2013); Guglielmo et al. (2015); Leja et al. (2019c); Lower et al. (2020a) and references therein). Secondly, the most massive galaxies are fantastic laboratories; one need only utilise modest resources to conduct spectroscopy programs resulting in high signal-to-noise ratio (SNR) observations that shed light on galaxy properties.

Survey observations of representative samples of galaxies indicate that nearby massive galaxies seem to have formed the majority of their stellar mass at higher redshifts ($z > 3$), and build mass through mergers with other galaxies thereafter (e.g., see Heavens et al. (2000); Gallazzi et al. (2005); Muzzin et al. (2013); Pacifici et al. (2016); Belli et al. (2019); Carnall et al. (2019b)). Semi-analytical galaxy formation simulations have not ruled out this scenario (Kauffmann et al., 1993; Guo & White, 2008; De Lucia et al., 2006; Oser et al., 2010; Rodriguez-Gomez et al., 2016; Rong et al., 2018). That being said, recent discoveries of higher redshift massive galaxies (at $z > 2$; Mobasher et al. (2005); Wiklind et al. (2008); Carnall et al. (2019b)) requires us to rethink this "quench and grow" mode of mass assembly. Studies of nearby massive galaxies (which are mostly quiescent) need to be connected with higher redshift massive galaxies (which are star-forming, post-starburst or quiescent systems) in a descendent-antecedent manner. This thesis is an attempt to aid in this quest.

1.2 Galaxy Clusters

Galaxy clusters are communities of galaxies, gas and dark matter. These are the largest gravitationally bound structures in the Universe, and are powerful tracers of the modes of structure formation at megaparsec scales. Clusters are mostly dominated by dark matter

(by mass), and emit light panchromatically — X-ray Bremsstrahlung emission and radio synchrotron emission by the hot intracluster medium plasma, as well as ultraviolet (UV), optical and infrared (IR) stellar and nebular continuum and line emission from their constituent galaxies. Clusters sample a broad range of galaxy overdensities and mass accretion histories, and studies of the constituent cluster members provide insight into the evolutionary paths that member galaxies take in cluster environments (Oemler, 1974; Dressler, 1980; Dressler & Gunn, 1983; Balogh et al., 1997; Blanton & Moustakas, 2009; Webb et al., 2020; Khullar et al., 2021a)).

1.2.1 History

Once it was well understood that some "nebulous" regions in the night sky were extragalactic objects, astronomers began to study clustering of galaxies. Two of the most well studied clusters in the nearby Universe are Virgo and Coma clusters. The measurements of individual galaxy velocities in the Coma cluster and the stable gravitational potential well assumption enabled Hubble, Humason and Zwicky to derive an approximate total mass of the cluster (Hubble & Humason, 1931; Zwicky, 1951), and was one of the first results pointing towards dark matter-dominated massive bound structures in the Universe. The first n-body simulations in the 1960s (von Hoerner, 1963; Hénon, 1964; Peebles, 1970) connected the formation of clusters today to initial small density fluctuations, as predicted by a Λ-Cold Dark Matter (LCDM) cosmological model. Finally, with observations of X-ray emission, galaxy dynamics and gravitational lensing observations of clusters, astronomers were able to study the presence of 10^8 K gas in the intra-cluster medium (Lahav et al., 1989; Edge et al., 1990) and a deep gravitational potential well (Soucail et al., 1988).

1.2.2 Formation of Clusters

According to the ΛCDM model of hierarchical structure formation, dark matter dominated clusters form via minor and major mergers with other dark matter halos. Cluster formation can be modeled by collapsing perturbations from cosmological initial conditions, and reproduce bulk properties observed in surveys for the most part in a "self-similar" (Kaiser, 1986) manner (e.g., cluster mass, abundance, and clustering). For a detailed description of the formation and evolution of small-scale cluster components, one needs to model nonlinear processes of collapse and account for radiative processes associated with baryons. For example, in addition to the complexities of star formation, we must also consider heating of gas due to adiabatic shocks, supermassive black hole feedback suppressing star formation at the core of clusters, active galactic nuclei (AGN) activity increasing the metallicity of the broader cluster volume, etc.

To summarise, galaxy clusters are robust probes of the assembly and evolution of large-scale cosmic structure, and hence are ideal laboratories for cosmological studies. Simulations with prescriptions for cosmological models (e.g., ΛCDM) are sensitive to the initial conditions that led to the growth of structure as detected today in galaxy and cluster surveys (see Kravtsov & Borgani (2012) for a detailed review, as well as references therein). Measurements of cluster abundance (number density of galaxy clusters per unit volume) constrain the shape of the matter power spectrum, the matter density, as well as models of cosmic acceleration (or dark energy).

1.2.3 Building a Sample of Galaxy Clusters: SZ Effect

Although massive clusters are easy to observe in the local universe, discovery of clusters with similar properties in the high-redshift universe is still a technical challenge. This is due to two main reasons. Firstly, we see a decrease in optical and X-ray fluxes at cosmological distances — probes that are used as observational tracers of galaxy clusters. Secondly, massive galaxy

clusters are extremely rare at higher redshifts.

Each wavelength regime has its unique advantages : optical and IR surveys are efficient since they using imaging to see the starlight from cluster galaxies (with observed bandpasses matched to cluster redshifts), and X-ray observations provide us with a direct observation of the ICM electron density and temperature — a tracer of cluster mass (Rosati et al., 2004, 2009; Mullis et al., 2005; Stanford et al., 2006; Culverhouse et al., 2010; Bartalucci et al., 2018a; Stanford et al., 2005a, 2012, 2014; Brodwin et al., 2006, 2011; Elston et al., 2006; Wilson et al., 2006; Eisenhardt et al., 2008; Muzzin et al., 2009; Papovich et al., 2010; Demarco et al., 2010; Santos et al., 2011; Gettings et al., 2012; Zeimann et al., 2012; Gonzalez et al., 2015; Balogh et al., 2017; Paterno-Mahler et al., 2017).

By comparison, cluster surveys based on the Sunyaev-Zel'dovich Effect (SZE) are particularly advantageous because they can offer redshift-independent mass limit, and a wide survey area. The SZE is the minute distortions in the cosmic microwave background (CMB) spectrum due to the inverse comptonization of CMB photons by hot ICM electrons in a galaxy cluster (Sunyaev & Zeldovich, 1972). The majority of baryonic matter in a galaxy cluster is in the form of hot ICM electrons and diffuse ionized gas, which is not necessarily associated with member galaxies of a cluster.

The observed temperature difference Δ T, relative to the mean CMB temperature, $\mathrm{T_{CMB}}$, is

$$\begin{aligned} \Delta T &= T_{\rm CMB}\ f_{\rm SZ}(x) \int n_{\rm e} \frac{k_{\rm B} T_{\rm e}}{m_{\rm e} c^2} \sigma_{\rm T} dl \\ &\equiv T_{\rm CMB}\ f_{\rm SZ}(x)\ y_{\rm SZ}, \end{aligned} \tag{1.1}$$

where the integral is along the line of sight, $x \equiv h\nu / k_{\rm B} T_{\rm CMB}$, $k_{\rm B}$ is the Boltzmann constant, c the speed of light, $T_{\rm e}$ the electron temperature, $\sigma_{\rm T}$ the Thomson cross-section, $n_{\rm e}$ the electron density. $f_{\rm SZ}(x)$ encodes the frequency dependence of the thermal SZ effect:

$$f_{\rm SZ}(x) = \left(x \frac{e^x + 1}{e^x - 1} - 4 \right) (1 + \delta_{\rm rc}). \tag{1.2}$$

Here, $y_{\rm SZ}$ is the Compton-y parameter, and the term $\delta_{\rm rc}$ accounts for relativistic corrections that are crucial to note here.

The surface brightness of the SZE relative to a CMB spectrum is nearly independent of the distance to the galaxy cluster, because it only depends on the line-of-sight integral of thermal pressure in the ICM. Hence, the SZE signature of a galaxy cluster is a direct tracer of a cluster's mass and temperature. This makes SZE surveys a powerful tool to detect galaxy clusters at all redshifts, due to the fact that SZE probes a nearly redshift independent mass-limited sample, i.e., constrained only by the sensitivity of the instruments in SZE survey observations (Carlstrom et al., 2002a) — this statement holds if the telescope beam size is smaller than the angular size of the cluster ICM (e.g., this is true for the South Pole Telescope and clusters observed out to $z \sim 2$, and not for the Planck telescope). Several SZE surveys are either underway or have reached completion, having produced extensive galaxy cluster catalogs : *Planck* (Planck Collaboration et al., 2014), Atacama Cosmology Telescope (ACT, Marriage et al. (2011)), and the South Pole Telescope (SPT, Bleem et al. (2015a)).

1.2.4 Star Formation in Cluster Members

Studying star formation and mass assembly in galaxies residing in clusters is a path to understanding the assembly of baryons in the clusters themselves. At lower redshifts, clusters are dominated by populations of giant quiescent (and elliptical) galaxies, that have formed most of their stars at higher redshifts and have evolved passively ever since. The Butcher-Oemler effect (Butcher and Oemler 1978) is well observed in clusters, i.e., cores of galaxy clusters at higher redshifts contain a larger fraction of blue star-forming (and emission-line) galaxies than nearby clusters.

Numerous studies have discussed both the timescales of cessation of star formation, and the likely processes responsible for quenching, noting that the efficacy of some of these processes is a strong function of environment (some recent works include Carnall et al. 2018, 2019a; Leja et al. 2019a; Tacchella et al. 2021). Ram pressure stripping is seen to be effective in dense environments — i.e., the cores of galaxy clusters (Gunn & Gott, 1972; Larson et al., 1980; Balogh et al., 2000) — whereas strangulation of a galaxy's cold gas supply through a variety of possible mechanisms, resulting in a slow cessation of star formation, is operative over a larger range of environmental densities (Peng et al., 2015). Other processes that play a role could be galaxy harassment — high speed dynamical encounters that are particularly common in the cluster environment — which could drive the morphological transformation that accompanies the cessation of star formation in quenched systems (e.g., Moore et al. 1998). Internal feedback processes, in particular AGN feedback, are also thought to influence quenching (Davé et al., 2016, 2019; Nelson et al., 2019).

When investigating galaxy clusters, we have the opportunity to utilise the host cluster halo evolution — which is well described and understood from even dark matter-only simulations (see Kravtsov & Borgani 2012 and references therein) — to connect the cluster galaxy populations in antecedent-descendant *clusters*. Galaxy clusters are unique environments with an abundance of observational constraints.

Studies that analyze cluster galaxies (both as individual objects and in aggregate) at $z < 1$ suggest that cluster galaxies conduct rapid and early star formation (at $z >\sim 3$), before quickly settling into a mode of quiescent evolution (Dressler & Gunn, 1982; Stanford et al., 1998a; Balogh et al., 1999; Dressler et al., 2004; Stanford et al., 2005b; Holden et al., 2005a; Mei et al., 2006a; Cooke et al., 2015; Webb et al., 2020; Khullar et al., 2021a). Thus, observations of clusters at higher redshifts should sample an epoch where this star formation — or at least its end stages — is observed *in situ*. Several studies of often small heterogeneous samples of galaxy clusters at $1 < z < 2$ have shown high star formation, AGN activity, and

blue galaxy fraction compared with lower redshifts, as well as an evolving luminosity function (Hilton et al., 2009a; Tran et al., 2010a; Mancone et al., 2010a, 2012a; Fassbender et al., 2011a; Snyder et al., 2012a; Brodwin et al., 2013a; Alberts et al., 2016a). This is evidence that cluster galaxies are undergoing significant stellar mass assembly in this epoch, inviting further investigation into properties of member galaxies as well as the intra-cluster medium (ICM) at $z > 1$.

Studies have also compared galaxy cluster environments with field galaxies to chart the role that these dense environments and deep gravitational potential wells play in the transition of galaxies from star-forming to quiescent (Balogh et al., 1999; Ellingson et al., 2001; Dressler et al., 2013; Webb et al., 2020; Khullar et al., 2021a). To study this evolution, we need to look towards higher redshift galaxies that might be progenitor candidates of lower redshift cluster galaxies. A comparison of star formation histories between low and high redshift galaxies might offer a clue into potential descendent-antecedent connections. For massive cluster galaxies at $z < 1$, high-redshift ($z > 3$) massive galaxies (such as dusty star-forming galaxies (Marchesini et al., 2014) or optically bright systems Khullar et al. (2021b)) could be potential progenitor candidates.

1.3 Galaxies in the Early Universe

The high-redshift Universe — the first few gigayears after the big bang, i.e., $z \sim 3 - 10$ — is currently being extensively explored in the field of extragalactic astrophysics. Galaxies discovered and characterized at the earliest epochs have the ability to shed light on the epoch of reionization (how emission from stellar populations in galaxies reionized the neutral Universe), as well as the physics of escape of Lyman continuum emission and production of ionizing photons from galaxies.

A census and detailed study of a diversity of galaxies (massive or dwarf, bright or faint, blue vs red) will substantially improve (and have substantially improved) our understanding

of whether the earliest formed galaxies have different evolutionary pathways than their lower redshift counterparts. Moreover, if we have any ambition of uncovering the exhaustive set of stellar mass assembly pathways in lower redshift massive galaxies, that knowledge can only be uncovered by a comprehensive understanding of high redshift systems close to the epoch of reionization, and how these galaxies turn into their descendents that we observe in the local Universe. Detailed spectroscopy of high-redshift galaxies can unpack the role of AGN and quasars in the evolution of early Universe galaxies, as well as help describe how luminosity density and the cosmic star formation rate density evolved, and eventually peaked at lower redshift ($z \sim 2$). Due to the redshifts in question, key spectroscopic indicators that allow us to constrain physical properties in these systems are observed in the optical, near and mid-IR. As an example, by z=5, the only bright nebular line that is accessible from ground-based telescopes is the [OII] 3727,3729 Å doublet, and observation of all redward spectral features require space-based telescopes in the near and mid-IR. Additionally, high resolution space telescope observations are required to even marginally resolve these systems.

1.3.1 Gravitational Lensing

Gravitational lensing is an outcome of general relativity, where the trajectories of photons from a background object are bent by the gravity of an intervening massive object. This may result in observations of multiple distorted and magnified images of the background "source" (Einstein, 1936), and the shape of distortions and amplitude of the magnification is dependent upon the intervening "lens" mass and the relative positions of the lens and the background source. Strong gravitational lensing is the name attributed to the specific phenomena of multiple images of the same source being observed around an intervening massive object, such as a galaxy or galaxy cluster.

For point-like sources, strong gravitational lensing produces multiple images, while extended sources are distorted in the shape of bright arcs (more specifically, most arcs are

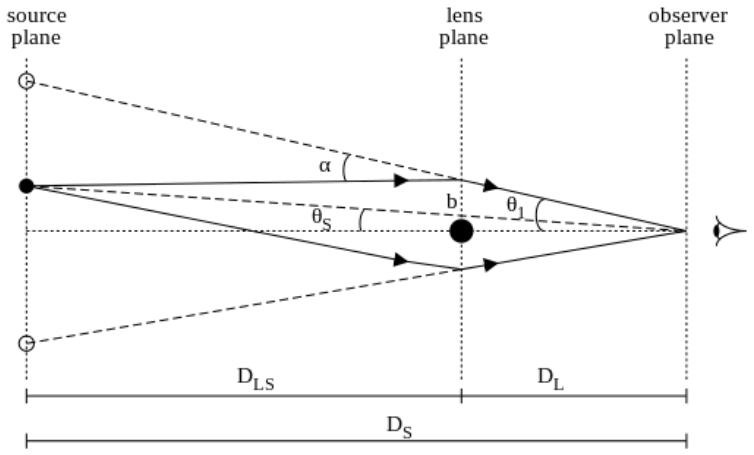

Figure 1.1 Graphical representation of a lens-source system, to aid the lensing formalism described in Section 1.3.1. Image Credit: Krishnavedala (Author, Gravitational lens geometry, Wikimedia Commons; made available under Creative Commons CC0 1.0 license.)

multiple partial images of the extended source). Consider Figure 1.1, which shows the case of light from a point source being lensed by point mass M, where the light is deflected by and bending or deflection angle α:

$$\alpha = 4MG/bc^2, \tag{1.3}$$

where G is Newton's constant, c is the speed of light, and b is the impact parameter (or the distance of closest approach from the point mass M). This is an outcome of general relativity.

There are a few approximations that enable us to quantify the effects of strong gravitational lensing in a galaxy-galaxy lens-source system. Firstly, the lens mass profile is assumed to be analogous to a flat sheet, relative to the distances between source, lens and observer (the thin lens approximation). Moreover, we assume that the lens and source are nearly aligned along the line of sight (i.e., for a given angular separation θ, $\sin(\theta) \sim \theta$).

According to the gravitational lens system schematic in Figure 1.1, if the lens is at distance $D_{\rm L}$, source at distance $D_{\rm s}$, the distance between the lens and source is $D_{\rm LS}$, and $\theta_{\rm s}$ as the angle at which one would see the source behind the lens ($\theta_{\rm s} = 0$ if the source is

directly behind the lens), the bending angle can be re-expressed using the *lens equation* as:

$$\theta_1 - \theta_S = \frac{4G}{c^2}\frac{M}{\theta_1}\frac{D_{LS}}{D_S D_L}. \tag{1.4}$$

We derive the Einstein radius θ_E (limiting case of θ_s=0) as:

$$\theta_E = \left(\frac{4GM}{c^2}\frac{D_{LS}}{D_L D_S}\right)^{1/2}, \tag{1.5}$$

and the lens equation for a point mass is:

$$\theta_1 = \theta_S + \frac{\theta_E^2}{\theta_1}. \tag{1.6}$$

Moreover, gravitational lensing preserves surface brightness, but changes the apparent solid angle of the source, which results in magnification. Via the moments of the lens equation, we can calculate the magnification and/or shear of the image(s) of the lensed background source. See Dodelson (2017) for more details.

There are several astrophysical applications of gravitational lensing. Since the amount of lensing depends on the gravitational potential of the lens, this technique can be used to constrain lens masses. Moreover, multiple bright and magnified images of the same background source can provide spatially resolved information about the internal properties of high-redshift galaxies which would have otherwise not been observed without lensing. Finally, since light rays get delayed by local gravitational potentials of different strengths along their paths to the observer and due to different path lengths, the "time delay" across multiple images of the same source can be observed, and constraints on the cosmological model (including the value of the Hubble constant) used to predict the aforementioned time delays can be measured.

In this work, gravitational lensing is employed as a magnification tool that provides observations of massive galaxies at high redshifts (that may have otherwise been too faint

to observe).

1.4 Thesis Outline

This thesis focuses on the study of stellar mass assembly in the most massive galaxies at different epochs, situated in different environmental conditions. This work uses galaxy cluster members and high-redshift bright gravitationally lensed galaxies as laboratories to infer star formation histories in these massive systems. Chapter 2 describes the photometric and spectroscopic data, as well as analysis techniques used in this work. Chapter 3 describes the discovery and spectroscopic characterization of five $z > 1$ SZ-selected clusters, and Chapter 4 describes the comprehensive work to connect stellar populations in the above $z > 1$ clusters to 800 galaxies residing in lower redshift clusters. Chapter 5 illustrates the discovery of the brightest galaxy in the $z > 5$ Universe. Chapter 6 describes the COOL-LAMPS collaboration and our efforts to build samples of high-redshift lensed quiescent and star forming galaxies, along with new methodologies to conduct fast and efficient SED fitting. In Chapter 7, I summarize this thesis, with a few words on my perspective on the field of observational extragalactic astrophysics.

CHAPTER 2

OBSERVATIONAL DATA AND ANALYSIS TECHNIQUES

In this thesis, I study the properties of both star-forming and quiescent galaxies, across a broad redshift range from 0.3-5, using spectroscopy and imaging from numerous telescopes and instruments. Given this complexity, this chapter describes in some detail the types of data used, and the analysis techniques used to interpret those data to derive various physical properties of the targeted galaxies.

The detailed characterization of stellar populations in galaxies can be conducted from a diversity of observations at different wavelengths and resolutions. The discovery of these systems occurs across a wide range of wavelengths — with optical, infrared (IR) and sub-mm telescopes. Comprehensive follow-up observations allow the detailed study of their properties.

The combination of photometry and spectroscopy can shed light on the internal properties of galaxies, via techniques such as stellar population synthesis (SPS). The stellar mass, ages and chemical properties of differently aged stellar populations, gas and dust within galaxies can be interpreted once an adequate library of empirical/theoretical models exists to map observations to quantitative parameters.

2.1 Building a sample of galaxy clusters

As noted above, galaxies — depending on their spectra — can be selected across a broad range of wavelengths. Galaxy clusters, conversely, are typically selected through specific techniques. An understanding of the selection of galaxies in those clusters also requires an understanding of the cluster selection.

Clusters discovered via the SZE with the South Pole Telescope (SPT, Carlstrom et al. 2002b, 2011a) and the Atacama Cosmology Telescope (ACT, Sifón et al. 2016a) provide a

nearly mass-limited sample of clusters with a redshift-independent mass threshold set by instrument sensitivity. The SZ effect describes the inverse comptonization of CMB photons by free electrons in the ICM of clusters — one detects a deficit (excess) of CMB photons with respect to the mean CMB signal at low (high) frequencies in the mm wavelength regime (see Section 1.2.3 for more details). Thus, this (distance-independent) tool of building a cluster sample that does not directly rely on member galaxy properties enables the study of the member galaxies without any selection bias. Moreover, a lower mass threshold at high redshifts allows us to conduct population-level studies that connect high redshift low mass clusters to low-redshift high mass clusters, much better than cluster samples built via other methods. Recent SZ-based galaxy cluster searches from SPT have taken advantage of this redshift independence to reveal new samples of galaxy clusters at high redshifts (z>$\sim$1 (Bleem et al., 2015b, 2020a; Huang et al., 2020a)), extending the viability of SZ cluster studies to redshifts that have not been previously studied comprehensively in cluster samples. This long redshift baseline and the ability to connect clusters in a descendent-antecedent fashion is a key step forward in cluster galaxy studies.

The galaxy clusters in this thesis' stellar populations study have been drawn from the South Pole Telescope-SZ (SPT-SZ) survey (Bleem et al. 2015b, hereafter B15). The SPT-SZ survey covers 2500 sq. degree in the southern sky at 95, 150, and 220 GHz, with an angular resolution of 1'. The cluster survey catalog contains 677 galaxy cluster candidates with a statistical significance > 4.5. The full cluster catalog is $\sim 100\%$ complete at $z > 0.25$ for a mass threshold of $M_{500c} \geq 7 \times 10^{14}$ M$_\odot$ h_{70}^{-1}. 37 clusters in this sample are at $z > 1$, at a lower mass limit of $M_{500c} \sim 2 \times 10^{14}$ M$_\odot$ h_{70}^{-1}.

2.2 Photometry

Photometry is the measurement of of light from objects in images, typically over specificied wavelength passbands defined in imaging instruments by physical filters. An image of a

galaxy (or a collection of galaxies, such as in a cluster) is used to measure its brightness and morphology. In the chapters that follow, I use both wide-area survey imaging from smaller survey telescopes equipped with extremely wide format mosaiced CCD arrays, and pointed deep follow-up observations from large aperture telescopes.

In different photometric bands/filters, a galaxy emits different fluxes, such that the amplitude and shape of the spectral energy distribution (flux density as a function of wavelength, or SED) can allude to the general properties of stellar populations within the said galaxy. To measure brightness in each filter, we use model photometry tools (e.g., GALFIT Peng et al. (2002)) that produce AB magnitudes for a given galaxy via suitable physical models (e.g., elliptical or sersic (Sérsic, 1963) light distribution in a galaxy).

2.2.1 Galaxy Cluster Members

For detailed characterization of SZ-selected clusters, optical and IR followup imaging is necessary. For cluster studies in this thesis, optical photometry in the *griz* bands was obtained by collaborators through several campaigns, using the CTIO (4 m) facility, ESO/New Technology Telescope (NTT, 3.58 m) or the Magellan/Baade Telescope (6.5 m) in Chile (see Bleem et al. (2015c) for details on observing and data reduction strategies). This was followed up by collaborators with Spitzer/IRAC observations in the 3.6 and 4.5 m bands for NIR photometry, which is crucial for observations of higher redshift clusters for member galaxy candidate selection Ashby et al. (2009); Bleem et al. (2015c).

2.2.2 Gravitationally Lensed Galaxies

Wide-area, multi-band photometric surveys from ground-based telescopes have revolutionized our understanding of high-redshift lensed galaxies. Galaxies that are otherwise distant or dim are now observed as magnified bright and extended sources of emission in the sky due to gravitational lensing. In this thesis, I have aided in the discovery and characterization

of the brightest galaxy at redshifts $z > 5$, as well as rare intermediate-redshift quiescent lensed galaxies. This has been enabled by the availability of new public imaging surveys, in particular DECaLS.

The DECam Legacy Survey (DECaLS) is one part of the DESI Legacy Imaging Surveys (Dey et al., 2019). An optical/IR imaging survey spanning $14,000\,\mathrm{deg}^2$, DECaLS is built of DECam imaging across the northern and southern Galactic caps in the grz bands, incorporating existing imaging in the region. The g, r and z-band depths for the catalogue attached to the latest public data release are g =24.7, r =23.9, z =23.0 AB mag (e.g., the z-band depth is approximately 1 magnitude shallower than other ground-based photometric surveys (e.g., the Dark Energy Survey or DES; Abbott et al. 2018).

I have also collaboratively conducted followup imaging observations to obtain deeper and more precise photometry for these systems, with the Magellan Telescopes (optical $griz$, with PISCO, LDSS3, and IMACS, and infrared $JHKs$, with FourStar Infrared Camera FOURSTAR; Persson et al. 2008).

2.3 Spectroscopy

Spectroscopy is the detection of electromagnetic radiation (flux or flux density) from a galaxy as a function of wavelength, allowing high-resolution measurements of dynamic and chemical properties corresponding to a given galaxy. A galaxy spectrum consists of stellar emission (approximately behaving like emission from a combination of black bodies), nebular line and continuum emission (from hot nebular gas surrounding stars) and absorption (light absorbed or scattered by intervening gas clouds or, light attenuated by dust between the emitter and observer).

2.3.1 Galaxy Cluster Members

The initial motivation for spectroscopy of South Pole Telescope clusters (as well as cluster-scale lenses in our lensed sources studies) is to obtain spectroscopic cluster redshifts. We measure these from spectral emission features from nebulae as well as absorption features from stellar populations and the interstellar medium. Because galaxies in a virialized cluster have peculiar velocities relative to the center of mass of the cluster, their redshifts are clustered. Once we measure spectra of multiple candidate members and obtain their redshifts, this usually results in a robust aggregate cluster redshift (see Section 2.4.1).

In the cluster galaxy analyses that follow, I use low-redshift cluster spectroscopy from the Gemini/GMOS spectrograph obtained by the SPT collaboration (Bayliss et al., 2016a). For high-redshift cluster spectroscopy, I use Magellan/LDSS3 spectra collected and reduced in conjunction with the SPT collaboration. In both spectroscopic datasets, potential red-sequence cluster members were targeted first for slit placement, selected by apparent color, brightness, morphology, and their proximity to the SZ center and galaxy overdensity.

The GMOS spectra were obtained as part of the SPT-GMOS survey (Bayliss et al., 2016a) between 2011 and 2015 to conduct cosmological mass-observable relations studies for SPT clusters discovered in the SPT-SZ Survey (Bleem et al., 2015c). By measuring line-of-sight velocity dispersions (via disentangling cosmological redshifts — and therefore galaxy velocities in the Hubble flow — and pecular velocities of cluster members), Bayliss et al. (2016a) combine these with X-ray and SZ mass proxies to calibrate scaling relations and constrain dark energy. We use spectroscopy of cluster members in 62 galaxy clusters from Bayliss et al. (2016a) and Bayliss et al. (2017a) to constrain cluster galaxy properties via well-tested spectral signatures (see Section 2.4.1 for more information).

Spectroscopy for redshifts $z > 1.2$ SPT clusters were obtained at the 6.5 m Magellan/Clay Telescope between 2014 August and 2015 January using the 600 lines/mm VPH-Red grism on the Low Dispersion Survey Spectrograph—3C (LDSS3C) (typical observed seeing of 1”).

These spectra were primarily used to confirm spectroscopic redshifts using optical absorption and emission features, and at the time of observation were the largest sample of high-redshift massive cluster galaxy spectra confirmed via absorption line spectroscopy (Khullar et al. (2019); presented in Chapter 3).

2.3.2 Gravitationally Lensed Galaxies

To obtain precise spectroscopic redshifts in our lens and high-redshift lensed source studies, we obtained spectra of a) bright lens galaxies (main lens in a galaxy lens system, and brightest cluster galaxies in a cluster lens system) as well as b) prominent bright clumps across arcs (that may correspond to partial but magnified images of stellar populations internal to the lensed galaxies).

Spectra for high-redshift lensed galaxies studied in this work were obtained at the 6.5 m Magellan Telescopes using the spectrographs LDSS3-C and the Inamori-Magellan Areal Camera Spectrograph (IMACS). The Alhambra Faint Object Spectrograph and Camera (ALFOSC) at the 2.6m Nordic Optical Telescope (Canary Islands, Spain), was also used to obtain certain lensed galaxy spectra and measure observed frame optical emission and absorption features.

2.4 Techniques

2.4.1 Redshift Characterization

Measurement of the redshifts of distant galaxies can be conducted with UV, optical and IR spectroscopic observations. The methodology of matching of model and observed spectra of high-redshift galaxies is built upon the idea of the Doppler effect and cosmological redshift. Galaxies in the "Hubble Flow" exhibit a recessional velocity in an expanding Universe (Hubble, 1929; Lemaître, 1927), resulting in a redshifting of rest-frame wavelengths which can be

seen in spectra.

To confirm spectroscopic redshifts for galaxies, I use in this thesis cross-correlation methods, emission and absorption line identification, and Bayesian SED fitting (see Chapters 3, 4, 5 and 6). Prominent rest-frame UV and optical emission and absorption features to measure the redshift are the Lyman-break, Hδ, G-band, the [O II] 3727, 3729 Å doublet emission lines, the molecular CN ((0, 0) violet 3850–3880 Å) feature, and the Ca II HK 3968, 3934 Å absorption lines. Atomic spectral features like [O II], [O III], and H trace the direct light from excited nebular gas around young O, B stars. Atomic Ca II HK and molecular CN ((0, 0) violet 3850–3880 Å) features are pronounced in older galactic stellar populations, coming from K-giant stars that dominate the total flux. For more details, we refer the reader to Bruzual & Charlot (2003) and Conroy (2013).

For cross-correlation redshift analysis, I use RVSAO, an IRAF based programming package that enables redshift characterization via correlation methods in Fourier space. RVSAO estimates a "lag" in Fourier space between a template spectrum (e.g., *fabtemp97*, Kurtz & Mink (1998)) and the observed spectrum, while simultaneously correcting for biases due to prominent emission line features. We also ensure that appropriate spectroscopic uncertainties are utilized, as it is seen empirically that RVSAO specifically underestimates systematic uncertainties by a factor of $\sim$1.7 (Quintana et al., 2000).

I have also cross-checked and confirmed redshift calculations with the Bayesian SED fitting framework `Prospector` (see next section) that simultaneously fits for physical parameters such as stellar mass, ages and metallicities in flux space, and observed wavelengths in wavelength space (and hence directly estimates redshifts with physically motivated uncertainties).

2.4.2 Bayesian Spectral Energy Distribution Fitting

The approach to map a galaxy's physical properties to its photometric and spectroscopic observations via evolutionary "stellar population synthesis" was pioneered by Beatrice Tinsley Tinsley & Gunn (1976); Tinsley (1980) and Hyron Spinrad (Spinrad & Taylor, 1971) in the 1970s-1980s. The idea was to consider that a galaxy's SED (as a reminder: a galaxy's observed flux density as a function of wavelength) comprises emission, attenuation and absorption by a non-linear combination of stellar populations, molecular and ionized gas, and dust, that evolves with age.

Today's SED fitting tools use state-of-the-art statistical techniques to simultaneously fit for multiple physical properties and systematic effects exhibited in observations. These tools map observed photometry and spectroscopy to model libraries built of a) stellar spectral libraries, b) isochrone libraries, and prescriptions for a) the initial mass function (IMF), b) star formation histories (star formation rate as a function of time), c) dust properties and d) metallicity evolution within a given galaxy. These model libraries are often built from theory (where completeness in parameter space is traded off for sometimes aphysical inferences) or empirical observations collected with ground-based telescopes (where physically plausible galaxy parameters and uncertainties are traded off for incompleteness)[1]. For a more comprehensive and detailed review of stellar population synthesis, often used SED fitting tools and the benefits and limitations of using various components of an SED model, please see Conroy (2013) and references therein.

In this work, I employ the Bayesian SED fitting framework `Prospector` (Johnson et al., 2021), that uses the Flexible Stellar Populations Synthesis (`FSPS`; Conroy & Gunn (2010a); Foreman-Mackey et al. (2013)) code in a single self-consistent and flexible inference frame-

1. It is worth noting that significant resources are being utilized towards achieving completeness in stellar populations models' parameter space that reflects the importance of SED fitting as a technique, e.g., the current Space Telescope Science Institute (STScI) director has allocated Director's Discretionary Time for the Hubble UV Legacy Library of Young Stars as Essential Standards (ULLYSES) project (Roman-Duval et al., 2020), to serve as a UV spectroscopic reference sample of high- and low-mass young stars.

work to fit galaxy SEDs. I use `Prospector` to infer simultaneous posterior distributions of parameters such as stellar mass, ages (mass-weighted ages based on simple stellar populations, or complex star formation histories — both parametric and non-parametric), metallicities, dust properties, velocity dispersion, and a host of systematic effects exhibited by UV, optical and IR observations of galaxies. In Chapter 6, I also describe my ongoing work to build efficient SED fitting frameworks using machine learning (ML) and simulation-based inference (SBI), and compare results to Bayesian MCMC inferences of galaxy parameters from SEDs.

CHAPTER 3

CHARACTERIZING THE HIGHEST-REDSHIFT SZ-DISCOVERED GALAXY CLUSTERS

The text of this chapter was adapted from the publication Khullar et al. ApJ 870, 7 (2019).

3.1 Introduction

Observations of galaxy clusters at $z < 1$ suggest that galaxies in clusters form stars in an epoch of early and rapid star formation (at $z > 3$), before quickly settling into a mode of passive and stable evolution (Stanford et al., 1998b, 2005a; Holden et al., 2005b; Mei et al., 2006b). Thus, observations of clusters at higher redshifts should sample an epoch where this star formation − or at least its end stages − is observed *in situ*. Recent studies of modest heterogeneous samples of galaxy clusters at $1 < z < 2$ have shown high star formation and active galactic nuclei (AGN) activity compared with lower redshifts, and a luminosity function that is evolving (Hilton et al., 2009b; Mancone et al., 2010b, 2012b; Tran et al., 2010b; Fassbender et al., 2011b; Snyder et al., 2012b; Zeimann et al., 2012; Brodwin et al., 2013b; Alberts et al., 2014, 2016b). This is evidence that galaxy clusters are undergoing significant mass assembly in this epoch, inviting further investigation into properties of member galaxies and the intra-cluster medium (ICM) at $z > 1$.

Although massive clusters are easy to observe in the local universe, the discovery of clusters with similar properties in the high-redshift Universe is still technically challenging. This is due to two main reasons. First, optical and X-ray fluxes — which are observational tracers of galaxy clusters — decrease at cosmological distances (due to cosmological dimming). Second, massive galaxy clusters are extremely rare at higher redshifts. Thus, surveys that aim to find distant clusters by directly detecting emission from either the ICM or member galaxies must be both wide and deep. Despite these obstacles, the current status of observations

in the $z > 1$ regime is promising, and the science is transforming from the characterization of individual objects to comprehensive analyses of statistically well-defined samples of clusters. A combination of deep X-ray observations (Rosati et al., 2004, 2009; Mullis et al., 2005; Stanford et al., 2006; Culverhouse et al., 2010; Bartalucci et al., 2018a) and optical + near-infrared (IR) imaging and spectroscopy (Stanford et al., 2005a, 2012, 2014; Brodwin et al., 2006, 2011; Elston et al., 2006; Wilson et al., 2006; Eisenhardt et al., 2008; Muzzin et al., 2009; Papovich et al., 2010; Demarco et al., 2010; Santos et al., 2011; Gettings et al., 2012; Zeimann et al., 2012; Gonzalez et al., 2015; Balogh et al., 2017; Paterno-Mahler et al., 2017) has improved our understanding of galaxy clusters that have large X-ray, optical, and IR fluxes at $1 < z < 2$.

Sunyaev-Zel'dovich effect (SZE) cluster surveys from the *Planck* mission (Planck Collaboration et al., 2014), Atacama Cosmology Telescope (ACT, Sifón et al. 2016b; Hilton et al. 2017), and the South Pole Telescope (SPT, Bleem et al. 2015a, hereafter B15) offer a new opportunity to study galaxy clusters selected by their ICM signal. Both ACT and SPT provide a nearly-redshift independent, mass-limited sample of clusters, due to their arcminute angular resolution which is well matched to cluster sizes, with a mass-threshold set by the sensitivity of the instruments (Carlstrom et al., 2002a). Of these, only the SPT-SZ and ACT cluster catalogs yield a significant sample of $z > 1$ clusters.

The 2500 deg^2 South Pole Telescope Sunyaev-Zel'dovich (SPT-SZ) survey catalog contains 677 galaxy cluster candidates with a statistical significance > 4.5, with 37 at $z > 1$ (B15) based primarily on photometric red-sequence redshifts. Spectroscopic confirmations along with astrophysical and cosmological analyses of multiple high redshift and massive galaxy clusters from the SPT-SZ survey, many unique to the SPT-SZ sample, have been previously published (Brodwin et al., 2010a; Stalder et al., 2013a; Ruel et al., 2014a; Bayliss et al., 2014b, 2016b; McDonald et al., 2013a, 2017a). This includes spectroscopic confirmation of two particularly distant massive clusters at $z = 1.322$ (Stalder et al., 2013a) and $z =$

Table 3.1. Galaxy Clusters in the SPT-SZ High-z Cluster Sample[a]

Cluster ID (SPT Cat.)	RA (J2000)	Dec (J2000)	ξ[a]	Redshift[b]	M_{500c} ($10^{14}\ h_{70}^{-1}\ M_\odot$)
SPT-CL J2341-5724	355.3568	−57.4158	6.87	1.38 ± 0.08	3.05 ± 0.60
SPT-CL J0156-5541	29.0449	−55.6980	6.98	1.22 ± 0.08	3.63 ± 0.70
SPT-CL J0640-5113	100.0645	−51.2204	6.86	1.25 ± 0.08	3.55 ± 0.70
SPT-CL J0607-4448	91.8984	−44.8033	6.44	1.43 ± 0.09	3.14 ± 0.64
SPT-CL J0313-5334	48.4809	−53.5781	6.09	1.37 ± 0.09	2.97 ± 0.64
SPT-CL J0205-5829	31.4428	−58.4852	10.50	1.322[c]	4.74 ± 0.77
SPT-CL J2040-4451	310.2483	−44.8602	6.72	1.478[d]	3.33 ± 0.66
SPT-CL J0459-4947	74.9269	−49.7872	6.29	1.70 ± 0.02[e]	2.67 ± 0.55

[a]SZ significance from Bleem et al. 2015a. See Section 3.2.1 for more details.

[b]Photometric or previously published.

[c]Spectroscopic follow-up in Stalder et al. 2013a.

[d]Spectroscopic follow-up in Bayliss et al. 2014b.

[e]Preliminary result from Mantz et al (in prep).

Note. — Galaxy clusters in bold are analyzed in this paper.

1.478 (Bayliss et al., 2014b). This paper provides spectroscopic confirmation and optical-NIR spectroscopic follow-up of a further five SPT-SZ clusters at $1.25 < z < 1.5$.

This paper is organized as follows: Section 3.2 describes the sample selection, optical-NIR imaging, and optical spectroscopy used to derive spectroscopic redshifts for the clusters. In Section 3.3, we describe the spectral analysis performed on the data from member galaxies of the sample population, while Section 3.4 describes the resulting spectroscopic redshifts and confirmation of member galaxies. In Section 3.5, we consider several analyses of these data (cluster velocity dispersions, a stacked velocity-radius diagram, and a stacked spectral analysis) which demonstrate — despite the challenge presented by spectroscopy of individual member galaxies in these distant systems — that the spectroscopic results are as expected. We summarize our results in Section 3.6.

Magnitudes in this work have been calibrated with respect to Vega. The fiducial cosmology model used for all distance measurements as well as other cosmological values assumes a standard flat cold dark matter universe with a cosmological constant (ΛCDM), $H_0 = 70$ km s^{-1} Mpc^{-1}, and matter density $\Omega_{\rm M} = 0.30$. All Sunyaev-Zel'dovich (SZ) significance-based masses from B15 are reported in terms of $M_{\rm 500c,SZ}$, i.e., the SZ mass within $R_{\rm 500c}$, defined as the radius within which the mean density ρ is 500 times the critical density $\rho_{\rm c}$ of the universe.

3.2 Observations and Data

3.2.1 Cluster Sample Selection and Imaging Follow-up

The 2500 deg^2 SPT-SZ survey (Carlstrom et al., 2011b), completed in 2011, discovered 37 galaxy clusters with high significance at $z > 1$, via the SZE. These clusters were detected via the SPT-SZ campaign that observed the CMB at frequencies 95, 150, and 220 GHz. The full cluster catalog, B15, is $\sim 100\%$ complete at $z > 0.25$ for a mass threshold of $M_{\rm 500c} \geq$

7×10^{14} $M_\odot$ h_{70}^{-1}. Survey strategy and analysis details can be found in previous work by the SPT collaboration (Staniszewski et al., 2009; Vanderlinde et al., 2010; Williamson et al., 2011; Reichardt et al., 2013).

For optical and near-IR (NIR) photometric follow-up of this cluster sample, several programs were initiated (see Song et al. 2012a and B15 for details on observational strategies). Optical photometry in the *griz* bands was obtained for the sample clusters using either the CTIO (4m) facility, ESO/New Technology Telescope (NTT, 3.58m) or the Magellan/Baade Telescope (6.5m) in Chile, to depths that can detect galaxies at $0.4L_*$ at $z = 0.75$ at 5σ in red bands. This was followed up by Spitzer/IRAC observations in the 3.6μm and 4.5μm bands for NIR photometry, which is crucial for observations of higher redshift clusters for member galaxy candidate selection. The final NIR images detect $z = 1.5$ $0.4L_*$ galaxies at a 10σ significance.

The IR and optical photometry is complemented by observations in bands $J, H, H-$long and K_s bands (modified versions of the standard H and K filters, respectively), using the wide-area near-IR instrument FOURSTAR on the Magellan/Baade telescope (Foreman-Mackey et al., 2013). Data were acquired between January 2014 − January 2016; the data used here are a small subset of the overall dataset, with details of the reduction and analysis to be provided in a future paper (Bayliss et al., in prep). Deep optical photometric follow-up was also acquired for four of the five clusters discussed in this paper using the simultaneous *griz* imager Magellan/PISCO (Stalder et al., 2014a) on 2 November 2016. Deep *HST*/WFC3 photometry in the F814W and F140W filters (PI: Strazzullo, HST Cycle 23 program) is available for the fifth cluster, SPT-CL J0607-4448. RGB images for the sample clusters are shown in Figure 3.1.

The cluster sub-sample analyzed in detail here comprises five of the eight most massive $z > 1.2$ clusters from the SPT-SZ sample, all of which have deep *Chandra* X-ray imaging (McDonald et al., 2017a). The remaining three are SPT-CL J2040-5541 (spectroscopically

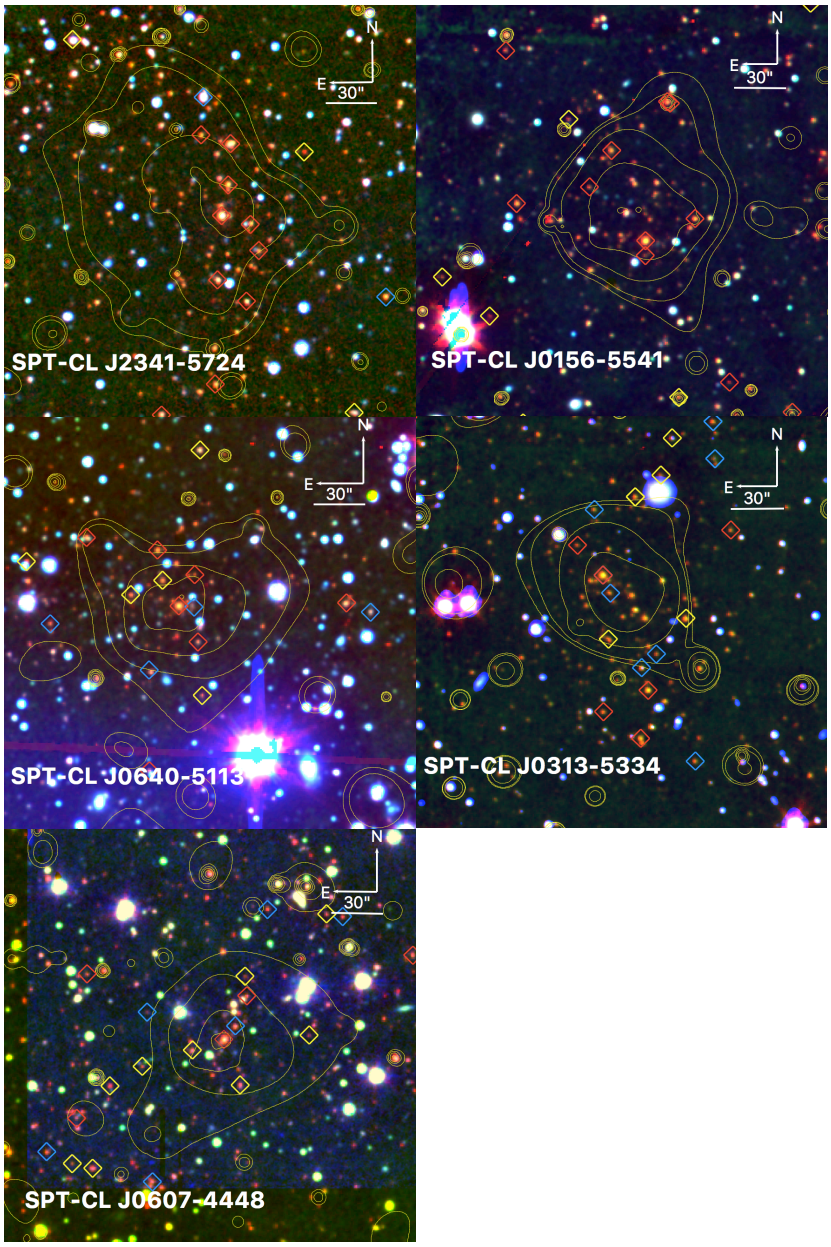

Figure 3.1 RGB 4 × 4 images for the sample clusters. Data are *Spitzer* IRAC 3.6 (red channel), Magellan/FOURSTAR J,H or Ks (green channel), and Magellan/PISCO z (blue channel), except for SPT-CL J0607-4448, for which the blue channel is ESO/NTT z band data. Images are centered on their SZ centers. Diamonds indicate all objects targeted for spectroscopic observations. Red diamonds indicate spectroscopically confirmed cluster members (see Sections 3.3 and 3.4). Yellow diamonds indicate objects for which no redshifts could be measured, while blue diamonds indicate confirmed field galaxies. Contours are drawn from smoothed *Chandra* X-ray data for these clusters (McDonald et al., 2017a), spaced equally in $\log_{10}$(flux) from the lowest discernible value that isolates the cluster, up to just beyond the peak of diffuse emission from the cluster.

confirmed at $z = 1.478$ in Bayliss et al. 2014b), SPT-CL J0205-5829 (spectroscopically confirmed at $z = 1.322$ in Stalder et al. 2013a), and SPT-CL J0459-4947, for which current data provides an X-ray spectroscopic redshift of 1.71 ± 0.02 (Mantz et al., 2020). This collection of clusters is referred to as the "SPT High-z Cluster" sample.

In Section 3.2.2, we describe the spectroscopic optical observations of this five cluster sub-sample. The cataloged properties of these five clusters, and the further three systems that complete the set of the most massive high-redshift clusters in the SPT-SZ sample, are reproduced from B15 in Table 3.1. The photometric data used for constructing RGB images in this work are summarized in Table 3.2.

3.2.2 Spectroscopy: Optical and Near-IR

Spectral Observations

The primary motivation of optical and NIR follow-up of this cluster sample is securing spectroscopic redshifts of clusters and their member galaxies. Optical spectroscopy of these five clusters was carried out between August 2014 and January 2015 on the 6.5m Magellan/Clay Telescope using the 600 lines/mm VPH-Red grism on the Low Dispersion Survey Spectrograph[1] – 3C (LDSS3C) in Normal mode (as opposed to nod-and-shuffle). These data represent some of the earliest spectroscopy acquired with the new LDSS3C system, and include both unfiltered spectra, and spectra acquired using the OG590 order separating filter — the latter being used to remove second order contamination in cluster spectra where imaging showed higher blue-end flux.

The slits for target galaxy spectra were typically cut 6" long (along the spatial axis) on the mask and 1" wide (along the dispersion axis); LDSS3C has a scale of 0.188"/pixel. In most instances, the target galaxy was positioned at the slit center, with some misalignment

1. http://www.lco.cl/Members/gblanc/ldss-3/ldss-3-user-manual-tmp

on the spatial axis tolerated in order to optimize slit packing. Square boxes, typically 6 per mask, were used to target nearby stars for mask alignment on the sky. Spectra of individual galaxies typically cover the wavelength range $7500-10000$Å, with a typical exposure time of 7200s and an observation airmass of $\sim 1.2-1.5$. The typical seeing during the observations was ~ 1".

Designing Spectroscopic Masks

Potential red-sequence cluster members were targeted first for slit placement, selected by apparent color, brightness, morphology, and their proximity to the SZ center and galaxy overdensity. Further slits were placed on fainter or bluer galaxies.

Some spatial misalignment ($\sim$ 1/10th of an arcsecond) was allowed to optimize slit packing. This process typically results in an elongated (rather than circular) layout of targeted galaxies, as can be seen in Figure 3.1. In most cases, a slit was placed on any apparent brightest cluster galaxy (BCG).

3.3 Spectral Analysis

3.3.1 Spectra Reduction

The spectra were processed using The Carnegie Observatories System for Multi-Object Spectroscopy (COSMOS)[2] reduction package, which is specifically designed to reduce raw spectra acquired using the Magellan Telescopes.

We describe the data reduction briefly below. All images were de-biased using bias frames acquired each afternoon. We used a HeNeAr comparison arc line for wavelength calibration. The analysis is focused on the range where the VPH-red grism is most sensitive and over which we expect useful features from red member galaxies : 7500-10000Å. A flat field image

2. http://code.obs.carnegiescience.edu/cosmos

Table 3.2. Photometric Data in this study

Cluster Name	Imaging (RGB) (Telescope and Instrument)
SPT-CL J2341-5724	Spitzer/IRAC 3.6μm Magellan/FOURSTAR J Magellan/PISCO z
SPT-CL J0156-5541	Spitzer/IRAC 3.6μm Magellan/FOURSTAR H Magellan/PISCO z
SPT-CL J0640-5113	Spitzer/IRAC 3.6μm Magellan/FOURSTAR J Magellan/PISCO z
SPT-CL J0607-4448	Spitzer/IRAC 3.6μm Magellan/FOURSTAR J ESO/NTT z
SPT-CL J0313-5334	Spitzer/IRAC 3.6μm Magellan/FOURSTAR Ks Magellan/PISCO z

Note. — See Section 3.2.1 for more details on imaging follow-up of sample clusters.

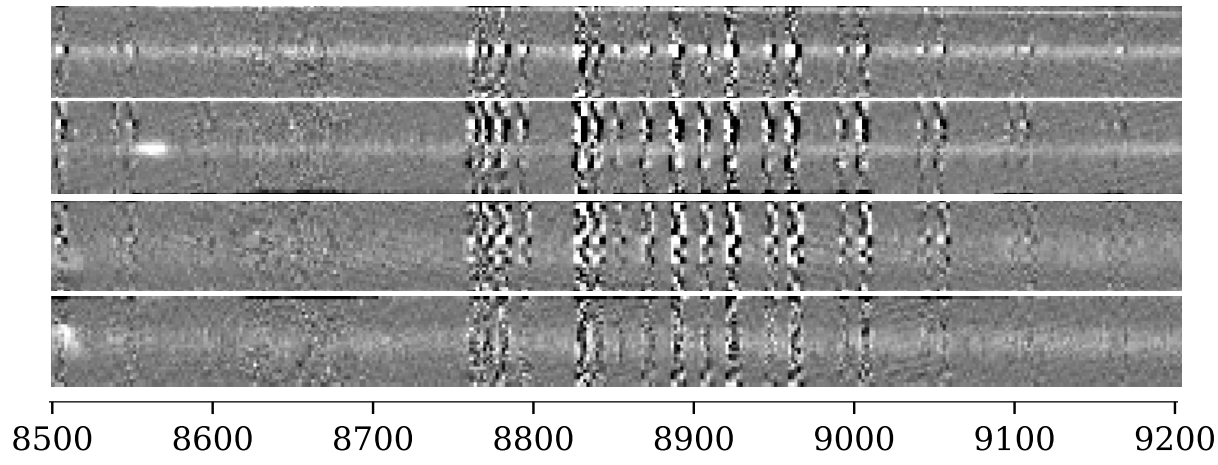

Figure 3.2 Example of 2D spectra used in the analysis described in Section 3.3, for four candidate member galaxies of the cluster SPT-CL J0156-5541. The vertical direction is the spatial dimension, and the horizontal direction is the dispersion axis, which runs from $8500-9200$Å from left to right. Emission features ([OII], λ3727,2729Å doublet at restframe) can be seen in the 8500-8600Å region.

acquired temporally adjacent to each science frame was used to define the spectral trace for each slit. This flat image was also used to flat-field the slit response. Sky subtraction was performed by fitting a one-dimensional third-order spline along the dispersion axis, following the techniques outlined in Kelson (2003). Different exposures of the sky-subtracted science spectra were stacked and 2D cosmic ray cleaning was performed by outlier rejection. COSMOS also generates a noise image that is dominated by photon noise in bright sky lines at these wavelengths.

Figure 3.2 shows examples of 2-D sky-subtracted spectra from 4 potential member galaxies of the galaxy cluster SPT-CL 0156-5541. The y-axis depicts the spatial width of individual slits, against the horizontal dispersion axis (or wavelength), over the wavelength range 8500-9200Å. Emission features ([OII] λ3727,2729Å doublet) and a strong spectral continuum can be clearly seen in some cases. It is crucial to note that there are sections of the spectra in the wavelength range of interest that are dominated by poor sky subtraction with significant systematics. A thorough exploration of the tunable parameters available in the COSMOS reduction package did little to ameliorate this − the poor sky subtraction is not due to an

insufficient description of the slit geometry. In principle, fringing could contribute to this effect, but the LDSS3C detector is a thick fully depleted CCD, the same as the chips used in the Dark Energy Camera (Flaugher et al., 2015), and is not expected to show fringing at this level. Our current understanding is that these artifacts are predominantly the result of slit roughness, and are not fully removed by flat-fielding because the roughness produces both a transmission variation and small scale variation in the wavelength solution. The quality of 2D spectra is a major factor in selecting analysis strategies for 1D spectra, which are described in the following sections.

Table 3.3. Spectroscopic Redshifts of Member Galaxies

Cluster Name	Galaxy RA (J2000)	Galaxy Dec (J2000)	z	δz	Principal Spectral Feature
SPT-CL J2341-5724	23 : 41 : 24.792	−57 : 25 : 01.25	1.2570	0.0010	Ca II H&K
SPT-CL J2341-5724	23 : 41 : 24.077	−57 : 24 : 19.71	1.2610	0.0020	Ca II H&K
SPT-CL J2341-5724	23 : 41 : 29.282	−57 : 26 : 56.12	1.2550	0.0010	Ca II H&K
SPT-CL J2341-5724	23 : 41 : 24.277	−57 : 24 : 43.50	1.2582	0.0020	Ca II H&K
SPT-CL J2341-5724	23 : 41 : 25.135	−57 : 25 : 38.42	1.2501	0.0008	Ca II H&K
SPT-CL J2341-5724	23 : 41 : 25.396	−57 : 26 : 38.72	1.2510	0.0030	Ca II H&K
SPT-CL J2341-5724	23 : 41 : 23.082	−57 : 25 : 50.93	1.2581	0.0004	Ca II H&K
SPT-CL J2341-5724	23 : 41 : 22.732	−57 : 25 : 06.47	1.2638	0.0016	Ca II H&K
SPT-CL J2341-5724	23 : 41 : 26.185	−57 : 24 : 14.38	1.2687	0.0008	Ca II H&K
SPT-CL J2341-5724	23 : 41 : 22.169	−57 : 25 : 21.68	1.2701	0.0006	Ca II H&K
SPT-CL J0156-5541	01 : 56 : 09.109	−55 : 42 : 10.51	1.2935	0.0015	Ca II H&K
SPT-CL J0156-5541	01 : 56 : 03.382	−55 : 43 : 32.36	1.2877	0.0050	[OII]

[a]Second trace of galaxy that fell serendipitously into the slit. Possible member galaxy.

[b]BCG of SPT-CL J0607-4448, confirmed after revisiting the spectrum (See Section 3.5.2 for details).

Note. — Spectroscopic redshifts of member galaxies of sample clusters, in increasing order of the cluster redshifts. Also mentioned are the spectral features used to determine each galaxy's redshift. See Section 3.3 and 3.4 for more details.

Note. — For the full version of the table with spectroscopic redshifts of all member galaxies in SPT high-redshift clusters, please refer to the publication in The Astrophysical Journal (Khullar et al., 2019).

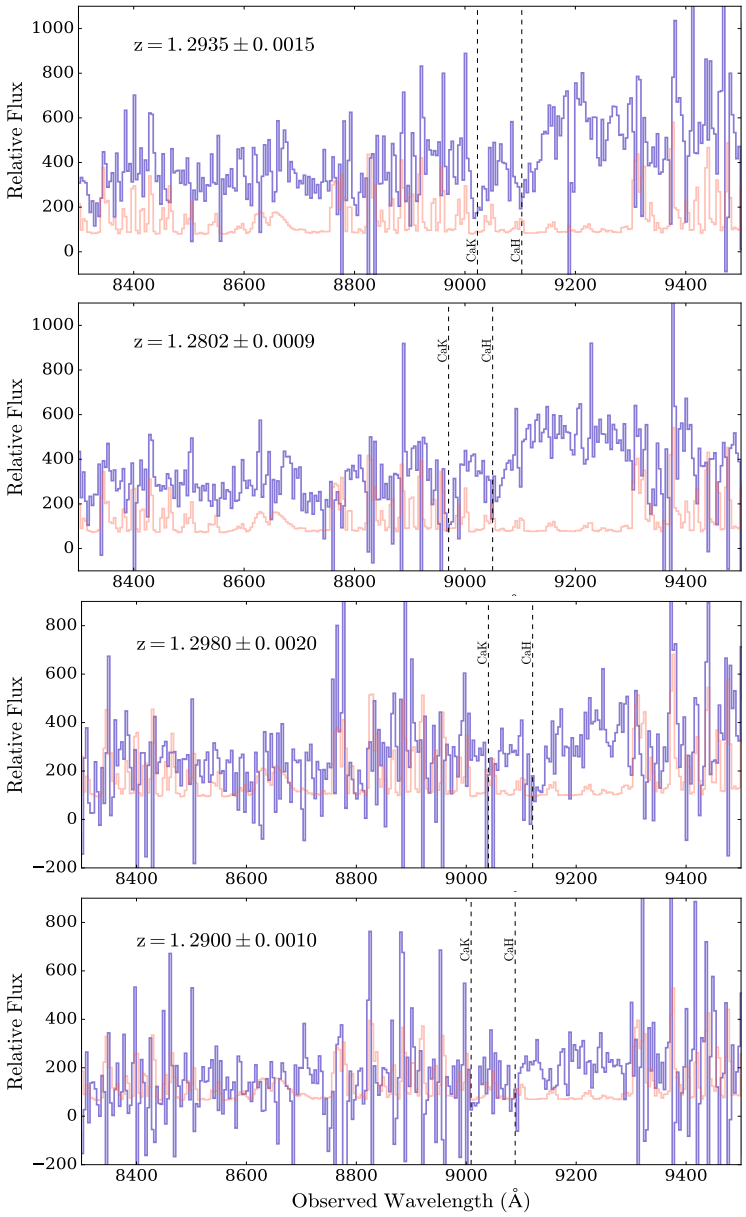

Figure 3.3 Extracted 1-D spectra (purple) for 4 member galaxies of the cluster SPT-CL J0156-5541 (see Table 3.3), along with 1σ uncertainties (orange). Ca II H&K absorption features are indicated (black dashed lines), corresponding to robust redshift fits from RVSAO cross-correlation. Redshift values reported in this figure are final redshifts from the combined RVSAO and line identification analyses.

3.3.2 One-dimensional Spectra

Two-dimensional spectra are condensed into one dimensional spectra for analysis using the IRAF/NOAO package *apall* that fits polynomial functions to the spectral continuum (along the dispersion axis) in individual 2D spectra. Along the spatial axis, the process involved clipping slit edges for defects, and fitting a boxcar model to the counts distribution. At any wavelength, the RMS of the sky subtracted residuals defines the uncertainties.

3.3.3 Extracting Redshifts and Spectral Features

Due to sub-optimal sky subtraction in the LDSS3 pipeline, the resulting 1D wavelength-calibrated (albeit not flux-calibrated) spectra are dominated by systematic noise at some wavelengths, and not suitable for sophisticated spectral analysis techniques that can be employed to analyze galaxy spectra (e.g. principal-component analysis). Several strong spectral features are apparent in some spectra, and we base much of the analysis that follows on the detection of these features, namely the [OII] $\lambda\lambda$ 3727, 3729Å doublet emission lines, and Ca II H&K $\lambda\lambda$ 3968, 3934Å absorption lines. Atomic spectral features like [OII], [OIII], and Hβ (more on this in Section 3.5.5) trace the direct light from excited nebular gas around young O,B stars that is unobscured by dust in star-forming regions in galaxies. Atomic Ca II H&K and molecular CN ((0,0) violet 3850-3880Å; also discussed in Section 3.5.5) features are pronounced in K stars in galaxies, tracing older stellar populations in galactic environments. For more details, we refer the reader to Bruzual A. & Charlot 1993.

28 out of 44 galaxies were confirmed via Ca II H&K, while 16 redshifts were measured via [OII] as the principal spectral feature. In the case of some passive galaxies, a modest Hδ 4102Å line may also be observed corresponding to the Ca II H&K-based redshifts, but not extracted independently. These spectral features were first identified visually in both 2D and 1D spectra, and analysed using two separate methods that are described below. It is important to note that spectral features and redshifts can robustly be identified without

flux calibration of spectra (see further discussion in Section 3.5).

Redshifts from Cross-Correlation: RVSAO

We use the Harvard Smithsonian Astrophysical Observatory's Radial Velocity (RVSAO) IRAF package (Kurtz & Mink, 1998) to implement a cross-correlation analysis between our wavelength-calibrated 1D spectrum and a galaxy template spectrum. To this end, we employed a standard template, *fabtemp97*, that contains absorption features commonly seen in spectra of cluster member galaxies. For the low S/N data at our disposal, we use the Ca II H&K absorption lines at rest-frame wavelengths of $\lambda 3968, 3934$Å which fall in the observer-frame wavelength range of 8800-9400Å for the redshifts of our sample clusters. Challenges in obtaining the redshift solutions for our dataset via this method are further discussed in Section 3.4.

Redshifts from Line Identification

In order to estimate redshifts as an independent probe of low-S/N, sparsely featured spectra, and to substantiate our RVSAO redshift measurements in moderate- and high- S/N spectra, we use the detections of [OII] $\lambda\lambda$ 3727,3729Å doublet emission features, which fall in the observer-frame wavelength range of 8300-8700Å for the redshifts of our sample clusters. Since the dispersion of our 1D spectra is 2Å/pixel, we do not expect to resolve individual lines in this doublet feature. However, the width of the features we identify as [OII] emission is consistent with a redshifted blended [OII] doublet line profile. In our analysis, we also consider the uncertainty — albeit typically subdominant — in the median wavelength of the blended [OII] doublet feature, due to the range in the [OII] doublet line ratio from varying physical conditions. In most cases where a single emission feature is used to characterize the galaxy redshift, we are able to visually confirm a 4000Å break at the observed wavelength corresponding to the redshift candidate. In one case (a galaxy observed within the field-of-

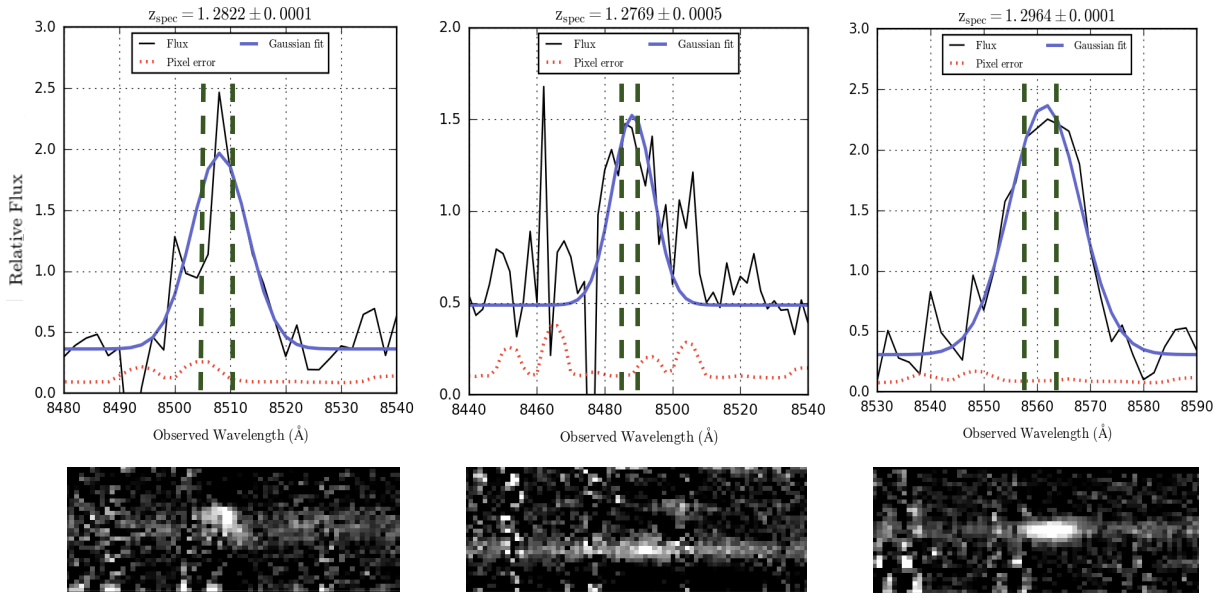

Figure 3.4 *Upper panels*: Examples of individual 1D spectra (black solid line) for individual member galaxies of SPT-CL J0156-5541 (see Table 3.3) that show strong [OII] emission lines. Uncertainties are indicated with red dotted lines. The main emission feature reflects the emission from the [OII] 3727,3729Å doublet, which is blended at our resolution. The mean redshift (corresponding to a rest-frame wavelength of 3728.1Å) is used to constrain spectroscopic redshifts for these galaxies. The dashed vertical lines indicate the observed wavelengths of the two lines in the [OII] doublet. The purple curves are Gaussian fits to the emission features. *Lower panels*: 2D spectra corresponding to the galaxies above. The lower central panel contains two [OII]-emitting cluster members serendipitously observed with the same slit.

view of SPT-CL J0156-5541), this clear a diagnosis was not possible, i.e., the emission feature could potentially correspond to an [OIII], Hβ or [OII] emission peak. [OIII] was disfavored because it is generally accompanied by a blueward Hβ peak, that was not observed. Hβ was ruled out because a nominal redward [OIII] peak was not seen, and the existence of an [OII] peak corresponding to the cluster redshift (confirmed by 14 other cluster members in the field-of-view) increased our confidence in this feature being attributed to [OII].

We also independently analyze our sample spectra using a custom IDL code (from here on, *customcode*) designed to help identify multiple low S/N spectral features. This custom code allows for the joint identification of multiple features by direct comparison to the data

while considering both the S/N and regions contaminated by sky-lines (also see Bayliss et al. 2016b). We visually examined each spectrum, with typically multiple redshift solutions considered to fit apparent spectral features present in the data. Final redshifts were derived from the median of the individual line fits, with the variance providing an estimate of redshift uncertainties.

We discuss the methodology of calculating uncertainties (provided in Table 3.3) in Section 3.4.2.

3.4 Data Products and Results

3.4.1 Spectroscopic redshifts of member galaxies

Table 3.3 contains galaxy coordinates and spectroscopic redshifts for all galaxies being considered as member galaxies for our 5 sample clusters. Also mentioned are the spectral features that were used to characterize the redshift. The total number of target galaxies upon which slits were placed is 109, excluding objects that serendipitously fell onto the slit. Of these, we consider 39 redshifts to be of high confidence. In addition, we include 4 galaxies with lower confidence redshifts, that correspond to measurements with higher uncertainties than are usual for spectroscopic redshifts for galaxies ($\Delta z > 0.002$). We also include the moderately robust redshift for the brightest cluster galaxy (BCG) in SPT-CL J0607-4448 (see Section 3.5.2 for a detailed discussion). Inclusion of these 5 galaxies does not affect the scientific results of this analysis.

Figure 3.3 shows examples of one-dimensional spectra of 4 member galaxies of SPT-CL J0156-5541 at $z = 1.2935$, 1.2802, 1.2980 and 1.2900, along with 1σ pixel errors as a function of wavelength. The absorption features corresponding to Ca II H&K can be observed, indicating the presence of a dominant older stellar population.

Some of the spectra correspond to non-member galaxies (foreground or background) as

well as stars. We describe non-member galaxy spectra in Table 3.4. This list of galaxies includes a $z = 2.48$ background galaxy with potential FeII/MgII outflows. This galaxy sits at a projected distance of 12" from the SZ center of SPT-CL J0640-5113; given the mass of the cluster this implies at least modest magnification due to lensing, though there is no indication in present data of significant shear or other suggestions of strong lensing effects. Of all the background galaxies identified, this galaxy has the most favorable geometry for strong lensing, and so we note it here for future reference. One field galaxy shows signatures of [NeIII] that may be associated with AGN activity.

Another background galaxy that was spectroscopically confirmed in the field of SPT-CL J0313-5334 is a distant Lyα emitter (LAE) at $z = 6.15$; this galaxy shows little continuum in available imaging, and was found as an additional source in a slit targeting a potential cluster member (itself not confirmed by these data). The observed serendipitous line shows the asymmetry typical of distant LAEs, and that location on the slit shows no other spectral features, making a distant LAE the most likely interpretation.

3.4.2 Redshift uncertainties

Many of the extracted 1D spectra have significant sky-subtraction residuals. Thus, a differentiation between statistical and systematic errors across the different analysis methods is needed to comprehensively quantify the redshifts.

The median cross-correlation uncertainty reported by RVSAO is $\Delta z \sim 10^{-5} - 10^{-4}$, whereas the combined median line fit uncertainty (from *customcode*) is $\Delta z \sim 10^{-4} - 10^{-3}$. The specific value and the ratio of uncertainties from the two methods for an individual spectrum depends on the S/N of the spectrum. Uncertainties in flat-fielding and wavelength calibration for these spectra also contribute to systematic uncertainties ($\Delta z \sim 10^{-4}$ each). The RVSAO code is known to underpredict uncertanties by at least a factor of 2 even absent any systematic uncertainties (Quintana et al., 2000; Bayliss et al., 2016b).

Table 3.4. Spectroscopic Redshifts of Field Galaxies in the Dataset

Spectroscopic Mask ID	Galaxy RA (J2000)	Galaxy Dec (J2000)	z	δz	Principal Spectral Feature
SPT-CL J0640-5113	06 : 40 : 25.283	−51 : 13 : 14.46	0.6404	0.0001	[OIII]
SPT-CL J0640-5113	06 : 40 : 05.611	−51 : 13 : 07.66	0.8189	0.0002	Hβ / [OIII]
SPT-CL J0640-5113	06 : 40 : 16.445	−51 : 13 : 04.79	2.4840	0.0010	FeII / MgII
SPT-CL J0640-5113	06 : 40 : 19.209	−51 : 13 : 41.13	1.3590	0.0010	Ca II H&K
SPT-CL J0607-4448	06 : 07 : 33.586	−44 : 47 : 49.66	1.4933	0.0005	Ca II H&K
SPT-CL J0607-4448	06 : 07 : 38.992	−44 : 47 : 59.12	1.7181	0.0004	[OII]
SPT-CL J0607-4448	06 : 07 : 24.579	−44 : 47 : 26.57	1.4716	0.0011	Ca II H&K
SPT-CL J0607-4448	06 : 07 : 28.380	−44 : 47 : 03.95	1.3078	0.0013	Ca II H&K
SPT-CL J0607-4448	06 : 07 : 42.238	−44 : 47 : 37.27	1.4787	0.0004	[OII]
SPT-CL J0607-4448	06 : 07 : 42.844	−44 : 48 : 59.94	1.4965	0.0004	[OII] / Hδ
SPT-CL J0313-5334	03 : 13 : 49.369	−53 : 32 : 45.96	1.0926	0.0008	Ca II H&K / G-band
SPT-CL J0313-5334	03 : 13 : 49.369	−53 : 32 : 45.96	0.86851[c]	0.0001	[OIII] / Hβ
SPT-CL J0313-5334	03 : 13 : 49.248	−53 : 33 : 07.39	1.0680	0.0001	Hg / Hβ / [OIII]
SPT-CL J0313-5334	03 : 13 : 49.248	−53 : 33 : 07.39	1.3586	0.0003	[OII]
SPT-CL J0313-5334	03 : 13 : 57.024	−53 : 33 : 36.79	1.3029	0.0008	[OII]
SPT-CL J0313-5334	03 : 13 : 56.472	−53 : 34 : 14.611	1.2320	0.0010	[OII]
SPT-CL J0313-5334	03 : 13 : 55.993	−53 : 34 : 24.96	1.2313	0.0003	[OII] / Hδ
SPT-CL J0313-5334	03 : 13 : 53.040	−53 : 35 : 00.24	1.2150	0.0010	[OII]
SPT-CL J0313-5334	03 : 13 : 53.982	−53 : 35 : 08.11	1.2620	0.0004	[OII]
SPT-CL J0313-5334	03 : 13 : 50.521	−53 : 36 : 02.16	6.1480	0.0010	Lyα
SPT-CL J0313-5334	03 : 13 : 56.017	−53 : 36 : 59.91	1.1591	0.0006	Ca II H&K

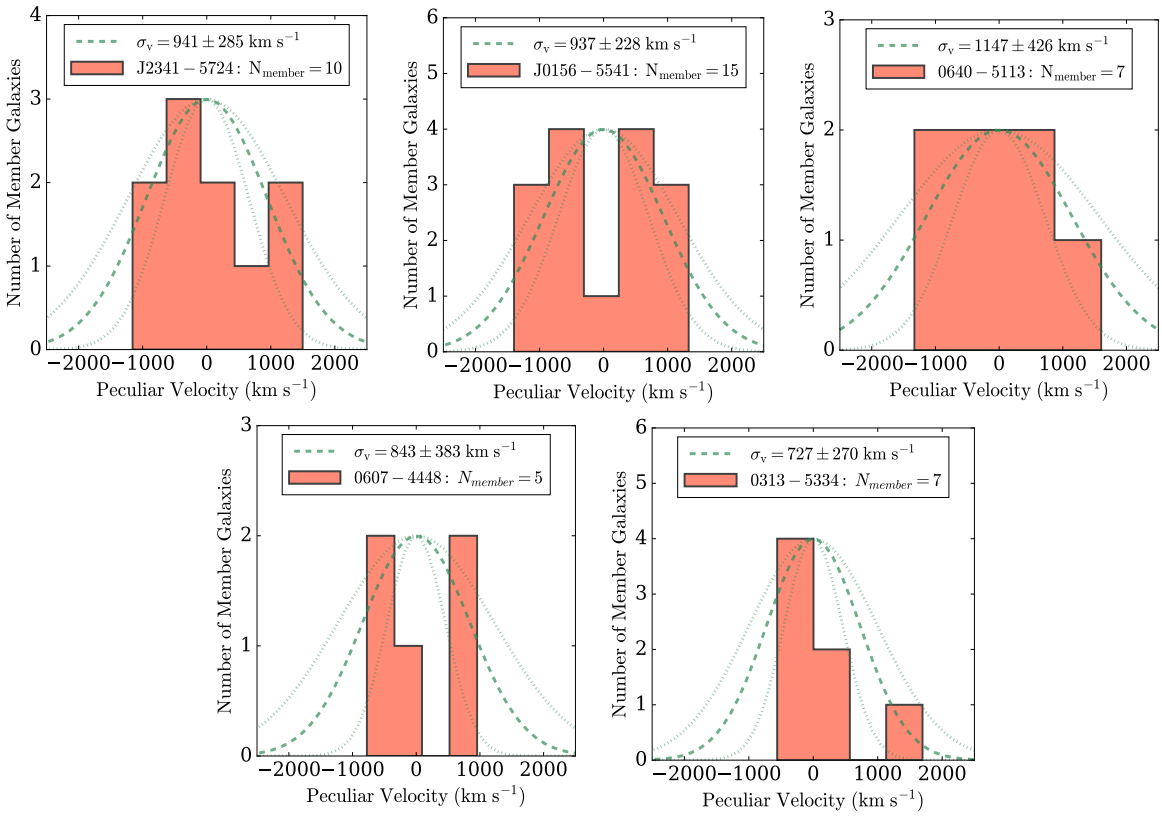

Figure 3.5 Histogram of peculiar velocities (in orange) from the 5 sample clusters (with a total of N=44 galaxies with their respective peculiar velocities). Over-plotted is a Gaussian distribution fit of member galaxy velocities with the standard deviation of $\sigma_{v,G}$ (in dotted green, mean with uncertainties) and a normalization factor corresponding to the maxima of bin counts. See Table 3.5 for details on dispersions and masses of individual galaxy clusters.

Accounting for systematic uncertainties involved requires a discussion of the RVSAO pipeline. Details of the functioning of RVSAO and physical motivations behind the algorithm are given in Kurtz & Mink (1998) and Tonry & Davis (1979), but it is worth revisiting some aspects of the pipeline and choice of parameters that are relevant to the redshift extraction at hand. RVSAO calculates redshifts based on a modified Maximum-Likelihood Estimator, that generates errors based on a cross-correlation peak width obtained from processing an input spectrum. RVSAO assumes every spectral pixel contains a flux value with uniform uncertainty,which limits our ability to interpret RVSAO output uncertainties physically, since our observed spectra have uncertainties that vary significantly with wavelength.

This is best observed in our analysis if each galaxy spectrum is run through RVSAO over multiple trials, in which most parameters are kept fixed except the following: number of columns in which the data is re-binned in Fourier space, number of times the template spectrum is required to pass through the input galaxy spectrum, wavelength range in which cross-correlation is to be considered, initial redshift guess, and selection cutoffs for Fourier modes to be considered (highest and lowest). The results can be sensitive to these parameters, and the scatter across redshift solutions is expected to reasonably sample the systematic uncertainty. We ran multiple RVSAO trials with all parameters fixed, except cross-correlation wavelength range and initial redshift guess.

Each unique wavelength range corresponds to a single trial, used as an input to RVSAO, with different output cross-correlation peaks. Moreover, in trials with relatively small wavelength ranges, care is taken to eliminate wavelength regions of high noise.

The median scatter in output redshifts observed across multiple trials for the same galaxy spectrum is $\Delta z \sim 10^{-3}$, which matches the statistical uncertainties obtained from the *customcode* analysis. Keeping the wavelength range and initial redshift guess intact while changing the template spectrum (e.g. SAO's *habtemp90*) returns a similar range of uncertainties.

As mentioned above, in the presence of these limitations, we quote the most conservative uncertainties for individual redshifts. We start with considering median redshifts from multiple RVSAO cross-correlation trials. For RVSAO, we quote the root mean square (RMS) uncertainties from multiple cross-correlation trials. In the few cases that [OII] emission was observed, we then consider the median of RVSAO cross-correlation and [OII] emission line redshifts, with RMS errors.

The results from the above analysis are then compared with the *customcode* uncertainties. To be consistent with our approach of reporting the most conservative errors due to presence of unquantifiable sky subtraction systematics, the largest of the three — RVSAO+[OII] uncertainties, *customcode* uncertainties, and the difference in redshift solutions from the two

Table 3.5. Mean Redshifts, Velocity Dispersions and Mass Comparisons of Sample Galaxy Clusters

Cluster Name	Members (no.)	z	δz	$\sigma_{\rm v,G}$[a] (km s^{-1})	$M_{\rm 200c,SZ}$[b] (10^{14} h_{70}^{-1} M$_\odot$)	$M_{\rm 200c,X-ray}$[c] (10^{14} h_{70}^{-1} M$_\odot$)	$M_{\rm 200c,dyn}$[d] (10^{14} h_{70}^{-1} M$_\odot$)
SPT-CL J2341-5724	10	1.2588	0.0021	941 ± 285	$4.90^{+1.00}_{-1.00}$	$5.40^{+1.20}_{-1.20}$	$5.10^{+5.90}_{-3.30}$
SPT-CL J0156-5541	15	1.2879	0.0018	936 ± 228	$5.90^{+1.20}_{-1.20}$	$6.30^{+1.00}_{-1.00}$	$4.90^{+4.40}_{-2.70}$
SPT-CL J0640-5113	7	1.3162	0.0031	1147 ± 426	$5.80^{+1.20}_{-1.20}$	$4.70^{+1.00}_{-1.00}$	$8.80^{+13.20}_{-6.50}$
SPT-CL J0607-4448	5	1.4010[e]	0.0028	843 ± 383	$5.10^{+1.10}_{-1.10}$	$4.30^{+0.90}_{-0.90}$	$3.40^{+6.80}_{-2.80}$
SPT-CL J0313-5334	7	1.4741	0.0018	727 ± 270	$4.90^{+1.10}_{-1.10}$	$3.20^{+2.60}_{-2.50}$	$2.20^{+3.20}_{-1.60}$

[a]Using the robust and resistant gapper estimator, recommended for N≤15 member galaxies, described in Beers et al. (1990) and Ruel et al. (2014a).

[b]SZ masses reported in B15 and scaled up to $M_{\rm 200c}$.

[c]X-ray-temperature based masses reported in McDonald et al. (2017a).

[d]Using the gapper velocity dispersion, and the M-$\sigma_{\rm v}$ relation (see Saro et al. 2013 for details).

[e]Cluster redshift determined out of two redshift 'groups', $z = 1.40$ and $z = 1.48$. See Section 3.5.2 for more details.

sets of analyses — is taken as the galaxy redshift uncertainty. RVSAO's ability to observe spectral features across different pixel scales (or Fourier modes) in a galaxy spectrum, the agreement in redshifts from three independent analyses, and the confirmation of redshift results by visual inspection of these spectra gives us confidence in our redshift estimates and the characterization of redshift uncertainties. Moreover, individual galaxy redshift uncertainties do not have a significant effect on the primary scientific result of this work, which are the cluster redshifts.

3.5 Discussion

3.5.1 Galaxy Cluster Redshifts (and Velocity Dispersions)

Redshift estimation in this work follows the same procedure as all previous SPT follow-up studies, described in Ruel et al. (2014a). It involves using the bi-weight location estimator

to calculate the average redshift, $\overline{z}_{\rm cluster}$, assuming a redshift sample drawn from a Gaussian distribution. For the calculation of velocity dispersion, the bi-weight estimator is robust and resistant to outliers and low number statistics. However, in cases of very small samples (N $\leq$ 15), the gapper estimator is preferred, and is used in this work. We calculate $\overline{z}_{\rm cluster}$ as best determined using the procedure formulated in Beers et al. (1990). The line-of sight velocity for individual galaxies is computed using the following relationship:

$$v_{\rm i} = c\frac{(z_{\rm i} - \overline{z}_{\rm cluster})}{(1 + \overline{z}_{\rm cluster})}. \tag{3.1}$$

where $\overline{z}_{\rm cluster}$ is the bi-weight location-estimated mean redshift, and the denominator accounts for the difference between the emitter's rest-frame and the cosmological expansion of the universe. The list of velocities v_i is used as an input to the gapper estimator to calculate the line-of-sight velocity dispersion $\sigma_{\rm v}$, once $\overline{z}_{\rm cluster}$ is finalized. This gives us an initial estimate of $\sigma_{\rm v,G}$. We then account for outliers/interlopers in velocity-space by making a hard $\pm 3\sigma$ cut on the distribution of $\sigma_{\rm v,G}$ and ejecting them from the next iteration of calculations until convergence is reached (also see Section 3.5.4). Uncertainties on $\overline{z}_{\rm cluster}$ are calculated using the following expression in Ruel et al. (2014a) for estimating standard deviation (once again, assuming the measured redshifts are close to a normal distribution):

$$\Delta z = \frac{1}{c}\frac{\sigma_{\rm v}(1 + \overline{z}_{\rm cluster})}{\sqrt{N_{\rm members}}}, \tag{3.2}$$

where $\sigma_{\rm v} = \sigma_{\rm v,G}$ is the relevant gapper velocity dispersion, $1+z$ is needed because $\sigma_{\rm v,G}$ is defined in the rest frame, and $1/c$ converts velocity to redshift. Jackknife and bootstrap estimates of this uncertainty also converge to this expression (Ruel et al., 2014a). Confidence intervals on velocity dispersions are estimated to be:

$$\Delta\sigma_{\rm v} = \frac{\pm C}{\sigma_{\rm v}\sqrt{N_{\rm members} - 1}}. \tag{3.3}$$

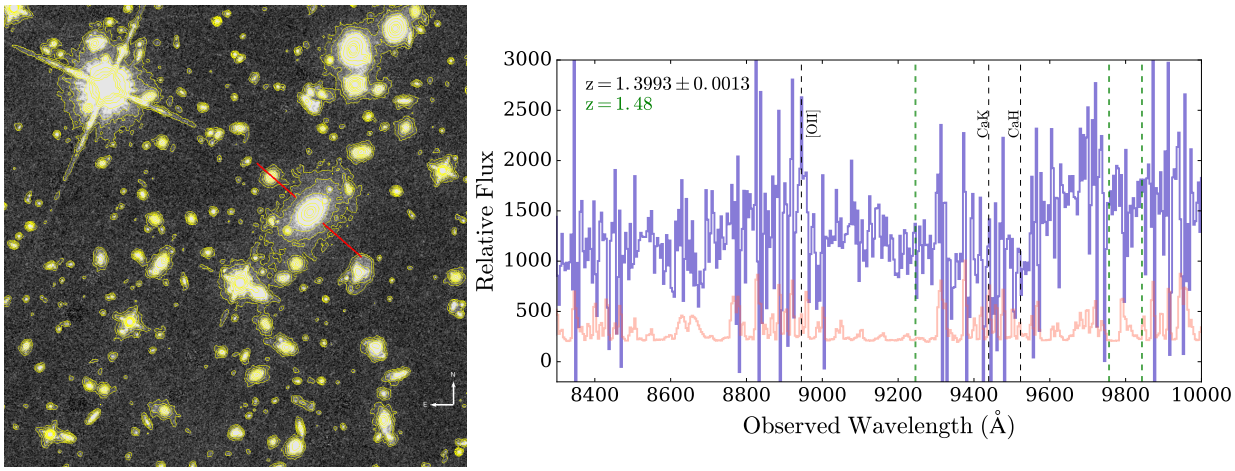

Figure 3.6 *Left*: A 500 kpc cutout of the HST+WFC3 F140W image (Strazzullo et al., 2019) at the cluster redshift $z = 1.40$ for SPT-CL J0607-4448 centered on the SPT-SZ position. Contours are [1.25,2.5,5,10,20,40,60,80,160] times the standard deviation of the sky values, chosen to highlight low-level extended emission seen around galaxies in the image. The galaxy (indicated with red lines) has all the hallmarks of a brightest cluster galaxy (BCG); it is an early type galaxy with an extended stellar halo larger than 100 kpc, and has an appropriate color. *Right*: 1D spectrum for the BCG identified in the left panel. Purple corresponds to observed flux, orange is the 1σ error-bars (offset for clarity). Despite absence of a clear diagnostic spectral feature for a redshift, this spectrum favours a $z = 1.40$ solution, based on the vertical green dotted lines corresponding to a redshift Ca II H&K doublet feature and a feature consistent with [OII] 3727,3729Å emission. The green dotted lines correspond to the same 3 spectral features, but at $z = 1.48$, clearly inconsistent with the spectrum.

This expression accurately captures the confidence interval on the total measurement. For the gapper statistic, C = 0.91.

The final redshifts and velocity dispersions are tabulated in Table 3.5. Figure 3.5 shows the distribution of individual cluster member velocities (with an over-plotted Gaussian distribution of mean 0, standard deviation $\sigma_{v,G}$ and an amplitude corresponding to the maxima of the histogram bin counts), where the distribution of member galaxy velocities and the estimated values of the cluster velocity dispersions are consistent with each other.

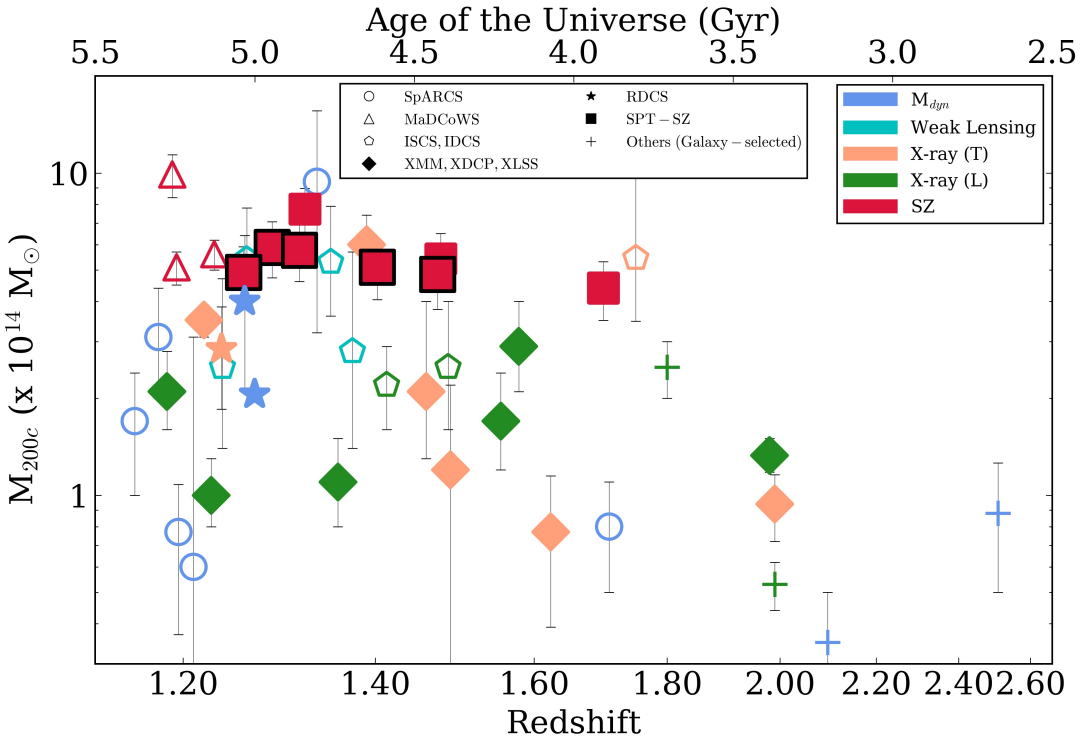

Figure 3.7 Mass vs. redshift (or Age, in Gyr) distribution of all spectroscopically confirmed galaxy clusters with reported masses at $z > 1.15$, including clusters identified in the 2500 deg^2 SPT-SZ galaxy clusters (Bleem et al. (2015a)). Red filled squares correspond to the SPT High-z Cluster sample; five clusters with black outline correspond to those analyzed in this work. Also plotted are clusters from major surveys like SpARCS, MaDCoWS, and XMM (marked with different shapes) with their respective cluster mass measurements M_{200c} (marked with different colors). Galaxy luminosity/color-selected clusters are represented by hollow shapes, while ICM-selected clusters are marked with filled shapes in this figure. In cases where M_{500c} is reported, M_{200c} is calculated with the assumptions of an NFW profile and a concentration $c_{500c} = 5$.

3.5.2 The curious case of SPT-CL J0607-4448

SPT-CL J0607-4448 ($z_{\rm phot} = 1.43 \pm 0.09$, $M_{500c,SZ} \sim 3.14 \pm 0.64 \times 10^{14} h^{-1} M_\odot$) was targeted for LDSS3 spectroscopy with 20 slits on a multi-object mask, with 10 delivering reliable redshifts (including two field galaxies not associated with the cluster). Eight of the resulting galaxy redshifts were found to be grouped around two redshifts — $z \sim 1.40$ (1.4087, 1.4077, 1.3973 and 1.3948), and $z \sim 1.48$ (1.4933, 1.4716, 1.4787, and 1.4965). These two redshift groups are separated enough along the Hubble flow that they are certainly distinct objects.

However, it is unclear which object dominates the SZ signal that led to the detection of SPT-CL J0607-4448 in the SPT-SZ survey. Based on the properties of four galaxies measured in each redshift group, the velocity dispersions and member galaxy velocity distributions do not clearly favor any one candidate ($\sigma_{\rm v,G}$ for $z\sim$1.40 and $z\sim$1.48 are 843$\pm$383 and 1587$\pm$834 km s^{-1}, respectively). While the $z\sim$1.40 dynamics (namely, the numerical value of the velocity dispersion) are relatively more consistent with expectations and the other clusters measured in this paper, the associated large uncertainties need to be noted. The spatial distribution of spectroscopically confirmed galaxies in each group does not indicate a preference for one of the redshifts. However, the detailed photometric analysis of the stellar bump and red sequence colors for SPT-CL J0607-4448 in Strazzullo et al. (2019) favors the lower redshift solution.

The BCG spectrum (Figure 3.6) does not possess a spectral feature (emission or absorption) that produced a clear spectroscopic redshift, due to the presence of particularly strong sky subtraction residuals. Both *customcode* and RVSAO cross-correlation fail to converge to a reliable redshift, but considered against the two choices (z = 1.40 or 1.48) the spectrum favors a z = 1.40 solution. The black vertical lines correspond to the Ca II H&K doublet feature redshift to z = 1.40, that are in close proximity to a potential 4000Å feature at $\sim$ 9600Å (as opposed to the break presenting itself at $\sim$ 9880Å in the case of a z = 1.48 solution). Moreover, there is a potential emission feature at 8944Å that, in isolation, is not compelling, but can be interpreted as [OII] emission at $z \sim 1.3993$. This indicates that the cluster redshift for SPT-CL J0607-4448 is $z = 1.4010$. The galaxies in the $z \sim 1.48$ structure (which may or may not be a virialized group or cluster) are noted in Table 3.4.

3.5.3 The SPT High-z Cluster sample in the context of other clusters in the literature

This sample contains five high mass, high redshift SPT-SZ detected galaxy clusters that have been determined photometrically to be above $z > 1.25$. From literature, we find $\sim$ fifty confirmed galaxy clusters at $z > 1.15$, which implies that spectroscopic confirmation of clusters in our sample increases the number of clusters in this regime by 10%. The SPT high-redshift cluster sample also lies at significantly higher masses than most spectroscopically confirmed clusters at such redshifts; in the high-mass/high-redshift space bounded by the lowest mass and lowest redshift SPT-SZ clusters in this sample, these five spectroscopic confirmations roughly double the total number of confirmed clusters from all previous work.

Figure 3.7 depicts the distribution of M_{200c} as a function of redshift (or age of the Universe) of all spectroscopically confirmed galaxy clusters at $z > 1.15$ for which masses were reported in literature. The census includes infrared-selected clusters from SpARCS (Nantais et al. 2016,Noble et al. 2016), MaDCoWS (Brodwin et al., 2015; Gonzalez et al., 2015) and ISCS (Jee et al., 2011; Brodwin et al., 2011, 2016) surveys, X-ray selected clusters from XMM (Stott et al., 2010), XDCP (Fassbender et al., 2011b), XLSS (Tran et al., 2015), and RDCS (Rosati et al., 1998) surveys, and SZ-selected clusters from the SPT-SZ survey. This census covers a mass range of $M_{200c} \approx 0.3\text{-}10 \times 10^{14}$ $M_\odot$. The colors show the method used to estimate cluster mass: X-ray temperature, X-ray luminosity, SZ, and weak lensing.

The three clusters in red squares without black outlines are SPT-SZ clusters spectroscopically confirmed elsewhere at redshifts greater than 1.2 — SPT-CL J2040-4451 ($z = 1.48$, Bayliss et al. 2014b), SPT-CL J0205-5829 ($z = 1.32$, Stalder et al. 2013a) and SPT-CL J0459-4947 (X-ray spectroscopy-based redshift $z = 1.71 \pm 0.02$, Mantz et al. 2020). The red squares with black outlines represent the 5 SPT high-redshift clusters analyzed in this paper.

It is crucial to note that most of the redshifts confirmed in this work are derived from absorption features despite observational difficulties, while higher redshift clusters are typically

confirmed by virtue of strong emission observed, e.g., clusters JKCS 041 ($z = 1.8$, Andreon et al. 2014), XLSSC 122 ($z = 2.0$, Mantz et al. 2017), CL J1001+0220 ($z = 2.5$, Wang et al. 2016), and the COSMOS-ZFOURGE overdensity ($z = 2.1$, Yuan et al. 2014).

3.5.4 Validation of Redshift Results

As previously discussed, obtaining redshifts for primarily passively evolving galaxies at well beyond $z = 1$ is difficult, and the spectra discussed here are further compromised by systematic sky-subtraction issues. We thus consider in the subsections that follow several analyses of these data beyond cluster redshift estimation, primarily to demonstrate that the redshifts derived above are consistent with expectations for high redshift clusters.

Consistency of Dynamical Masses with SZE and X-ray Masses

We estimate the dynamical masses of these five galaxy clusters using the dispersion-mass scaling relation from Saro et al. (2013):

$$M_{200\mathrm{c,dyn}} = \left(\frac{\sigma_{\mathrm{DM}}}{A \times h_{70}(z)^{C}} \right)^{B} 10^{15} \mathrm{M}_{\odot}, \tag{3.4}$$

where A=939, B=2.91, C=0.33, $M_{200\mathrm{c,dyn}}$ is the dynamical mass within $R_{200\mathrm{c}}$, defined as the radius within which the mean density ρ is 200 times the critical density ρ_{c} of the universe. σ_{DM} is the dispersion computed from galaxy clusters in dark matter simulations, where subhalos correspond to galaxies, while $h_{70}(z)$ is the redshift-dependent Hubble constant.

It is assumed here that the average velocity dispersion of galaxies in our clusters can be substituted in the above expression, i.e., $\sigma_{\mathrm{DM}} \sim \sigma_{\mathrm{v,G}}$, to give a crude estimate of the cluster dynamical masses, which is sufficient given the significant uncertainties associated with velocity dispersion from small numbers of members, and the uncertainty floor imposed by projection and orientation effects in individual clusters (White et al., 2010).

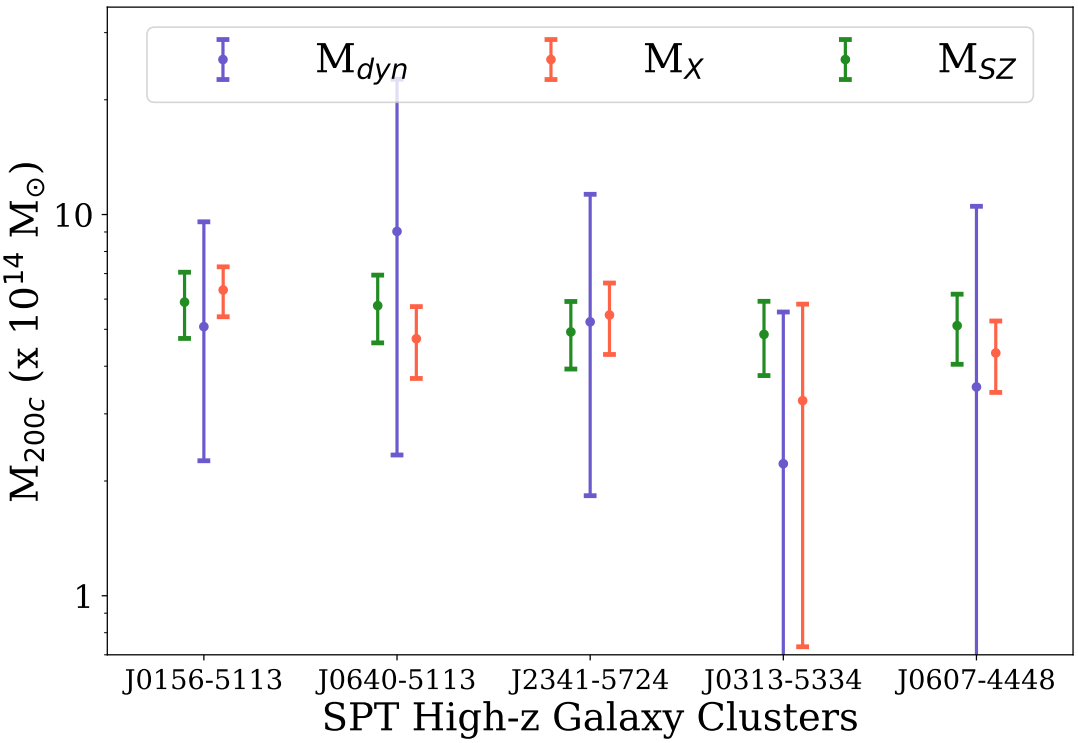

Figure 3.8 M_{200c} comparisons for the SPT High-z cluster sample — dynamical (purple), X-ray (orange) and SZ (green). $M_{200c,dyn}$ calculated in this paper are not inconsistent with other published masses for these galaxy clusters (see Table 3.5 for details).

Additionally, other potential systematic uncertainties should be considered when comparing the dynamical mass to other estimators. An example is the conversion from $M_{500c,SZ}$ to $M_{200c,SZ}$ (B15 reports M_{500c}) — the scale factor is ~ 1.65 in this redshift regime, assuming an NFW profile and a mass-concentration scaling relation from Duffy et al. (2008).

Table 3.5 reports the velocity dispersion, the implied dynamical masses, the SZ-derived masses (B15), and the X-ray temperature-derived masses (McDonald et al., 2017a) for all five clusters. All masses are reported in M_{200c}, scaled where necessary. The dynamical mass to SZ mass ratio for this sample (calculated by fitting a line to the $M_{200c,dyn}$–$M_{200c,SZ}$ plane) is 0.73 ± 0.36, and the dynamical mass to X-ray mass ratio is 0.87 ± 0.42. The uncertainty in these ratios is dominated by the high uncertainties in the dynamical masses.

Figure 3.8 shows the masses with uncertainties for all five clusters; the dynamical masses

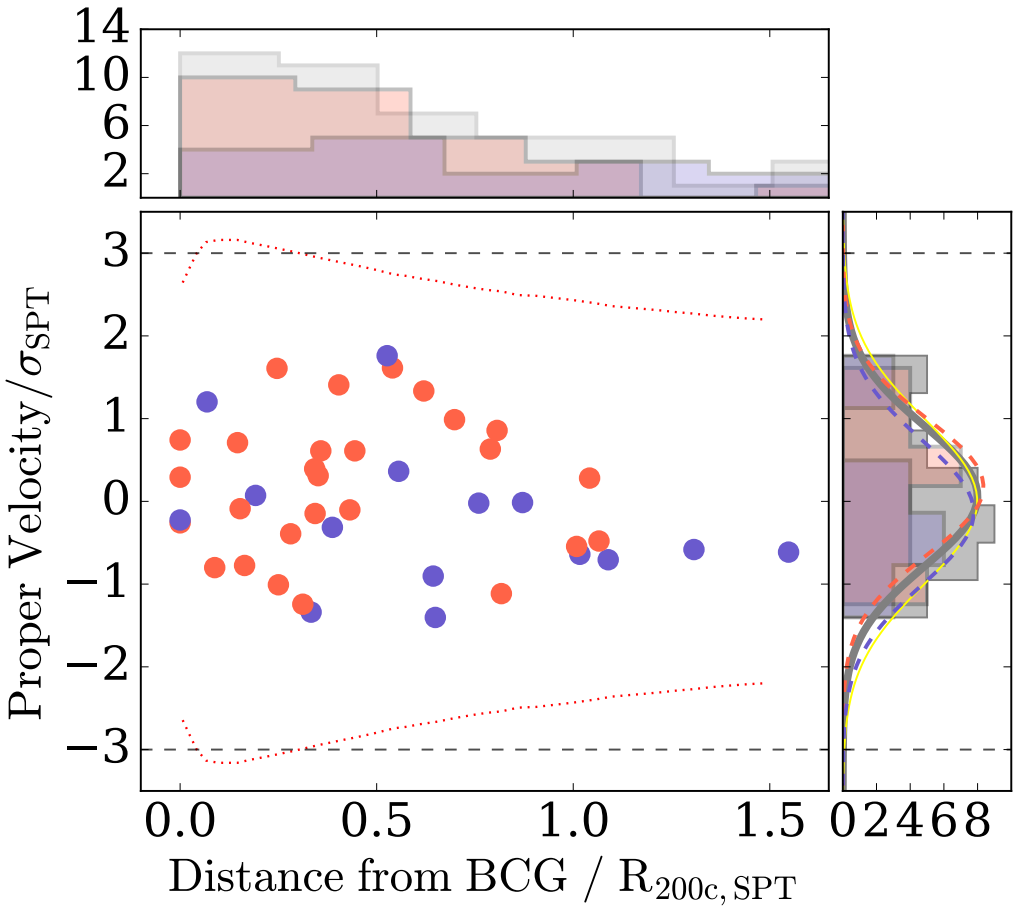

Figure 3.9 Normalized proper velocities vs. normalized distance of member galaxies from SZ center, for the 5 sample clusters (with a total of N = 44 galaxies with their respective peculiar velocities) stacked as a composite cluster. Orange dots represent passive galaxies, and purple dots represent galaxies that exhibit [OII] emission (designated as non-passive galaxies). The red dotted (black dashed) contours represent the radially dependent $\pm 2.7\sigma$(R) (hard $\pm 3\sigma$) threshold for interloper rejection. Both velocity and radius histograms show [OII] emitting (purple), passive (orange) and total (grey) population distribution. Over-plotted on the velocity histograms are Gaussian curves corresponding to mean and standard deviation of velocity distributions of the [OII] emitting (dotted purple), passive (dotted orange) and all (solid grey) galaxies. The yellow curve is Gaussian, with a mean of zero and standard deviation of one. The amplitudes for the curves are arbitrary, for pictorial representation. See Table 3.5 for details on dispersions and masses of individual galaxy clusters.

are uncertain, but there is no evidence of deviations from expectation that would suggest any systematic issue with the derived galaxy (and in turn, galaxy cluster) redshifts.

Velocity-Radius Diagrams for a Stacked Cluster

As mentioned previously, when calculating the velocity dispersion for a single cluster, we account for outliers/interlopers in velocity-space by making hard $\pm 3\sigma$ cuts on the distribution of $\sigma_{\rm v,G}$ and ejecting them from the next iteration of calculations until convergence occurs.

To examine this phase space further, we create a stacked cluster from the composite distribution of all 44 member galaxy velocities and galaxy distances from the SZ centers (the caustic technique; Diaferio & Geller 1997; Gifford et al. 2013). The SZ mass is used to normalize velocities by an equivalent dispersion $\sigma_{\rm 200c,SZ}$, calculated using the dispersion-mass scaling relation (Saro et al., 2013) from $M_{\rm 200c,SZ}$ (scaled up from the SPT mass $M_{\rm 500c,SZ}$) akin to the previous section. The projected radial distances of individual member galaxies are also normalized by $R_{\rm 200c,SPT}$. The resulting phase-space diagram is shown in Figure 3.5.4, along with the peculiar velocity distribution in the 'stacked cluster'. The horizontal dotted lines correspond to $\pm 3\sigma$ threshold, while the orange dotted curve is the radially dependent $\pm 2.7\sigma(R)$ threshold from an NFW profile, for optimal interloper rejection (Mamon et al., 2010). From Figure 3.5.4, we conclude that: a) the simple 3-sigma outlier rejection used in Section 3.5.1 is sufficient, and b) the radial profile of velocities in the stacked cluster look as expected (i.e., small at the center, rising to a maximum, and decreasing at large radii), suggesting that cluster members have been robustly measured and identified. We would like to acknowledge the possibility that this radial profile evolution exhibited within the $\pm 3\sigma$ threshold can be attributed to the low number of member galaxies with confirmed redshifts.

In addition, we run a Kolmogorov-Smirnov (K-S) test on the total galaxy population's velocity distribution (gray horizontal histogram, Figure 3.5.4). The K-S statistic is 0.08, i.e., it does not reject the hypothesis that normalized galaxy velocities in our cluster sample are drawn from a Gaussian distribution. This is consistent with expectations (see Ruel et al. 2014a; Bayliss et al. 2017b).

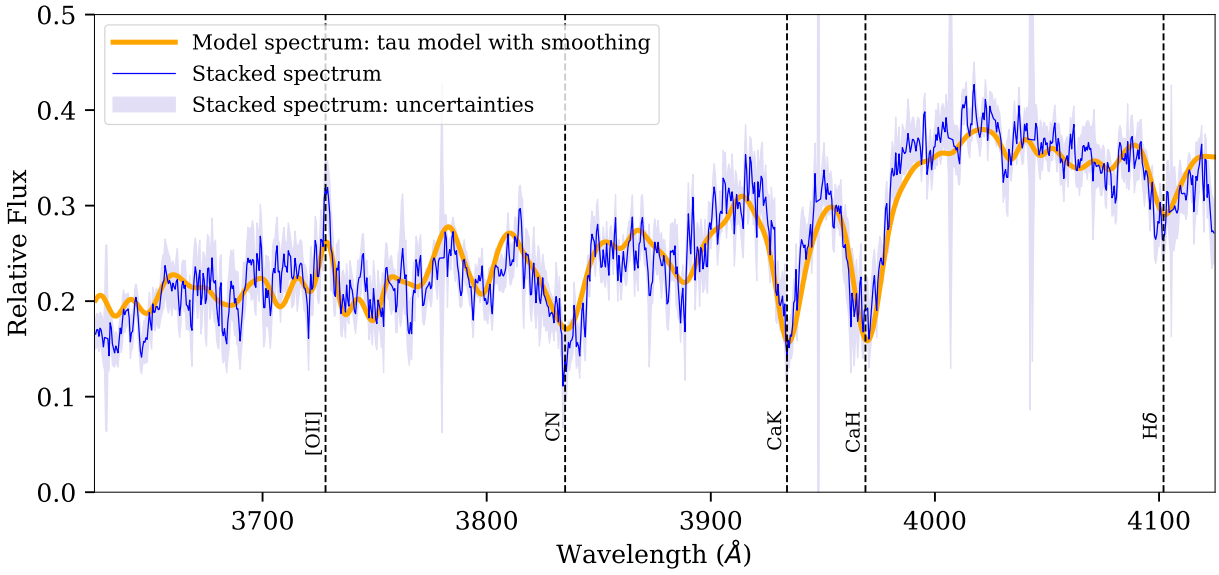

Figure 3.10 Stacked spectrum analysis for the 28 passive galaxies across 5 clusters reported in this paper. The light blue band corresponds to 68% confidence interval based on a linear combination of statistical and systematic uncertainties in the stack. Orange spectrum corresponds to an exponential tau model of star formation that is 1.7 Gyr old, at a metallicity $\log(Z/Z\odot) = +0.33$ (see Section 3.5.5 for a more detailed description). Dotted lines correspond to rest frame [OII], CN, Ca II H&K, and Hδ features.

We also analyze the distribution of cluster member galaxies in velocity-radius phase space by distinguishing passive (orange) from [OII]-emitting (purple) galaxies. Nominally passive galaxies describe a more centrally condensed distribution by comparison to the more extended distribution of galaxies exhibiting [OII] emission. This is likely a real trend and unlikely to be a simple selection effect — placing slits on bright red apparent cluster galaxies at larger radii is easier than in the cluster center due to less crowding, and there are potential red cluster members at all radii in the imaging data. Moreover, it is seen that the ratio of passive galaxy to [OII]-emitting galaxy velocity dispersion is 0.95±0.26, in good agreement with trends observed by Bayliss et al. (2017b) for low- and medium-redshift SPT-discovered galaxy clusters. This projected radius and velocity segregation between passive and emission-line galaxies is thought to indicate differences in formation timescales and accretion histories into the cluster environment (see Bayliss et al. 2017b for a comprehensive discussion). That

the entire galaxy population of the stacked cluster when dissected in this manner is again consistent with expectations from lower-redshift clusters also indicates that cluster member redshifts have been well measured.

3.5.5 Stacked spectral analysis of Passive Galaxies

We construct a composite spectrum of 28 passive member galaxies across 5 clusters, i.e., all galaxies for which an [OII] emission feature was not detected. To stack, we shift each spectrum to the rest frame (based on its final reported redshift), and map it to the wavelength range 3645-4125Å, with a flux normalization using the throughput curve for the instrument LDSS3-C in this configuration. This is followed by a weighted-sum stacking of the 28 spectra, where each flux value is weighted by the error vector for each galaxy spectrum. We further exclude a portion of each spectrum from the stack; the excluded data are any pixels with uncertainties greater than 2x the mean uncertainty of the 10 least uncertain pixels in each input spectrum. This typically excludes about 30% of the input pixels, which roughly correspond to the majority of the pixels that have large sky subtraction residuals.

A systematic uncertainty is calculated by varying the exclusion percentage upward and downward by 10% (i.e., typically from 20%-40% of the pixels are excluded) in steps of 1%, and computing a stacked spectrum at each cut. The variance at each pixel across the resulting 21 different stacks is taken as an estimate of the systematic uncertainty. The statistical uncertainty is calculated by bootstrapping the input spectra in the stacking process. The final reported uncertainty is the sum in quadrature of the systematic and statistical uncertainties, which typically are of comparable magnitude. The stacked spectrum (blue, with the 68% confidence interval in light blue) is shown in Figure 3.10.

Notably, in the stacked spectra, we detect a composite [OII] emission feature, not previously detected in individual spectra. Additionally the spectrum clearly shows a pronounced broad CN feature in the range of 3820-3850Å, as well as Hδ absorption at 4102Å. We also

perform stellar population synthesis modeling with our stacked spectrum using the MCMC code Prospector (Leja et al., 2017a; Johnson & Leja, 2017a; Foreman-Mackey et al., 2013; Conroy & Gunn, 2010b) to demonstrate that the aggregate spectrum is reasonable and as expected for cluster member galaxies at this epoch. In Figure 3.10, we overplot a best-fit spectrum using a simple tau (τ) model (e-folding time = 300 Myr, in orange) for a 1.7 Gyr old stellar population, at a metallicity log $(Z/\mathrm{Z}\odot) = 0.33$ with a velocity broadening over scales of 275 km s^{-1}. Dotted lines correspond to rest frame [OII], CN, Ca II H&K, and Hδ features. The clear emergence of [OII], Hδ and CN features — which were not used to establish redshifts for any of these galaxies — and the overall good correspondence between the stacked and the quite reasonable model spectrum, is yet one more validation of the redshifts of the individual galaxies that were used in the composite stacking. A comprehensive analysis of physical properties of stellar populations in the cluster members characterized here shall be presented in a future paper (Khullar et al., in prep).

3.6 Summary

We present spectroscopic follow-up of 5 of the most distant galaxy clusters in the 2500 deg^2 SPT-SZ survey — part of the SPT High-z Cluster sample. This work describes the observations, the spectroscopic analysis pipeline, and the data products that have been subsequently derived. We analyze this data set via cross-correlation, and manual emission and absorption line fits, to infer robust spectroscopic redshifts for member galaxies. We argue that despite the presence of mostly low S/N spectra dominated by sky background noise (associated with sky subtraction residuals, an artifact of the data quality and the reduction process), useful parameters can be extracted from the dataset. We perform several consistency checks for the reported spectroscopic redshifts — calculations of velocity dispersions and dynamical masses, exploration of the velocity-radius phase space for cluster member galaxies, and a composite stacked spectrum that exhibits features of nominally passive galaxies. The re-

ported set of galaxy cluster redshifts doubles the number of galaxy clusters spectroscopically confirmed at $M_{200c} \geq 4.5 \times 10^{14} M_{\odot} h^{-1}$ and at $z > 1.2$.

This work has been an effort to spectroscopically characterize the highest redshift massive galaxy clusters from the SPT-SZ catalog. The distant, massive cluster population presented in this work represents the progenitors of nearby massive clusters; as such it is imperative to study this sample both observationally and in comparison with simulations. Despite limitations in spectral observations (mostly pertaining to quantifying systematics in sky subtraction), as this work reports robust cluster redshifts, future spectroscopy of these distant and faint clusters would be able to employ techniques with optimal sky subtraction (e.g., nod-and-shuffle mode on Magellan/LDSS3 targets a narrower spectral range but is an improved handling of systematics; see Glazebrook & Bland-Hawthorn 2001). This spectroscopic confirmation study encourages further follow-up that targets observations of star formation rates and history, tracers of cluster dynamics, and estimation of velocity segregation and biases in these unique systems.

Acknowledgments

We thank Chihway Chang, Philip Mansfield, Andrey Kravtsov, Richard Kron and Huan Lin, for their helpful and thoughtful feedback that improved the analysis in this paper. GK would like to express gratitude towards the staff and workers at the 6.5m Magellan Telescopes at the Las Campanas Observatory, Chile, for their valuable labor. We would also like to thank the anonymous referee whose feedback was vital in improving this manuscript. This paper has gone through internal review by the South Pole Telescope collaboration.

This work is supported by the Department of Astronomy and Astrophysics at the University of Chicago, NSF Physics Frontier Center grant PHY-1125897 to the Kavli Institute of Cosmological Physics at the University of Chicago, as well as by the Kavli Foundation, and the Gordon and Betty Moore Foundation grant GBMF 947. The South Pole Telescope

is supported by the National Science Foundation through grant PLR-1248097.

BB is supported by Fermi Research Alliance, LLC under Contract No. DE-AC02-07CH11359 with the U.S. Department of Energy, Office of Science, Office of High Energy Physics. Argonne National Laboratory work was supported under U.S. Department of Energy contract DE-AC02-06CH11357. MB was supported by National Science Foundation through Grant AST-1009012. AS is supported by the ERC-StG 'ClustersXCosmo', grant agreement 71676. The data analyzed in this paper was taken on the 6.5m Magellan Telescopes at the Las Campanas Observatory, Chile, supported by the Carnegie Observatories. This work is partly based on observations made with the NASA/ESA Hubble Space Telescope, obtained at the Space Telescope Science Institute, which is operated by the Association of Universities for Research in Astronomy, Inc., under NASA contract NAS 5-26555, associated with SPT follow-up GO program 14252. This work is based in part on observations made with the *Spitzer Space Telescope*, which is operated by the Jet Propulsion Laboratory, California Institute of Technology under a contract with NASA. CR acknowledges support from Australian Research Council's Discovery Projects scheme (DP150103208).

CHAPTER 4

STELLAR MASS ASSEMBLY IN SOUTH POLE TELESCOPE CLUSTERS ACROSS REDSHIFTS 0.3-1.5

The text of this chapter was published in Khullar et al. (2021b; arXiv:2111.09318), and accepted for publication in The Astrophysical Journal on June 25, 2022.

4.1 Introduction

How and whether a given galaxy undertakes the path from initial star formation, to quenching, to passive evolution thereafter, is a fundamental question in the field of galaxy evolution. Studies that characterize galaxy mass assembly as a function of stellar content, halo mass, and environment are a path forward in both defining and solving the problem. Spectral energy distribution (SED) fitting and stellar population synthesis modeling originated as methods to study populations of elliptical galaxies with Tinsley & Gunn (1976). In the last several decades, with the extensive development of computational tools, photometry-based SED fitting has become a pivotal method to measure properties such as stellar masses, ages, and metallicities of a diverse population of galaxies, allowing us to study mass assembly in these systems.

This technique has been applied to a wide variety of spectroscopic, and in particular photometric, data across a range of galaxy populations that sample an abundance of intrinsic properties (e.g., star formation rate, stellar mass, metallicity, ages and environment). Recent multi-wavelength surveys have been successful in studying representative samples of quiescent galaxies in the field up to $z > 3$ (e.g., Heavens et al. 2000; Cimatti et al. 2004; Daddi et al. 2005; Gallazzi et al. 2005, 2014; Onodera et al. 2012, 2015; Jørgensen & Chiboucas 2013; Whitaker et al. 2013; Fumagalli et al. 2016; Pacifici et al. 2016). These observations have confirmed that the number density of massive quiescent galaxies in the

field has increased by an order of magnitude since z∼2 (Ilbert et al., 2013; Muzzin et al., 2013; Fumagalli et al., 2016). Numerous studies also discuss both the timescales of cessation of star formation, and the likely processes responsible for quenching, noting that the efficacy of some of these processes is a strong function of environment (some recent works include Carnall et al. 2018, 2019a; Leja et al. 2019a; Tacchella et al. 2021). Ram pressure stripping is thought to be effective in dense environments — i.e., the cores of galaxy clusters (Gunn & Gott, 1972; Larson et al., 1980; Balogh et al., 2000) — whereas strangulation of a galaxy's cold gas supply through a variety of possible mechanisms, resulting in a slow cessation of star-formation, is operative over a larger range of environmental densities (Peng et al., 2015). Galaxy harassment — high speed dynamical encounters that are particularly common in the cluster environment — also likely plays a role, and may be particularly effective in driving the morphological transformation that accompanies the cessation of star formation in quenched systems (e.g., Moore et al. 1998). Internal feedback processes, in particular active galactic nuclei (AGN)-feedback, are also thought to influence quenching (Davé et al., 2016, 2019; Nelson et al., 2019).

As conducting observational longitudinal studies of galaxies — that track the evolution of galaxies through cosmic time — is impossible, studies resort to drawing conclusions from observations of different galaxies at different redshifts; this approach is challenging since galaxies sample a diverse set of star formation histories (SFHs). Moreover, recent work (Kelson et al., 2014; Abramson et al., 2016) has shown that imprints of quenching are not necessarily distinguishable in the observations of quiescent galaxies. This makes an understanding of the evolutionary connection between galaxies across time difficult to elucidate in anything but the bulk statistical properties (e.g., luminosity or mass functions, color distributions, etc.).

When investigating galaxy clusters, we have the opportunity to utilise the host cluster halo evolution — which is well described and understood from even dark-matter-only sim-

ulations (see Kravtsov & Borgani 2012 and references therein) — to connect the cluster galaxy populations in antecedent-descendant *clusters* and hence construct a longitudinal sample of cluster galaxies. Galaxy clusters are unique environments with an abundance of observational constraints, and with a richness of passively evolving galaxies to study. In such analyses, one must carefully consider the effect of sample selection; for example, a fixed observational definition of quiescence applied at different redshifts results in some degree of progenitor bias (van Dokkum & Franx, 2001).

Studies that analyze cluster galaxies (both as individual objects and in aggregate) at $z < 1$ suggest that massive galaxies in clusters form stars in an epoch of early and rapid star formation (at $z >\sim 3$), before quickly settling into a mode of quiescent evolution (Dressler & Gunn, 1982; Stanford et al., 1998a; Balogh et al., 1999; Dressler et al., 2004; Stanford et al., 2005b; Holden et al., 2005a; Mei et al., 2006a). Thus, observations of clusters at higher redshifts should sample an epoch where this star formation — or at least its end stages — is observed *in situ*. Several studies of often small heterogeneous samples of galaxy clusters at $1 < z < 2$ have shown high star formation, AGN activity, and blue galaxy fraction compared with lower redshifts, as well as an evolving luminosity function (Hilton et al., 2009a; Tran et al., 2010a; Mancone et al., 2010a, 2012a; Fassbender et al., 2011a; Snyder et al., 2012a; Brodwin et al., 2013a; Alberts et al., 2016a). This is evidence that cluster galaxies are undergoing significant stellar mass assembly in this epoch, inviting further investigation into properties of member galaxies as well as the intra-cluster medium (ICM) at $z > 1$.

Studies have compared galaxy cluster environments with field galaxies to chart the role that these dense environments and deep gravitational potential wells play in the transition of galaxies from star-forming to quiescent (Balogh et al., 1999; Ellingson et al., 2001; Dressler et al., 2013; Webb et al., 2020). These studies characterize ages and SFHs of massive galaxies — both quiescent and star forming — and infer quenched fractions of galaxies in these environments.

Despite these successes, some challenges remain, especially constructing cluster samples across a wide range of redshifts. This is due to the following reasons. First, optical, IR and X-ray fluxes — which are observational tracers of galaxy clusters — become progressively more difficult to measure at high redshift due to cosmological dimming (Böhringer et al., 2013; Bartalucci et al., 2018b). Second, to conduct evolutionary studies and characterize the precursors of lower redshift clusters, we need to study the appropriate antecedents of lower redshift massive clusters — which are high-redshift lower mass systems. This is a non-trivial sample to build; $z > 1$ systems measured with these observations are few in number (Stanford et al., 2005a, 2012, 2014; Brodwin et al., 2006, 2011; Elston et al., 2006; Wilson et al., 2006; Eisenhardt et al., 2008; Muzzin et al., 2009; Papovich et al., 2010; Demarco et al., 2010; Santos et al., 2011; Gettings et al., 2012; Zeimann et al., 2012; Gonzalez et al., 2015; Balogh et al., 2017; Paterno-Mahler et al., 2017). Third, a challenge with optical and IR cluster surveys is whether the selection of galaxy clusters based on member galaxy properties systematically affects the studies of the said galaxies, e.g., while red-sequence selection of clusters has proven extremely fruitful for finding clusters and groups across a broad range of mass and redshift, it remains a concern whether this selection biases our understanding of quiescent (i.e., red-sequence) cluster galaxies, particularly at higher redshifts. By comparison, an ICM-selected cluster sample — a mass-limited sample where the limit doesn't evolve significantly with redshift — is likely to be less biased for galaxy evolution studies in clusters. Clusters discovered via the Sunyaev-Zel'dovich (SZ) effect with the South Pole Telescope (SPT, Carlstrom et al. 2002b) and the Atacama Cosmology Telescope (ACT, Sifón et al. 2016a) provide a nearly mass-limited sample of clusters with a redshift-independent mass threshold set by instrument sensitivity. Recent SZ-based galaxy cluster searches from SPT have revealed new samples of galaxy clusters at $z >\sim 1$ (Bleem et al., 2015b, 2020a; Huang et al., 2020a), extending the viability of SZ-cluster studies to redshift as distant as any other sample. These samples are now large enough to be a compelling

resource for cluster galaxy evolution studies (Brodwin et al., 2010b; Stalder et al., 2013b; McDonald et al., 2013b; Ruel et al., 2014b; Bayliss et al., 2016a; McDonald et al., 2017b; Khullar et al., 2019).

Another challenge in conducting SED-based studies is tied to how reliably we can interpret physical properties inferred from photometric observations compared with spectroscopic data. Studies relying on photometry alone are subject to many challenges, such as the age-metallicity-dust degeneracy (Worthey, 1994; Ferreras et al., 1999).

While large photometric samples of galaxy populations exist ranging from the present epoch to $z \sim$ 2-3 for L_*-type (and fainter) galaxies, only in the last two decades have statistical studies of galaxies with spectra and SED fitting been conducted, particularly on quiescent galaxies at intermediate and high redshifts in the field (e.g., Juneau et al. 2005; Gobat et al. 2008; Demarco et al. 2010; Moresco et al. 2010, 2013; Choi et al. 2014; Dressler et al. 2016; Belli et al. 2019; Carnall et al. 2019b; Estrada-Carpenter et al. 2020; Tacchella et al. 2021) and clusters (Sánchez-Blázquez et al. 2009; Muzzin et al. 2012; Jørgensen et al. 2017; Webb et al. 2020). Moreover, recent complex numerical simulations have been able to reproduce many physical conditions of galaxies and demonstrate hierarchical structure formation (e.g., Springel et al. 2005; Davé et al. 2019; Nelson et al. 2019), as well as approximately infer the parameters of evolution required to connect high-redshift galaxies to low-redshift descendants. Robust analyses of spectroscopic data can aid in comparison with these simulations, as well as inform simulations of galaxies at high-redshifts ($z > 1$).

We conduct here a study of stellar populations in quiescent cluster galaxies, and the influence of a systematically-selected cluster environment on the evolution of these member galaxies. We aim to answer the following questions:

1. On what timescales did galaxies that end up in galaxy clusters form their stars?

2. How does the cluster environment and location of a given galaxy within the cluster affect this timescale?

3. While studying these properties, does the galaxy cluster selection method matter?

We use 63 SZ-selected clusters from the SPT-SZ Survey (Bleem et al. 2015b, hereafter LB15) across $0.3 < z < 1.4$ with extensive spectroscopy (Bayliss et al., 2016a; Khullar et al., 2019), and characterize 837 quiescent galaxies spectrophotometrically to address the above questions. Because SZ cluster samples can reach lower mass thresholds at high redshifts, this SZ cluster sample connects high-redshift lower-mass antecedent clusters to low-redshift higher-mass descendents. Here, we study the evolution of quiescent galaxy population across redshift in this antecedent-descendent cluster sample.

This paper is organized as follows. Section 4.2 lays out the photometric and spectroscopic data used in this work, Section 4.3 describes the quiescent galaxy sample construction, and Section 4.4 describes the methods used in our analysis. Section 4.5 and Section 4.6 describe mass-weighted ages and formation redshifts for individual galaxies and subpopulations binned by various properties. We discuss some challenges in this work and future directions in Section 4.7. Finally, we summarise our work in Section 4.8.

Magnitudes have been calibrated with respect to the AB photometric system. The fiducial cosmology model used for all distance measurements as well as other cosmological values assumes a standard flat cold dark matter universe with a cosmological constant (ΛCDM), corresponding to WMAP9 observations (Hinshaw et al., 2013). All Sunyaev-Zel'dovich (SZ) significance-based masses from LB15 are reported in terms of $M_{500c,SZ}$, i.e., the SZ mass within R_{500c}, defined as the radius within which the mean density ρ is 500 times the critical density ρ_c of the universe.

4.2 Observational Data

In order to perform a comparative analysis on individual and aggregate stellar populations of quiescent member galaxies in our massive galaxy cluster sample, we combine the low-redshift SPT-GMOS cluster spectroscopic sample (from Bayliss et al. 2016a, 2017a, hereafter B16 and

B17) with spectra from the SPT Hi-z galaxy cluster sample (Khullar et al. 2019, hereafter K19), to give us a sample of 63 galaxy clusters from $0.3 < z < 1.4$.

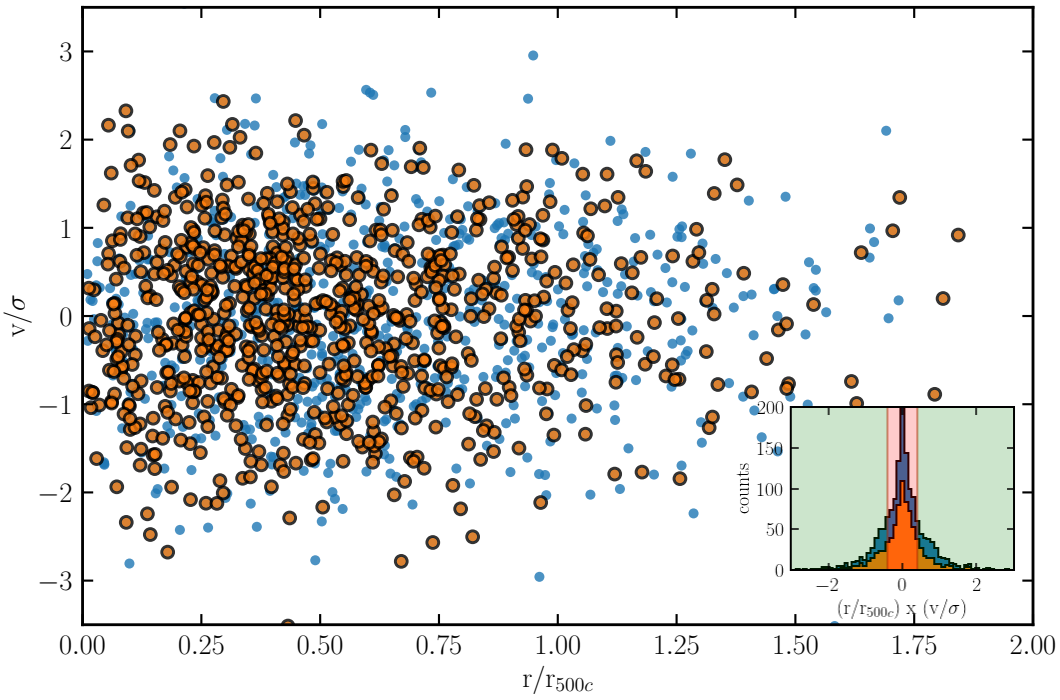

Figure 4.1 Normalized proper velocity vs. normalized distance of member galaxies in the sample from the nominal cluster SZ center. Velocities are normalized to the velocity dispersion of the galaxy cluster. Orange points correspond to quiescent galaxies in the sample, while blue points represent non-quiescent galaxies. (Inset) A histogram of the distribution of phase-space location (or proxy for 'infall time') for all galaxies (blue) and quiescent galaxies (orange), defined as $p = r_{\rm projected}/r_{\rm 500c} \times v_{\rm peculiar}/\sigma_{\rm v}$. The shaded red region corresponds to galaxies in the 'early+mixed infall' subpopulation, i.e., $p < 0.4$.

For all spectra considered in this work, we ensure that spectroscopic features being used to characterize SFHs are consistent across redshift and surveys in the rest frame. In this study, we use all spectra across galaxies in the rest frame wavelength range 3710-4120Å. To classify galaxies at the catalog level, and isolate the passively evolving subset, we use rest-frame [OII] λ 3727,3729Å doublet emission lines (blended here) and the D4000 spectral index (ratio of the spectral flux blueward and redward of the 4000Å break); these rest-frame optical signatures in spectral data are age indicators of stellar populations and are used for making quiescent galaxy cuts in our data. Numerous spectral features such as the CN

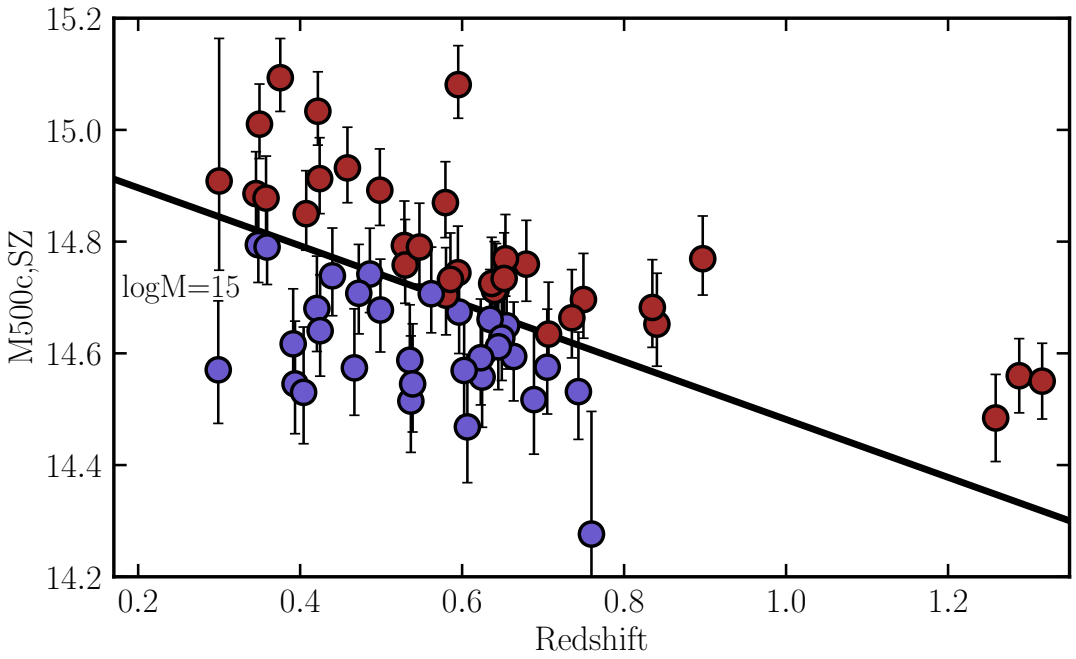

Figure 4.2 $\log(M_{500c,SZ}/\,M_\odot)$ vs redshift for 64 clusters in the High-z and Low-z samples. The black line demarcates the evolutionary path of galaxy clusters to final cluster mass at redshift 0 of $\log(M_{500c,SZ,z=0}/\,M_\odot) = 15$. The cluster sample is divided into two groups based on this demarcation, to facilitate a descendant-antecedent analysis of member galaxies (Fakhouri et al., 2010) — blue (red) points are clusters with final descendant cluster mass of $\log(M_{500c,SZ,z=0}/\,M_\odot) < 15$ (> 15).

molecular band, Ca II H&K λ 3968,3934Å Hδ, H9, H10 and H11 absorption features are also present in this wavelength range, and contribute to the full spectrophotometric SED fitting.

For all galaxies in our sample, we note environment- and cluster-specific properties, namely their velocity-radius phase space locations and the final descendant mass of the host galaxy cluster. To assign a proxy for galaxy 'infall time', we label each galaxy with its location in their proper velocities vs. normalized distance from cluster center space (see Noble et al. 2013, and Figure 4.1). This compares galaxies that are at different stages in their trajectory after infalling into their corresponding galaxy cluster. We also assign $M_{500c,SZ,z=0}$, which is the inferred final descendant cluster mass $M_{500c,SZ}$ at redshift $z = 0$ (assuming a halo mass growth history, Fakhouri et al. 2010), and label our galaxy sample

with their membership in clusters with $\log(M_{500c,SZ,z=0}/\,M_\odot)$ greater or lesser than 15 (see Figure 4.2). For further details, we direct the reader to Section 4.4.3.

4.2.1 High-z Cluster Spectroscopy: $1.2 < z < 1.4$

The high redshift cluster sample in this work is from K19, which spectroscopically confirmed five galaxy clusters at $1.25 < z < 1.5$. This sample, comprising 5 of the 8 most massive SPT-SZ clusters at $z > 1.2$, was assembled for a deep *Chandra* X-ray Observatory X-ray imaging program (McDonald et al., 2017b). We identify 10 of the 44 member galaxies characterized in K19 as passive (see Section 4.3), and include them in this work for analysis on individual spectra, as well as to construct a higher signal-to-noise ratio (S/N) composite spectrum for the redshift bin $1.2 < z < 1.4$ (see observation details in Section 2 of K19). Note that only 3 $z > 1.2$ clusters have been shown in Figure 4.2) — the 10 quiescent galaxies are member galaxies of these clusters.

The spectra in this sample typically cover the wavelength range 7500-10000Å in the observed frame, and the rest-frame range 3710-4120Å is common to all spectra across $1.2 < z < 1.4$; the low-redshift spectra sample's rest-frame wavelength range is matched appropriately. This dataset has low S/N observations, and these spectra are dominated in some spectral ranges by sky background noise associated with sky-subtraction residuals, an artifact of both the data quality and limitations of the reduction process. Due to the low S/N of the dataset, getting robust constraints on stellar population properties is difficult (see Section 4.2 in K19 for a discussion of constraining redshift uncertainties for these spectra). We present results from SED fitting of individual galaxies with this caveat in mind, but also lean on results from a stacked quiescent galaxy spectrum comprising 10 quiescent galaxies in the sample cut on [OII] and D4000 identically to the lower-z sample (see Section 4.3). This cut is more restrictive than that used in K19, in which an initial stacked spectral analysis was presented.

4.2.2 Low-z Cluster Spectroscopy: $0.3 < z < 0.9$

The South Pole Telescope — GMOS Spectroscopic Survey cluster sample (SPT-GMOS; from B16 and B17) — is a spectroscopic study of 62 galaxy clusters ($0.3 < z < 1.1$) from the SPT-SZ Survey cluster sample. The full sample of spectra contains 2243 galaxies including 1579 galaxy cluster members, confirmed in B16 and B17 via interloper exclusion and a velocity-radius phase space analysis (e.g., see Rhee et al. 2017; Pasquali et al. 2019 and references therein). The data set used here consists of 1D flux calibrated spectra, redshifts, positions, velocity dispersions, equivalent widths of spectral features([OII],Hδ) and the spectral index D4000. This sample contains one cluster between $0.9 < z < 1.1$ — SPT-CL J0356-5337 at $z = 1.03$ — with only 8 spectra of interest. We remove this cluster from consideration in this study; our analysis would require $0.9 < z < 1.1$ to be a single cluster redshift bin with 8 quiescent galaxies, which can significantly bias the results inferred from this bin.

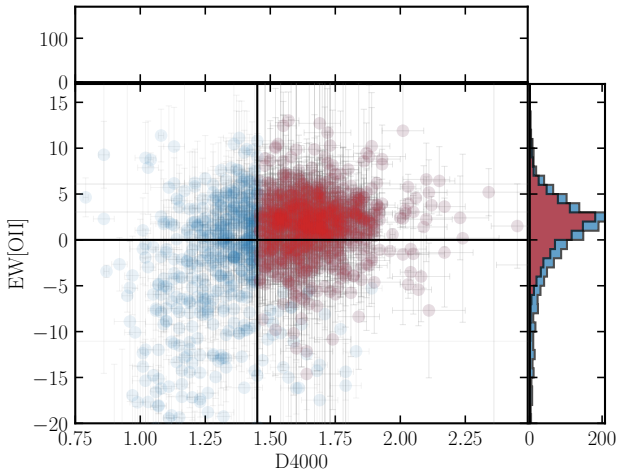

Figure 4.3 Distribution of equivalent width EW[OII] vs spectral index D4000 for sample galaxies (blue) and galaxies classified as quiescent in this work (red). EW[OII] vs D4000 is used here as an indicator for quiescent vs non-quiescent (actively star-forming, starburst or post-starburst) galaxies. Horizontal and vertical lines demarcating regions in the equivalent-width phase spaces are taken from Bruzual A. (1983) and Balogh et al. (1999) — quiescent galaxies have D4000 > 1.45 and no detection of an [OII] emission feature at $> 2\sigma$. We also test a more probabilistic cut for D4000 (i.e., D4000> 1.45 at $> 2\sigma$), which does not significantly impact our results.

4.2.3 Photometry

The flux calibration of the spectra used here suffers from the usual limits of multi-object spectroscopy of extended sources: aperture losses that are a complex function of observing conditions, source morphology and slit-mask details. Neither of the spectrographs — Gemini/GMOS and Magellan/LDSS3 — that contribute to these data have atmospheric dispersion correctors, and hence the flux calibration has potential wavelength dependencies that result from observing multi-object slit-masks at generally non-parallactic angles and a range of airmasses.

We use *griz* photometry for the purpose of doing joint spectrophotometric SED fitting such that flux calibration is a fitted nuisance parameter in our analysis. This correction allows us to calculate robust stellar masses for member galaxies in our cluster sample, which is a key property to characterize stellar populations. These stellar masses aid in making completeness cuts, as well as in assigning bins for stacking. The methodology, SED model definitions, and the analysis are described in Section 3.

We use available photometry for SPT Cluster galaxies used in B16 and B17, taken from a pool of optical imaging data used for SPT-SZ cluster confirmation and follow-up (High et al. 2010; Song et al. 2012b, LB15). This contains 1-4 band photometry (*griz*) for 60% of member galaxies in our sample. To increase the number of galaxies for which at least one photometric data point is available (and hence allowing us to flux calibrate the spectra to the photometry and calculate robust stellar masses), we use additional photometry from the Parallel Imager for Southern Cosmology Observations (PISCO; Stalder et al. 2014b) catalog described in Bleem et al. 2020a (uniform depth *griz* imaging data for over 500 SPT-selected clusters and cluster candidates). In summation, of a total of 1251 member galaxies, 978 quiescent galaxies in our sample have photometric data to supplement spectroscopic analysis.

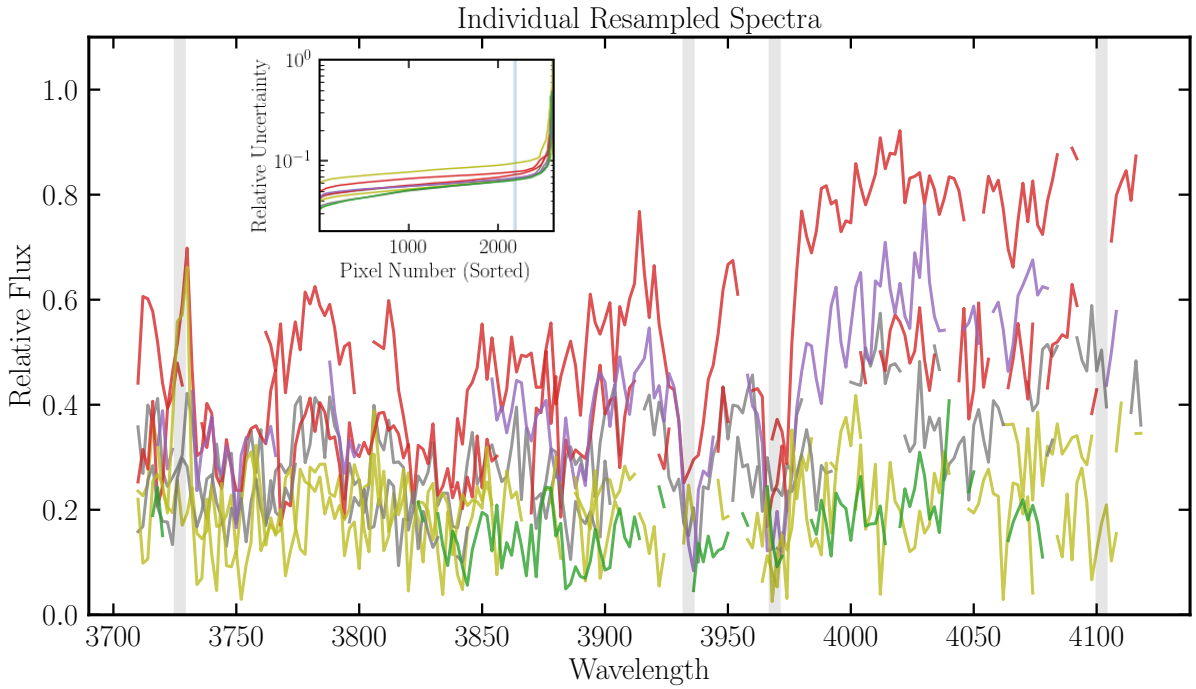

Figure 4.4 Noise-masked and resampled rest-frame spectra for all observed galaxies, prior to signal-to-noise, quiescent galaxy and stellar mass selection, in the cluster SPT-CL J0013-4906 at z=0.41 (colors represent spectra from different member galaxies). Shaded gray regions represent spectral features of interest in SED fitting (from left to right) — [OII] λ3727, 3729Å doublet, Ca II K&H λ 3934,3968Å and Hδ at 4102$\mathring{A}$. [OII] and 4000Å break are used here to make quiescent galaxy cuts. (Inset) Relative sorted flux uncertainties per pixel for the same spectra in SPT-CL J0013-4906. The blue vertical lines denote the error threshold (84th percentile) above which spectral pixels are masked, followed by resampling.

4.3 Constructing a sample of quiescent galaxies

4.3.1 Spectroscopic Target Selection

B16 and B17 placed slits on targets in the SPT-GMOS survey as follows: the highest priority was assigned to candidate brightest cluster galaxies (BCGs), followed by likely cluster member galaxies that were selected from the red sequence (identified as an overdensity in color-magnitude and color-color space) down to an absolute magnitude limit of $M^* + 1$ (see Page 14 in B17 for a detailed description). Within this red-sequence selected galaxy sample, no magnitude prioritization was used, so the slits should randomly sample the red-sequence

galaxy population down to the chosen limit. A similar procedure was followed for the high-z cluster galaxy sample in K19, though we note that the effective limiting absolute magnitude is brighter in these distant clusters.

Based on these selection criteria for multi-object slits and completeness of observations in both the SPT-GMOS survey (B16, B17) and the SPT Hi-z survey (K19), we expect the member galaxy spectra to be least biased and most representative for red or quiescent galaxies, with brighter galaxies in a given cluster being observed with a high signal-to-noise ratio (SNR). We emphasize here that the B16 cluster galaxy sample is not a mass complete sample, but a representative sample of quiescent member galaxies in SPT galaxy clusters. For more details, see Section 4.6.2.

For our SED analysis, we isolate this representative sample of galaxies by the following cuts in catalog space.

4.3.2 Equivalent Width and Signal-to-Noise ratio

B16 and B17 make informative cuts on quiescent, actively star-forming and post-starburst galaxies using physically motivated spectral indices (we invite the reader to view Table 3 from B17, and Balogh et al. 1999 for more details). For our main analysis, we use the B16 and Balogh et al. (1999) data cuts to identify quiescent galaxies, as galaxies with no [OII] emission feature at $> 2\sigma$, and D4000 > 1.45.

We test the distribution of galaxies categorized as quiescent with stricter cuts — assuming Gaussian uncertainties on each EW, if a galaxy's EW (e.g., EW([OII]) is above or within 1σ of the "passive" threshold, we label the galaxy passive; the resulting sample is not significantly different from galaxies selected via the B16 quiescent galaxy cuts on the equivalent widths. See Figure 4.3 for equivalent width and spectral index cuts implemented in this work.

We also calculate the mean SNR per pixel across each galaxy spectrum in the wavelength range 3710-4120, and remove galaxies with SNR$<$5 from our sample, since these are mostly

galaxies without any robustly detected spectral features, and/or uncertainties that are non-Gaussian and dominated by systematic uncertainties due to sky subtraction.

4.3.3 Excluding Brightest Cluster Galaxies

Our analysis focuses on the evolution and build-up of stars in the quiescent galaxy population in massive galaxy clusters, and it is important to note the role BCGs may play in biasing this analysis. BCGs are objects evolving through complex pathways near/at the center of the gravitational potential in clusters, and at the hub of merging and feedback activity in the cluster (Rawle et al., 2012; Webb et al., 2015; McDonald et al., 2016; Pintos-Castro et al., 2019). We treat this population of galaxies as unique, dissociated from the quiescent galaxy analysis that is central to this paper.

Extensive follow-up optical/IR photometry and X-ray observations for the clusters in this work was undertaken since the SPT-GMOS Spectroscopic Survey was published. These allow robust identifications of BCGs, via X-ray and IR peak/centroid characterization, through Chandra and Spitzer data respectively (Calzadilla et al., in prep). Table 3 in B16 provides a list of candidate BCGs for the SPT-GMOS sample. These are galaxies selected on the basis of their optical/IR flux and the projected spatial location in the cluster. We find that only 36 of these galaxies correspond to BCGs identified via X-ray and IR peak/centroid characterization through *Chandra* and *Spitzer* data respectively. 3 BCGs in the sample of high-z clusters ($z > 1.25$) are reported in K19. These 39 galaxies are removed from the galaxy sample characterized here. Note that the number of BCGs excluded is less than the number of clusters, with the understanding that not all BCGs were spectroscopically observed/confirmed in the surveys considered here, or passed our data cuts.

4.3.4 Stellar Mass

We calculate SED fitting-based stellar masses for all galaxies with available spectrophotometry (see Section 4 for model and analysis details). For galaxies passing a nominal "quiescent galaxy" threshold (lack of [OII] emission, D4000 > 1.45), we adopt a homogenous cut (across redshift) at $M > 2{\times}10^{10}$ $M_{\odot}$, that ensures a uniform distribution of stellar masses across redshift bins; this removes a further 102 low-mass galaxies from the sample. See Section 4.6.2 for more details.

4.4 Methods and Analysis

4.4.1 Data Preparation

Masking 1D spectral pixels with unreliable noise properties

In this work, we incorporate data from multiple instruments with a wide variety of operational parameters, e.g., type of grism, observational seeing, etc. Moreover, the 1D spectra in our dataset contain pixels with significant sky subtraction residuals. In almost all cases, these pixels are represented by high noise/uncertainty which is assumed to be Gaussian, which may not be a robust assumption, especially for low SNR spectra observed from high-redshift galaxies, in multi-object slit observations where either the slit roughness or saturated sky contributes to poor sky subtraction. See work such as K19 and the Gemini Deep-Deep Survey (Abraham et al., 2004) for details on artefacts and mitigation strategies.

We mask these pixels in 1D spectra to prevent them from being taken into account in our SED analysis with the following framework. For each galaxy, we sort all uncertainties in increasing order, and attempt to characterise the knee of the uncertainty array, i.e., the value at which the uncertainty increases rapidly. For the majority of 1D galaxy spectra, this transition is captured by $\sim$ 84th percentile pixel in the uncertainty array (see inset of Figure

Table 4.1. `Prospector` Analysis: Free Parameters in SED Model A

Parameter	Description	Priors
$M_{\rm total}(\rm M_\odot)$	Total stellar mass formed	$\rm Log_{10}$ Uniform: [10^9, 10^{13}]
z	Observed Redshift (Mean Redshift from B16 and K19)	TopHat: [$z - 0.002$, $z + 0.002$]
$\log(Z/\rm Z_\odot)$	Stellar metallicity in units of $\log(Z/\rm Z_\odot)$	Clipped Normal: mean=0.0, σ=0.3, range=[-2, 0.5]*
t_{age}	Age of Galaxy in the SED model (Time between start of SF and observed redshift, Gyr)	TopHat: [0, Age(Universe) at $z_{\rm obs}$]
τ	e-folding time of SFH (Gyr)	$\rm Log_{10}$ Uniform: [0.01, 3.0]
$\rm spec^{**}_{norm}$	Factor by which to scale the spectrum to match photometry	TopHat: [0.1, 3.0]
σ_v	Velocity smoothing (km $\rm s^{-1}$)	TopHat: [150.0, 500.0]
$(p1, p2, p3)^{**}$	Continuum Calibration Polynomial (Chebyshev)	TopHat: n=3: [-0.2/(n + 1), 0.2/(n + 1)]

Note. — $*$ Mean, σ and range of the clipped normal priors based on the Mass-Metallicity relation (MZR) from Gallazzi et al. 2005.
$**$ Considered as nuisance parameters.
Please note that $\rm t_{age}$ is an internal parameter to the SED model and is only used towards inference in combination with τ.

4.4). We mask all pixels between 84th-100th percentile of the sorted uncertainty array, as well as adjacent pixels, to eliminate pixels for which the uncertainty is large and poorly characterized.

Resampling

We resample 1D spectra and corresponding uncertainties to a common rest-frame wavelength grid, which facilitates both individual and stacked analysis. This is especially important since our spectra sample a wide redshift range, and as in any stellar population synthesis analysis it is crucial to avoid biases associated with non-uniform sampling of absorption line features (e.g., Leja et al. 2019c). As mentioned in Section 2, the wavelength range common to all spectra in our sample is approximately 3710-4120Å (rest frame). The resampling is performed on each spectrum using SPECTRES (Carnall, 2017), to a common wavelength range (3710-4120Å rest frame) at 2Å/pixel, coarser than both GMOS and LDSS3 1D spectral sampling. SPECTRES preserves integrated flux, and propagates uncertainties by calculating the covariance matrix for the newly binned/sampled spectra.

See Figure 4.4 for examples of masked and resampled spectra from a representative cluster in our sample, SPT-CL J0013-4906 at z=0.41.

4.4.2 SED fitting — Spectrophotometry of individual galaxies

To characterise physical properties of member galaxies in our sample, we perform SED fitting to our spectrophotometry using the Markov Chain Monte Carlo (MCMC)-based stellar population synthesis (SPS) and parameter inference code, `Prospector` (Johnson et al., 2021). `Prospector` is based on the `Python-FSPS` framework, with the MILES stellar spectral library and the MIST set of isochrones (Conroy & Gunn, 2010b; Leja et al., 2017a; Foreman-Mackey et al., 2013; Falcón-Barroso et al., 2011; Choi et al., 2016).

To test the robustness of our parameter inference and the model-dependence of physical

properties, we fit our data with a fiducial model (Model A), and a minimalist model (Model B, see Appendix C). In this work, we specifically use two parametric SFHs — a delayed exponentially declining SFH (delayed-tau), and a single burst. These models incorporate physical priors seen in studies of quiescent galaxies — low specific star formation rates (sSFRs), and a lack of rising star formation in galaxies (e.g., see Belli et al. 2019).

- **Model A**: In this (fiducial) model, we fit as free parameters the total stellar mass formed (M_*), the stellar metallicity ($\log(Z/\mathrm{Z}_\odot)$), a delayed exponentially declining SFH, with age (t_{age}) and e-folding time (τ), and an internal smoothing parameter (σ_{v} (km s^{-1}), to account for the contribution of Doppler broadening by stellar velocities, and resolution of the model libraries). The SFH, defined as the star formation rate as a function of time, is given by:

$$\mathrm{SFR}(t, \tau) \propto t/\tau * e^{-t/\tau} \tag{4.1}$$

  To remove continuum calibration residuals (e.g., related to spectral response, flat fielding) from the spectra, we fit for a spectrophotometric calibration polynomial (a third-order Chebyshev polynomial; see Leja et al. 2019c; Webb et al. 2020).

- ***Model B***: Historically, simple stellar population (SSP) models with instantaneous episodes of star formation have been employed to characterise star formation in early-type galaxies. While not physical, such simple burst models are often assumed to be a proxy for a passively evolving stellar population when observed sufficiently long after a star forming episode. In order to compare our work with prior studies, we also fit a minimally complex model, comprising as free parameters the total stellar mass formed (M_*) and a single burst age t_{age} that accounts for all the mass formed. We fix the metallicity to $\log(Z/\mathrm{Z}_\odot) = 0.0$ (solar metallicity), and treat the internal velocity smoothing as a fixed parameter at σ_{v}=280 km s^{-1}. See analysis and results for Model

B in Appendix A.

Both models assume a Kroupa IMF (Kroupa, 2001a), and no dust attenuation. Nebular continuum and line emission are turned off, as these are not expected to have significant contributions in fluxes of quiescent galaxies. Moreover, the flux normalization in our spectra is uncertain in practice and suffers from aperture losses; we account for this by including a nuisance parameter $\mathrm{spec}_{\mathrm{norm}}$ (spectrum normalization factor), to capture this. We do the fitting in observed wavelength space, and fit for a redshift parameter with narrow priors to capture uncertainties in the measured redshift.

There is considerable evidence shown in the literature that the prior probability densities assumed for the parameters related to the SFHs significantly impact the inferred parameter values; a linearly uniform prior in τ imposes a peaked and more informed prior probability density on the specific star formation rate (sSFR, the parameter of interest when fitting an SFH; see Figure 2 in Carnall et al. 2019a). Thus, the e-folding time parameter τ is constrained by fitting with a uniform prior in log-space, which is seen to be a less informative prior in sSFR. We implement uniform priors for the age parameter from 0 Gyr to the age of the Universe at the epoch of observation. The $\log(Z/\mathrm{Z}_{\odot})$ parameter is sampled with a Gaussian prior, clipped at -2.0 and 0.2. These bounds are limited by the extent of metallicity sampling in the MILES and MIST model libraries. The mean and σ of this Gaussian are based on the Mass-Metallicity relation (MZR) from Gallazzi et al. (2005); please see Appendix A for more discussion.

Within `Prospector`, we use `emcee` (Foreman-Mackey et al., 2013) to sample the posterior distribution of free parameters in each model, where burn-in, number of walkers, and number of iterations are selected iteratively, until convergence is seen to be reached (via visual confirmation) in the traces/steps of 32 randomly sampled walkers.

The details of these models, the model parameter definitions, and priors used here are laid out in Table 4.1. See Section 4.5.3 for a discussion of analyses using the inferred SED

Table 4.2. Binning Criteria and Description

Bin Description	No. of Bins	Criterion
Observed Redshift (z)	4	$0.29 < z < 0.45 \vert 0.45 < z < 0.61 \vert 0.61 < z < 0.91 \vert 1.2 < z < 1.5$
Stellar Mass (M_*)	2	$10.3 < \log M < 10.9 \vert 10.9 < \log M < 12.1$
Final descendant cluster mass ($\log(M_{500c,SZ,z=0}/\,\mathrm{M}_\odot)$)	2	$\log M_{500c,finaldesc} > 15 \vert \log M_{500c,finaldesc} < 15$
Phase-space location ($p = r_{projected}/r_{500c} \times v_{peculiar}/\sigma_v$)	2	Early+Mixed infall:$p < 0.4$| Late infall: $p > 0.4$

parameters.

4.4.3 Binning and stacking quiescent galaxy spectra

To demonstrate aggregate properties of galaxies in our sample, we calculate median properties for different sub-populations of galaxies, and we perform stacking analyses on these same sub-populations.

Before considering which galaxy spectra to stack and the implementation of a robust algorithm to do so, it is worth noting that stacking can result in biased inferences of galaxy properties, especially in scenarios where there is a highly non-linear correlation between spectral flux and the said property (e.g., metallicity evolution does not scale linearly with flux in any part of a typical galaxy spectrum). Thus, stacking should be considered with appropriate caution. That being said, the highest-redshift galaxies (at $z > 1.2$) have severe sky subtraction residuals with non-Gaussian and ill-measured uncertainties, which do not allow us to reliably interpret these spectra via individual galaxy SED fitting only. Moreover, the galaxies in this subpopulation are at different redshifts between $1.2 < z < 1.4$; each individual spectrum is impacted at different rest wavelengths by skylines, allowing the stacking to "fill in" much of the gaps. Therefore, to boost SNR as well as wavelength coverage, stacking

provides us with an aggregate indication of galaxies' physical properties of interest.

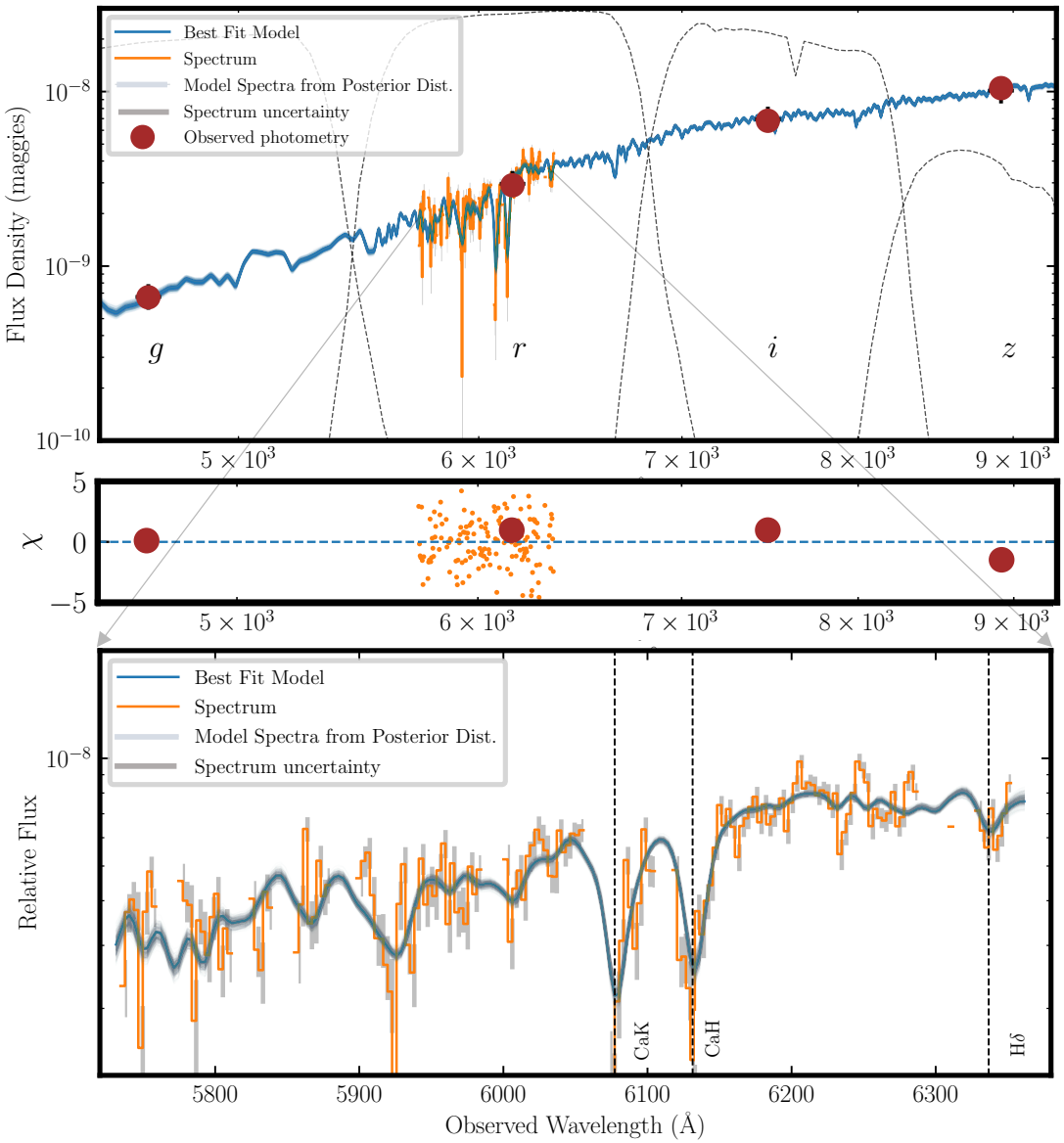

Figure 4.5 (Top) SED of a massive quiescent member galaxy of SPT-CL J2335-4544 at $z = 0.55$, shown as flux density (maggies, Jy/3631) vs. observed wavelength (Å). Model fits (blue) to photometry (brown) and spectrum (orange) are shown. (Middle) Residual (χ) values for spectrum and photometry. Photometric data considered here is precise (uncertainties < 0.03 mag). (Bottom) Zoomed-in version of the spectrum, uncertainty and best-fit model.

We bin galaxies along the following axes to generate subsamples for stacking:

- **Galaxy Stellar Mass (M_*)**: as calculated by SED fitting for a given SFH model.

- **Observed Redshift**: redshift measured from spectroscopy (see B16 and K19).

- **Final Cluster descendant mass, log($M_{500c,SZ,z=0}/\,M_\odot$)**: as classified by simulation-based predictions (Fakhouri et al., 2010; McDonald et al., 2017b) to determine nominal evolutionary paths for SPT clusters across redshift. We sort clusters based on whether their final cluster mass at redshift 0 ($M_{500c,z=0}$) would fall above or below the locus for $\log(M_{500c,SZ,z=0}/\,M_\odot)$=15 — a value of convenience chosen because it splits the cluster sample into two approximately equal parts. In the B16 cluster sample, we anticipate a uniform distribution of galaxies as a function of clustercentric radius and redshift and hence do not further divide the galaxy sample as a function of radius (the cluster size does not change significantly across the redshift range 0.3<z<0.9, and the spectroscopic slit sizes are much smaller than cluster radii at a given redshift; see Muzzin et al. (2012).

- **Phase-space location**: It is common to consider cluster member galaxy properties mapped to cluster-centric radius (e.g., scaled by r_{500c}, r_{200c}, or virial radius $R_{\rm virial}$; Ellingson et al. 2001; Wetzel et al. 2012; Brodwin et al. 2013a; Strazzullo et al. 2019), and stack observations across a wide range of cluster mass for fixed radius. This has value because there will be some degree of sorting of galaxies by their accretion history, i.e., the galaxies first added to the building cluster will tend to appear closer to the cluster center and with more recent additions often observed further out in projection. In this paper, we choose to use a more direct proxy for accretion history, namely the infall time $p = r_{\rm projected}/r_{500c} \times v_{\rm peculiar}/\sigma_{\rm v}$ (Noble et al., 2013; Pasquali et al., 2019). Much like the scaling for R_{200}, the scaling for cluster core size and velocity dispersion captures the relationship between observed position of the galaxy in phase-space and the cluster virial radius. We use $M_{500c,SZ}$ to compute r_{500c} with cluster SZ centroids, and use dispersion $\sigma_{\rm v}$ values as calculated in B16 and B17. For the spectroscopic sample of SPT cluster members in B16, Kim et al. (in prep) have determined a value

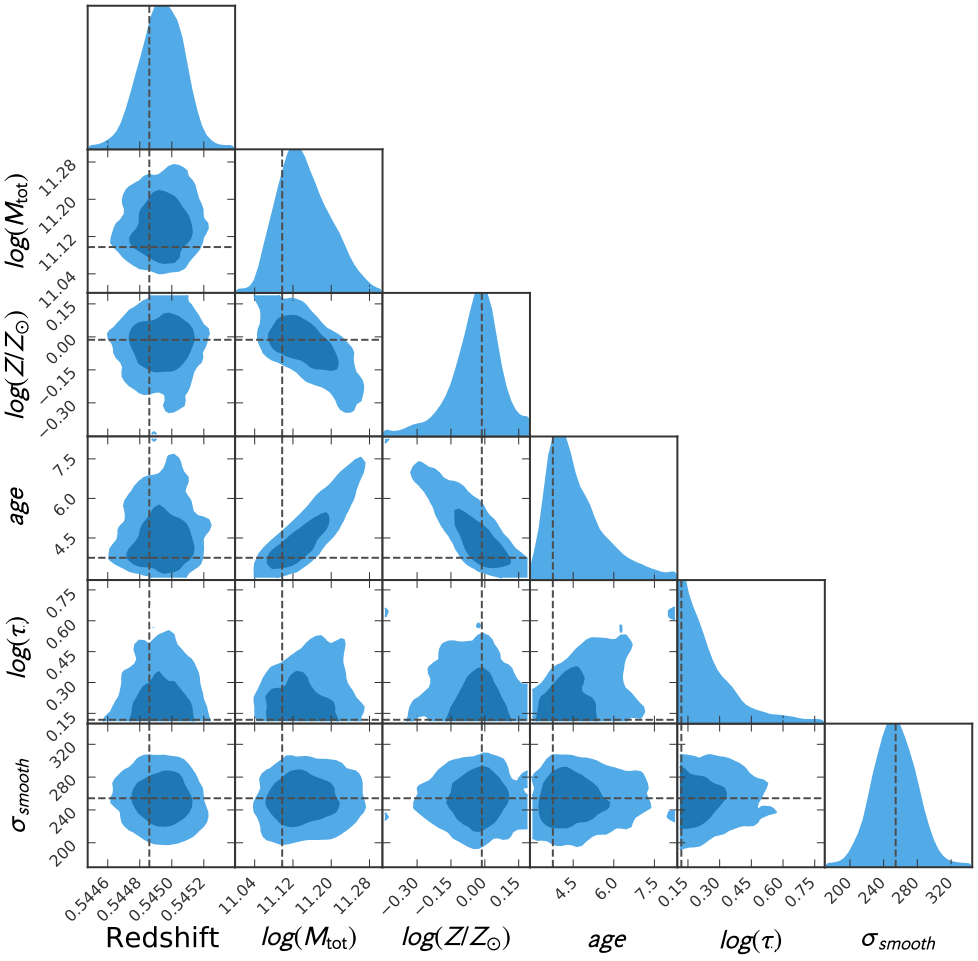

Figure 4.6 Corner plot with posterior distributions and correlations for inferred parameters in the `Prospector` SED fitting analysis for a single member galaxy of SPT-CL J2335-4544 at $z = 0.55$.

of $p < 0.4$ implies early or mixed infall, and $p > 0.4$ implies late infall of the galaxy into the cluster's potential well. We use these cuts to distinguish galaxy subpopulations by their accretion history.

We determine bin boundaries using a number of factors, e.g., having similar number counts in each stack bin (for galaxies, as well as clusters), physical considerations (e.g., dynamical infall timescales of galaxies in clusters to match redshift bin sizes;$\sim$ 1-1.5 Gyr), having $>$ 30 galaxies per bin for a given subsample (except in the highest redshift bin). See a summary of bin criteria and description in Table 2.

To produce a median-stacked spectrum from all of the spectra that contribute to a chosen bin, we proceed as follows: First, each spectrum is normalized by the median flux value between rest-frame 4020-4080Å, a wavelength region lacking any strong spectral features. In this normalization, as in all other aspects of the stacking algorithm, we consider only the spectral pixels not previously masked due to uncertain sky line subtraction. To further guard against outlier pixel values across the sample that weren't previously masked, the stacking algorithm exclusively uses median rather than mean values. At a given pixel in the stacked output spectrum, the algorithm considers as inputs all unmasked spectral pixels that contribute at that wavelength, each of which has been renormalized and resampled as above. To capture the uncertainties on each input flux, while using median estimates exclusively, the algorithm then calculates 10000 instances of the median stack by Monte-Carlo sampling the input flux values with their uncertainties, and taking the median value of each instance. We take the median (50th percentile) of these 10000 instances as the stacked flux. To calculate uncertainties, we bootstrap the above process and use the standard deviation of the resulting distribution of stacked flux values at a given pixel as the uncertainty on the above flux value. Further details of these uncertainty calculations compared against other methods are given in Appendix B.

4.5 Results

4.5.1 SED Fitting

In Figure 4.5, we show an example of observed photometry, optical spectrum, and the best-fit SED models for a single member galaxy in the cluster SPT-CL J2355-4544 at $z = 0.545$, fit via Model A. Figure 4.6 shows a corner plot with posterior distributions of the various fit parameters. We find the best fit total stellar mass formed to be $M_{\rm total} = 1.32^{+0.11}_{-0.10} \times 10^{11}$ $\rm M_\odot$, best-fit metallicity to be $\log(Z/\rm Z_\odot) = -0.03^{+0.07}_{-0.10}$, and the best-fit dispersion $\sigma =$

252^{+24}_{-21}kms^{-1} (instrumental dispersion convolved with intrinsic velocity dispersion). Under the assumption of a delayed-τ SFH, the best-fit age=$4.35^{+1.25}_{-0.62}$ Gyr and $\tau = 0.20^{+0.13}_{-0.08}$ Gyr, making this a galaxy that formed a majority ($> 50\%$) of its stars rapidly at $z > 1.5$.

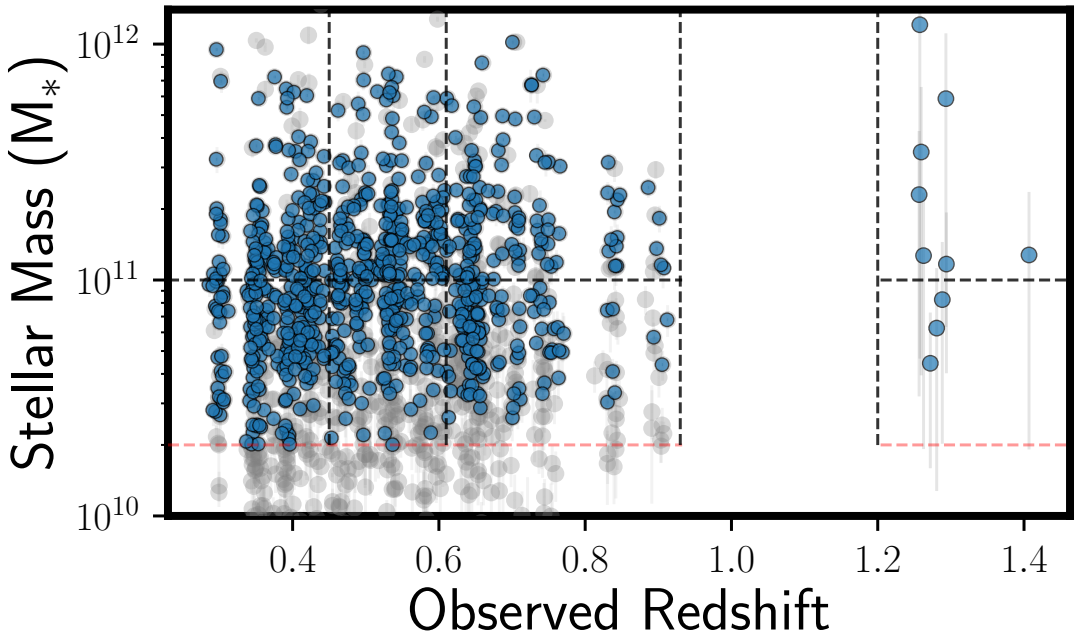

Figure 4.7 Stellar mass as a function of redshift for member galaxies in the SPT-GMOS survey for clusters at $0.3 < z < 0.9$, as characterized by an SED fit to individual galaxies via a delayed-tau SFH model (i.e., Model A, grey points). We exclude a small fraction of galaxies with masses $< 2 \times 10^{10}$M$_\odot$($\log M < 10.3$) to create a uniform lower limit on the galaxy masses and median mass per bin; the quiescent galaxies considered in this sample are marked with blue points. The dotted lines mark the stellar mass and redshift bins used in this work.

4.5.2 Stellar masses

Our fitting framework calculates total stellar mass formed in the duration of each galaxy's SFH ($M_{\rm total}$, in units of M$_\odot$). `Prospector` allows us to model the remnant stellar mass (the parameter of interest) for each galaxy, accounting for 20-40% mass loss from winds and supernovae for a given SFH model. Throughout this work, we refer to the 'remnant stellar

mass' as stellar mass, unless otherwise noted (M, in units of $M_\odot$, or $\log(M/M_\odot)$).

The median stellar mass for the fiducial model across the sample is $\log M = 10.90$, with a range of $10.3 < \log M < 12.0$ (see Figure 4.7). The signal-to-noise ratio cut (SNR$>$ 5) implemented here, in combination with the stellar mass cut, results in a cluster galaxy sample with a uniform stellar-mass distribution (flat lower-mass limit and similar median stellar mass per bin) as a function of redshift (for a discussion on SNR, see Appendix D). We also note that we keep consistent the rest-frame optical spectral features that allow us to measure ages and metallicities uniformly (as noted in previous sections), while the photometry for each galaxy — which is a dominant contributor to the calculation of stellar mass M — samples different portions of a given galaxy's SEDs.

We note that for calculating stellar masses in galaxies, parametric SFHs such as a delayed-tau model show a difference of as much as 0.1-0.2 dex when compared with stellar masses calculated via non-parametric SFHs (Carnall et al., 2019a; Leja et al., 2019a,c; Lower et al., 2020b), though this difference is much more prominent in samples of star forming galaxies compared with quiescent galaxies. We note this potential systematic in stellar mass, when comparing results in this work with inferences in the literature.

Table 4.3. Definitions of age metrics used in this work. Please note that t_{age} is an internal parameter to the SED fits and is not used for physical interpretation.

Parameter	Description
t_{50}	Mass-weighted age; lookback time from the redshift of observation when 50%of a galaxy's total stellar mass M_{total} was formed
Age of Universe (t_{50})	Age of the Universe when a galaxy has formed 50% of its total stellar mass (for the assumed cosmology)
z (Age of Universe at t_{50})	Formation Redshift; redshift at Age of Universe (t_{50})

4.5.3 Star Formation Histories of Individual Galaxies

Using the delayed-tau SFH model, we constrain the age and e-folding time (τ) of each quiescent cluster galaxy in our sample. One of the biggest advantages of a functional form of SFH for a given galaxy is the ability to physically interpret the different stages of galaxy evolution, i.e., a nominal star formation start time, a peak of star formation activity, and declining and subsequently quiescent evolution. To consolidate the two parameters age and τ into one physically interpretable parameter, and to facilitate comparison with studies of massive galaxies exploring mass assembly, we do the following:

1. We calculate the integral of the assumed delayed-tau SFH (see Equation 1). The normalization of the integral corresponds to the total mass formed $M_{\rm tot}$ of the galaxy, a parameter being fit in the SED fitting process.

2. For quiescent galaxies in our sample, we define t_{50} as lookback time from the measured redshift of the galaxy to when the galaxy has formed 50% of its total stellar mass, or its mass-weighted age. We acknowledge that many studies also use t_{30}, t_{70} and t_{90} as parameters of similar interest (e.g., Pacifici et al. 2016). The definition of t_{50} we use in this work is similar in nature to the mean stellar age or mass-weighted age for a delayed-tau SFH. This allows us to compare our results with mass-weighted age calculations for massive quiescent galaxies in the literature.

The age of the Universe at the median t_{50} across the sample is 2.3±0.3 Gyr, corresponding to a formation redshift $z(t_{50}) = 2.8 \pm 0.5$ (see Section 4.6.2 for more details).

4.6 Ages of Stellar Populations in Cluster Quiescent Galaxies

The objective of this study is to constrain formation redshifts and stellar masses in massive quiescent galaxies in galaxy clusters, and address the dependence of these properties on accretion history of the galaxies and the cluster mass assembly pathways.

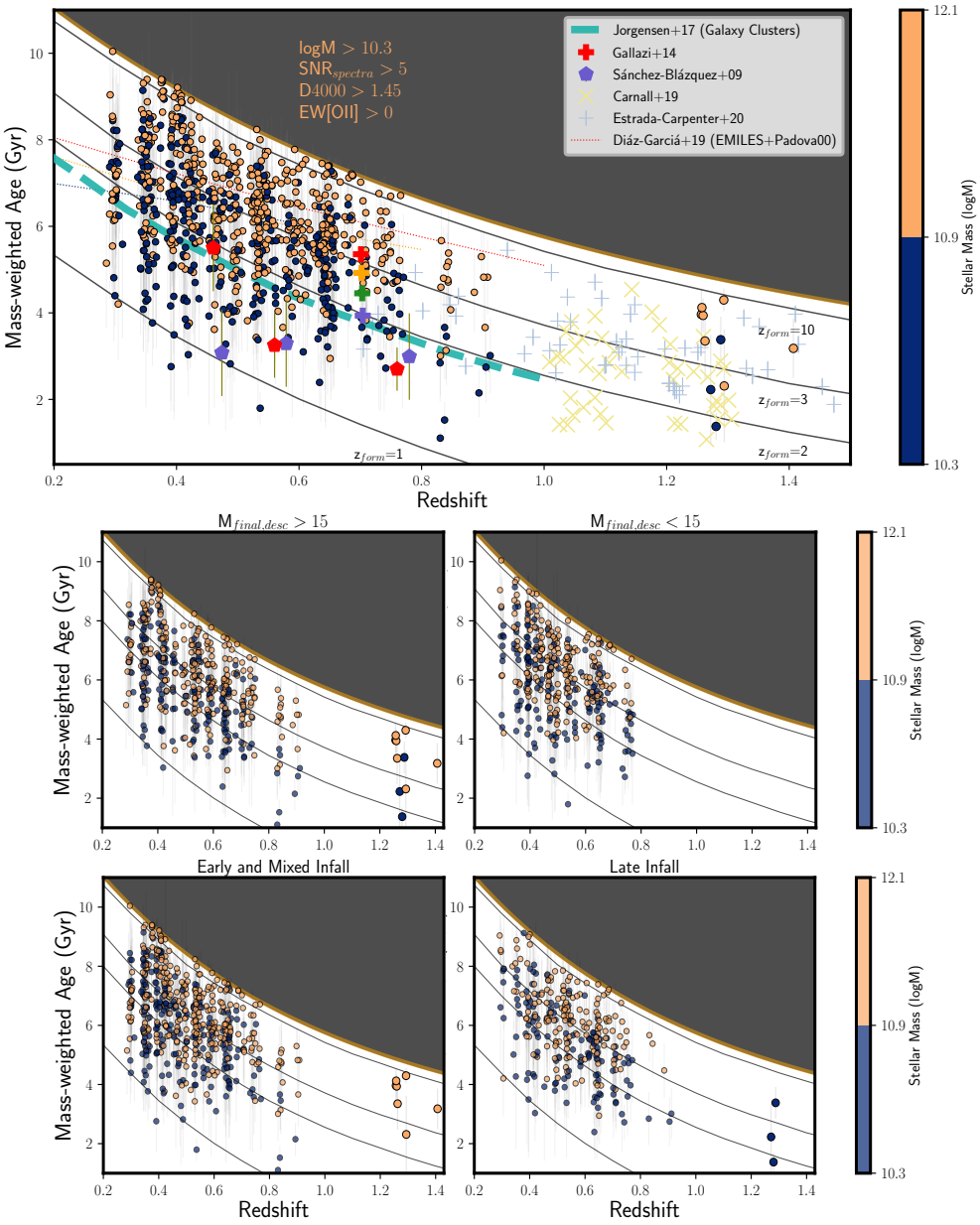

Figure 4.8 (Top) Mass-weighted Age (Gyr) as a function of observed redshift. The circle points represent ages of galaxies from this work, with blue (orange) points representing galaxies with low (high) stellar mass, as calculated via the SED fitting analysis. These measurements are compared to a wide range of literature on cluster galaxies and massive quenched galaxies in the field (see Section 4.6 and Table 4.4). (Middle) Age vs redshift for galaxies in clusters with $M_{\rm final,desc} > 15$ (left) and $M_{\rm final,desc} < 15$ (right). (Bottom) Age vs redshift for galaxies with early and mixed infall (left) and late infall (right), as measured from their phase-space location in velocity-radius space. Black lines indicate the age of simple stellar populations (SSPs) with different formation redshifts.

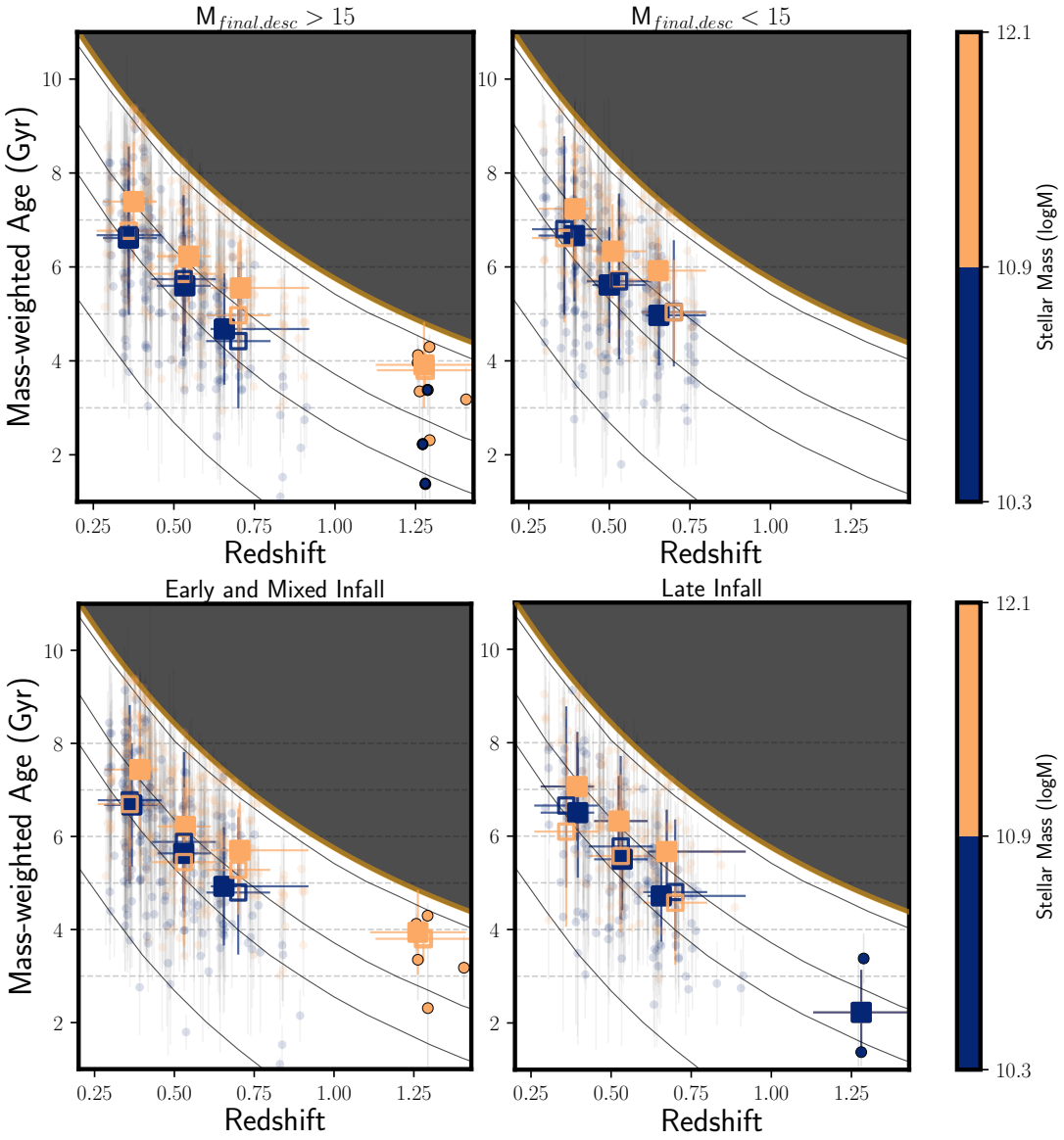

Figure 4.9 (Top) Mass-weighted Age (Gyr) as a function of observed redshift (same as Figure 4.8), to illustrate aggregate and stacked spectra properties of each subpopulation considered in this work. Solid filled squares correspond to median ages per redshift and stellar mass bin (with standard deviation of the ages represented by the error bars). Non-filled squares correspond to stacked spectra ages.

In particular, we characterise these variables as:

1. The final descendent galaxy cluster mass $\log(M_{500c,SZ,z=0}/\,M_{\odot})$, a proxy for the mass evolution of the host galaxy cluster, and

2. The nominal infall time of the galaxy within the cluster, given by a galaxy's phase space location.

Here, we discuss the ages and formation redshifts of these galaxies, and compare these to other massive and quiescent cluster and field galaxy studies. In this section, we refer to mass-weighted ages (t_{50}) as **ages**, and refer to the epoch corresponding to that age as **age of the Universe at (t_{50})**, unless otherwise specified. See Table 4.5.2 for a summary of key age and redshift metrics used in this work.

4.6.1 Mass-Weighted Ages vs Redshift

Low-z Galaxies

In Figure 4.8, we plot t_{50} (or mass-weighted ages) as a function of galaxy redshift, and compare these to sample ages in other published works on massive quiescent galaxies in the field and cluster environments. We show (with black solid lines) evolutionary tracks of simple stellar populations (SSPs) corresponding to an instantaneous episode of star formation at formation redshifts of $z = 10$, 3, 2 and 1 to visually assess typical formation redshift ranges for these galaxies (Tacchella et al. 2021). The colors correspond to remnant stellar mass $\log M$ of a given galaxy, divided into two bins. Consistent with other studies of large samples of massive quiescent galaxies, we identify a diversity of SFHs across redshift and masses in our sample as seen from the distribution of ages (16th, 50th and 84th percentile ages as $6.23^{+1.41}_{-1.38}$ Gyr, with an uncertainty of $\sim$1.2 Gyr for a representative quiescent galaxy in the sample). We note that the most massive galaxies (dark orange circles in Figure 4.8) are seen to have the largest ages possible at the redshift of observation allowed in our SED models (bound by the age of the Universe). Lower mass galaxies (blue circles in Figure 4.8) prefer a mass-weighted age corresponding to an SSP formation redshift of $z < 2$, while the highest mass galaxies show formation redshifts of $z > 3$, up to $z > 10$. This is consistent with downsizing

Table 4.4. Description of studies of massive quiescent galaxies used in this work for comparison

References	Type	Number of Galaxies	Redshift	Stellar Mass $\log(M/\mathrm{M}_\odot)$	Age Measurement
Estrada-Carpenter et al. (2020)	Field	100	$0.7< z <2.5$	$\log M >10$	CSP + non-parametric SFH
Tacchella et al. (2021)	Field	161	$0.4< z <1.25$	$10< \log M <12$	CSP + non-parametric SFH
Carnall et al. (2019b)	Field	75	$1.0< z <1.3$	$\log M >10.3$	CSP + parametric SFH
Díaz-García et al. (2019)	Field	8500	$0.1< z <1.1$	$10< \log M <11.2$	SSP
Gallazzi et al. (2014)	Field	33	$z \sim 0.7$	$\log M >10.5$	SSP
Jørgensen et al. (2017)	Cluster	221	$0.2< z <0.9$	$\log M >10.3$	SSP
Sánchez-Blázquez et al. (2009)	Cluster	215	$0.4< z <0.8$	$\sigma^1 >100$	SSP
Webb et al. (2020)	Cluster	331	$1< z <1.5$	$10< \log M <11.6$	CSP + non-parametric SFH
This work	Cluster	837	$0.3< z <1.4$	$10.3< \log M <12.1$	CSP + parametric SFH

Note. — SSP = single stellar populations, CSP = composite stellar populations. [1]Sánchez-Blázquez et al. (2009) use velocity dispersion σ as a stellar mass proxy.

trends seen in other studies — star formation rate and stellar mass assembly of massive galaxies peaked at earlier times relative to lower mass systems (Cowie et al., 1996; Cimatti et al., 2006), which implies that massive galaxies should form their stellar mass earlier than lower mass galaxies.

Table 4.4 summarises the literature we have used extensively in this work for comparing ages and formation redshifts; these are studies of cluster and field galaxy samples across a wide range of stellar masses and redshifts. Also shown are the sizes of the sample, and the methodology used to measure ages — either SSPs, single stellar populations (SSPs), or composites of SSPs (composite stellar populations, CSPs).

In Figure 4.8, we also show results from Estrada-Carpenter et al. (2020) (blue plus points) and Carnall et al. (2019b) (yellow crosses) at $z > 0.8$, who calculated ages of massive quiescent field galaxies from CSP-based SED models. We plot data from stellar mass bins given in Gallazzi et al. (2014) (plus points) and Díaz-García et al. (2019) (dotted lines) at $0.4 < z < 0.8$ where, the mass bins are defined as $10 < \log M < 10.4$ (purple), $10.4 < \log M < 10.8$ (yellow), $10.8 < \log M < 11.2$ (green) and $\log M > 11.2$ (red). These studies show ages calculated via SSP-based models (which tend to be lower, and bias ages towards the most recent episode of star formation; see e.g., Carnall et al. 2018).

There are limited cluster-based studies that calculate galaxy properties using SED models that are non-SSP based (i.e., without assuming an instantaneous burst of star formation) in this redshift range. Jørgensen et al. (2017) (cyan dashed line) and Sánchez-Blázquez et al. (2009) (green pentagon points) use SSP-based models to calculate ages of galaxies from clusters between $0.2 < z < 0.9$ (with a sample lower limit of masses and velocity dispersions of galaxies similar to this work). While ages from these lowest mass galaxies are consistent with these studies, we anticipate a systematic bias of > 1 Gyr in these studies given model assumptions (Carnall et al., 2019a), when compared to this work.

In middle panels of Figure 4.8, we plot a subset of galaxies divided by membership in

clusters above or below $\log(M_{500c,SZ,z=0}/\,M_\odot) = 15$. Comparing the two subsets, we do not see a substantial difference in ages and stellar mass distribution as a function of redshift (except galaxies in the redshift $z > 0.61$ clusters). This is explored further in Section 4.6.1 and Figure 4.9.

Bottom panels of Figure 4.8 show the subset of galaxies tagged as early+mixed infall times (bottom left) and late infall times (bottom right). We note that the oldest galaxies in our sample (at $z_{\rm form,SSP} > 10$) are mostly located in the early+mixed infall subsample — 28 galaxies (26 with high stellar mass (orange)), relative to only 7 in the late infall subsample. This indicates that these galaxies have spent one or multiple turnaround times around the center of a cluster gravitational potential well and have the highest mass-weighted stellar ages, consistent with a hierarchical picture of a grow-and-quench evolution mechanism; see Section 1 of Tacchella et al. (2021) and references therein.

Mass-weighted ages of galaxies observed at $z > 1.2$

The 10 highest redshift massive quiescent galaxies in our sample span $1.22 < z < 1.42$, and belong to the high $\log(M_{500c,SZ,z=0}/\,M_\odot) > 15$ bin. The median and 16th-84th percentile range of ages is $t_{50} = 3.4^{+0.7}_{-1.1}$ Gyr. Three of the galaxies have a phase-space location corresponding to late-infall time (median age $t_{50} = 2.2$ Gyr), while 7 galaxies belong to the early+mixed infall bin (median age $t_{50} = 4.1$ Gyr); see middle and bottom panels of Figure 4.8.

The range in mass-weighted ages is consistent with the diversity seen in massive field galaxy samples in Carnall et al. (2019b) ($2.7^{+0.8}_{-1.1}$ Gyr) and Estrada-Carpenter et al. (2020) ($3.0^{+0.9}_{-0.8}$ Gyr), studies of massive quiescent galaxies sampling similar redshift ranges. The lack of a substantial offset in median ages of cluster members and standard deviation of ages compared with field galaxies (albeit for 10 galaxies only) is consistent with other cluster and field galaxy studies (Raichoor et al., 2011; Webb et al., 2020). Moreover, qualitatively, if we

consider galaxies in the $\log(M_{500c,SZ,z=0}/\,\mathrm{M}_\odot)> 15$ bin, we find that the formation redshifts of high-z galaxies are consistent with those of the most massive low-z galaxies (i.e., these can be considered to be antecedents of low-z galaxies), and consistent with a purely passive evolution scenario.

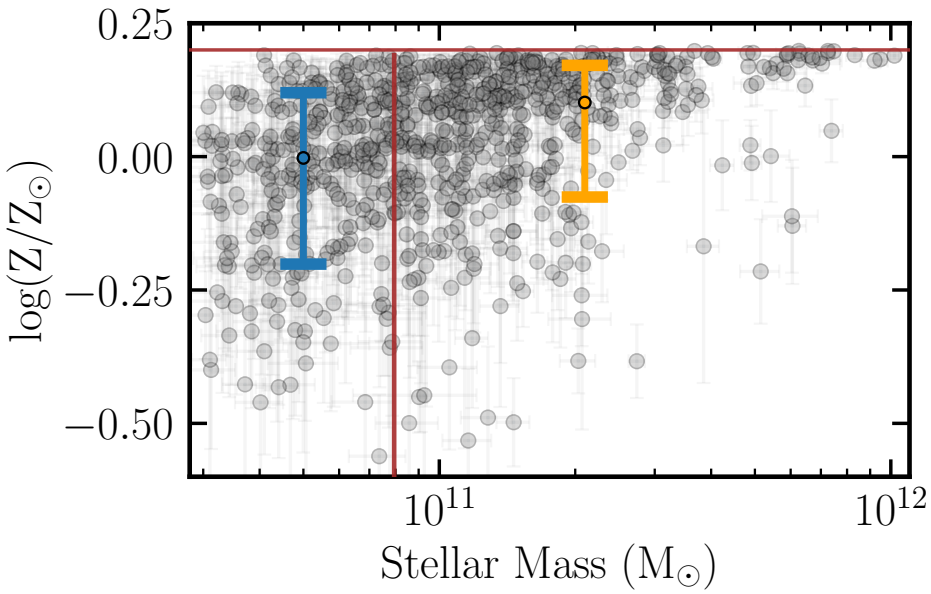

Figure 4.10 Metallicity ($\log(Z/\mathrm{Z}_\odot)$) distribution for galaxies considered in this work, as a function of stellar mass. The red horizontal line corresponds to the prior boundary, and the red vertical line is the bin boundary for stellar mass considered in this work. Median, 16th and 84th percentile distribution for metallicity is shown in blue (low mass) and orange (high mass). The median uncertainty in $\log(Z/\mathrm{Z}_\odot)$ is 0.15 dex.

Median and Stack Properties

To demonstrate the aggregate spectral properties of our galaxies, and reliably measure median galaxy properties in our $z > 1.2$ sample (with only low SNR spectra that are seriously compromised by sky-subtraction residuals at some wavelengths), we illustrate mass-weighted ages of stacked spectra as a function of redshift in Figure 4.9. We show ages from stacked spectra (with hollow squares) and median ages per redshift and stellar mass bin (with filled

squares) for a given subpopulation divided by either cluster mass or phase-space location, akin to discussions in the previous sections. The highest redshift bin ($z > 1.2$) only has 3 galaxies in the late infall subpopulation, and is not stacked.

Our stacking results are observed to be consistent with the median properties of galaxies in a given bin — we recover marginal downsizing (increasing formation redshifts with increasing stellar mass), and a marginal increase in formation redshifts with increasing observed redshift in the highest redshift bins (see SSP evolutionary tracks in Figure 4.9 corresponding to $z_{\rm form}$=10, 3, 2 and 1) — which gives credence to the spectral properties of the stacked spectrum of the $z > 1.2$ stack. We also advocate for the uncertainties in each stacked spectrum to reflect the diversity in mass-weighted ages of the constituent galaxies, which is achieved here by Monte-Carlo sampling individual galaxy spectra and measuring the standard deviation of the sampled spectra. This methodology does not underestimate uncertainties in each stack (unlike the stacking methodology where the uncertainty is measured by obtaining the uncertainty on the mean flux in the Monte-Carlo sampled spectra per bin).

Additionally, we observe significant impact of metallicity on obtaining consistency between stacked spectra ages and median ages per bin. If the constituent galaxies cover a wide range of metallicities — > 0.1 dex in $\log(Z/{\rm Z}_\odot)$ — it is challenging to ascribe appropriate priors to the metallicity parameter in constructing a stacked spectrum. This is especially true for galaxies with stellar masses $\log M < 10.90$; see Figure 4.10 that shows the distribution of $\log({\rm Z/Z}_\odot)$ as a function of $\log M$, and median and 16th-84th percentile range of metallicities per stellar mass bin.

Moreover, we note a particularly wide distribution of metallicities in galaxies in the lowest redshift bins ($0.29 < z < 0.61$; ~ 0.1 dex) relative to higher redshifts ($z > 0.61$; ~ 0.05 dex). This is consistent with the idea that at high redshifts, massive quiescent galaxies have a restricted set of pathways to achieve quiescence (D4000 > 1.45 and a lack of [OII] emission), whereas at low redshifts galaxies can achieve quiescence through multiple

pathways (regardless of binning by cluster mass or phase space location).

A detailed discussion of the metallicity distribution of individual galaxies and the alternate stacking method is given in Appendix A and B, respectively.

4.6.2 Formation Redshifts

To quantify the suggestive age differences and downsizing observed in various subpopulations of galaxies considered in this work, and to compare galaxy evolution from different epochs of observation on a common timescale, we plot formation redshifts (corresponding to **age of the Universe at** t_{50}) as a function of stellar mass ($\log M$); see similar analysis of downsizing and trends between observed and formation redshift in samples of field quiescent galaxies (Carnall et al., 2018, 2019b; Estrada-Carpenter et al., 2020; Tacchella et al., 2021).

Figure 4.11 shows the age of the Universe at t_{50} (in Gyr) vs $\log M$ for all galaxies considered in our sample, with color denoting the redshift of observation. The distribution of ages demonstrates both downsizing trends (higher formation redshifts for higher mass galaxies) as well as decreasing formation redshifts with decreasing observed redshifts, consistent with both cluster and field galaxy studies mentioned above.

The distribution of galaxy ages also shows that the majority of quiescent galaxies in our cluster sample have formed 50% of their stellar mass between z=2-3. Note that while the highest redshift galaxies in our sample (at z$\sim$1.3, large black points) are not a statistically large sample — 10 galaxies with a median uncertainty $\Delta t_{50,\text{age of Universe}} = 0.56$ Gyr — the individual formation redshifts are consistent with a downsizing trend.

We also fit a linear age-mass relation to each subpopulation, depicted with solid lines in the top panel. The linear fits to each subsample are given by the following model:

$$t_{50,\text{age of Universe}}(Gyr) = \alpha \log_{10}\left(\frac{M}{10^{11}\,\mathrm{M}_{\odot}}\right) + \beta. \tag{4.2}$$

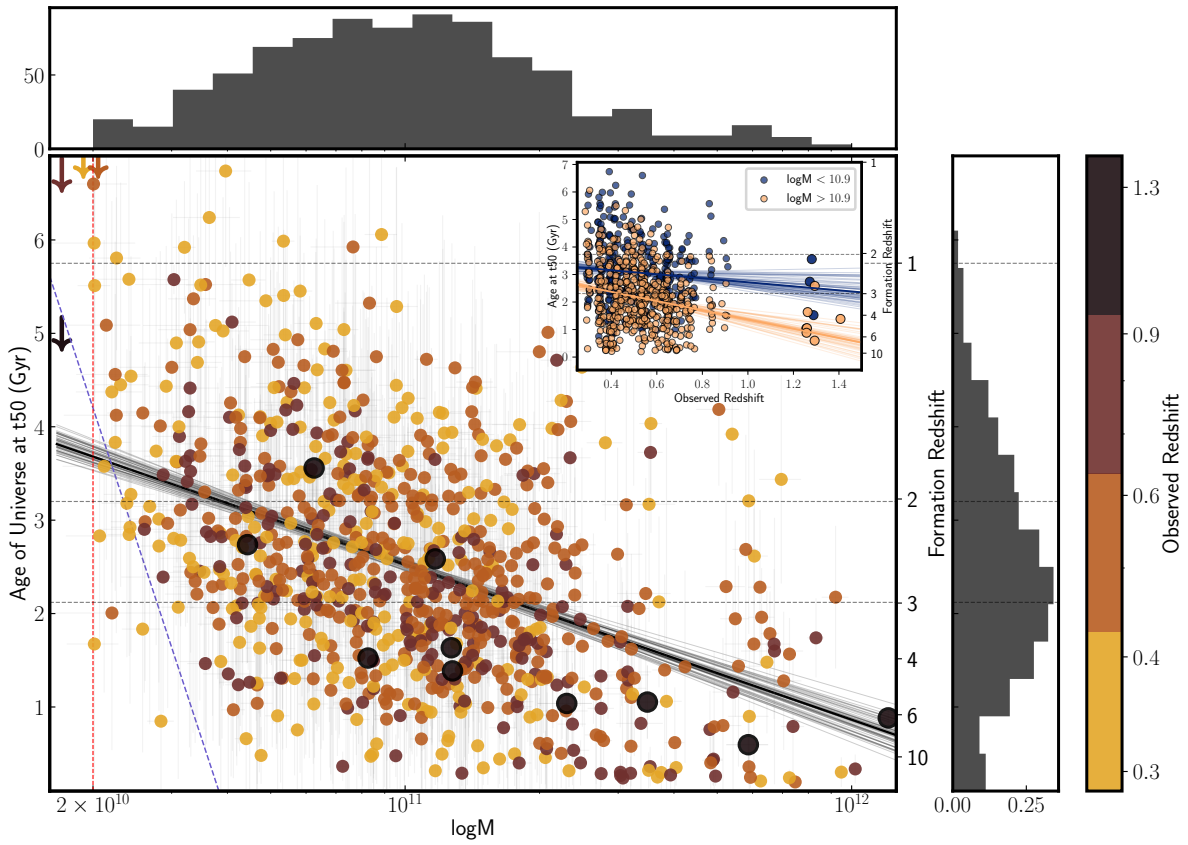

Figure 4.11 Age of Universe at which the galaxy has formed 50% of its mass (corresponding to t_{50}, in Gyr) vs $\log M$ for quiescent galaxies considered in this work. Color at each point denotes the observed redshift, with orange points at $z \sim 0.3$ and large black points at $z \sim 1.3$, the highest redshift galaxies in the sample. Best-fit age-mass relation is plotted in black, with grey lines sampling 50 lines from randomly sampled combinations of slopes and intercepts in the range of best-fit values and 1σ uncertainties. Downward arrows correspond to the maximum age of the Universe allowed for the median redshift in each bin — 5.1 Gyr at $z = 1.28$, and 9.1 Gyr at $z = 0.37$. Overplotted are the fixed mass cut considered in this work (dotted red line). We also show a fixed detectability (or SNR) cut for the lowest mass galaxies near the B16 survey detection limit (in dotted blue), with the slope of the line equal to the best-fit age-(L/M) relation; see Section 4.6.2 for details. (Inset) Age of Universe at t_{50} (Gyr) vs Observed redshift, for galaxies studied in this work, split by stellar mass.

The formation ages/redshifts of the full sample of massive quiescent cluster galaxies in this work is described by $t_{50,\text{age of Universe}}\,(\text{Gyr}) = 2.52(\pm0.04) - 1.66(\pm0.11)\,\log_{10}(M/10^{11}\,\text{M}_{\odot})$. This relationship becomes marginally steeper in the highest redshift bins. The best-fit slopes α and intercepts β for the binned sub-populations are given in Table 4.5.

Age-Stellar Mass Relation and Sample Representativeness

The spectral data for the B16 cluster galaxy sample were taken with the intent of measuring the same mean signal-to-noise ratio per spectrum across redshift for a given absolute magnitude. The sample is not complete (e.g., in that at no absolute magnitude or cluster-centric radius were all cluster galaxies observed, at any redshift). However, it is a representative sample of quiescent member galaxies in SPT galaxy clusters, intended to have a uniform galaxy mass limit across the redshifts considered. As can be seen in Figure 4.7, this is approximately true, and we have imposed a lower stellar mass threshold of $\log M > 10.3$ to further ensure this. Within this sample, the median stellar mass as a function of redshift is flat to within uncertainties. In the analysis presented here, we do not measure the bulk properties of clusters (e.g., luminosity function, stellar mass function, blue fraction, etc.) for which a careful accounting of incompleteness would be critical. Instead, the focus of this study is the spectroscopic analysis of quiescent galaxies that are a representative (and not complete) sample of cluster members.

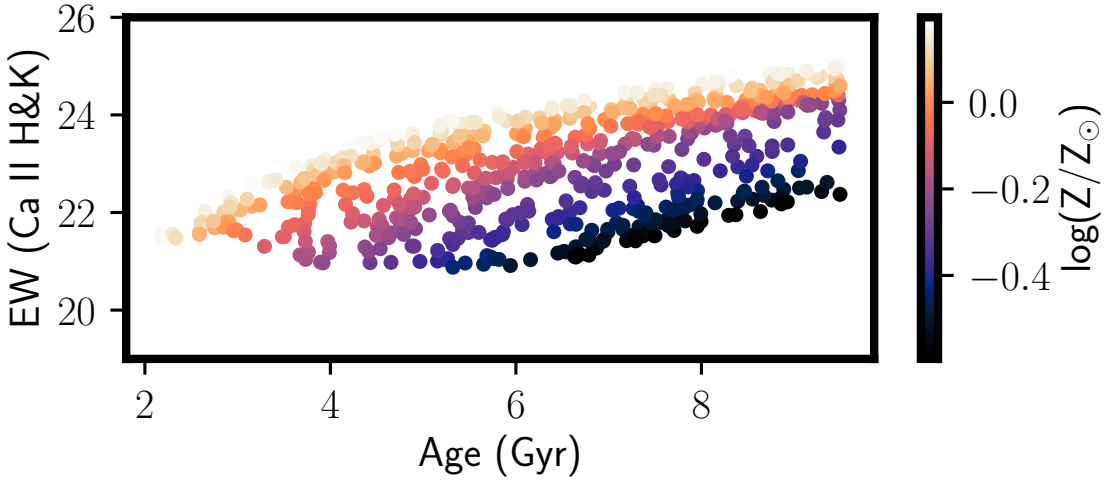

Figure 4.12 Equivalent width of Ca II H&K as a function of age for model SEDs of quiescent galaxies (D4000>1.45). Colors correspond to metallicity $\log(Z/Z_\odot)$.

Nevertheless, because the galaxy spectroscopy discussed here is not a complete sampling of all cluster galaxies within a fixed physical aperture for each cluster, we must also consider

whether subtler incompleteness exists that is correlated with any parameter of interest, e.g., age, metallicity and stellar mass. Such incompleteness might particularly influence results on the low mass end. For example, if the strengths of primary spectral features used to measure redshifts in B16 have a strong negative correlation with age, we might worry that an absence of old low-mass cluster galaxies is due to a failure to measure redshifts for such galaxies, as opposed to an actual absence of such galaxies in clusters.

We test this by measuring equivalent widths of the features that were primarily used to characterize redshifts in B16 and K19 — Ca II H&K and the G-band. These are the strongest absorption features in quiescent galaxy spectra that are visible across the redshift range considered. We compare these measurements with formation redshifts of galaxies in Figure 4.11, and explore whether we are missing spectroscopic confirmation of galaxies in the bottom left (early formation, low stellar mass) and top right (late formation, high stellar mass) corners. We generate 1000 model SEDs for quiescent galaxies using `Prospector` and the models described in Section 4.4.2 by randomly sampling parameters from the priors used in our study (Table 6.2). For these models, we find that EW(Ca II H&K) and EW(G) in galaxies with D4000$>$ 1.45 increases marginally with age. Figure 4.12 shows EW(Ca II H&K) as a function of age for model SEDs. For galaxies with ages > 6 Gyr (corresponding to a maximum formation redshift of $z = 10$ allowed by our sample redshift range), the fractional change in EW(Ca II H&K) ($< 10\%$), and the impact on the probability of redshift success is negligible.

This implies that the probability of redshift success for a given spectrum's signal-to-noise ratio is not negatively correlated with strength of spectral features. We also show that the mean signal-to-noise ratio (SNR) per spectrum does not change as a function of redshift (above a threshold of SNR$>$ 5; Appendix D, Figure 4.23), as was the intent of B16.

While these tests suggest the the B16 input sample has robust sampling in SNR with redshift, and as shown previously has a flat mass cut across redshift, there is a further

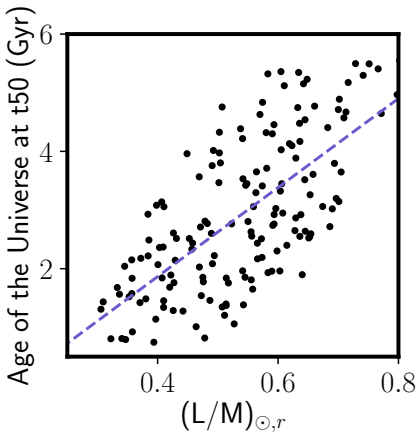

Figure 4.13 Age of Universe at which the galaxy has formed 50% of its mass (corresponding to t_{50}, in Gyr) vs inverse of mass-to-light ratio (L/M) (in solar units) for D4000>1.45 quiescent galaxies drawn from model SEDs. The best-fit relation is plotted as a dotted blue line.

effect to consider at the low mass end — namely that the mass-to-light (M/L) ratio of a stellar population of fixed mass changes as it ages. To test this further we generate model SEDs for galaxies with a fixed stellar mass ($\log M$=10.4) and fixed redshift (z=0.5), and spanning the same metallicity and age range as galaxies in Figure 4.11. We calculate the formation redshifts and M/L ratios, corresponding to r band (AB) luminosities (a close match to the rest-wavelength interval over which spectra have been fit), in units of $(M/L)_{\odot}$) for D4000>1.45 galaxies in this sample. Figure 4.13 shows the distribution of ages of the Universe at t_{50} (Gyr) as a function of the inverse of (M/L), i.e., light-to-mass ratio; lower values of (L/M) correspond to fainter galaxies for a fixed stellar mass. We also calculate the best-fit age-(L/M) relationship, plotted in blue; this implies that for a fixed stellar mass, our observing strategy preferentially chooses brighter late-formed galaxies and is likely to miss the lowest (L/M) (or low mass early-formed) galaxies. In Figure 4.11, we overplot the flat stellar mass cut (dotted red), and also use the slope from the best fit age-(L/M) (dotted blue) to plot a 'fixed detectability' (or equal SNR) line in the lowest-mass end of the distribution. Note that the two lines by choice intercept at the median age (4.2 Gyr) in the lowest stellar mass subsample ($\log M < 10.4$). Quiescent galaxies in the normal direction

to the 'fixed detectability' line to the left are less likely to be detected in the spectroscopy sample and those to the right are more likely to be present. While this will slightly shape the distribution in the age of the Universe at t_{50} versus stellar-mass plane, it is not primarily responsible for the observed distribution.

For completeness we also note that the high-mass late-forming corner of this diagram (i.e., upper right in Figure 4.11) is highly unlikely to be affected by incompleteness that would shape the distribution, as such galaxies would be observed at high SNR. Thus the upper envelope of the distribution of galaxies in this plane, which traces the same slope as the overall fit, is robust.

We also compare the D4000 spectral index distribution measured in this work to that of other cluster and field galaxy studies (Balogh et al., 1999; Hutchings & Edwards, 2000; Kauffmann et al., 2003; Noble et al., 2013; Haines et al., 2017). At our cut (D4000 > 1.45), the D4000 distributions in these studies are similar to this work. We also note that the secondary peak of D_n4000 distribution in Figure 21 of Kauffmann et al. (2003) at D_n4000=1.8 differs from the D4000 peak we see in this work (Figure 4.3) by 0.5σ.

Formation Redshift across bins of Observed Redshift

To quantify downsizing trends inferred from our SED fitting analysis across our sample, we analyse sub-populations based on the binning criteria described in Section 4.4.3.

Row 1 of Figure 4.14 illustrates formation redshifts and stellar masses for galaxies divided into three observed redshift bins. On comparing median formation ages of each subpopulation, we see an average downsizing trend of ~ 0.5 Gyr (across a range of 1.5 dex in $\log M$), which agrees with both field quiescent galaxies at $0.3 < z < 3$ in Carnall et al. (2019a) and cluster galaxy work seen at $z > 1$ in the GOGREEN survey (Webb et al., 2020). The most massive galaxies lie in the bottom right corner of each panel in this plot, as is expected in the scenario of a simple hierarchical structure formation and mass assembly (e.g., Springel

et al. 2005). The diagonal dashed lines plotted in all panels correspond to the best-fit mean age-mass relation for the lowest observed redshift bin ($0.29 < z < 0.45$), to facilitate visual comparison of the relation gradient across redshift. The highest redshift bin $0.61 < z < 0.93$ has the steepest gradient, with a ~ 0.75 Gyr difference from corresponding galaxies in the lower redshift bins.

Figure 4.14 demonstrates that the two lower observed redshift bins contain galaxies with a diversity of formation redshifts in each stellar mass subpopulation, with similar median formation times and age-mass relations. This indicates that the dependence of formation time on stellar mass does not evolve significantly between $0.3 < z < 0.6$ ($\sim$ 2 Gyr in time), over a wide range of stellar masses. For a given stellar mass, this could be either because galaxies in the two lowest observed redshift bins could be derived from the same population, or newer galaxies joining the quiescent population sample the same range of formation redshifts.

In Figure 4.14, we also overplot age and stellar mass values from two snapshots of the IllustrisTNG simulations at $z = 0.1$ (dotted dark green line, 3" aperture) and $z = 1.0$ (solid dark green line, 1" aperture) as seen in Carnall et al. 2019b and Tacchella et al. 2021, with approximately matched quiescent galaxy criteria, to specifically compare the gradient of the age-mass relation seen in simulations with our work. It is interesting to note that the gradient in none of the studies mentioned above (including our work) agree with the $z = 1$ snapshot; in fact, our work indicates a steeper gradient in the $z > 0.6$ population , and steeper still when we overplot the formation redshifts of the 10 highest redshift cluster galaxies in our sample (black stars, in top right panel). This work agrees with the slope of the $z = 0.1$ simulation snapshot, which potentially indicates that for galaxies in our low-z sample ($z < 0.95$), either the steep $z = 0.1$ relation is already in place, or simulations are not able to reproduce the physical properties of quiescent galaxies at z$\sim$1. Note that the TNG simulations considered here contain both cluster and galaxy-scale halos, but are primarily

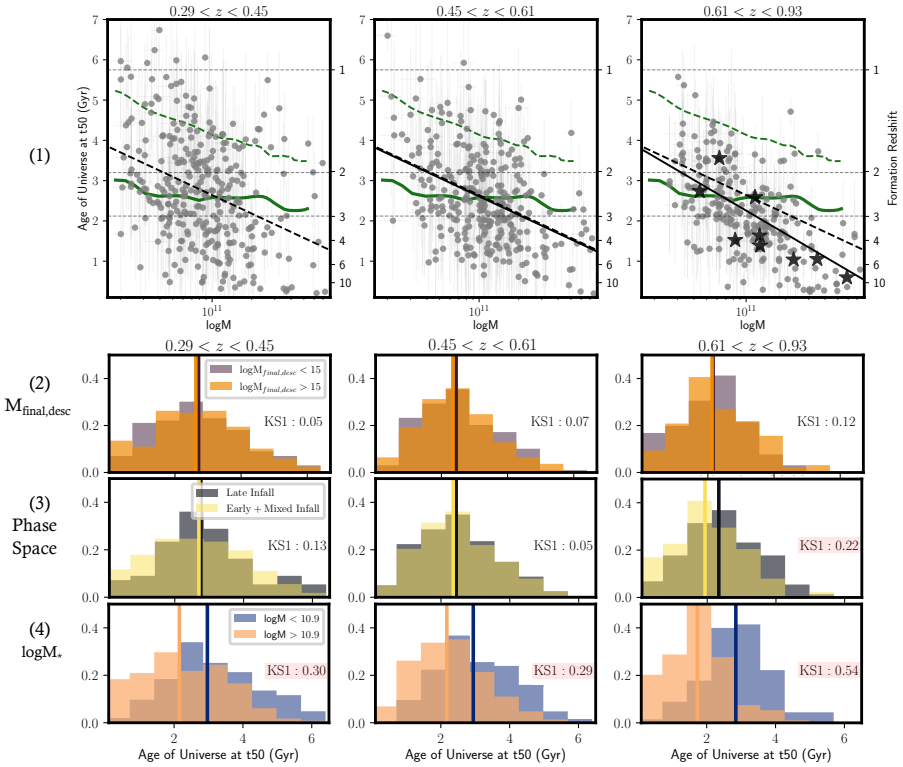

Figure 4.14 (**Row 1**) Age of the Universe at t_{50} in Gyr (or formation redshift) vs. stellar mass $\log M$ for each galaxy. Each subplot displays the galaxy subpopulation in redshift bins $0.29 < z < 0.45$, $0.45 < z < 0.61$, and $0.61 < z < 0.93$ (star symbols in panel 3 correspond to 10 $z > 1.2$ galaxies). Dotted horizontal grey lines represent ages of the Universe corresponding to redshifts 1,2 and 3. Dark green dashed and solid lines represent ages of Universe at formation times vs $\log M$ from the TNG100 field galaxy simulations and redshifts at 0.1 and 1 respectively, as seen in Figure 8 of Carnall et al. 2019b. We fit for a mean relationship between formation redshifts and log(M), indicated by black lines. The diagonal dashed black lines correspond to the mean relationship from panel 1 (the lowest redshift subsample), plotted in all three panels to facilitate comparisons across redshift bins. (**Row 2**) Distributions of age of the Universe at t_{50} per redshift bin, split by $\log(M_{500c,SZ,z=0}/\,\mathrm{M}_\odot)$. Vertical lines correspond to median ages. Inset text refers to KS1 statistic values for the pair of distributions in each panel (see Section **??**). High values of KS1 indicate that the hypothesis that the distributions are the same can be ruled out; statistically significant values are shaded in red. (**Row 3**) Same as Row 2 panels, but galaxies split by phase space ($r_{\mathrm{projected}}/r_{500c} \times v_{\mathrm{peculiar}}/\sigma_{\mathrm{v}}$). (**Row 4**) Same as Row 2 panels, but galaxies split by stellar mass.

designed and executed to sample field galaxies (e.g., the small volume of TNG100 does not contain a representative sample of $M_{500c} \sim 10^{15}\,\mathrm{M}_\odot$ clusters). Dynamically, massive clusters are regions of the Universe with an accelerated clock, and if the star formation in associated

halos is similarly accelerated relative to the field, we might expect better agreement in age-mass relations between lower redshift field galaxy simulations and higher redshift cluster observations, as is seen here.

Formation redshifts across $M_{500c,SZ,z=0}$, phase-space location and $\log M$

In Figure 4.14 (rows 2, 3 and 4), we show distributions of ages of the Universe at galaxy formation redshifts for subpopulations divided by final descendant cluster mass $\log(M_{500c,SZ,z=0}/\,\mathrm{M}_\odot)$, phase-space location $p = r_{\mathrm{projected}}/r_{500c} \times v_{\mathrm{peculiar}}/\sigma_{\mathrm{v}}$ (a proxy for infall time), and stellar mass ($\log M$). We conduct this exercise to determine the galaxy property that contributes the most to the difference in formation redshifts observed in our sample: the cluster mass, galaxy stellar mass, or the phase-space location of the galaxy. Vertical lines in each panel correspond to median ages.

Qualitatively, we find that the galaxy stellar mass subpopulations show the largest difference in formation redshifts, while subpopulations cut by 'environmental' factors like cluster subpopulations or phase-space location have similar median formation redshifts. We quantify this observation by using the two-sample Kolmogorov-Smirnov (K-S) test (Hodges, 1958), and obtain the K-S statistic for the following null hypothesis, to check whether the age distributions in each panel in Figure 4.14 are identical or not:

Hypothesis KS1 : The distributions of formation ages/redshifts — assumed to be *probability distributions* — in each panel are identical (the alternative is that the distributions are not identical).

For large samples being considered in a two-sample K-S test, the null hypothesis is rejected at a 5% significance level if the K-S statistic is $D > D_{\mathrm{threshold}}$, where $D_{\mathrm{threshold}} = 1.358 \times ((n+m)/n{\cdot}m)^{1/2}$ (Knuth, 1997), and n and m are number of elements in the two

Table 4.5. Slopes and Intercepts for Age-Mass relationship

Subsample	$0.29 < z < 0.45$		$0.45 < z < 0.61$		$0.61 < z < 0.93$	
	α	β	α	β	α	β
$\log(M_{500c,SZ,z=0}/\,M_\odot) < 15$	-1.68 ± 0.25	2.66 ± 0.09	-1.56 ± 0.26	2.69 ± 0.09	-1.74 ± 0.29	2.09 ± 0.10
$\log(M_{500c,SZ,z=0}/\,M_\odot) > 15$	-1.37 ± 0.24	2.62 ± 0.08	-1.50 ± 0.26	2.54 ± 0.08	-2.10 ± 0.28	2.37 ± 0.09
Early+Mixed Infall	-1.43 ± 0.19	2.63 ± 0.07	-1.59 ± 0.22	2.63 ± 0.08	-1.81 ± 0.26	2.14 ± 0.09
Late Infall	-1.92 ± 0.43	2.62 ± 0.13	-1.40 ± 0.33	2.58 ± 0.09	-1.93 ± 0.32	2.39 ± 0.10

Note. — Model for the age-mass relation is described by $t_{50,\mathrm{ageofUniverse}}\,(\mathrm{Gyr}) = \alpha \log_{10}(M/10^{11}\,M_\odot)+\beta$

distributions. For each distribution considered here, $D_{\mathrm{threshold}}$ is in the range [0.13,0.19].

In Figure 4.14, we show values of the KS statistic (labeled KS1) in each panel. We see that the null hypothesis is rejected in the higher redshift panels of Row 3 (phase-space) and all panels in Row 4 (stellar mass). We also cannot rule out the hypothesis that the distributions of ages split by $\log(M_{500c,SZ,z=0}/\,M_\odot)$ are identical at all redshifts (Row 2).

As expected, we find that there is a significant difference in ages when galaxies are divided by stellar mass $\log M$ (Row 4), i.e., high mass galaxies are formed earlier than low mass galaxies. To validate this result, we calculate bootstrapped uncertainties for each age bin (in Row 4), and visually confirm that the distributions of galaxy formation redshifts split by stellar mass are not identical.

The KS statistic value of subpopulation of galaxies in the $0.61 < z < 0.93$ clusters split by phase-space location implies that a marginal difference in formation redshifts between phase-space subpopulations cannot be ruled out. As discussed in Section 4.6.1 with respect to Figure 4.8, we observe a subpopulation corresponding to a single burst SSP formation redshift of $z > 10$ in the early+mixed infall subpopulation. We see this subpopulation (of

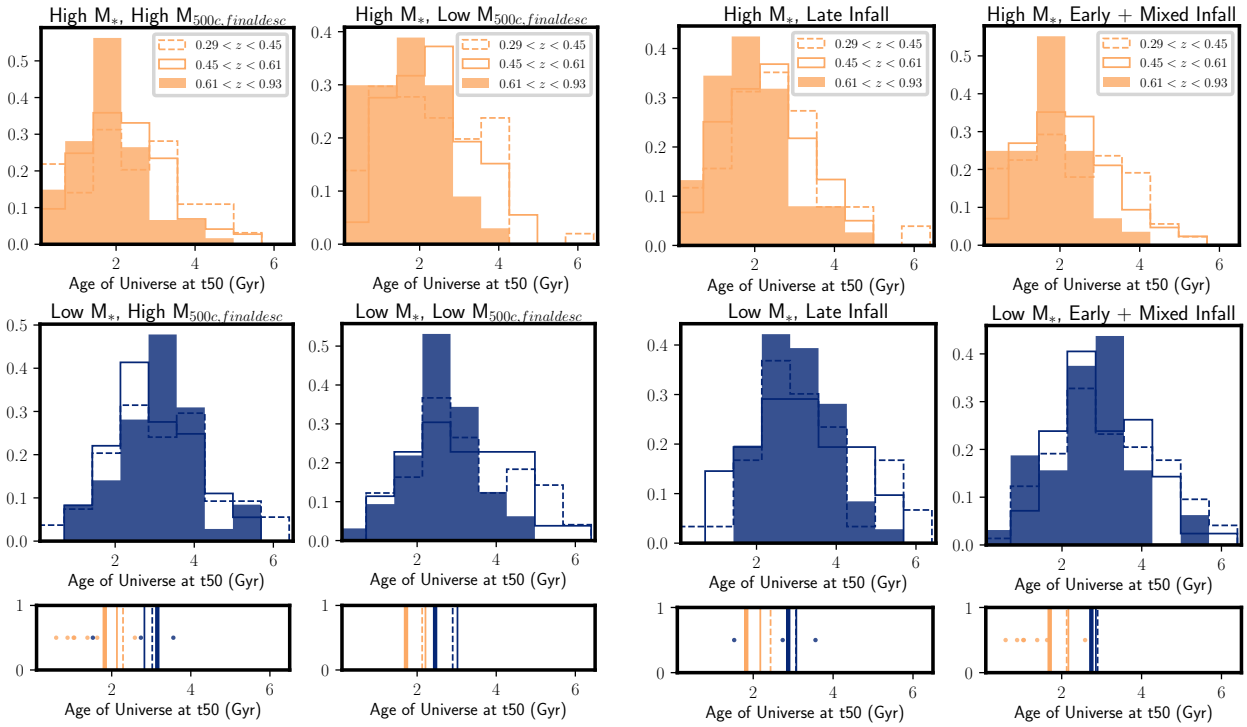

Figure 4.15 Distributions for ages of the Universe at t_{50} (in Gyr) in redshift bins $0.29 < z < 0.45$ (hollow dashed), $0.45 < z < 0.61$ (hollow solid), and $0.61 < z < 0.93$ (filled). Left six panels show distributions for ages where the population is split by $\log(M_{500c,SZ,z=0}/\,M_{\odot})$, whereas the right six panels show distributions for ages where the population is split by phase-space location, or 'infall time'. Stellar mass for each subpopulation is denoted by colors ($\log M < 10.90$ = blue, $\log M > 10.90$ = light orange). The vertical lines in the bottom panels correspond to median ages in each redshift bin (dotted, thin solid and thick solid lines in increasing order of redshift.) Overplotted as dots are the ages of the Universe at t_{50} for the $z > 1.2$ galaxies.

27 galaxies) in the low age tails (age of Universe at $t_{50} < 2$ Gyr) in Row 3 of Figure 4.14 (yellow histogram). When considering the entire distribution of these subpopulations, we find no difference in the median formation age. In cluster environments, we expect galaxies to move along an evolutionary path from late infall to early+mixed infall subpopulations from high to low redshifts. We anticipate this transition to lower the median formation redshifts of the early+mixed infall subpopulation (due to progenitor bias), assuming that the late infall subpopulation has lower median formation redshifts relative to the early+mixed infall subpopulation (as is observed in the highest redshift age distribution). We observe this trend

in Figure 4.14 (yellow vertical line, a difference of $\sim$ 1 Gyr across redshift bins).

This lack of an accretion history-specific difference in formation age for quiescent galaxies in the two lower redshift bins ($0.29 < z < 0.61$) is consistent with findings of intermediate redshift cluster studies at $z < 0.7$ (Sánchez-Blázquez et al., 2009) and SDSS DR7 massive galaxies in Pasquali et al. (2019) (where they find that only the lowest mass — $\log M{<}10$ — show sensitivity to cluster environmental effects). If the galaxy cluster is directly affecting the formation of quiescent galaxies (as opposed to being an overall environment in which the 'clock' of galaxy evolution runs faster), we would expect to see a signal in the formation redshifts of galaxies tagged as quiescent at that epoch when they are split by accretion history (i.e., phase-space). We only see a hint of this in the highest redshift ($0.61 < z < 0.93$) subpopulation. This suggests that even in observably quiescent galaxies, higher redshift clusters are the correct location to observe the echos of cluster-specific transformations that quench star formation (Brodwin et al., 2013a; Webb et al., 2020). An in-depth comparison of accretion histories of member galaxies and star formation timescales will be conducted in a future publication.

As we find stellar mass to be a major contributing attribute in ascribing a formation redshift (or potentially an evolutionary path) to a given galaxy, we inspect each age distribution in Rows 2 and 3 of Figure 4.14 — divided by $\log(M_{500c,SZ,z=0}/\,M_{\odot})$ and phase-space location — as a function of stellar mass.

We use the ages plotted in Figure 4.14 to show the age distributions of galaxies in each redshift bin, divided by the two stellar mass bins, to investigate whether the distributions and median ages across redshift for massive quiescent cluster galaxies are drawn from the same parent distribution. See Figure 4.15, where each panel is a subpopulation split by stellar mass, and environment. This demonstrates that the lower redshift bins have galaxies with extended distributions of formation ages, and the highest redshift bin contains the oldest galaxies. Moreover, the lower mass galaxies in each subpopulation have similar median

formation times and distributions.

In Figure 4.8, we see a median difference in mass-weighted ages between the two stellar mass bins (regardless of redshift bin) of $\sim$ 0.75 Gyr. In Figure 4.15, this translates to a median difference of $\sim$ 1 Gyr (regardless of redshift, final descendant cluster mass, or phase-space location subpopulation). Therefore, this allows us to conclude that the results in this work are consistent with Raichoor et al. (2011), Muzzin et al. (2012), Woodrum et al. (2017), and Webb et al. (2020), that suggest that formation timescales are more varying across stellar mass, and there is only a weak link between formation redshifts for fixed stellar mass across 'environment'.

In Figure 4.15, we can quantify the lower half (0-50th percentile) of age distributions for a given redshift bin, as the fraction of galaxies formed before the median redshift ($z > 3$) in each subpopulation. This metric illustrates that a) *a higher fraction* of more massive galaxy subpopulations forms at $z > 3$, compared with low mass galaxies, b) more massive galaxy subpopulations forms on average a Gyr earlier than their corresponding low mass galaxy subpopulation (see bottom panel of Figure 4.15. We also note a minor difference in formation redshifts between early and late infall galaxies, between 0.2-0.4 Gyr. The highest redshift subpopulations have similar fractions of galaxies with formation redshifts z$>$ 3, indicating that quiescent galaxies at high-redshifts potentially have similar observational signatures and properties. As galaxies within clusters evolve, and newer systems merge with clusters at lower redshifts, we expect these systems to have ages drawn from wider distributions.

4.6.3 Star Formation Timescales and Mass-Dependent Evolution

Akin to Pacifici et al. (2016) and Tacchella et al. (2021), we characterize a notional star formation timescale as the time elapsed between 20% and 80% of stellar mass formed for a given galaxy, t_{20}-t_{80} (in units of Gyr). In Figure 4.16, we plot t_{50} vs $\log M$, with colors indicating the star formation timescale. We find that the most massive galaxies on average

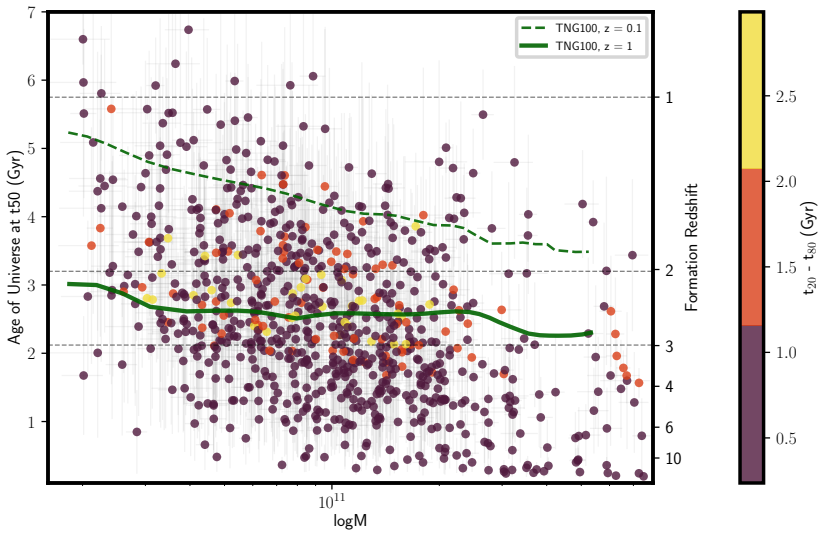

Figure 4.16 Same as Figure 4.11, with points color-coded to represent star formation timescale, as calculated with the parameter t_{20}-t_{80} (Gyr). Dark green dotted and solid lines represent ages of Universe at formation times vs $\log M$ from the TNG100 simulations and redshifts 0.1 and 1 respectively, as seen in Figure 8 of Carnall et al. 2019b. The most massive galaxies have mostly formed before $z > 2$, while the lowest mass galaxies have formation redshifts of $z < 3$. While the most massive galaxies have formed stars in the shortest time-scales, we observe that the most extended star formation is shown by galaxies at formation redshifts between 1.5-3.5.

exhibit shorter star formation timescales (i.e., for $\log M > 11.5$, the median star formation timescale is $0.45^{+0.08}_{-0.07}$ Gyr, whereas median timescales for the $\log M < 11.5$ is $0.64^{+0.04}_{-0.02}$ Gyr); this is consistent with other studies (see references below). This analysis has its shortcomings; see Appendix D in Tacchella et al. (2021) for comparisons between parametric and non-parametric SFH vis-a-vis prior imprints on calculations of timescales (such as quenching and star formation timescales). They find that galaxies with formation redshifts $z < 3$ have longer star formation timescales, but our analysis interestingly only reproduces that trend for a subset of galaxies with $z_{\rm formation}$ between $1.5 < z < 3.5$ for timescales > 1 Gyr.

The majority of star formation in massive quiescent galaxies (most of which morphologically look like early-type galaxies) occurs at high redshifts, with passive evolution thereafter

(see Section 1, and van Dokkum et al. 1998; Jørgensen et al. 2006; Saracco et al. 2020; Tacchella et al. 2021). Sánchez-Blázquez et al. (2009) study stellar populations in red-sequence galaxies in clusters and groups at $0.4 < z < 0.8$ and measure formation redshifts of $z > 2$, and find that those massive galaxies are compatible with passive evolution since. Sánchez-Blázquez et al. (2009), Gallazzi et al. (2014), and Webb et al. (2020) also find that the most massive galaxies in their datasets form stellar mass earlier and quicker, relative to lower mass systems; higher-redshift studies also point towards this trend (see Section 5.1 on mass-dependent evolution in Webb et al. (2020) and Section 6.2 in Díaz-García et al. (2019) for more information, and references therein).

Our objective is to quantify star formation timescales in quiescent galaxies. We observe the above mass-dependent evolution in our studies, where formation redshifts between high and low-mass systems differs substantially. Studies have attempted to explain this mass-dependent evolution either by accounting for the different methods to calculate metallicity, or due to the parameterization (or lack thereof) of SFHs, that can potentially bias formation redshifts (see Section **??**). t_{20}-t_{80} is a simple parameterization to achieve this goal; a given value of t_{20}-t_{80} does not correspond to a unique shape of the SFH. Non-parametric SFHs could be key to solving the issue here (a study to measure quenching timescales in SPT galaxies using non-parametric SFH models will be shared in a follow-up work; Khullar et al., in prep).

4.6.4 Formation of galaxies observed at $z > 1.2$

In the bottom panels of Figure 4.15, we overplot as dots the ages of the Universe at t_{50} for 10 massive cluster quiescent galaxies at $z > 1.2$ in our sample ($z_{\rm median}$=1.3). All 10 galaxies belong to the $\log(M_{\rm 500c,SZ,z=0}/\,{\rm M}_{\odot})$> 15 subpopulation. The median age of the Universe at t_{50} calculated via a stacked spectrum (see Figure 4.17) SED fit for this subpopulation is 1.42 ± 0.74 Gyr, corresponding to a formation redshift of $4.33^{+3.38}_{-1.31}$ (a 1σ range of $z = 3-7$).

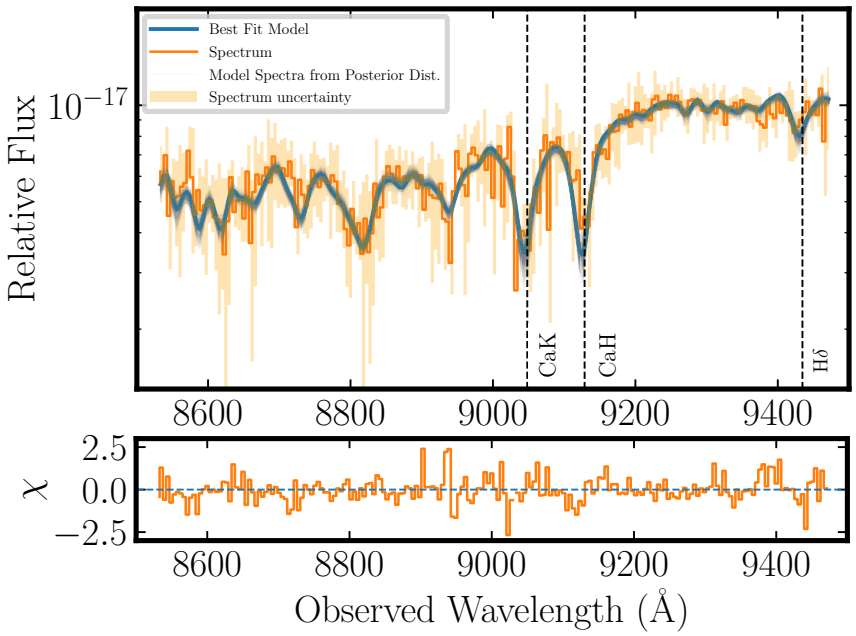

Figure 4.17 (Top) Stacked spectrum (orange) and best-fit SED models (blue) for 10 galaxies in the $z > 1.2$, $\log(M_{500c,SZ,z=0}/\,M_{\odot})> 15$ bin.

Conducting a direct comparison with recent field galaxy studies, we find that the formation redshifts of galaxies in our $z > 1.2$ sample are either similar or marginally higher. By determining SFHs for 75 massive quiescent field galaxies at $1 < z < 1.3$ with a median stellar mass of $\log M \sim 11$, Carnall et al. (2019a) find a mean formation redshift of 2.6, with a range of formation redshifts between 1.5-6. Tacchella et al. (2021) measure quenching timescales and SFHs for 161 galaxies, with ∼20 galaxies at $z > 1$ and an aggregate formation redshift of 4, consistent with this work. Saracco et al. (2009) find that their study of 32 quiescent early-type galaxies (ETGs) at z∼1.5 divides them into young and old systems, with the older population forming the bulk of their stars between redshifts $z \sim 5 - 6$, while the younger galaxies form at z∼2-3. While our sample has a small number of $z > 1.2$ quiescent galaxies, Figure 4.14 indicates that our highest-redshift high mass galaxies ($\log M > 11$) form at $4 < z < 10$.

When considering cluster galaxies, Raichoor et al. (2011) measure ages and stellar masses

for 79 cluster ETGs at $z \sim$1.3 (albeit with multi-band photometry and Bruzual & Charlot (2003) SED models); for galaxies with $\log M > 10.5$, they find formation redshifts of $2 < z < 10$, marginally wider than the distribution in this study. For 331 quiescent galaxies in galaxy clusters at $1 < z < 1.4$, Webb et al. (2020) sample a similar range of masses as our study, and find that the majority of the highest stellar mass galaxies have an aggregate formation redshift of $z \sim 5.4$ ($\log M > 11.3$, with a range of $z = 3 - 10$), while lower mass galaxies have a formation redshift of $z \sim 3.3$ ($\log M < 10.5$, with a range of $z = 2 - 8$); our results (both the median and range) for the $z > 1.2$ sample are in agreement.

4.7 Challenges and Future Work

Comparing ages of stellar populations in massive and quiescent galaxies across cosmic time in various studies is a non-trivial task, especially due to the fact that ages across studies are calculated via different methods and modeling techniques. Moreover, the impact of metallicity is crucial, and the extent to which age-metallicity degeneracy is broken in this work needs to be investigated further, by measuring other age and metallicity indicators, especially via direct absorption line measurements (e.g., Choi et al. 2014, and see Appendix in Webb et al. 2020). Finally, it should be noted that most studies of massive galaxies use UVJ color-based selection to select quiescent galaxies, which is an approach we did not utilise.

Further photometry and spectroscopy in the infrared would allow us to characterize properties of dust-unobscured stellar populations in these systems. Datasets like the just-completed SPT-HST SNAP cluster imaging of 137 SPT clusters at $0.3 < z < 1.5$ with F110W and F200LP photometry (Remolina-Gonzalez et al. in prep) will allow us to morphologically characterize the brightest galaxies in these systems as well (see examples of such analyses in Belli et al. 2015; Estrada-Carpenter et al. 2020; Akhshik et al. 2020; Matharu et al. 2020). We also note that a study of cluster mass accretion histories in simulations could highlight

the (possibly non-negligible) population of 'pre-processed' quiescent galaxies in our sample, i.e., galaxy group environments that could cause infall-based quenching of galaxies before they enter accrete to their final cluster halo Zabludoff & Mulchaey (1998); Pallero et al. (2019).

The ability of delayed-tau SFH models to constrain quenching timescales has been called into question (Carnall et al., 2019a; Leja et al., 2019a). A modification of the current methodology that will be explored in future work (Khullar et al., in prep) is the usage of non-parametric SFHs, and by using frameworks that constrain star formation episodes in SFHs via the dense basis method (Iyer et al., 2019). We will also explore mass-weighted ages with calculations of mass accretion histories of cluster haloes studied in simulations (e.g., IllustrisTNG, Pillepich et al. 2018).

4.8 Summary

In this work, we characterize stellar populations in massive cluster quiescent galaxies from the SPT-GMOS survey (Bayliss et al., 2016a) and the SPT Hi-z survey (Khullar et al., 2019), to constrain stellar masses, ages and SFHs in 837 galaxies at $0.3 < z < 1.5$. We constrain these properties via SED analysis of individual systems' photometry and optical spectroscopy, with the Bayesian fitting framework `Prospector` and primarily a delayed-tau SFH model. We calculate mass-weighted ages and formation redshifts for galaxies as a function of stellar mass to quantify mass evolution with time. We measure formation redshifts in different environments; 'environment' in this work is characterized by placing galaxies in subpopulations divided by final descendant galaxy cluster mass $M_{\rm final,desc}$, and phase space location — a proxy for infall time — $r_{\rm projected}/r_{\rm 500c}$ x $v_{\rm peculiar}/\sigma_{\rm v}$). We also employ stacked spectra to robustly characterize aggregate properties of the the highest redshift galaxies with low SNR spectra and boost wavelength coverage, as well as to cross-check our analyses of median properties. We find that:

- Quiescent galaxies in our dataset sample a diverse set of SFHs, exhibiting a range of mass-weighted ages as a function of redshift, and environment — with $6.23^{+1.41}_{-1.38}$ Gyr being the 16th, 50th and 84th percentile age distribution (median uncertainty of 1.22 Gyr).

- The median formation redshift in our sample is 2.8 ± 0.5, with a range of $z = 1-6$, and is on aggregate similar or marginally older than massive quiescent field galaxy studies, and similar to cluster studies at $z > 1$. On average, we find that more massive galaxies form $\sim$0.75 Gyr earlier than lower mass galaxies.

- The highest redshift galaxies in our sample ($z > 0.6$) show a marginally steeper age-mass relation relative to lower redshift subpopulations, indicating that the age-mass relation does not change (within uncertainties) at ($z < 0.6$) in our cluster quiescent galaxies sample.

- The median age-mass relation (slopes and intercepts) of the full sample is $t_{50,\mathrm{ageofUniverse}} = 2.52(\pm0.04) - 1.66(\pm0.12)\ \log_{10}(M/10^{11}\ \mathrm{M}_{\odot})$, similar to other massive field quiescent galaxy studies seen in the literature.

- Lower mass quiescent galaxy subpopulations across $M_{\mathrm{final,desc}}$ and phase-space location form approximately at the same formation redshifts ($z \sim 2$), regardless of the observed redshift bin.

- Subpopulations that have interacted the most with their respective galaxy cluster's gravitational potential, i.e., $\log(M_{500\mathrm{c,SZ,z=0}}/\ \mathrm{M}_{\odot}) > 15$ and $(r_{\mathrm{projected}}/r_{500\mathrm{c}} \times v_{\mathrm{peculiar}}/\sigma_{\mathrm{v}}) < 0.4$ (early infall time) have steeper age-mass relations relative to other subpopulations, indicating marginal influence of environmental quenching.

This is the first publication in a series which will enable studies of stellar mass assembly in clusters across a wide range of redshifts. With upcoming spectroscopic datasets of clusters

at $z > 1$, we will comprehensively determine star formation and quenching timescales in quiescent galaxies, and connect galaxies at high redshifts to lower redshift objects in an antecedent-descendent manner.

4.9 Acknowledgments

GK thanks Tom Crawford, Ben Johnson, Joel Leja, Sandro Tacchella, Kate Whitaker, Nora Shipp and Lucas Secco for their feedback on the methods and analysis shown in this paper. The authors would like to express gratitude towards the staff and workers at the 6.5m Magellan Telescopes at the Las Campanas Observatory, and the Gemini-South telescope in Chile, for their valuable labor.

The South Pole Telescope program is supported by the National Science Foundation (NSF) through grants PLR-1248097 and OPP-1852617. Partial support is also provided by the NSF Physics Frontier Center grant PHY- 1125897 to the Kavli Institute of Cosmological Physics at the University of Chicago, the Kavli Foun- dation, and the Gordon and Betty Moore Foundation through grant GBMF#947 to the University of Chicago. Argonne National Laboratory's work was supported by the U.S. Department of Energy, Office of Science, Of- fice of High Energy Physics, under contract DE-AC02- 06CH11357. The University of Melbourne authors acknowledge support from the Australian Research Council's Discovery Projects scheme. GM received funding from the European Union's Horizon 2020 research and innovation programme under the Marie Skłodowska-Curie grant agreement No MARA-CAS - DLV-896778. AS is supported by the ERC-StG 'ClustersXCosmo' grant agreement 716762, by the FARE-MIUR grant 'ClustersXEuclid' R165SBKTMA, and by INFN InDark Grant.

Magellan Telescopes 6.5m (Clay/LDSS3C, Clay/PISCO, Baade/FOURSTAR), Gemini-North Telescope (GMOS)

`Python 3.6 | Prospector, python-FSPS, SEDpy, pygtc, Matplotlib, Numpy, Scipy,`

4.10 Appendix A. Metallicity: $\log(Z/Z_{\odot})$

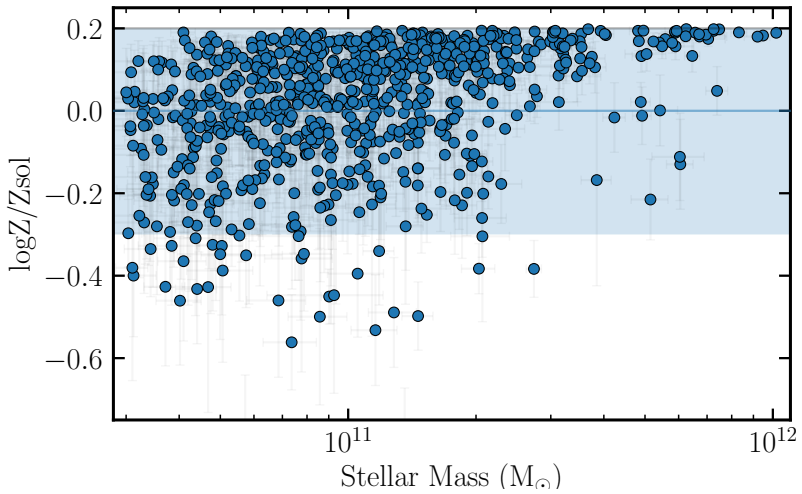

Figure 4.18 Metallicity distribution for galaxies considered in this work, as a function of stellar mass. The blue horizontal line corresponds to the mean metallicity assigned to a clipped normal prior for each SED model fit, with the shaded region corresponding to the 1σ prior range bound on the upper end at $\log(Z/Z_{\odot})$=0.

Metallicity for individual galaxies in our SED analysis is fit as a free parameter within the `Prospector` framework. In Model A, we fit for metallicity by using the mass-metallicity relation (MZR) from Gallazzi et al. (2005) as a starting point, and incorporate studies about the evolution of stellar mass-metallicity relation in clusters (Ellison et al., 2009; Leethochawalit et al., 2018) such that for each individual galaxy fit, we use a clipped-normal prior centered at $\log(Z/Z_{\odot})$=0.0, with a dispersion of 0.3, clipped at [-2.0,0.2]; the bounds are defined by MIST and MILES libraries used in `Prospector`. With optical spectroscopy, we rely on spectral signatures in the rest-frame 3710-4120 Å range to mitigate the age-metallicity degeneracy.

Figure 4.18 shows the median metallicities $\log(Z/Z_{\odot})$ as a function of stellar mass (simultaneously fit with metallicity) from Model A fits. We find that the highest mass galaxies

($\log M > 11$) have median metallicities in a narrow range, while low-mass galaxies have a diverse set of median metallicities. This result has an impact on the creation of stacked spectra, as care is needed to assign and fit metallicity in a stacked spectrum, especially when the constituent individual spectra span a wide range of metallicities (variation in $\log(Z/\mathrm{Z}_\odot)$ does not scale linearly with flux).

4.11 Appendix B. Age biases in median stacking of spectra

As mentioned in Section 4.2, we explore an alternate method of stacking, where uncertainty per flux element is characterized by calculating the uncertainty on the median flux (from median fluxes per wavelength element in a given stack bin); this is the usual approach to stacking seen in SED studies, to visually qualify and quantify spectral features and galaxy properties. We find that this method severely underestimates uncertainty, and generates median mass-weighted ages that are biased by $\sim$ 1.5 Gyr ($\sim$ 0.8 Gyr) in higher (lower) stellar mass stacks in the lowest redshift bins. See Figure 4.19, which plots stack ages as a function of redshift for galaxies divided by $\log(M_{500\mathrm{c,SZ,z=0}}/\,\mathrm{M}_\odot)$ subpopulations, and compares them with median ages in a given bin.

To quantify this bias, we generate stacks via this alternate method for a given redshift and stellar mass bin, for mock galaxies. We do this by sampling galaxy SEDs via `Prospector` from the allowed parameter space for the $\log(M_{500\mathrm{c,SZ,z=0}}/\,\mathrm{M}_\odot) > 15$, $\log M > 10.90$ and $z = 0.53$ bin galaxies, using Model A (see Section 4.2). This corresponds to an age range of [0,8] Gyr, and a stellar mass range of $\log M$=[10.90,12.0].

We make three samples, with each galaxy samplying varying range of metallicities:

1. Sample 1: fixed metallicity $\log(\mathrm{Z}/\mathrm{Z}_\odot) = 0.1$.

2. Sample 2: Metallicity in a restricted range $\log(Z/\mathrm{Z}_\odot) = [0.0,0.2]$ (range observed in our highest mass galaxies)

3. Sample 3: Metallicity in a restricted range $\log(Z/\mathrm{Z}_\odot) = [-0.4,0.2]$ (range observed in our

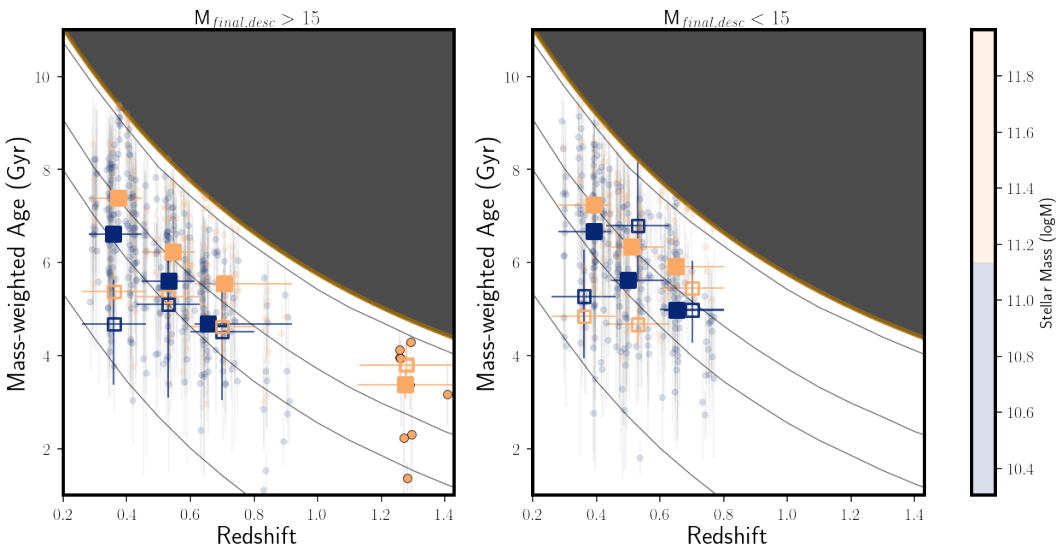

Figure 4.19 Same as top panels of Figure 4.9, but hollow squares signifying stacked spectra mass-weighted ages where stacking is performed using the alternate method described here.

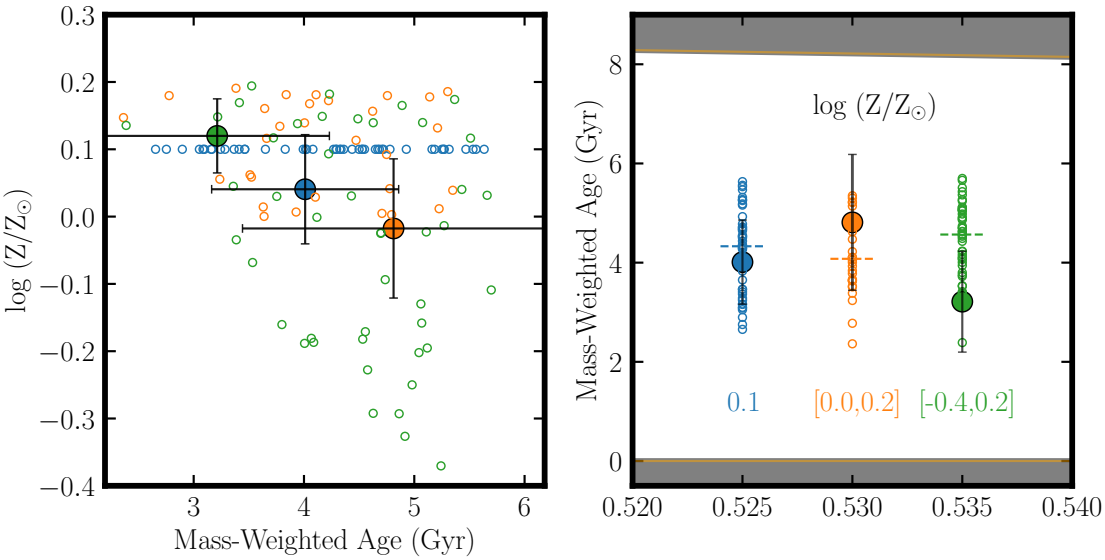

Figure 4.20 Physical properties of three mock samples of quiescent galaxies: Sample 1 (fixed metallicity $\log(Z/Z_\odot) = 0.1$, in blue), Sample 2 (Metallicity in a restricted range $\log(Z/Z_\odot) = [0.0,0.2]$, in orange) and Sample 3 (Metallicity in a restricted range $\log(Z/Z_\odot) = [-0.4,0.2]$, in green). (Left) Metallicity vs mass-weighted age for stacked spectra from three samples with varying metallicities (filled circles) and individual galaxy per sample (empty circles). (Right) Mass-weighted ages for the three samples, with median ages for each sample annotated with horizontal dotted lines.

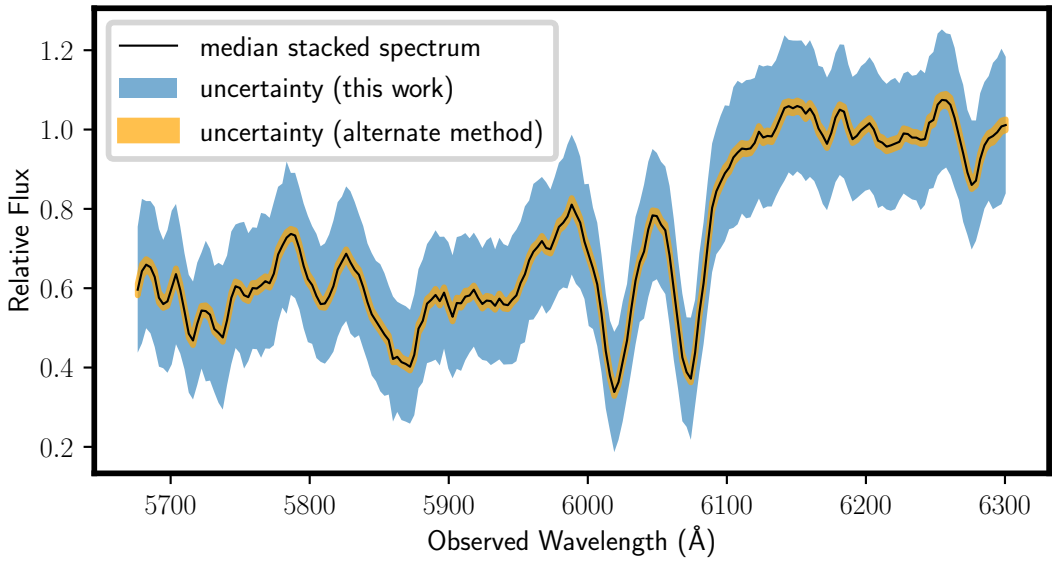

Figure 4.21 Stacked spectrum generated for galaxies in the $\log(M_{500c,SZ,z=0}/\,M_{\odot}) > 15$, $\log M > 10.90$ and $z = 0.53$ bin in our sample. The median stacked spectrum is plotted in black, while the stacked spectrum uncertainty considered in this work is plotted in blue. Orange denotes the uncertainty derived from the alternate stacking method, which — as we argue in this section — biases age calculations and may underestimate uncertainty.

lowest mass galaxies).

We make a D4000 > 1.45 cut on the sampled SEDs, with an average of 40 galaxies in each sample. We use similar priors on all parameters as Model A, while the metallicity prior is approximately 2σ times the priors from Model A. We pass these stacked spectra through a similar analysis as is conducted in this work.

Figure 4.20 shows the distribution of stacked metallicities and ages for each sample, with filled points corresponding to stack values, and hollow points corresponding to parameter values for the individual mock galaxies in each sample. Horizontal dotted lines correspond to median mass-weighted ages per sample.

We find that the stack metallicity and age is the most biased for Sample 3, with the highest range in metallicity, while Sample 1 is the least biased, i.e., for fixed metallicity, we find that the stacked spectra retrieves ages matching median age of the sample of constituent

galaxies. In Sample 3, we see a bias as wide as 1.5σ (in this specific case, an age that is younger than the median age by ~ 1.5 Gyr). Hence, we attribute that the dominant source of the bias in ages from this stacking method, is the range of metallicities in the constituent galaxies per stacking bin. This is a bigger contributing factor in stacks from the lower mass galaxies, since these subpopulations are where we see the largest range in metallicities. Hence, we do not employ this stacking method in this work.

4.12 Appendix C. Single Burst SFHs

Beyond the delayed-tau SFHs, we also calculate the age/epoch of star formation (in the form of a single burst-like star formation age) for the single burst model (Model B). This is a more limiting model for galaxies with more than one episode of star formation (which would better be approximated by the delayed-tau SFH), but is an exercise to test the robustness of approximating quiescent galaxies as simple stellar populations, a model employed by many studies in the past (e.g., Fumagalli et al. (2016); Jørgensen et al. (2017). See Figure 4.22 for stellar age of quiescent galaxies as a function of stellar mass (M) for galaxies in our sample at $0.3 < z < 0.9$. Color of points in the figure indicates observed redshift of the member galaxy. As is expected, the most massive galaxies are formed earliest, with a median-age of ~ 5 Gyr for a massive quiescent cluster member galaxy in our sample.

As expected, objects observed at lower redshifts have older ages, i.e., for a given stellar mass, low redshift galaxies sit on the top end of the plot. To physically motivate this, and compare this distribution of ages to the evolution of galaxies in the Universe, we map these ages and observed redshifts to the formation redshift of each galaxy for a distribution of stellar mass M as a function of observed redshift, where color indicates the formation redshift of a galaxy $z_{\rm form}$). The median mass galaxy (M) has formed at $z_{\rm form} = 2$-3, given the assumptions of a single burst model; this is significantly younger than results seen from Model B, as is expected in an SSP-model based age characterization.

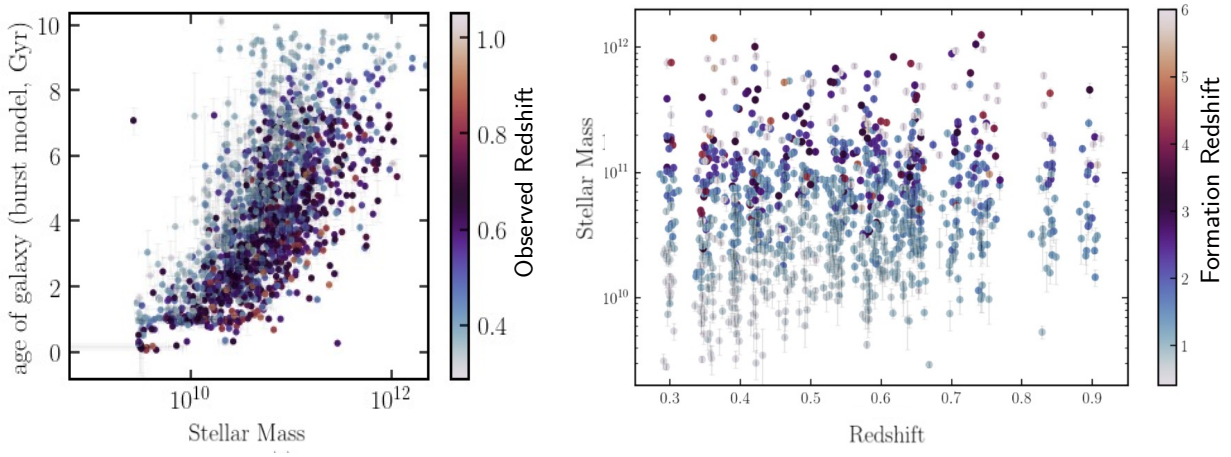

Figure 4.22 (Left) Ages (in Gyr) as a function of stellar mass (in $M_\odot$) for a single burst fixed metallicity model-based (Model B), with color indicating observed redshifts. (Right) Stellar Mass vs redshift for the low-z member galaxies in our sample, corresponding to Model B. Colors correspond to formation redshifts, where more massive galaxies ($\log M > 11$) were formed at $z > 3$.

4.13 Appendix D. SNR of quiescent galaxy spectra

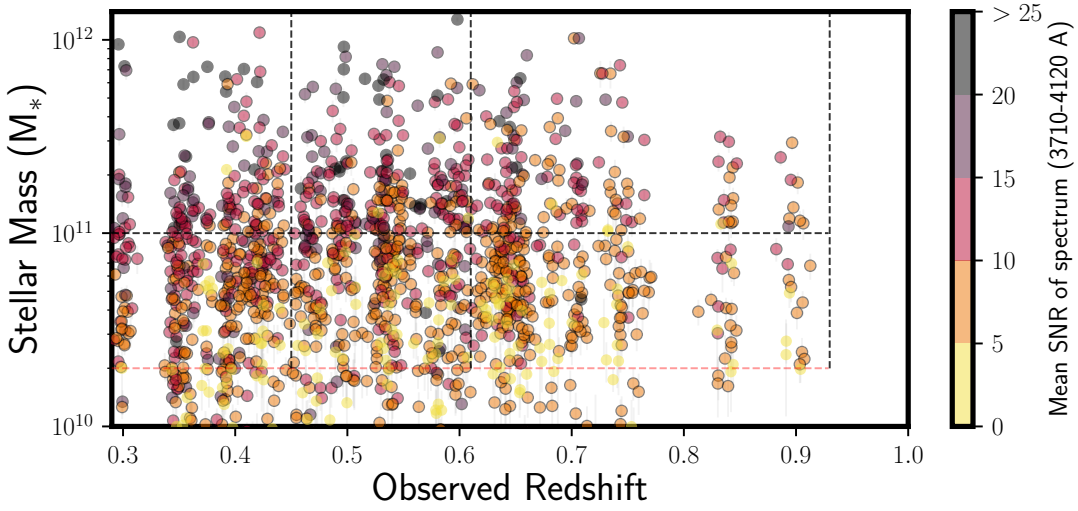

Figure 4.23 Same as Figure 4.7, with average signal-to-noise ratio of the observed spectrum coded with color for each galaxy spectrum in the low-z cluster sample ($0.3 < z < 0.9$), where we employ an SNR cut. Points with black borders are the 827 galaxies considered in this study from the low-z cluster sample. The highest SNR spectra were observed from the higher mass galaxies in the sample.

We apply a mean spectrum SNR cut to our quiescent galaxy spectra in the range $0.3 < z < 0.9$. Figure 4.23 shows the distribution of stellar mass as a function of observed redshift, with color indicating mean SNR per galaxy spectrum.

We find that the highest SNR spectra are observed in the highest mass galaxies, which is expected, without a strong redshift dependence, as is expected from observational design of the program in B16. Intermediate mass galaxies are seen to have been derived from a flat distribution of intermediate SNR spectra, mostly independent of redshift in the low-z sample. The SNR distribution also indicates that the lowest SNR (< 5) galaxies are cut from the sample by applying the mass cut ($\log M > 10.3$, dotted red lines in Figure 4.23).

CHAPTER 5

STELLAR POPULATIONS IN THE BRIGHTEST GALAXY IN THE REDSHIFT > 5 UNIVERSE

The text of this chapter was published in Khullar et al. ApJ 906, 107 (2021).

5.1 Introduction

Strong gravitational lensing can transform typically small, faint, marginally-resolved field galaxies into highly-magnified arcs that can appear very bright. The brightest and most magnified lensed galaxies enable exquisite studies of internal galaxy morphologies down to scales of only tens of parsecs even in the most distant galaxies (e.g.,Bayliss et al., 2014a; Livermore et al., 2015; Johnson et al., 2017; Johnson et al., 2017; Cornachione et al., 2018; Rivera-Thorsen et al., 2019; Ivison et al., 2020; Florian et al., 2020). Such lensed sources are exceedingly rare, and are generally found by searching many thousands of square degrees of ground-based survey imaging (e.g.,Allam et al., 2007; Belokurov et al., 2007; Koester et al., 2010) or by dedicated imaging programs targeting massive galaxy clusters not previously explored (Bleem et al., 2015c, 2020b; Coe et al., 2019). Conversely, deep observations of known strong lenses with large lensing cross-sections (c.f. the Hubble Frontier Fields; Lotz et al., 2017) discover many more lensed galaxies, but these are magnitudes fainter than the rare systems found in wide searches.

Studies of the brightest lensed galaxies are complementary to studies of faint lensed galaxies, and unlensed field galaxies, offering both enhanced spatial resolution in the source plane, and sufficient photons to allow exceptional spectral resolution at useful signal-to-noise ratios. Hence, the brightest strongly lensed galaxies are the observational signposts with which we navigate the more abundant but much fainter deep-field samples. To date, searches of the Sloan Digital Sky Survey (SDSS; Ahumada et al., 2020) have identified

hundreds of bright lensed sources at $z < 3$, the brightest of which typically have integrated $g_{\rm AB}$ magnitudes of $\sim$20 (e.g., Kubo et al., 2010; Bayliss et al., 2011a; Stark et al., 2013).

This success is due to the depth and filter selection of the SDSS, sufficient to find the bright blue arcs that are the hallmark of UV-bright lensed galaxies at these redshifts. Many of these lensed targets have been followed up with HST imaging that has revealed details of star formation and structure on spatial scales down to tens of parsecs (e.g., Johnson et al., 2017; Cornachione et al., 2018). The brightest of these lensed galaxies — a few of which predate the discoveries from the SDSS — have been followed up with high-quality spectroscopy (e.g., Pettini et al., 2000; James et al., 2014; Rigby et al., 2018b,a) that exceeds in both spectral resolution and signal-to-noise what is available for stacks of dozens or even hundreds of field galaxies (Shapley et al., 2003; Steidel et al., 2016).

Beyond $z \sim$3 however, bright lensed samples rapidly decline, and by $z \sim$5, there are only a few known strongly lensed galaxies of even modest brightness at optical/infrared (OIR) wavelengths; the SDSS, which has been so effective for discovery at $z \sim$2-3 has proven mostly insufficient in depths at $z \sim$5, particularly in key redder filters as the galaxies drop out of the bluer filters due to intervening IGM absorption. The brightest three $z \sim$5 spectroscopically confirmed lensed galaxies published to date have AB magnitudes of i=22.2 (z=4.88, Gladders et al., 2002), i=22.6 (z=4.92, Franx et al., 1997; Soifer et al., 1998), and i=23.3 (z=4.87, Frye et al., 2002). The brightest was found through a wide-area search for arcs; the other two were found by targeting massive galaxy clusters. In addition, the Reionizing Lensing Cluster Survey (RELICS) program reports 5 candidate lensed galaxies with $z_{\rm phot}$=5.5–6 and F160W<23.6 (Salmon et al., 2020), that as yet lack published spectroscopic redshifts. For comparison, the brightest galaxies at $z \sim 5$ in the Hubble Ultra Deep Field (HUDF) have magnitudes fainter than $i_{\rm AB} = 25$ (Inami et al., 2017).

Strong lensing searches in the latest generation of imaging surveys, particularly the Dark Energy Camera Legacy Survey (DECaLS; Huang et al., 2020b), the Dark Energy Survey

(DES; Diehl et al., 2017; Jacobs et al., 2019), the Kilo-Degree Survey (KiDS; Petrillo et al., 2019), the Hyper Suprime-Cam Subaru Strategic Program (HSC-SSP) Survey (Jaelani et al., 2020), should significantly increase the number of known bright $z > 3$ lensed galaxies, as these data are deeper, particularly in redder filters, than the SDSS. Here, we report and characterize one such object, a spectroscopically confirmed z=5.043 strongly-lensed galaxy, with an extraordinarily bright $z_{\rm AB}$ apparent magnitude of 20.47. As such, this is the brightest $z \gtrsim 5$ UV-bright galaxy found so far.

This paper is structured as follows. Section 5.2 lays out the details of the public data search that led to the discovery of COOL J1241+2219. Section 5.3 describes follow-up imaging and spectroscopy of COOL J1241+2219, while Section 5.4 describes the analyses of these data and the results from stellar population synthesis and strong lens modeling. Section 5.5 places these results in the context of other objects known in the $z > 5$ Universe.

All reported magnitudes are calibrated to the AB system. The fiducial cosmology model used assumes a standard flat cold dark matter universe with a cosmological constant (ΛCDM), corresponding to WMAP9 observations (Hinshaw et al., 2013). For inferred parameters with uncertainties, we report 16th, 50th and 84th percentile values, unless otherwise specified.

5.2 Discovery

The COOL-LAMPS project — ChicagO Optically selected strong Lenses - Located At the Margins of Public Surveys — initiated as the central focus of an undergraduate research class, is an effort to find strong gravitational lenses in recent public imaging data. Though the lensing search is designed to find a wide variety of lenses and lensed sources, the particular focus of our follow-up is sources that are photometrically at the margins of the distributions of source color and brightness. The details and results of this search will be presented in an upcoming publication (COOL-LAMPS Collaboration in prep.), and we provide only a brief

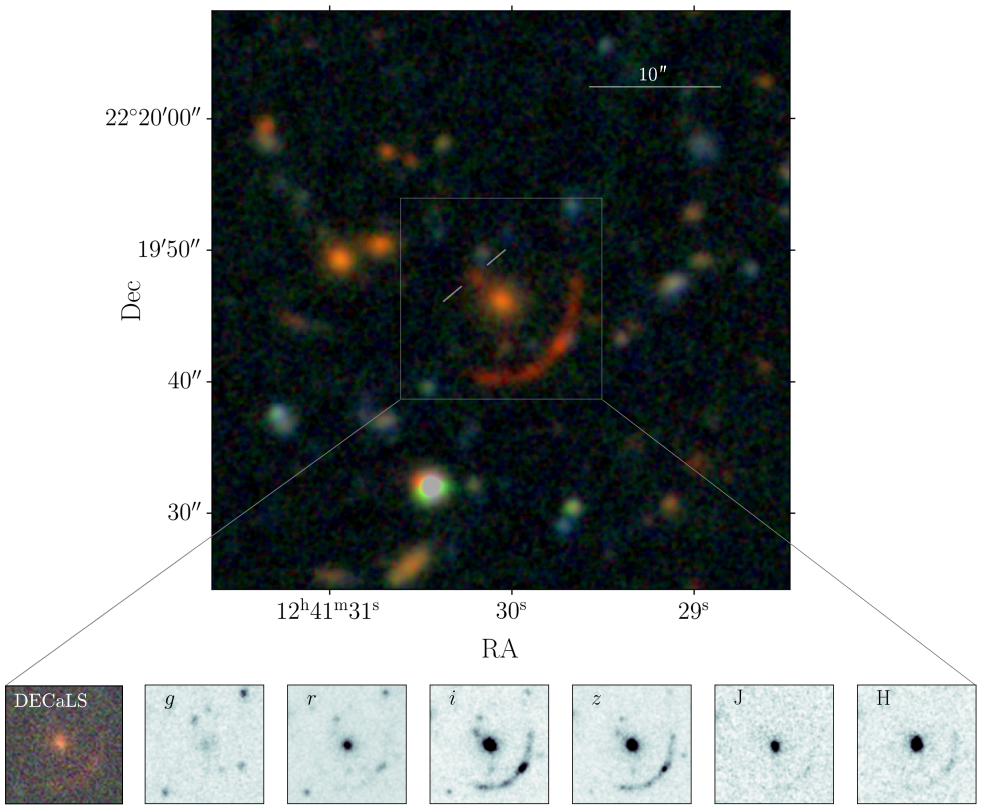

Figure 5.1 (Top) RGB image of the lens and COOLJ1241+2219. This was constructed using the Magellan/PISCO g, r and $i + z$ images in each channel. The arc radius about the central lens galaxy is ∼6", indicating that the lens has the mass of a large group or small cluster, consistent with the presence of other red sequence galaxies. The faint red source immediately NW of the main lens galaxy has colors and surface brightness suggestive of a lensed counterimage, marked with solid white lines. (Inset images) $grizJH$ images from a 16"x16" field-of-view centered at the lens. (Inset image: far left) The central portion over the same area of the 45"x45" DECaLS grz discovery image.

description here.

COOL J1241+2219 was found in the DECaLS grz Data Release 8 (DR8, Dey et al., 2019) imaging data, as part of a comprehensive visual search of the northern galactic cap portion of the DECaLS dataset. The complete search comprised two separate efforts, one targeting potential lenses at low redshift ($z < 0.7$) and the other extending to higher redshift potential lenses. COOL J1241+2219 was found in the latter.

We selected luminous red galaxies, classified as having de Vaucouleurs profiles (de Vau-

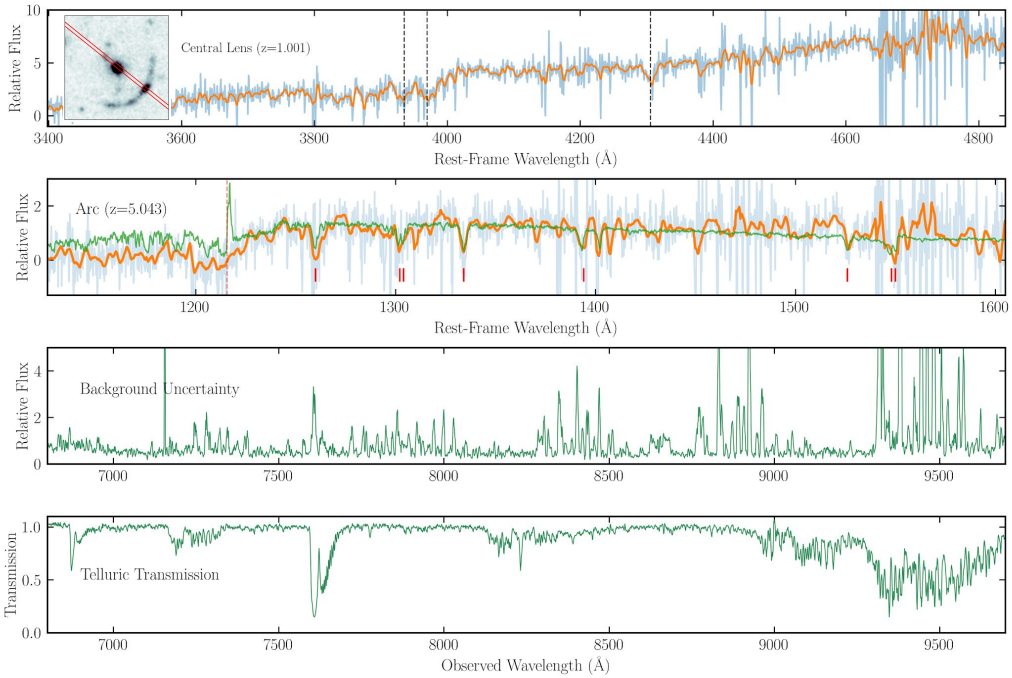

Figure 5.2 The extracted optical/near-IR Magellan/LDSS3 spectra of the central lens galaxy (top), brightest knot in the arc (middle top), the noise spectrum (middle bottom) and telluric correction applied (bottom). The noise and transmission spectra are shown covering the same observed wavelength range, corresponding to the indicated restframe wavelength range for redshifts of 1.001±0.001 and 5.043±0.002 for the top and middle top panels respectively. The raw spectra are plotted in pale blue, and versions of those data filtered to visually emphasize features relevant for redshift determinations, are over plotted in orange. The inset top-left shows the slit positioning for these observations. In the top panel, vertical dotted lines indicate significant spectral features used to infer the redshifts for the lens galaxy; the redshift is also determined from an uncertainty-weighted cross correlation with the reference spectrum (from Rigby et al., 2018a) overplotted in green. To visually confirm the redshift, we mark UV stellar and nebular absorption features with red lines.

couleurs, 1948), and appropriate colors and magnitudes, as potential lenses. Color and magnitude cuts were informed by prior experience with strong lens selection in the SDSS (Bayliss et al., 2011a; Sharon et al., 2020; to first-order, the selected galaxies are objects brighter and redder than a color-magnitude model corresponding to a passively evolving galaxy formed at z=3, with an absolute magnitude tuned to capture a reasonable number of target objects. In practice, this magnitude limit is approximately M_*. Specifically, COOL J1241+2219 's measured photometry puts it at $\sim$ 0.2 magnitudes redder and brighter than

the selection cut, and further away from the selection cut than the median potential lens selected by that cut.

We followed a visual examination strategy employed by the Sloan Giant Arcs Survey (SGAS; e.g., Bayliss et al., 2011b; Sharon et al., 2020). In the high-redshift portion of our search, a total of 271,460 lines of sight were examined by at least 3 of the co-authors, primarily via a custom `Python`-based image viewer and lens-ranker. We examined lines of sight four-at-a-time in a 2×2 grid, with each individual cutout covering 45" × 45" centered on each potential lens. We constructed custom color images from the DECaLS grz imaging data, tuned to emphasize faint extended features. Each 2×2 composite image was given an integer score from 0 to 3 by each examiner, with a score of 3 indicating a definite strong lens, a score of 0 indicating no evidence for strong lensing, and the remainder shading between those extremes. The initial average score for COOL J1241+2219 was 2. The central portion of the image in which COOL J1241+2219 was found is shown in the first inset panel of Figure 5.1.

The lensed arc is detected in the DECaLS catalogs at RA, Dec (J2000) = (190.3743, 22.3282) with reported AB magnitudes of g=25.10, r=23.82, z=21.13; the model-based photometry of these catalogs assumes elliptical sources, and must therefore miss a significant fraction of the source light in this case. However, this initial photometry and the observed red color and morphology of this apparent arc motivated follow-up observations.

5.3 Follow-up Observations and Redshifts

5.3.1 Photometry

Near-infrared imaging of COOL J1241+2219 in the J- and H-bands was obtained using the FourStar Infrared Camera (FOURSTAR; Persson et al., 2008) on the Magellan/Baade

telescope, Chile, on 2020 February 22. The total integration times were 335s and 3578s in the J- and H-bands respectively. Data were reduced to final astrometrically and photometrically calibrated stacked images using a custom pipeline built via IRAF and PHOTPIPE (Rest et al., 2005; Garg et al., 2007; Miknaitis et al., 2007).

We then obtained deep simultaneous optical imaging — *griz* — using the Parallel Imager for Southern Cosmology Observations (PISCO; Stalder et al., 2014c) on the Magellan/Clay telescope, on 2020 February 29. The total integration time for the imaging with a field-of-view of 5.5' x 7.5' was 3060s. Data were processed and stacked to final astrometrically calibrated images using a custom pipeline that makes standard corrections, as well as removing effects of non-linearity and bright stars peculiar to the PISCO detectors. Figure 5.1 shows a color image for COOL J1241+2219 constructed from the PISCO images, as well as smaller greyscale cutouts for all of the follow-up imaging focused on the arc and central lens galaxy.

5.3.2 Spectroscopy

Spectroscopic observations for COOL J1241+2219 were obtained on 2020 March 2, using the Low Dispersion Survey Spectrograph - 3C (LDSS-3C[1]), with the VPH-Red grism and a $1''.0$ longslit placed to cover a wavelength range of $6700\mathring{A}$ and redward, to the limits of the instrument response at $\sim 10500\mathring{A}$. The slit was oriented to include the brightest clump in the lensed arc, the fiducial counter-image, and the apparent lens galaxy (with a slight offset). The precise slit placement is shown in the top inset portion of Figure 5.2.

We acquired six 900s integrations, dithered between two slit positions along the slit diection, in non-photometric conditions at airmasses of 1.6-1.8, with a typical on-instrument seeing of $1''.1$, as well as observations of a spectrophotometric standard for both flux calibration and the removal of telluric features in the spectra. Reduction to wavelength- and

1. http://www.lco.cl/Members/gblanc/ldss-3/ldss-3-user-manual-tmp

flux-calibrated 1D spectra was accomplished using a combination of standard routines and custom software, implemented in IRAF and IDL. The spectra for the apparent central lens galaxy and COOL J1241+2219 are shown in Figure 5.2, along with an estimate of the noise spectrum, and the applied telluric correction. We measure the lens redshift from the marked features in Figure 5.2 as $z = 1.001 \pm 0.001$, and the lensed source redshift from cross-correlation with the stacked rest-UV galaxy spectrum from Rigby et al. (2018a) as $z = 5.043 \pm 0.002$.

The high-airmass and non-parallactic slit positioning of these observations in sub-optimal conditions makes the fluxing and telluric calibrations irretrievably uncertain. However, as is obvious from Figure 5.2, both spectra are sufficient to establish redshifts robustly.

At the measured redshift, the entire restframe optical band for the lensed galaxies is shifted to wavelengths not readily accessed from ground-based observatories. The only observable standard emission line used in studies of galaxies at lower redshifts is the [O II] 3727,3729Å doublet. We observed COOL J1241+2219 using the Gemini-North Near-infrared Spectrograph (GNIRS) spectrograph (Elias et al., 2006) at NOIRLAB/Gemini, Mauna Kea, in Director's Discretionary Time on July 4th, 2020 in an attempt to measure this feature. We acquired eight 257s integrations using GNIRS with a $0''.675$ slit in cross-dispersed mode and with the short camera, at an airmass$\sim$1.5, with a typical on-instrument seeing of $0''.6$. These observations targeted the same bright peak along the arc observed with LDSS-3C. The data were reduced primarily using the Gemini/GNIRS pipeline[2]. The resulting spectrum was calibrated against a telluric standard star observed immediately after. Analysis of these data is detailed in Section 5.4.

2. https://www.gemini.edu/instrumentation/gnirs/data-reduction

5.4 Analysis and Results

5.4.1 Zeropoint Calibration

The J- and H-band images are calibrated to 2MASS stars (Jarrett et al., 2000) within the field of view, with the calibration derived automatically by PHOTPIPE routines. Uncertainties on these zeropoints relative to 2MASS are ~ 0.03 magnitudes.

The PISCO data are calibrated to existing DECaLS (grz-bands) and Pan-STARRS (DR2,Chambers et al., 2016) (i-band) data. We used SExtractor (Bertin & Arnouts, 1996) MAG_AUTO magnitudes for detected objects in all bands to establish image zeropoints. The PISCO data are much deeper than the reference data, and so object-by-object uncertainties in the comparison are dominated by uncertainties in the reference measurements. Limiting the comparison to objects with a measured DECaLS SNR of >20 yields a matched catalog sufficient to established zeropoints, and linear color terms, accurate to better than 0.02 magnitudes, and we derive a similar result in comparison to the Pan-STARRS data.

5.4.2 Model Photometry with GALFIT

We used the parametric fitting code GALFIT (Peng et al., 2002, 2010) to create a model of the arc, its candidate counterimage, the central lens galaxy, and other nearby contaminating objects, as well as to extract relevant photometry. Point-spread functions (PSFs) were measured directly from the images; these are simply small cutouts of two isolated and bright but unsaturated point sources near the modeled region. Differences in photometry from choices of PSF are substantially smaller than all uncertainties below. Multiple two-dimensional Sérsic components were used to model each image. Model construction proceeded iteratively, with bright objects fit first, and further components added until the residual was consistent with the background noise.

To estimate statistical photometric uncertainties we added the final fitted model to blank

Table 5.1. Model photometry-based magnitudes for COOL J1241+2219

	g	r	i	z	J	H
Central Lens Galaxy	$23.86\,^{+0.24}_{-0.20}$	21.960±0.046	20.76±0.05	19.630±0.048	18.955±0.059	18.564±0.054
Arc	>25.11	$23.197\,^{+0.353}_{-0.358}$	$21.616\,^{+0.049}_{-0.050}$	$20.472\,^{+0.047}_{-0.048}$	$20.53\,^{+0.273}_{-0.285}$	$20.556\,^{+0.084}_{-0.087}$
Counterimage	—	—	$24.164\,^{+0.233}_{-0.297}$	$22.705\,^{+0.105}_{-0.127}$	$23.074\,^{+0.453}_{-0.793}$	$23.774\,^{+0.613}_{-1.545}$

Note. — Magnitudes calculated via GALFIT, with output in AB system. *griz*-band imaging from Magellan/PISCO simultaneous multi-band imager. JH band imaging from Magellan/FOURSTAR infrared imager.

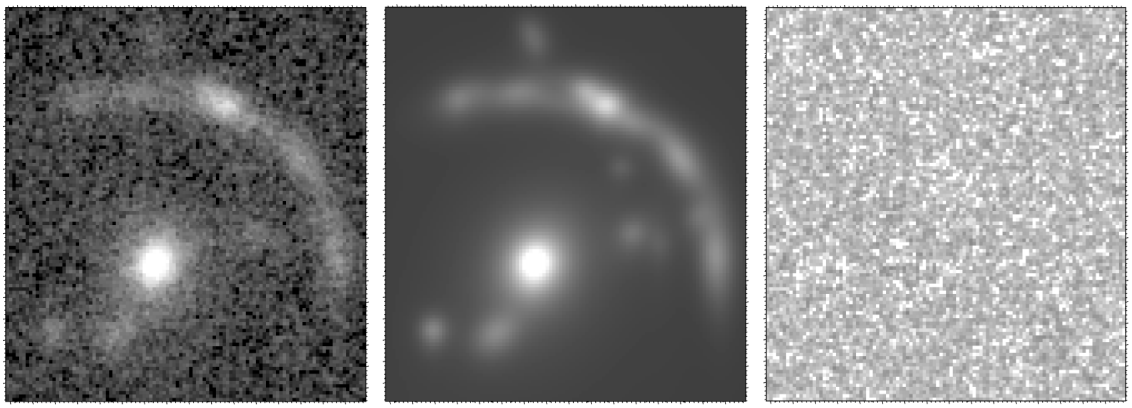

Figure 5.3 12"x12" cutouts, all at the same intensity scaling, of the (left) PISCO i band image, (center) GALFIT model of the central lens galaxy, the arc, and other galaxies, and (right) the residual image (with inverted colors to highlight the lack of residual structures).

sky regions around the image, and re-fit the models on these new images. The measured magnitude distribution of each object then gives an uncertainty. If the flux distribution had significant outliers (presumably due to poor convergence of the model instance) we computed the uncertainty from the flux distribution iteratively clipped at 3σ. Additionally, to estimate the systematic uncertainty caused by modeling choices, three co-authors independently created models for the z-band data, and the range in final fitted magnitudes for these models was taken as an estimate of the systematic uncertainty for the PISCO images. Additionally

these models were re-optimized to fit the H-band image, and provide an estimate of the systematic uncertainty in the J- and H-bands.

Finally, calibration zeropoint uncertainties, and the statistical and systematic uncertainties estimated as above, were combined in quadrature to compute total uncertainties for each measurement of each physical object.

The i-filter image, GALFIT model and residuals for the lens field are shown in Figure 5.4.2. Table 1 gives the model magnitudes for the arc and the candidate counter-image.

Lens Galaxies

As part of the modeling, we have measured photometry for the central lens galaxy, as well as two other nearby galaxies to the east that have similar apparent colors and morphologies (and are visible in Figure 1). These two other galaxies were fit together, but independently of other objects. These two galaxies have colors similar to the apparent central lens galaxy, as is indicated also by the DECaLS photometry of these galaxies. Independent of strong-lensing mass modeling, this suggests that the lens is a lower-mass galaxy cluster.

Arc and Possible Counterimage

The lensed source is absent in the g-band and nearly so in the r-band, both due to absorption from the intergalactic medium (IGM). It is not possible to fit a model directly in the g-band. Rather, we took the initial i-band model, solved for any residual astrometric shift between the two bands using visible objects in the modeled region, and then performed a constrained refit of the model allowing only the magnitudes to vary of any components that describe the arc. This model was pushed through the same statistical error analysis as other filters, though in the case of the g-band image the distribution of notional measured magnitudes represents an upper limit, and we report the 95th percentile value.

In the r-, J-, and H-band data, the arc is visible but measured at a markedly lower

SNR than the i- and z-bands. In each of these cases we explored both direct modeling, and re-optimized models taken from bands with larger SNR detections of the arc, and the measurements we report come from the latter. Note that in all of these cases, including the g-band, components which describe well-detected objects were allowed to vary structurally, as well as in brightness.

The suggested counter-image (see Figure 5.1) is photometrically consistent with the arc; it has consistent colors across filters where both objects are visible, and the apparent surface brightness of this object matches much of the arc. The candidate counter image was observed via LDSS-3C optical long slit spectroscopy (and not with GNIRS), but given that the lensed source has no emission lines in the rest-frame UV, we have not attempted to extract a spectrum of this much fainter source. We note, however, that there is no evidence in the 2D spectral image of any emission lines from this object that would be inconsistent with the identification of it as a lensed counterimage.

5.4.3 SED Fitting with `Prospector`

Using the model photometry in *grizJH* filters, we perform spectral energy distribution (SED) fitting for the central lens galaxy and the COOL J1241+2219 arc using the Markov Chain Monte Carlo (MCMC) — based stellar population synthesis (SPS) and parameter inference code, `Prospector`. `Prospector` is based on the the Python-FSPS framework, with the MILES stellar spectral library and the MIST set of isochrones (Conroy & Gunn, 2010a; Johnson & Leja, 2017b; Leja et al., 2017b; Foreman-Mackey et al., 2013; Falcón-Barroso et al., 2011; Choi et al., 2016). We exclude the LDSS3 spectrum from the fitting procedure because at its low signal-to-noise ratio, it mostly samples saturated interstellar absorption lines that are not directly constrained by `Prospector` libraries.

We have chosen to perform the SED fitting on the observed photometry, a choice which assumes that there are no correlations within the SED fitting that couple parameters that are

Table 5.2. `Prospector` Analysis: Free Parameters in Galaxy SED Model

Parameter	Description	Priors	Best Fit Value
$\log(M_{\rm tot}/{\rm M}_\odot)$	Total stellar mass formed	Tophat: [10, 13]	$11.77^{+0.20}_{-0.25}$
$\log({\rm SFR}_{\rm ratio})$	Ratio of the SFRs in	Student-T: Bin 1: mean=0.0,scale=0.3, $\nu = 2$	$0.10^{+0.33}_{-0.26}$
	adjacent age bins	Bin 2: mean=0.0,scale=0.3,$\nu = 2$	$0.10^{+0.34}_{-0.28}$
$\log(Z/{\rm Z}_\odot)$	Stellar metallicity in units of $\log(Z/{\rm Z}_\odot)$	Tophat: [-2, 0.5]	$-1.32^{+0.56}_{-0.40}$
$\tau_{\lambda,2}$	Diffuse dust optical depth	Tophat: [0.01, 1.00]	$0.14^{+0.13}_{-0.09}$
${\rm spec}^*_{\rm norm}$	Factor by which to scale the spectrum to match photometry	Tophat: [0.1, 3.0]	$1.94^{+0.53}_{-0.51}$
${\rm gas}^*_{\log(Z/{\rm Z}_\odot)}$	Gas-phase metallicity in units of $\log(Z/{\rm Z}_\odot)$	Tophat: [-2, 0.5]; depends on $\log(Z/{\rm Z}_\odot)$	$-0.94^{+0.90}_{-0.73}$
$\log(U)^*$	Ionization Parameter $U = n\gamma/n_{\rm H}$	Tophat: [-4.0, -1.0]	$-2.48^{+1.00}_{-1.09}$

Note. — 1. Mean, σ and range of the clipped normal priors based on the Mass-Metallicity relation (MZR) from Gallazzi et al. 2005.*Considered as nuisance parameters.

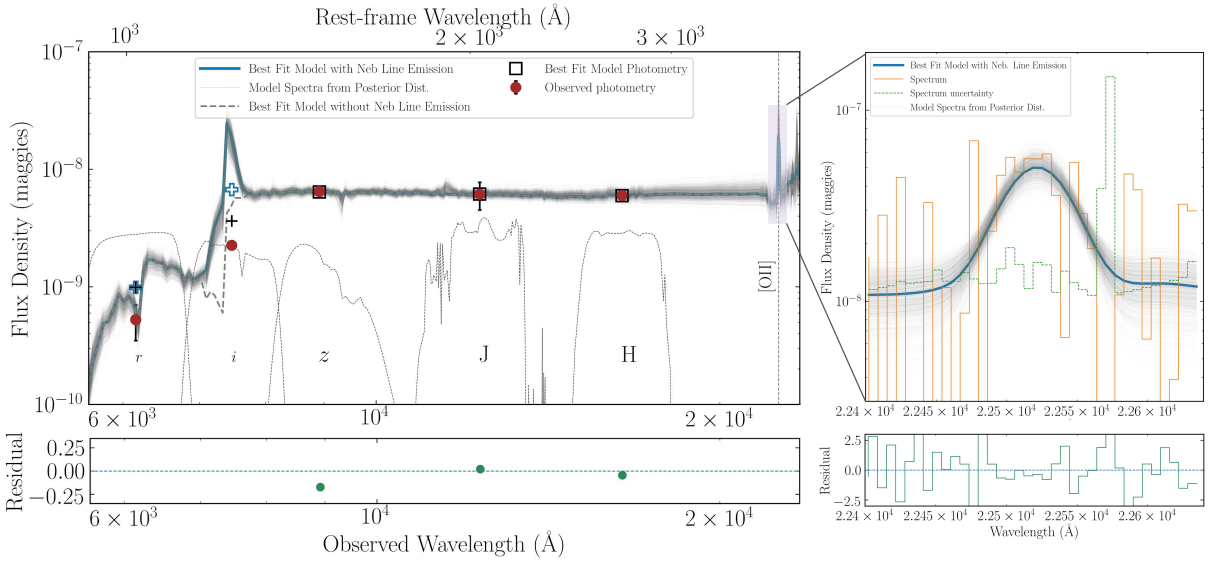

Figure 5.4 (Left) Best fit SED model with nebular line emission (blue) and corresponding Residual (χ) values (green) for COOL J1241+2219 , calculated via `Prospector`, and using zJH photometry and IR spectroscopy. Best-fit SED model without nebular line emission is displayed as short-dashed grey curve. Best-fit photometry for zJH data is shown as black squares. Photometric projections for the masked ri data corresponding to the model with and without nebular line emission are shown as blue 'plus' and black 'plus' symbols, respectively. (Right) Best-fit model spectrum with nebular line emission (blue) zoomed into the observed wavelength range corresponding to the blended [O II] 3727, 3729Å emission, with IR spectroscopic data (orange) and uncertainties (dotted green), with model χ values (in green) displayed in the bottom panel. Two black vertical lines mark the locations of the [O II] 3727,3729Å doublet peaks.

magnification-dependent (such as stellar mass, star formation rate) with those that are not magnification-dependent (such as metallicity, dust extinction). This assumption has been tested by arbitrarily rescaling the input photometry by the measured mean magnification (see Section 5.4.5), and the resulting SED fits are entirely consistent with the results presented below.

In these models, we assume a non-parametric star formation history (with age bins with $[0-50]$, $[50-100]$, and $[100-1000]$ Myr in lookback time), represented by the parameters

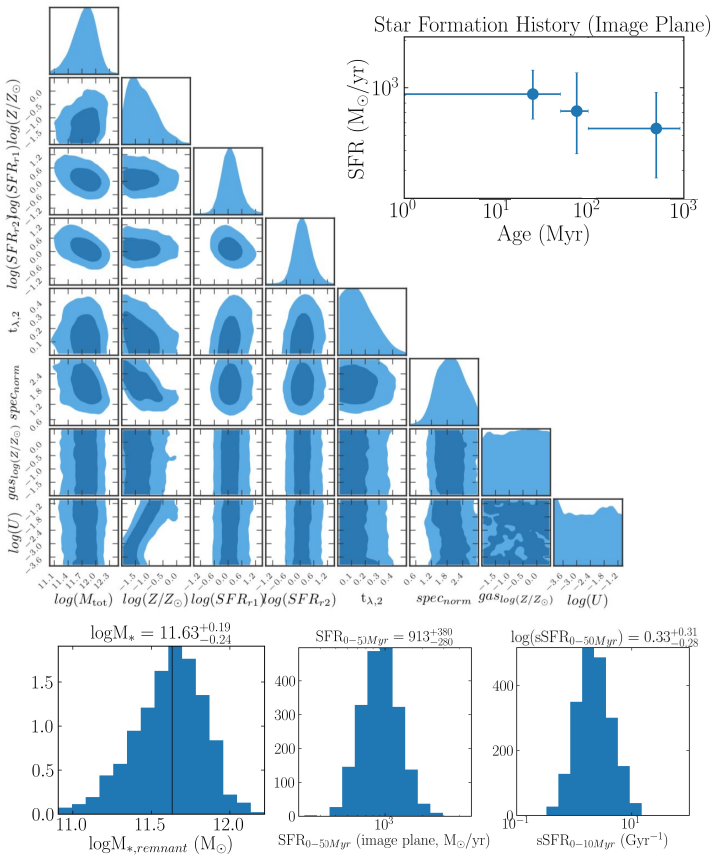

Figure 5.5 (Top left) Corner plot with posterior distributions and correlations for inferred parameters in the `Prospector` SED fitting analysis for the lensed source, with contours corresponding to 1σ (in dark blue) and 2σ (in light blue). (Top right) The star formation history, i.e., the SFR as a function of age bins. (Bottom) The posterior probability distributions of the remnant stellar mass of COOL J1241+2219 , the star formation rate (SFR) in the youngest age bin, and the specific star formation rate (sSFR).

SFR_{ratio}, referring to the ratio of total star formation in adjacent time bins. These bins correspond to redshift bins [5.04-5.22], [5.22-5.41] and [5.41- 20.50]. The priors for the star-formation rate ratios in adjacent time-bins is the continuity prior, that fits directly for the change in log(SFR) between the bins and weights against sharp transitions in SFR (see Leja et al., 2019b).

We also fit for dust attenuation — using the Calzetti et al. (2000) attenuation — applied to all light from the galaxy (in units of opacity at 5500Å), stellar metallicity $\log(Z/Z_\odot)$

(where $Z_\odot = 0.0142$), gas ionization parameter U, gas-phase metallicity (linked to stellar metallicity) and total mass formed in the galaxy ($M_{\rm tot}$, in units of $M_\odot$), as free parameters. For each chain in the MCMC analysis, the remnant stellar mass $M_{*,\rm remnant}$ after compensating for mass loss from post main sequence stars, and stellar mass locked in stellar remnants. The dust extinction and metallicities have flat and liberal priors, roughly covering the range allowed by the spectral model libraries. These models each assumed a Kroupa IMF (Kroupa, 2001b). Nebular continuum and line emission are present, and a nominal velocity smoothing of 250 $\rm kms^{-1}$ was used for the spectrum, informed by and consistent with both an SED fit with this as a free parameter as well as a direct fit of the spectrum using a simple Gaussian (see below).

The arc is not visible in g band, while the r- and i-bands sample the Lyα forest, Lyα and Lyβ in the arc. To avoid biases arising from a lack of correlation between star formation activity and the complexity of Lyα absorption/emission in galaxies, which is not captured in the stellar population synthesis models, we use only zJH photometry for the arc SED fitting. We add to this the IR spectroscopy sampling the [O II] 3727,3729Å doublet. The spectrum and photometry are fit here simultaneously.

We assume that the [O II] equivalent width is uniform across COOL J1241+2219 in the source plane, and we scale the emission line spectrum to be representative of the whole arc by considering the entire arc flux against the portion contained within the slit, in the $i-$band. This flux normalization is uncertain in practice, quite apart from the underlying assumption of uniform equivalent width, so we include a nuisance parameter, $\rm spec_{\mathit{norm}}$ (spectrum normalization factor), to capture any unresolved differences between model photometry and spectroscopy. This parameter is simultaneously fit with other parameters within `Prospector`. Note however, that fits computed without this parameter in place are consistent with conclusions from models (e.g., stellar mass) that include $\rm spec_{norm}$.

The best fit SED model is shown in Figure 5.4. We also show corner plots constructed via

`pyGTC` (Bocquet & Carter, 2016), with one and two dimensional projections of the posterior probability functions (to demonstrate both one dimensional marginalized probabilities and two dimensional covariance) in Figure 5.5 for the free parameters fit in the arc SED modeling (see Table 6.2).

It is also crucial to note that the best fit SED model fits a nominal Gaussian to the observed wavelength range where we expect [O II] emission. The result here — mean, width and amplitude — of the [O II] emission feature, is consistent with results from fitting a 1D Gaussian profile to just the spectroscopic data (see Section 5.4.4 for details).

The parameter M_{tot}, total stellar mass formed, converges to a tailed Gaussian posterior distribution for these sources, which corresponds to a model-generated remnant stellar mass distribution, displayed in the bottom panel of Figure 5.5. The median value for the remnant stellar mass (M_*) in the image plane (i.e., the magnified value) is $\log M\ (\mathrm{M}_\odot) = 11.63^{+0.19}_{-0.24}$. The precision of this result may surprise the reader, given that it is based on rest-UV photometry, which is under most circumstances — e.g., at lower redshifts, and in the presence of significant extinction — insufficient to constrain stellar mass reliably. However, only modest dust columns are allowed by the data, and at $z = 5.043$ the Universe was not old enough to conceal much stellar mass in older stars that do not produce significant UV flux.

We further test different models to check the robustness of our results. The stellar mass of the arc is found to be robust when varying parameters as follows:

1. Stellar metallicity fixed at the median best fit value in Figure 5.5.

2. Removing nebular line emission from the model.

3. Altering the number of age bins from three to four, which is recommended by Leja et al. (2019b) (as well as from three to two), spanning the same time period.

4. Changing mean and standard deviation of the star formation history priors.

5. Assuming a parametric star formation history (decayed-tau with a single burst).

6. Constraining SFH only to 0-500 Myr, as opposed to 0-1000 Myr.

7. Using velocity smoothing as a free parameter for the [O II] emission line fitting.

8. Fixing gas ionization parameter to -2 and -2.5, as well as gas-phase metallicity to that of the stellar value (i.e., 0).

We use the Bayesian Information Criterion (BIC) to quantify our model selection, for the greater penalty imposed by BIC on the number of free parameters used in our fitting procedure. Given a candidate model and M models to compare with, the magnitude of ΔBIC ($\mathrm{BIC_M}$ — $\mathrm{BIC_{candidate}}$) can be inferred as evidence against a candidate model being the best model (Kass & Raftery, 1995). The candidate best-fit model has a BIC value of -1245.5, and the models discussed above have a —ΔBIC— < 5, which implies that the evidence against our candidate best-fit model is positive, albeit low. Qualitatively, all models constrain stellar mass and dust attenuation, while leaving metallicities and the gas ionization parameter unconstrained (albeit used here as nuisance parameters).

It is important to note that the SED fitting model contains contribution by nebular line emission in order to fit [O II] emission, and hence depicts Lyα in emission even though it is absent in the spectrum and photometry (as indicated by mismatch between observed photometry and the synthetic magnitudes marked by plus symbol in Figure 5.4). This does not impact our results since the photometry sampling Lyα is not included in our candidate best-fit model, and M_* derived from removing nebular emission contribution is within uncertainties consistent with that derived from our best-fit model.

To cross-check the complete end-to-end pipeline from raw data to SED fits, we have also applied a `Prospector`-based analysis to measurements of the central lens galaxy and two likely cluster members discussed in Section 5.4.2 above, and find that these galaxies are well fit by passively aging old stellar populations at the notional lens redshift — as expected.

5.4.4 Instantaneous SFR: [O II]

Distinct from the simultaneous spectro-photometric SED fit to the data, we cross-check our SFR result by calculating the [O II] 3727,3729Å doublet line flux to characterize the instantaneous SFR (Rosa-González et al., 2002) for COOL J1241+2219 from a scaling relation. We fit a 4 parameter 1-D Gaussian profile (with mean, width, amplitude and continuum pedestal) to the spectroscopic data, in the rest-frame region 3720-3735Å, to capture the blended-doublet emission line. The observed [O II] line flux, corrected for the entire arc, is $4.5^{+2.1}_{-2.0} \times 10^{-16}$ ergs cm^{-2} s^{-1}. The redshift derived from blended-doublet line is 5.041 ± 0.001.

Using the oft-used Kennicutt-calibrated [O II]-SFR relation (Kennicutt, 1992):

$$\mathrm{SFR}([\mathrm{OII}], \mathrm{M}_{\odot}\mathrm{yr}^{-1}) = 1.4 \times 10^{-41} L_{[\mathrm{OII}]}(\mathrm{erg\ s}^{-1}). \tag{5.1}$$

In the image plane we find the SFR for COOL J1241+2219 to be 1700^{+800}_{-800} M$_{\odot}$ yr^{-1}. Instead, if we use the SFR-[O II] relation empirically corrected for stellar metallicity and takes as input the galaxy stellar mass (Equation 8 in Gilbank et al., 2010), we find the calculated SFR to be 4600^{+3400}_{-2400} M$_{\odot}$ yr^{-1}.

Without stronger constraints on metallicity and dust in our SED posterior distributions, their impact on the systematic uncertainties in the SFR-[O II] flux scaling relations cannot be mitigated (e.g., Kewley et al., 2004; Bicker & Fritze-v. Alvensleben, 2005). It is important to note that current constraints are within the metallicity values observed for local universe galaxies.

5.4.5 Lens Modeling and Magnification

We provide a brief summary of the gravitational lensing analysis used in this work here, and we refer the reader to Kneib & Soucail, 1996; Richard et al., 2010; Verdugo et al.,

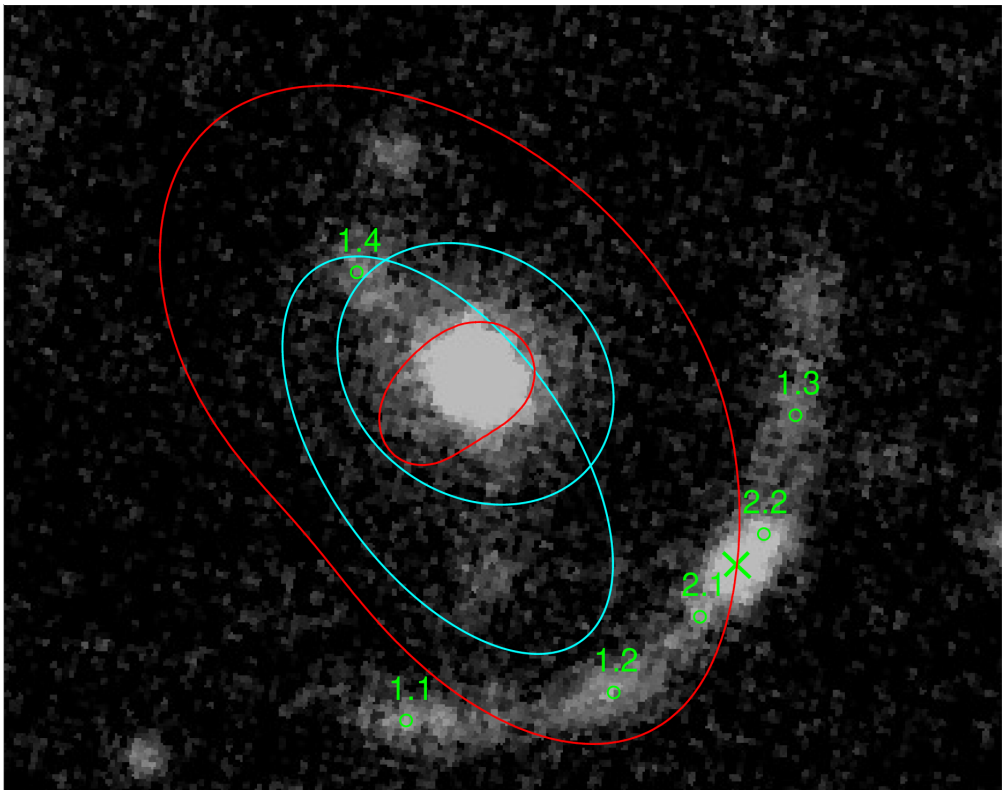

Figure 5.6 Lens model of the low-mass cluster lens based on ground-based imaging, using the positional constraints indicated in green. We include two halos — a galaxy-scale (smaller cyan ellipse) and cluster-scale halo (larger cyan ellipse) to explain the observed lensing. The size of the ellipses represent, on an arbitrary scale, the relative masses of the halos. The tangential critical curve in red trisects the arc — this is a classic 3-image arc with a counter image. This mass configuration is also informed by the bright knot along the arc, which we set as a critical curve crossing in the model (green cross).

2011 for a more in depth discussion of the lensing algorithm used. We adopt a parametric approach using `LENSTOOL` (Jullo et al., 2007) to model the mass distribution with dual pseudo-isothermal ellipsoids (dPIEs, Elíasdóttir et al., 2007), using an MCMC method to estimate the parameters and their uncertainties. The lens modeling strategy generally follows Sharon et al. (2020) (with a cosmology with $\Omega_{\rm M} = 0.3$, $\Omega_{\Lambda} = 0.7$). We model the lens plane with two dPIE potentials, one to represent a group-scale dark matter halo, and one that represents the contribution from the main lens galaxy. The geometric parameters of the galaxy-scale halo are fixed to its observed properties (position, ellipticity, and position

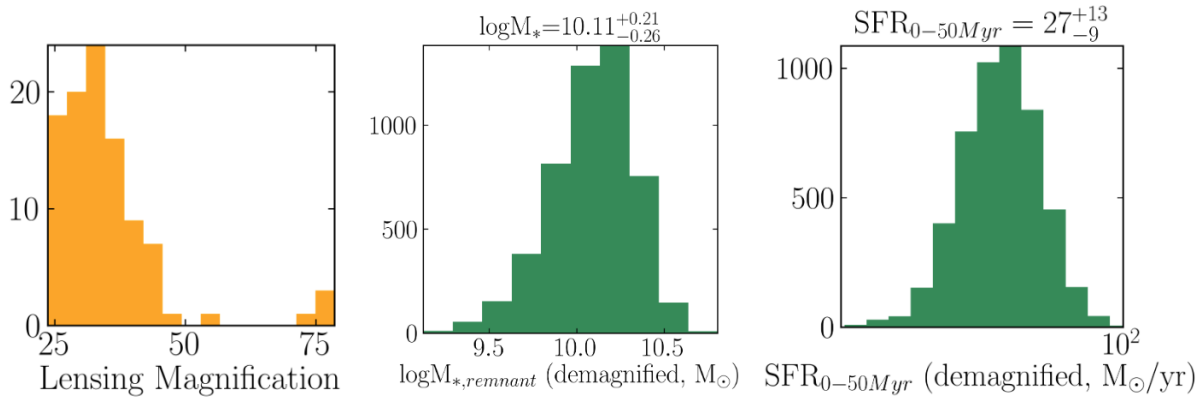

Figure 5.7 (Left) Distribution of magnification values, from a sample of 1000 magnification maps generated via an MCMC LENSTOOL analysis of the lens model fit to the data. Note that distribution is strongly asymmetric about the best fit value, which is in part a consequence of the choice to identify the brightest peak on the arc as a location of the critical curve. (Right) Current SFR in the source plane.

angle), while the slope and overall normalization are allowed to vary. The choice of two halos is motivated by the arc radius, which suggests the presence of a mass structure larger than a single massive galaxy, and the presence of other luminous early-type galaxies with colors consistent with the apparent central lens galaxy, again indicative of a more complex structure. Hence, the two dPIE clumps used here are combined to map the dark matter (DM) at the cluster scale and the central lens galaxy.

The smooth appearance of the arc in the ground based data limits the availability of lensing constraints; a more complex lens plane, with additional galaxy-scale halos, is not required in order to satisfy these constraints. Hence, we do not include any other galaxy-scale halos in this initial model (see Figure 5.6). We choose to use the peak of the galaxy core as a constraint (see system 1 with four images in Figure 5.6), the surroundings of the star-forming clump merging on the critical curve (system 2), and a critical curve constraint (see green cross). The precision assumed for the location of the constraints in the lens model is 0.1", with an RMS of the optimized model in the image plane of 0.12".

To estimate the magnification, we calculate the ratio of flux in the image plane using the

GALFIT modeling image of the arc and its pixel-matched source plane reconstruction for 100 realisations of the lens model posterior probability distribution, resulting in an estimate of the magnification of 32^{+8}_{-5}. We apply this as a division factor to the arc imaging in the image plane, to convert the derived physical parameter values to the source plane. The uncertainties used in the SED fitting do not include the system-wide magnification uncertainty, which when combined with the statistical uncertainties, yields a final stellar mass for COOL J1241+2219 of $\log M$ ($M_\odot$) $= 10.11^{+0.21}_{-0.26}$. Similarly, the demagnified current star formation rate (SFR, in units of $M_\odot$/yr) is calculated to be 27^{+13}_{-9} (see Figure 5.7), which makes this an active star-forming galaxy, given the constraints of the SED and lens modeling. This is assuming that the SFR in the age bin 0-50 Myr is a proxy for current star forming activity in COOL J1241+2219 .

5.5 Discussion

5.5.1 Luminosity Function

We compare the brightness of COOL J1241+2219 to M^{UV}, the characteristic absolute magnitude corresponding to a characteristic luminosity in the parametric luminosity function (Schechter, 1976). As a proxy for the UV absolute magnitude we compute M_{1600}, calculated from synthetic photometry applied to the best fit SED model, using a top-hat filter from 1550-1650 Å. The UV continuum is roughly flat, and hence differences in definitions of UV magnitudes in the literature do not significantly impact the comparison of our reported absolute magnitude to published values.

Taking into account the lensing magnification, $M_{\rm UV}$ for COOL J1241+2219 is $-22.2^{+0.2}_{-0.2}$. Bouwens et al. (2015) give a characteristic $M^*_{\rm UV}$ at $z = 5$ of -21.1±0.2 (see Table 6 in Bouwens et al., 2015; we use the higher uncertainty value). Hence, we find that for COOL J1241+2219 , $M^*_{\rm UV}$ — $M_{\rm UV}$= $1.0^{+0.5}_{-0.4}$. In other words, COOL J1241+2219 is $\sim$ 2-4 times

more luminous than an object with the characteristic UV luminosity at these redshifts.

5.5.2 The UV Continuum Slope

The observed UV continuum slope of star-forming galaxies is closely related to emission from massive stellar populations, as well as dust extinction in the galaxy. We fit the best-fit SED model for COOL J1241+2219 with a power law in f_λ, i.e., $f_\lambda \simeq \lambda^\beta$, between rest-frame 1268-2580Å (the entirety of the fitting windows described initially by Calzetti et al., 1994). For COOL J1241+2219 , the best-fit UV continuum slope is calculated to be β = -2.2±0.2. This is on the blue side of the distribution of β observed in (albeit fainter) galaxies at $z = 5$ in (e.g., Finkelstein et al., 2012) but consistent with their measured distribution. However, the mean relation between β and UV luminosity (Bouwens et al., 2014) for galaxies at $z = 5$ predicts a value of β for COOL J1241+2219 of ∼-1.6, significantly shallower than we observe. The observed β is in fact consistent with that for galaxies ~ 4 magnitudes fainter, emphasizing that COOL J1241+2219 is unusually blue for its total UV luminosity.

5.5.3 Star-forming Main Sequence

The relationship between SFR and stellar mass of a galaxy is a well-studied relationship in galaxy populations and large samples, known as the star-forming main sequence (SFMS; Noeske et al., 2007b; Rodighiero et al., 2011). It is informative to place these properties of COOL J1241+2219 in relation to the SFMS of a galaxy sample in the same epoch of observation. We compare the SFR and stellar mass of COOL J1241+2219 with galaxies at $4 < z < 6$ in the Hubble Space Telescope Frontier Fields. The SFMS for galaxies in this field in the redshift bins $4 < z < 5$, and $5 < z < 6$ has been reported in Santini et al. (2017). We direct the reader to the solid lines in bottom panels in Figure 2 of that publication, which reflect the best-fit SFMS, corrected for Eddington bias. The demagnified SFR and stellar mass of COOL J1241+2219 ($\log M$ ($M_\odot$) = $10.11^{+0.21}_{-0.26}$ and SFR ($M_\odot$/yr) = 27^{+13}_{-9}),

are consistent with these power-law fits for the SFMS within 1σ, but incompatible with high SFRs corresponding to bursty mode(s) of star formation during major mergers or in the densest regions. It is also important to note that the source plane properties of COOL J1241+2219 place this galaxy among the highest mass values reported in those data.

5.5.4 Stellar Populations in COOL J1241+2219

COOL J1241+2219 has a stellar mass consistent within a factor of a few of that of the present-day Milky Way (Licquia & Newman, 2015), and is forming stars $\sim$ 1-2 orders of magnitude faster. This rate of star formation is not surprising, given that the available time to build this galaxy at $z = 5.04$ is only $\sim$1 Gyr. COOL J1241+2219 is extremely UV-bright with little apparent extinction. This stands in strong contrast to some similarly massive galaxies known from this early epoch (e.g., Riechers et al., 2013; Strandet et al., 2017; Casey et al., 2019) which tend to be much dustier with SFRs an order of magnitude larger. This difference is of course due to the selection process used to identify these objects. What is less clear, however, is whether COOL J1241+2219 looked like these dust-enshrouded examples of early star formation at any point in its history. The relative contribution of dust-enshrouded star formation to the total star formation rate at this epoch is not well-measured (Casey et al., 2019) and so objects like COOL J1241+2219 that are bright enough to allow detailed studies are of particular interest.

The current constraints from SED fitting (see Figures 5.5 and 5.7) imply that the SFH of COOL J1241+2219 is consistent with a constant SFR across the $\sim$1 Gyr available. The current data however are insufficient to say more; the non-parametric model forms the bulk of its stars in the oldest (and widest) bin, and a briefer and much elevated star-formation episode in that interval is certainly possible.

Despite significant ongoing star-formation, and a blue UV slope that suggests little extinction, COOL J1241+2219 shows no evidence for Lyα emission in the extracted spectrum.

In addition, we carefully examine the stacked 2D spectrum, and see no evidence of spatially-extended Lyα emission outside of the continuum. This complete lack of emission indicates the presence of sufficient dust to suppress Lyα, as one would expect in a massive galaxy with a sustained SFH and resulting enrichment. These results are somewhat in tension. However, note that the measured scatter in galaxies between the Lyα escape fraction and continuum extinction is large (Hayes et al., 2011) and suppression of Lyα emission is possible even with extremely sparse dust columns.

5.6 Summary and Future Work

We report the discovery of COOL J1241+2219, a strongly lensed galaxy at z=5.043 $\pm$ 0.002 that is lensed by a moderate-mass galaxy cluster at z=1.00 $\pm$ 0.001. In this first work by the COOL-LAMPS collaboration, we characterise the lensed galaxy using *grizJH* band photometry and optical and NIR spectroscopy. Using `Prospector`, we perform a stellar population synthesis analysis spectro-photometrically, to constrain the stellar mass, SFH, stellar metallicity and dust properties. Our dPIE-halo-based lens mass modeling from `LENSTOOL`, based on ground-based imaging, implies a median source magnification of at least $\sim$30, which puts the stellar mass and star formation rate (in the youngest age bin, closest to the epoch of observation) at $\log M_* = 10.11^{+0.21}_{-0.26}$ and SFR $= 27^{+13}_{-9}$ M$_\odot$/yr, respectively. This places this galaxy on the star-forming main sequence, at the massive end of that relation, and we find that COOL J1241+2219 is 2-4x more luminous than a galaxy with the characteristic UV luminosity at these redshifts. We constrain a star formation history for COOL J1241+2219 starting at $z \sim 20$ that is consistent with constant star formation across $\sim$1 Gyr of cosmic time.

Current data are insufficient to constrain the metallicity and star formation history robustly. Also, as is almost always true, the lens model built on ground-based data limits the precision and accuracy of some aspects of our analysis; a lens model built from much sharper

imaging (e.g., with HST) will provide insights into fluxes, flux variations, and identification of a variety of faint spatial features within this galaxy much more comprehensively via a proper source plane reconstruction. Moreover, our current spectroscopy only samples the apparently brightest clump in this galaxy. Once lensed into the observed giant arc, COOL J1241+2219 is the brightest galaxy at $z > 5$ currently known, and thus presents a unique opportunity for the detailed study of a massive galaxy immediately after the epoch of reionization. COOL J1241+2219 is bright enough that precise high resolution observations will be possible across a broad range of wavelengths.

5.7 Acknowledgments

We would like to express gratitude towards the staff and workers at the 6.5m Magellan Telescopes at the Las Campanas Observatory, Chile, and the Gemini-North telescopes at Mauna Kea, Hawaii, USA, for their valuable labor. The authors wish to recognize and acknowledge the very significant cultural role and reverence that the summit of Mauna Kea has always had within the indigenous Hawaiian community. The authors are most fortunate to have the opportunity to conduct observations via the NOIRLab-operated Gemini-North facility from this mountain. GK acknowledges the impact of astrophysical observatories and research on this sacred Native Hawaiian land, and directs the reader towards resources on this matter for further consumption (e.g., Kahanamoku et al., 2020; Prescod-Weinstein et al., 2020, and references therein).

We would like to thank the anonymous reviewer for their thoughtful and helpful comments, that improved the quality of this manuscript and the robustness of ther results herein, substantially.

GK thanks Joel Leja and Benjamin Johnson for their responses, guidance and input related to specifics of the `Prospector` framework.

This work is supported by The College Undergraduate program at the University of Chicago, and the Department of Astronomy and Astrophysics at the University of Chicago. Magellan/PISCO operations are supported by NSF AST-1814719. This research was supported by an appointment to the NASA Postdoctoral Program at the NASA Goddard Space Flight Center administered by Universities Space Research Association through a contract with NASA. Work at Argonne National Lab is supported by UChicago Argonne LLC,Operator of Argonne National Laboratory (Argonne). Argonne, a U.S. Department of Energy Office of Science Laboratory, is operated under contract no. DE-AC02-06CH11357.

The Legacy Surveys consist of three individual and complementary projects: the Dark Energy Camera Legacy Survey (DECaLS; Proposal ID #2014B-0404; PIs: David Schlegel

and Arjun Dey), the Beijing-Arizona Sky Survey (BASS; NOAO Prop. ID #2015A-0801; PIs: Zhou Xu and Xiaohui Fan), and the Mayall z-band Legacy Survey (MzLS; Prop. ID #2016A-0453; PI: Arjun Dey). DECaLS, BASS and MzLS together include data obtained, respectively, at the Blanco telescope, Cerro Tololo Inter-American Observatory, NSF's NOIRLab; the Bok telescope, Steward Observatory, University of Arizona; and the Mayall telescope, Kitt Peak National Observatory, NOIRLab. The Legacy Surveys project is honored to be permitted to conduct astronomical research on Iolkam Du'ag (Kitt Peak), a mountain with particular significance to the Tohono O'odham Nation.

NOIRLab is operated by the Association of Universities for Research in Astronomy (AURA) under a cooperative agreement with the National Science Foundation.

This project used data obtained with the Dark Energy Camera (DECam), which was constructed by the Dark Energy Survey (DES) collaboration. Funding for the DES Projects has been provided 19 by the U.S. Department of Energy, the U.S. National Science Foundation, the Ministry of Science and Education of Spain, the Science and Technology Facilities Council of the United Kingdom, the Higher Education Funding Council for England, the National Center for Supercomputing Applications at the University of Illinois at Urbana-Champaign, the Kavli Institute of Cosmological Physics at the University of Chicago, Center for Cosmology and Astro-Particle Physics at the Ohio State University, the Mitchell Institute for Fundamental Physics and Astronomy at Texas A&M University, Financiadora de Estudos e Projetos, Fundacao Carlos Chagas Filho de Amparo, Financiadora de Estudos e Projetos, Fundacao Carlos Chagas Filho de Amparo a Pesquisa do Estado do Rio de Janeiro, Conselho Nacional de Desenvolvimento Cientifico e Tecnologico and the Ministerio da Ciencia, Tecnologia e Inovacao, the Deutsche Forschungsgemeinschaft and the Collaborating Institutions in the Dark Energy Survey. The Collaborating Institutions are Argonne National Laboratory, the University of California at Santa Cruz, the University of Cambridge, Centro de Investigaciones Energeticas, Medioambientales y Tecnologicas-Madrid, the University of Chicago,

University College London, the DES-Brazil Consortium, the University of Edinburgh, the Eidgenossische Technische Hochschule (ETH) Zurich, Fermi National Accelerator Laboratory, the University of Illinois at Urbana-Champaign, the Institut de Ciencies de l'Espai (IEEC/CSIC), the Institut de Fisica d'Altes Energies, Lawrence Berkeley National Laboratory, the Ludwig Maximilians Universitat Munchen and the associated Excellence Cluster Universe, the University of Michigan, NSF's NOIRLab, the University of Nottingham, the Ohio State University, the University of Pennsylvania, the University of Portsmouth, SLAC National Accelerator Laboratory, Stanford University, the University of Sussex, and Texas A&M University.

The Legacy Surveys imaging of the DESI footprint is supported by the Director, Office of Science, Office of High Energy Physics of the U.S. Department of Energy under Contract No. DE-AC02- 05CH1123, by the National Energy Research Scientific Computing Center, a DOE Office of Science User Facility under the same contract; and by the U.S. National Science Foundation, Division of Astronomical Sciences under Contract No. AST-0950945 to NOIRLab.

CHAPTER 6

MASSIVE LENSED QUIESCENT GALAXIES IN COOL-LAMPS AND NEW FRAMEWORKS FOR SED FITTING

6.1 Introduction

In Chapters 3 and 4, I described the discovery of five high redshift SZ-selected galaxy clusters, and characterized stellar mass assembly and star formation histories in 65 clusters across $0.3 < z < 1.5$ via Bayesian SED Fitting. In Chapter 5, I described the COOL-LAMPS collaboration, and the discovery of the unique and bright $z \sim 5$ massive lensed galaxy COOL J1241+2219.

In this chapter, I describe ongoing work to study massive galaxies in the COOL-LAMPS project at intermediate redshifts. The ambition to study bright gravitationally lensed quiescent galaxies at $z \sim 1$ is fundamentally linked to the quest to characterize the antecedents of ultra-massive galaxies we observe locally — massive galaxies in the early Universe must be representative progenitors of lower redshift massive systems. Establishing the connection — if one exists — between luminous lensed galaxies at high redshift, and lower redshift quiescent galaxies requires understanding the stellar mass of these distant systems. By definition, the COOL-LAMPS project (see Section 5.2) is discovering the brightest lensed systems at the margins of optical color-magnitude and color-color parameter spaces, and is a sample that can contribute to the study of the "descendent-antecedent connection".

In this chapter I also describe my initial efforts to contribute in the field of building state-of-the-art SED fitting frameworks; such novel methodologies are key to robustly measuring stellar mass and other physical parameters of galaxies. Bayesian SED fitting analyses have reached a crucial juncture today, where the increasing number of galaxy spectroscopic datasets and the large computation time required to analyse each galaxy's SED means that

we must seek newer and more efficient methods of star formation history analysis. I demonstrate a proof-of-concept by testing this new framework on a gravitationally lensed quiescent galaxy discovered by COOL-LAMPS, and comparing with traditional inference methods.

6.2 COOL-LAMPS: High-Redshift Lensed Quiescent Galaxies

6.2.1 Studies of Quiescent Galaxies

Observations of quiescent galaxies (galaxies with low levels of current star formation) across cosmic time contain signatures of mass accretion and star formation histories. Characterizing the morphological and spectral properties of distant quiescent galaxies, therefore, allows us to study modes of stellar mass growth. This is especially true for gravitationally lensed objects, where these properties can be robustly studied with ground-based facilities due to availability of more photons spread over a larger area better matched to ground-based seeing. The brightest (and hence rarest) lensed quiescent galaxies are particularly valuable objects for such studies.

Why are observations of lensed quiescent galaxies important? Massive quiescent galaxies at early times are much more compact than massive quiescent galaxies in the local universe (with 3-5$\times$ smaller radii, e.g., see Daddi et al. (2005); Trujillo et al. (2007); van Dokkum et al. (2008)). Any proposed evolution mechanism must therefore have to explain the growth in radius without a proportional increase in mass. Dissipationless mergers or progenitor bias may explain the evolution seen at $z < 1.5$ and for $M_* < 10^{11}\mathrm{M}_\odot$ galaxies, but is insufficient to explain their rapid evolution, as well as the scatter in radii observed at high redshifts (Fan et al., 2010; Newman et al., 2012; Fagioli et al., 2016).

Massive galaxies are thought to either quench and form "inside-out" via central starbursts (Wellons et al., 2015; Ceverino et al., 2015), or assemble from the "outside-in" by reduced cold gas accretion (Khochfar & Silk, 2006; Feldmann et al., 2016). The best way

to distinguish between scenarios is to reconstruct the star formation and mass buildup, as well as the structural evolution that leads to the formation of a compact galaxy, with spatially resolved stellar population gradients. Spatial maps of star formation histories (SFHs) would reveal the timescale for quenching, i.e., whether the galaxies shut off "fast" or "slow" (Moutard et al., 2018). Recent work at $z \sim 1$ hints that both "outside-in" and "inside-out" formation pathways are important (Costantin et al., 2021). Spatially resolved data of early-type galaxies (ETGs) from $0.5 < z < 2$ would certainly clarify which specific mechanisms fuel ETG evolution. Unfortunately, current telescopes can only observe the most luminous ETGs, with generally insufficient spatial resolution.

Strongly lensed ETGs offer enhanced spatial resolution, and high signal-to-noise ratio spectroscopy; the REQUIEM-HST survey (Akhshik et al., 2020) of 7 lensed ETGs at $1.6 < z < 2.9$, and a sample of 13 lensed ETGs at $0.4 < z < 0.7$ of (Oldham et al., 2017) are the two key samples currently published. Moreover, recent imaging surveys — Dark Energy Camera Legacy Survey (DECaLS; Huang et al. (2020b)), DECam Local Volume Exploration Survey (DELVE; Drlica-Wagner et al. (2022)), Pan-STARRS Chambers et al. (2016) — with enhanced red sensitivity offer the opportunity to discover a sample of lensed ETGs in the redshift range between the samples above; e.g., DECaLS has just released a catalogue of 1200 lenses, many newly discovered (Huang et al., 2020a).

6.2.2 Building a Sample of Lensed Quiescent Galaxies

Despite being rare, extremely bright lensed ETGs at high-redshift are gifts that keep on giving; even a single object — i.e., MRG-M0138 above — has proven immensely useful in advancing our understanding of stellar dynamics and mass accretion in high-redshift ETGs. Newman et al. (2018a) presented the discovery of MRG-M0138 at z=1.95; this is a lensed ETG which they note as the brightest lensed galaxy known in the near-IR, with H_{AB}=17.1. This recent discovery has already enabled studies of its mass assembly, stellar kinematics,

chemical abundance ratios and stellar age (Newman et al., 2018b; Jafariyazani et al., 2020).

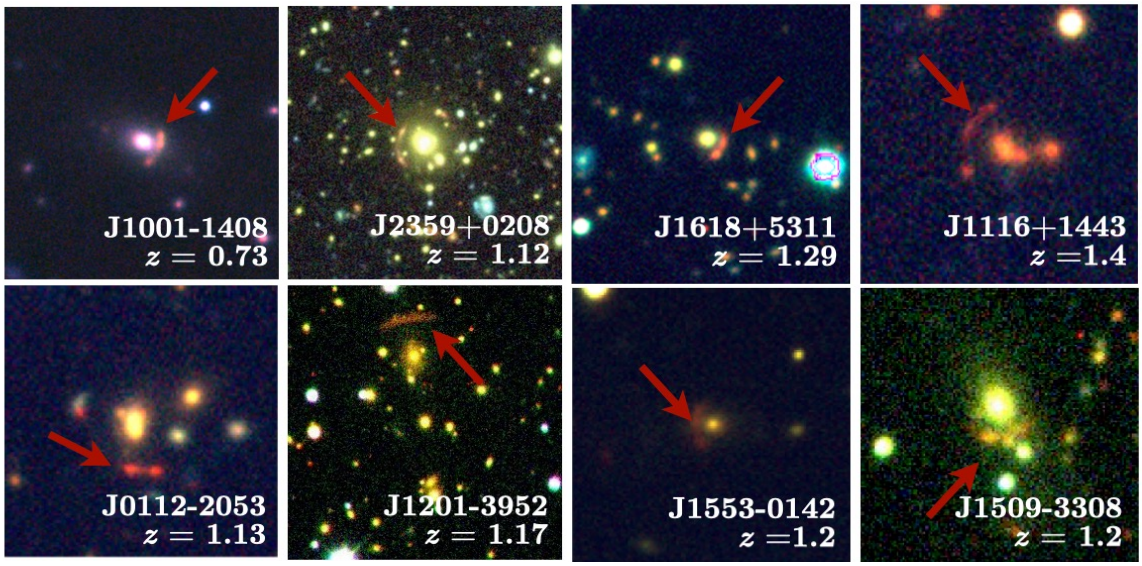

Figure 6.1 RGB ground-based telescope imaging of 9 lensed quiescent galaxies at z=0.7-1.4, discovered and characterized by the COOL-LAMPS collaboration. This sample includes COOL J1323+0343 (Sukay et al., 2022) at z=1.02 (see Figure 6.2.

Within the COOL-LAMPS collaboration, we have recently discovered and characterized a sample of nine lensed quiescent galaxies that are bright and potentially massive systems (see Table 6.1 and Figure 6.1). The discovery process is the same as for COOL J1241+2219 (see Chapter 5 for more details). SED fitting analyses with photometry and spectroscopy of this sample of extraordinarily bright lensed quiescent galaxies will allow us to measure their stellar masses and ages (and hence their star formation histories), and kinematics. Building properly scaled gravitational lens models to describe the lensed quiescent galaxy morphology in the source plane, and measuring their effective radii will allow us to compare their stellar masses and star formation histories to their sizes (in the source plane). The characterization of COOL-LAMPS quiescent galaxies in the mass-radius parameter space will fill in a crucial population in the broader landscape of lensed "red and dead" galaxies across cosmic time (between the lower redshift Oldham et al. (2017) sample and the higher redshift REQUIEM dataset). This analysis is ongoing in collaboration with undergraduate students

at the University of Chicago and other members of the COOL-LAMPS collaboration; I show here the developed sample, reduced follow-up data, and some initial results of analysis.

6.2.3 Discovery and Follow-up Observations

The lensed galaxies in this quiescent galaxy sample were discovered in the DECaLS, DELVE and Pan-STARRS public imaging surveys. All galaxies have existing grz imaging (in the discovery catalogs); some systems have iY imaging as well. We have also conducted extensive follow-up observations — near-infrared imaging (via follow-up $JHKs$ band observations with Magellan/FOURSTAR), and optical ground-based spectroscopy (with Magellan IMACS, LDSS3 and Nordic Optical Telescope/ALFOSC), which confirm these are quiescent systems. 4/8 targets in this sample (excluding J1201-3952) have preliminary lens models from the best ground-based data in hand. The galaxy cluster lensing J1201-3952 was discovered in the Planck SZ survey (Planck Collaboration et al., 2011), and has a reported X-ray redshift ($z = 0.3$) and weak-lensing map in Gruen et al. (2014), but no study of the lensed source.

Sukay et al. (2022) have already conducted an extensive study of COOL J1323+0343 (CJ1323), the first bright red arc in the COOL-LAMPS project (discovered in DECaLS DR8) that was classified as a quiescent galaxy after follow-up spectroscopy (see Figure 6.2). CJ1323, at $z = 1.015 \pm 0.001$, is strongly lensed by a cluster of galaxies at $z = 0.353 \pm 0.001$. With ground-based $grzH$ imaging and optical spectroscopy from Magellan Telescopes and the Nordic Optical Telescope, we (in Sukay et al. 2022) derive a stellar mass, metallicity, and star-formation history from stellar-population synthesis modeling. The lens modeling implies a total magnification of $\mu \sim$113. The median remnant stellar mass in the source plane is $\log M \sim 10.63$ (in units of $M_\odot$) and the median current star-formation rate in the source plane is SFR $\sim 1.55 \times 10^{-3}$ $M_\odot$ yr^{-1} (log sSFR = -13.4 yr^{-1}). These measurements place CJ1323 below the characteristic mass of the stellar mass function at these redshifts, and below the expected size-evolution of quiescent galaxies at this mass with an effective

Table 6.1. Coordinates, Redshifts and Brightness of 9 bright lensed galaxies in this analysis

Object	RA	Dec	Arc Redshift	Photometric Data	Arc Brightness (mag_{AB})
COOL J1001-1408	10:01:51.50	-14:08:48.00	0.73	$grizY \mid JHK_s$	z=19.0, H=18.5
COOL J1323+0343	13:23:4.10	+03:43:19.56	1.02	$griz \mid JHK_s$	z=18.6, H=17.1
COOL J2359+0208	23:59:0.00	+02:08:0.00	1.12	$grz \mid JHK_s$	z=19.5, H=17.7
COOL J0112-2053	01:12:3.50	-20:53:27.91	1.13	$grz \mid HK_s$	z=20.1, H=17.8
COOL J1201-3952	12:01:5.59	-39:52:8.76	1.17	$griz \mid JHK_sW_1W_2$	z=18.5, H=17.9
COOL J1553-0142	15:53:38.20	-01:42:33.54	1.28	$grz \mid JHK_s$	z=20.1, H=17.9
COOL J1618+5311	16:18:21.57	+53 11 13.56	1.29	grz	z=19.2
COOL J1509-3308	15:09:51.67	-33:08:11.04	$\sim$1.3	$grz \mid JHK_s$	z=19.4, H=18.0
COOL J1116+1443	11:16:57.90	+14:43:10.00	$\sim$1.4	$grzJHK_s$	z=20.0, H=18.7

Table 6.2. `Prospector` Analysis: Free Parameters in SED Model with Delayed-Tau SFH

Parameter	Description	Priors
$M_{\mathrm{total}}(\mathrm{M}_\odot)$	Total stellar mass formed	Log_{10} Uniform: [10^{10}, 10^{13}]
z	Observed Redshift (Mean Redshift from B16 and K19)	TopHat: [$z-0.02$, $z+0.02$]
$\log(Z/\mathrm{Z}_\odot)$	Stellar metallicity in units of $\log(Z/\mathrm{Z}_\odot)$	TopHat: [-2.0, 0.2]
t_{age}	Age of Galaxy	TopHat: [0, Age(Universe) at z_{obs}]
τ	e-folding time of SFH (Gyr)	Log_{10} Uniform: [0.1, 10.0]

radius $r_e \sim 0.5$ kpc.

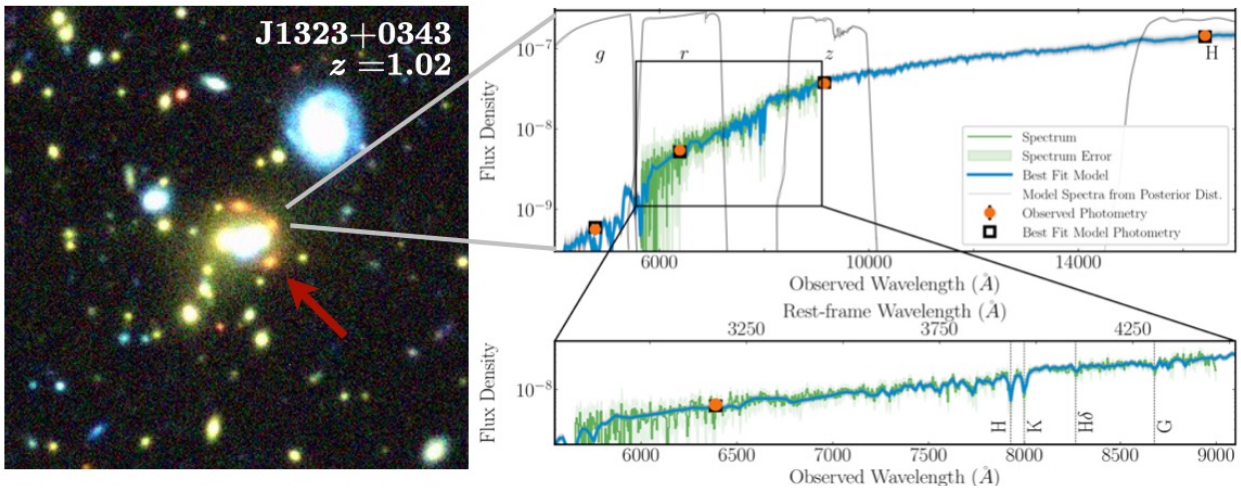

Figure 6.2 Best fit SED model for COOL J1323+0343 from Sukay et al. (2022) (blue) and other fits from the posterior distribution (gray) calculated via Prospector using $grzH$ photometry (orange) and optical/NIR Nordic Optical Telescope/ALFOSC spectroscopy (green), with the spectra's 1σ error shown in light green. Best-fit photometry is shown as black squares.

6.2.4 COOL J1553-0142: SED Fitting with `Prospector`

To build on the analysis from Sukay et al. (2022), we are conducting model photometry on this sample of bright, lensed quiescent galaxies with GALFIT (Khullar et al. 2022, in prep), with the purpose of:

a) using photometry and spectroscopy of each arc to conduct spectral energy distribution (SED) fitting and characterize star formation histories, stellar masses (in the image plane) and ages of these systems.

b) conducting lens modeling to create a source plane model of the galaxy, and assess stellar masses and star formation rates in the source plane.

c) situating this sample of quiescent galaxies in the mass-radius parameter space and assessing their formation and evolution mechanisms.

Using the model photometry in *grizJH* filters, we perform spectral energy distribution (SED) fitting for arcs using the Markov Chain Monte Carlo (MCMC) — based stellar population synthesis (SPS) and parameter inference code, `Prospector`. `Prospector` (as mentioned in other chapters) is based on the the Python-FSPS framework, with the MILES stellar spectral library and the MIST set of isochrones (Conroy & Gunn, 2010a; Johnson & Leja, 2017b; Leja et al., 2017b; Foreman-Mackey et al., 2013; Falcón-Barroso et al., 2011; Choi et al., 2016).

In these models, we assume a parametric star formation history (a delayed exponentially decaying model with age and τ parameters; see Chapter 4). We also fit for total stellar mass ($M_{\rm tot}$, in units of $M_\odot$), and stellar metallicity $\log(Z/Z_\odot)$ (where $Z_\odot = 0.0142$), while keeping dust attenuation fixed (at a notional optical depth at 5500Å of 0.2). For each chain in the MCMC analysis, the remnant stellar mass $M_{*,\rm remnant}$ after compensating for mass loss from post main-sequence stars, and stellar mass locked in stellar remnants. The metallicity parameter has flat and liberal priors, roughly covering the range allowed by the spectral model libraries. These models each assumed a Kroupa IMF (Kroupa, 2001b). Nebular continuum and line emission are present, and a nominal velocity smoothing of 250 $\rm kms^{-1}$ was used for the SEDs. See Table 6.1 for more details on the SED model used in this work.

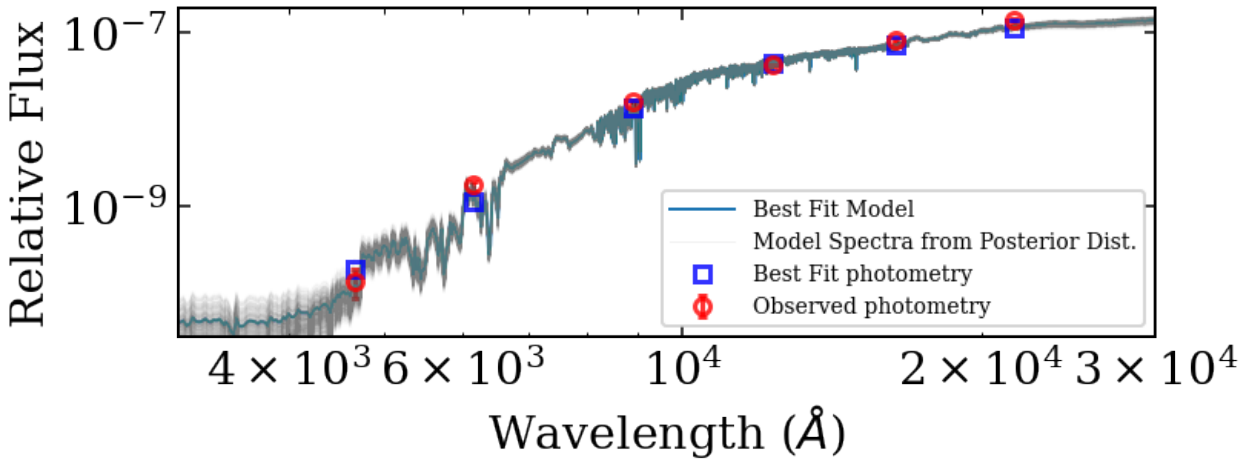

Figure 6.3 Best-fit SED model (in blue) for COOL J1553-0142 at $z = 1.28$, with *grz*JHKs photometry (in red circles) from Khullar et al. (in prep).

Figure 6.3 shows an example SED fit from this work, for COOL J1553-0142, at redshift $z = 1.28$. With GALFIT model photometry, we find this to be a bright lensed galaxy at AB magnitudes $g = 24.68 \pm 0.41, r = 21.91 \pm 0.13, z = 19.49 \pm 0.08$, J=$18.42 \pm 0.03$, H=$17.71 \pm 0.06$, and Ks=$17.14 \pm 0.06$. The best fit SED model for CJ1553 (photometry only) is shown in Figure 5.4. Based on one and two dimensional projections of the posterior probability functions (i.e., corner plots) for CJ1553, we find the median value for the total stellar mass (M_*) in the image plane (i.e., the magnified value) is $\log M\ (\mathrm{M}_\odot)) = 12.59 \pm 0.03$. The lens modeling, spectroscopy and mass-radius relation analyses will be presented in a future publication (Khullar et al. 2022 in prep, in collaboration with COOL-LAMPS undergraduate students).

6.3 SED Fitting with Machine Learning and Simulation-Based Inference

6.3.1 Characterizing Galaxy SEDs

In studies of galaxy evolution and structure formation, we seek to capture the assembly of mass, the formation of stars and quasars, and the feedback between these compact objects and surrounding gas and dust. Inferred star formation histories via SED fitting of millions of galaxies from these large scale surveys will also be a key input into measurements of the properties of dark matter and dark energy.

Today, ground-based telescopes have been used extensively for large galaxy surveys and to acquire multiwavelength data (extensive both by quality and quantity). These advanced datasets — containing galaxies possessing a wide range of metallicities, masses, star formation rates and dust attenuation — have allowed us to build state-of-the-art empirical galaxy SED models, which are then fit to newly observed galaxy SEDs. There are several cutting-edge SED fitting pipelines with Bayesian frameworks that use Markov Chain Monte

Carlo (MCMC) methods to infer galaxy properties (e.g., codes like CIGALE, MAGPHYS and PROSPECTOR (Leja et al., 2017b), the latter which we use in this thesis). Each of these rely on a library of spectra and stellar evolutionary tracks. The ability to quickly and reliably deduce the physical parameters of observed and simulated galaxies from available data is central to these analyses.

6.3.2 Challenge: SED Modeling of Large Spectral Datasets

The biggest challenges in the field of SED fitting are determining how well the stellar spectra and stellar evolutionary tracks (isochrones) are constrained by the library of empirical/simulated models, as well as the fitting algorithms themselves (for a comprehensive review, see Leja et al. (2017b); Carnall et al. (2019a); Leja et al. (2019b) and references therein).

Issues arise when the spectra in our dataset are highly resolved (resulting in higher information content in the data relative to the models being compared with), the model has a large number of free parameters to sample (higher dimensionality and hence typically a computational challenge), or the data maps to physical parameters outside the range of the grid of models. Moreover, there are significant degeneracies between some physical parameters; ages of stellar populations, stellar metallicity and dust attenuation in a galaxy can have similar effects on some spectral signatures (Worthey, 1994, 1999).

If the star formation history for a given galaxy is reconstructed incorrectly, this could lead to significant biases in our physical understanding — e.g., up to 70% higher/lower stellar masses than expected (Iyer & Gawiser, 2017). This is a catastrophic bias that can systematically shift our understanding of stellar mass assembly in galaxies, and subsequently the connection between baryons and dark matter in galaxies across the universe.

A Bayesian MCMC sampling approach to SED fitting allows us to simultaenously constrain multiple parameters, and provide confidence intervals to constrain uncertainties. While

Bayesian frameworks are well understood and established, they are time-intensive due to the complex nature of the problem. Moreover, with the next generation of telescopes, like the Vera Rubin Observatory/ Legacy Survey of Space and Time (VRO–LSST) and the Dark Energy Spectroscopic Instrument (DESI; DESI Collaboration et al. (2016)), tens of millions of galaxies and their optical and infrared photometry and spectra will be observed, which can be used to understand their stellar populations. It is also worth noting that with an increasing amount of datasets with spaxels (data units in integral-field-unit (IFU) spectrograph data, that contain spatial and spectral information) — e.g., with JWST IFU spectroscopy of a lensed galaxy (see Chapters 5 and 7) — it is now also necessary to build frameworks that efficiently analyse thousands of spectra from within one galaxy.

A 10-parameter spectral model within a typical SED fitting code — which describes a galaxy with adequate complexity, and contains stellar mass, dust attenuation, metallicity, star formation history components as free parameters — converges to a best-fit model solution within 2-10 CPU hours on a remote server machine. For tens of millions of spectra observed with large-scale surveys in the future, this complex task would take far too long to allow for the necessary iteration and refinement across these huge samples. Moreover, this also prevents us from exploring new models of galaxy formation — different forms of star formation history, dust attenuation laws, etc. — on these datasets. We need faster methods that don't sacrifice the robustness of a conventional Bayesian approach (which utilizes MCMC sampling in parameter space).

The need of the hour is to explore and solidify our understanding of algorithms that perform classification and regression on the same grid of models as our MCMC frameworks, but faster and more accurately. Machine learning (ML) is a key element of the path forward.

6.3.3 Towards a Solution: Machine Learning for Parameter Inference

An obvious potential solution to this challenge is some form of machine learning. I am investigating the use of fast and flexible ML models, in conjunction with new statistical frameworks like Simulation-Based Inference (SBI), that bypass built-in assumptions in Bayesian analyses and remove bottlenecks that slow down statistical calculations.

ML algorithms are capable of being flexible and fast. ML algorithms are becoming an effective way of performing classification and regression in cosmology and astrophysics — whether it's for classifying galaxies into different morphological types (Domínguez Sánchez et al., 2018) or reconstructing the gravitational lensing of the cosmic microwave background (see work by Caldeira et al. (2019)). ML algorithms are generally classified into two groups — unsupervised and supervised learning. Supervised learning — which I focus on here — learns information from existing data that is well-studied, and uses that learned information to either classify or infer properties of new data.

ML applied to galaxy SED fitting allows an algorithm, in principle, to model 'the relationship between the star formation history of a galaxy and the observed SED' (Lovell et al., 2019). Unlike traditional parameter-fitting frameworks where the analysis depends on a template library, ML directly infers the relationship between star formation histories and SEDs (whether this relationship can be mapped to physical parameters like template libraries, or not). This is an up-and-coming area of inquiry, with several new insights published in the last couple of years alone (see Hahn & Melchior (2022) and references therein).

Additionally, new statistical frameworks can bypass built-in assumptions in Bayesian analyses. As mentioned above, Bayesian SED fitting is well equipped to accurately infer parameters. Bayesian inference requires the calculation (or sampling) of the posterior probability distribution (the probability of model parameters given observed data), which is defined as

$$p(\theta|x) = p(x|\theta) * p(\theta)/\text{normalization factor} \tag{6.1}$$

Where x is the data, θ are the model parameters, $p(x|\theta)$ is the likelihood function, or the probability distribution of the data x given the model parameters θ, and p(θ) is the prior probability distribution of the model parameters.

Most SED fitting codes assume a functional form for the likelihood function $p(x|\theta)$, which may not always be a valid assumption, e.g., in the case of non-Gaussian spectral data uncertainties or placing upper limits on the detection/non-detection of flux in a certain wavelength regime (see footnote 12 in Chevallard & Charlot (2016)). This will certainly be the case for thousands of distant faint galaxies in upcoming surveys.

Moreover, both datasets and SED models are becoming more complex, with high-dimensional parameter spaces, which often contain non-functional (or distribution-free) internal correlations, or correlations that are unknown. Calculations of these likelihoods require more and more computational power (see Ishida et al. (2015)).

Therefore, what is required here is the combination of ML (which, as explained above, provides faster inference times) and statistical frameworks that bypass the need to calculate likelihoods explicitly. SBI frameworks are potentially the answer (Cranmer et al., 2019).

SBI allows us to calculate intractable likelihoods by performing simulations that mimic the observed data, and use summary statistics to reduce dimensionality and calculate the distance between the 'simulated' and observed data. Moreover, some SBI frameworks also allow us to compare different 'flavors' of models relative to the data (e.g., how the different descriptions of star formation histories in galaxies — bursts, exponentially decaying, non-parametric/flexible — can be pitted against each other, an approach that is only recently being built into state-of-the-art Bayesian SED fitting tools).

These frameworks also quantify parameter uncertainties that can be interpreted physically. Traditional ML neural network architectures do not assign uncertainties to inferred

parameters. Those that do generate uncertainties create values that cannot be interpreted physically, i.e., there is no straightforward connection between the concepts of systematic and statistical uncertainties that astrophysicists are familiar with, to those employed in ML analyses (aleatoric and epistemic; see Caldeira & Nord (2020), and references therein).

Architectures such as Bayesian Neural Networks (with weights in each network layer forming probability distributions of parameters of interest), and Deep Ensembles (where the network is retrained many times with different initializations) are attempting to solve this problem. Unfortunately, these techniques have not been robustly tested on galaxy spectral analysis (with Gilda et al. (2021) being the exception, although this work does not use neural networks or SBI).

6.3.4 Requirements of a Simulation-Based Inference (SBI) pipeline

I am currently building a framework to infer physical properties of millions of galaxies in large-scale surveys via SED fitting, in a fast and efficient manner — using SBI and neural networks.

The objectives of this work (Khullar et al. 2022b, in prep) are to:

1. Estimate physical parameters from galaxy spectra/SED observations accurately and precisely.

2. Quantify uncertainties from observations and modeling.

3. Use as few assumptions about galaxy spectral models as possible.

4. Perform this estimation/inference for millions of objects with efficient use of computational time. Amortization of likelihood calculations, often the bottleneck step in these analyses, is currently being implemented (see next section).

6.3.5 Methodology

A fully developed SBI inference pipeline capable of tackle the many SED-fitting regimes discussed in Section 6.3.2 will take time to develop, test, and deploy. Main features of such a pipeline include:

a) A training set of galaxy spectra of different ages, metallicities, star formation rates, dust attenuation, intergalactic medium absorption among other physical parameters, generated via an SED generator (e.g., `Prospector`).

b) A supervised ML pipeline within an SBI framework via the toolbox 'sbi' (Tejero-Cantero et al., 2020).

c) Training architectures such as SNPE (Sequential Neural Posterior Estimation; Papamakarios & Murray (2016); Greenberg et al. (2019)) that uses neural networks to train on model SEDs with realistic noise in the above step, and allows me to estimate amortized posterior distributions.

d) Testing mechanisms for this pipeline for accuracy and speed with different architectures of networks and existing datasets (e.g., galaxy spectra from the Sloan Digital Sky Survey), and identifying ways to improve upon current MCMC/Bayesian methods of parameter estimation.

e) A comparison of the results from this effort to complementary efforts employing galaxy simulations and empirical libraries (e.g., Bayesian Neural Networks and MCMC methods).

As a first step towards this goal, I present work to conduct efficient Bayesian SED characterization of galaxy photometry via SBI using the open-source Python package `sbi` (Tejero-Cantero et al., 2020), and apply it below to one of the lensed early type galaxies I am now studying, as an illustration of possibilities.

SBI and SEDs

Our objective is to calculate posterior distributions p(θ|x) of the galaxy parameters derived from a typical SED analysis, where θ represents the vector of galaxy properties, and x represents the galaxy observations (in this case, a collection of photometric datapoints). We do this by training our SBI algorithm on a large stochastically-sampled training set of SEDs that captures the multi-dimensional parameter space associated with galaxy properties. Here, we utilise a two dimensional parameter space — stellar mass and metallicity of a given galaxy. The training, using the SNPE algorithm, requires computational time in advance of the actual inference. This "amortized" calculation of posteriors then allows us to infer the posteriors of a "real" galaxy with computational time $<$ 1s. See an example of amortized neural network-based posterior estimation in Hahn & Melchior (2022) and references therein.

We create a simulator that produces a generative model for galaxy SEDs and maps physical parameters for these SEDs. In the proof-of-concept analysis presented here, the models are smoothed versions of galaxy SEDs spanning rest-frame 1000-10000Å, and generated via `Prospector`. As a reminder, `Prospector` is based on the the Python-FSPS framework, with the MILES stellar spectral library and the MIST set of isochrones (Conroy & Gunn, 2010a; Johnson & Leja, 2017b; Leja et al., 2017b; Foreman-Mackey et al., 2013; Falcón-Barroso et al., 2011; Choi et al., 2016). In these models, we assume a parametric star formation history (a delayed exponentially decaying model with age and τ parameters, used in many SED fitting studies, including in Chapter 4), and fixed age and dust attenuation parameters. These models each assume a Kroupa IMF (Kroupa, 2001b). Nebular continuum and line emission are present.

We generate 3×10^5 simulations of SEDs with varying total stellar mass ($\log M_{\rm tot}$, in units of $M_\odot$) $\in$ [8,13], and stellar metallicity $\log(Z/Z_\odot)$ (where $Z_\odot = 0.0142$) $\in$ [-2.0, 0.2]. Each simulated SED contains six data points, roughly analagous to grzJHKs data (similar to the analysis for COOL J1553-0142; see Figure 6.3). We also add stochasticity

to these simulations in the form of Gaussian noise, to the level of 5% of the flux at a given wavelength. This is similar to the noise levels seen in observed follow-up photometry for COOL J1553-0142. These 3×10^5 simulations are trained with an SNPE (Sequential Neural Posterior Estimation) algorithm, using 10 hidden units and 5 transform layers (this computation takes approximately 1.5 hours; a six datapoint 3 parameter `Prospector` fit takes approximately 3 hours to converge to a solution such as the one in Figure 6.3). This implies that for the upfront (or "amortized") cost of one traditional MCMC SED fit, we can conduct the above posterior estimation in advance for thousands of galaxies (and order of 1000-100000x improvement in speed). For details on how SNPE (or a generalized amortized posterior estimation algorithm) functions, see Greenberg et al. (2019) or Section 2 of Hahn & Melchior (2022).

6.3.6 First Results and Next Steps

To test the efficacy of our SBI framework and training/inference algorithm, we use the best-fit model from the `Prospector` SED analysis of COOL J1553-0142 in Section 6.2.4, and generate an SED "observed" at z=0 (or at a luminosity distance of 10 pc), corresponding to $\log M_{\rm tot}$= 12.58 ($M_\odot$) and $\log(Z/Z_\odot) = 0.11$.

We further smooth this SED with a 3rd degree spline (with 15 knots; same as the training set above), sample six data points (to match the six magnitudes in Figure 6.3) and add the same Gaussian noise as for the simulator described in the previous section.

Figure 6.4 (left panel) shows the results of the posterior inference for stellar mass and metallicity. We find a median stellar mass and metallicity of $\log M\ (M_\odot) = 12.59^{+0.03}_{-0.04}$, and $\log(Z/Z_\odot) = 0.10^{+0.06}_{-0.08}$, consistent with both the accuracy and precision recovered by the `Prospector` Bayesian MCMC analysis. The right panel of Figure 6.4 shows the best fit "photometry", higher likelihood model photometry (in blue), and the truth value from the model observations of COOL J1553-0142 (in red).

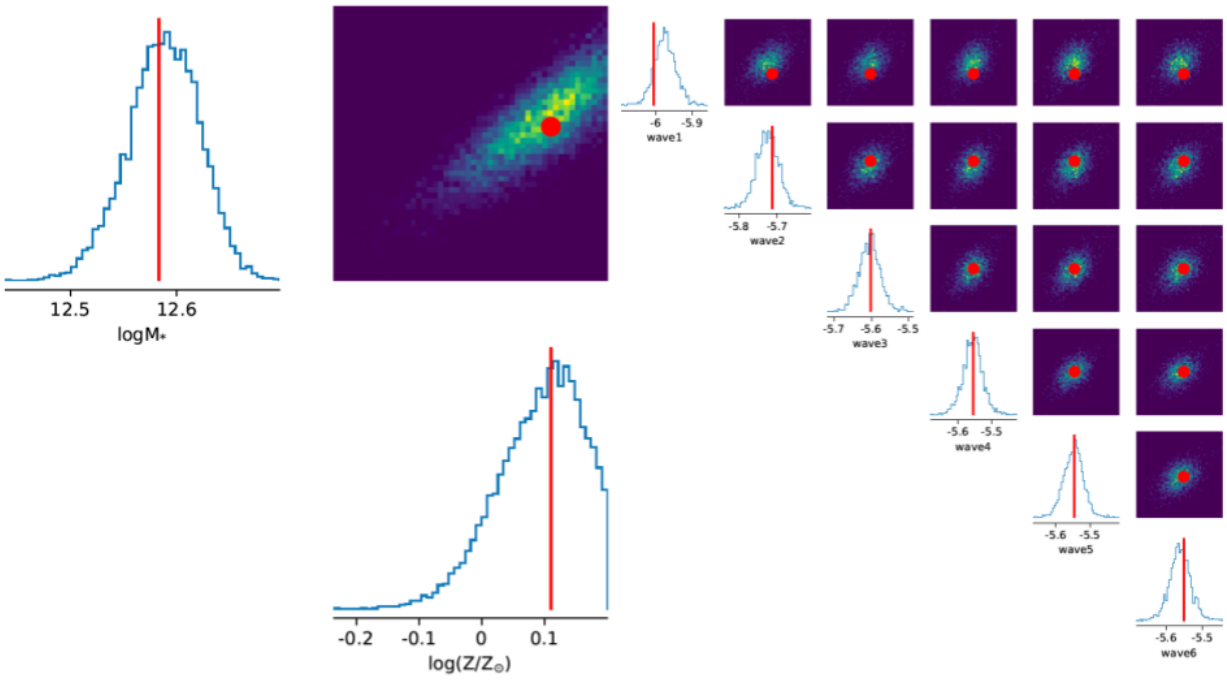

Figure 6.4 (Left) Posterior distribution of $\log M$ ($M_\odot$)) and $\log(Z/Z_\odot)$ for COOL J1553-0142, using our SBI analysis framework (red marks the truth values). (Right) A collection of posterior predictive model SEDs are shown here (flux value as a function of wavelength) from the $\log M$ and $\log(Z/Z_\odot)$ constraints in the left panel, demonstrating the health of the inferred parameters and predicted models.

Figure 6.5 shows the best fit photometry in the form of an SED, where the true SED (Flux as a function of wavelength) is displayed in green (a smoothed and sparsely sampled version of the SED for COOL J1553-0142, in blue), the SBI-inferred SED is shown in red, while the grey band represents the SED uncertainty. We observe that the scale of the SED uncertainties matches the combination of the scatter in the un-smoothed SED (green) and the Gaussian stochasticity of the simulator (blue, that was used to mimic the noise measured in real observations) which indicates that the parameter and model posteriors are well converged and sampled.

These preliminary yet encouraging results suggest that this is already a robust analysis framework to amortize SED posterior inference such that large datasets of galaxy photometry (and eventually spectroscopy) can be modeled efficiently. A future publication will showcase

results from a 10-parameter spectrophotometric model analysis using the above framework, which includes inference for dust parameters, star formation histories and velocity dispersion (Khullar et al. 2022b, in prep).

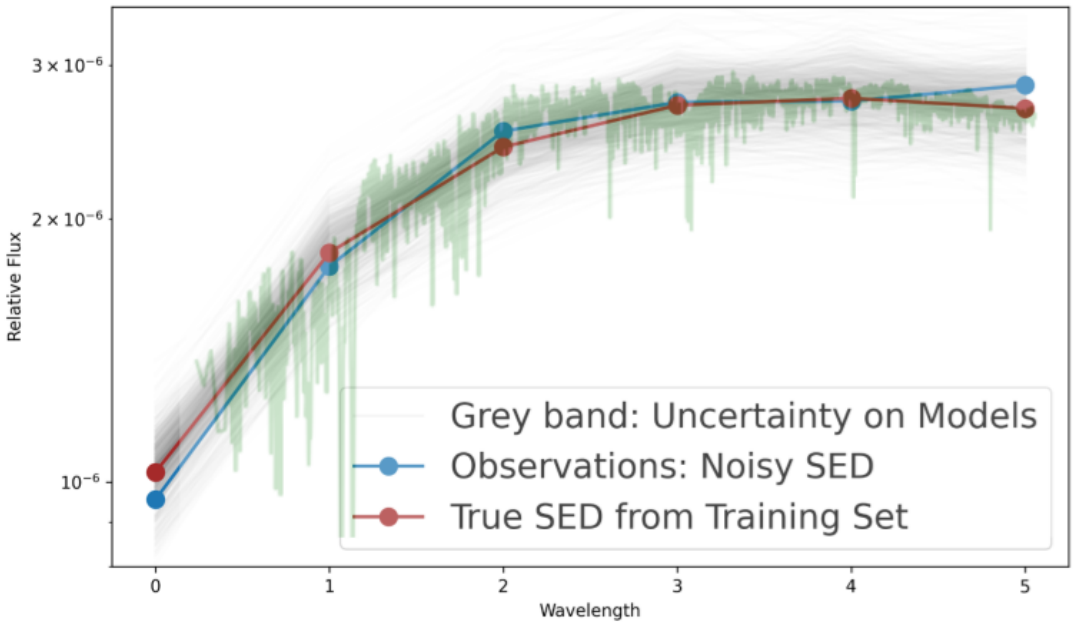

Figure 6.5 Best fit SED using observed photometry of COOL J1553-0142. The true SEDs (Flux as a function of wavelength) are displayed in green (a smoothed and sparsely sampled version of the SED for COOL J1553-0142 in blue), the SBI-inferred SED is shown in red, while the grey band represents the SED uncertainty.

6.4 Acknowledgments

We acknowledge the Deep Skies Lab as a community of multi-domain experts and collaborators who've facilitated an environment of open discussion, idea-generation, and collaboration. This community was important for the development of the projects described in this chapter.

CHAPTER 7

CONCLUSION

In this Chapter, I provide a brief summary of the results presented in this thesis, and discuss future work to characterize stellar mass assembly in the most massive galaxies across cosmic time.

7.1 Summary

As a PhD candidate at The University of Chicago, I have worked on two questions related to the formation and evolution of massive galaxies:

1. **How and when do quiescent galaxies in low and intermediate-redshift galaxy clusters assemble their stellar mass?**
2. **How do stellar populations evolve in bright lensed galaxies, in particular the brightest galaxy observed near the epoch of reionization?**

A major challenge in the field is understanding when the most massive galaxies form the bulk of their stars, and determining the pathways they take to assemble mass across a wide range of redshifts and environments. These most massive galaxies are much rarer than lower mass systems, but still contribute heavily to the Universe's stellar mass budget (Muzzin et al., 2013). At redshifts $z < 1$, many of the massive (and often quiescent) galaxies in the Universe reside in galaxy clusters. These massive ellipticals are typically red and dead at low redshifts (z$\sim$ 0.3). Studies of heterogenous samples of galaxy clusters show that most stars in massive quiescent member galaxies formed at $z > 2$ (Dressler et al., 2013; Webb et al., 2020).

At $z > 2$, studying in-situ star formation in the antecedents of massive galaxies is challenging, both because of cosmological dimming, and because some of the star formation is heavily obscured (Casey et al., 2014; Shanks et al., 2021). Nevertheless, from the consistency

of UV- and K-selected galaxy mass functions at $z > 3.5$, (Muzzin et al., 2013) argue that much of the star formation in high-redshift massive galaxies is relatively unobscured, making the case for detailed studies of both massive and UV-luminous systems in the distant universe. But, even massive galaxies at such redshifts appear small and faint; lensed examples of these antecedent objects at $z \sim 3-5$ offer the best opportunity for high-resolution spatial and spectral observations that can elucidate the details of formation and assembly of these objects. At $z > 3$ this sample is currently tiny. However, more bright lensed sources at $z > 3$ (and in particular $z > 5$) are now readily being discovered, due to the advent of deep large-area imaging surveys. This is a burgeoning opportunity to study these systems in great detail.

In my work, I have used *Magellan* spectra and photometry, spectral energy distribution (SED) fitting and stellar population models to characterize star formation histories of galaxies in these two epochs — at redshifts $z_{\rm mean}$ ∼0.5 and 5. I have studied large samples of cluster quiescent galaxies (Strazzullo et al., 2019; Khullar et al., 2021a) and individual star-forming high-redshift systems in great detail (Khullar et al., 2019, 2021b; Florian et al., 2021).

7.1.1 Characterizing the most distant Massive Galaxy Clusters at $z > 1$

To study the evolutionary properties of galaxies in galaxy clusters, it is necessary to build an unbiased cluster sample across redshift. However, constructing these cluster samples is extremely challenging: a) Optical, IR and X-ray fluxes are difficult to measure at high redshift (cosmological dimming) and b) for evolutionary studies, we need to study antecedents of lower redshift massive clusters, which are higher redshift and lower mass clusters. These challenges are mitigated by Sunyaev-Zel'dovich (SZ) effect-discovered clusters. SZ cluster samples (e.g., SPT, Bleem et al. (2015b, 2020a)) reach lower cluster mass thresholds uniformly at high redshifts and are uniquely suited for evolutionary studies.

In Khullar et al. (2019), I conducted spectroscopic follow-up of 5 of the most distant

galaxy clusters in the 2500 $\deg^2$ South Pole Telescope-SZ survey (SPT-SZ). In that work, I characterized emission and absorption line features of 44 member galaxies including 3 high-redshift BCGs with *Magellan*/LDSS3 spectroscopy and *Magellan*/PISCO photometry. At the time, this sample was the largest absorption-line spectroscopically confirmed cluster galaxy sample at these redshifts. I doubled the number of confirmed clusters at $M_{200c} \geq 4.5\times 10^{14}\mathrm{M}_{\odot}h^{-1}$ and $z > 1.2$. This distant, massive cluster population represents the antecedents of the most massive lower redshift clusters (e.g., Coma, Phoenix). Characterizing these systems is critical to tracing cluster evolution to the epoch when member galaxies formed the bulk of their stellar mass. Despite observational limitations (sky subtraction systematics), with thorough cross-validation I reported robust redshifts. My work has enabled new studies of star formation histories (Strazzullo et al., 2019) and cluster dynamics (McDonald et al., 2019).

7.1.2 Stellar Populations of Quiescent Galaxies in Clusters at $0.3 < z < 1.5$

In Khullar et al. (2019), I measured stellar population ages of a stack of 28 quiescent galaxies via Bayesian SED fitting. I found that the bulk of stars formed around $z = 2.5 \pm 0.5$, consistent with studies of low-redshift quiescent cluster galaxies that claim that these systems form stars early and rapidly (at $z > 2 - 3$), before settling into a mode of quiescent and stable evolution (Balogh et al., 1999; Dressler et al., 2004). Thus, cluster observations at $z > 1$ should sample an epoch where this star formation — or its end stages — is observed *in-situ*.

In Khullar et al. (2021a), I studied 63 SZ-selected clusters from the SPT-SZ Survey (Bleem et al., 2015b) across $0.3 < z < 1.4$ with extensive spectroscopy (Khullar et al., 2019; Bayliss et al., 2016a), and characterized 837 quiescent galaxies spectrophotometrically to address the following questions: a) When do galaxies that end up in clusters form their stars? b) What

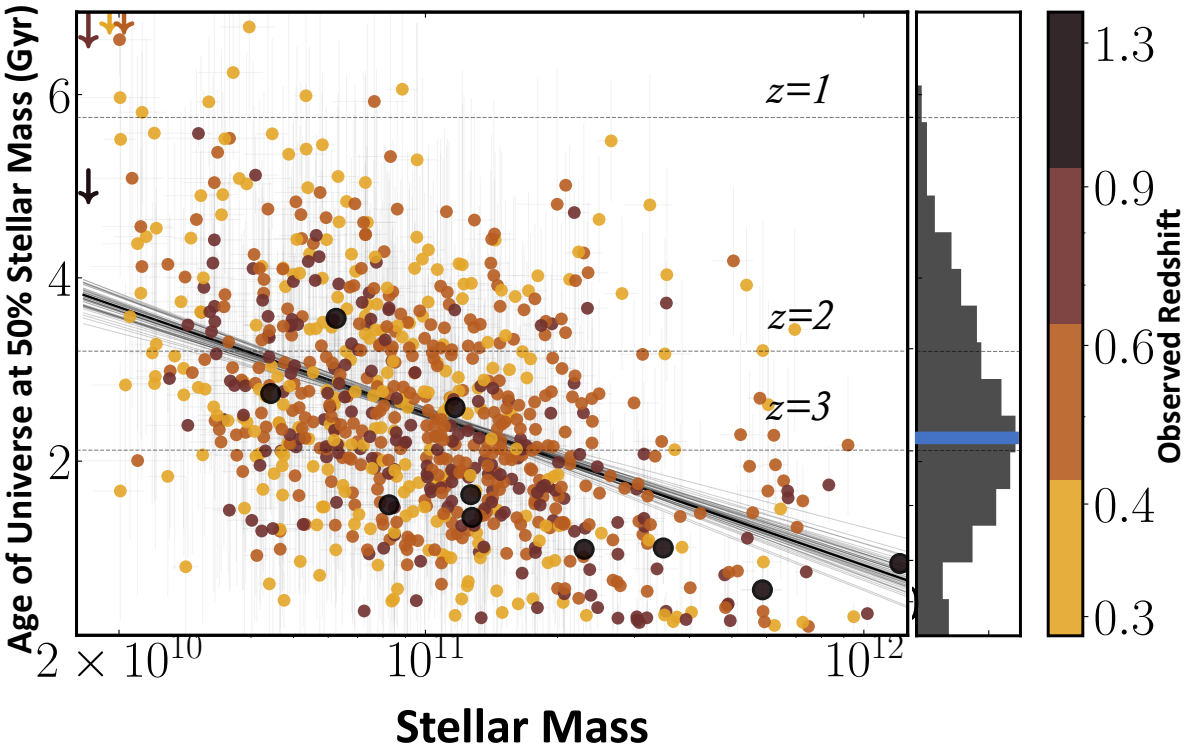

Figure 7.1 Age of Universe when the galaxy has formed 50% of its mass (or its Formation Redshift) vs stellar mass for 837 quiescent galaxies considered in the study K21a. Color at each point denotes the observed redshift, with orange points at $z \sim 0.3$ and highlighted black points at $z \sim 1.3$. Best-fit age-mass relation (with uncertainty) is plotted in black, with blue line marking the median formation redshift of SPT galaxies ($z = 2.8$).

roles do cluster environment and galaxy location within the cluster play in mass assembly within these galaxies? I calculated formation redshifts (when a galaxy has formed 50% of its stellar mass) as a function of stellar mass to quantify mass evolution in these galaxies (Figure 7.1). I found that quiescent galaxies have diverse star formation histories, exhibiting a range of ages across redshift and environment. The ages of these galaxies are on aggregate similar or marginally higher than massive quiescent field galaxies Pacifici et al. (2016); Carnall et al. (2019a); Tacchella et al. (2021), and similar to other clusters at $z > 1$ (Webb et al., 2020) — $z_{\rm median,form.}$=2.8 ± 0.5. I found that the formation epochs of SPT cluster quiescent galaxies depend more strongly on galaxy mass than environment. By characterizing the relationship between formation redshift and stellar mass, I confirmed that more massive cluster galaxies form $\sim$0.75 Gyr earlier than lower mass galaxies (i.e., galaxy 'downsizing' via mass-dependent evolution).

In ongoing work, I am measuring quenching timescales and comparing them to galaxy 'infall' timescales which will help confirm/rule out potential environmental influence (Wetzel et al., 2013). I am also characterizing stellar population properties in these systems by building individual galaxy SED models combined with metamodels describing population-level properties (cluster mass, velocity-radius phase-space location, etc.). This analysis (Khullar et al. in prep) will further generalize the framework we use to describe high-redshift galaxies as they are influenced by their host clusters, across redshift.

7.1.3 The Brightest Object in the $z > 5$ Universe

In Khullar+2021 (Khullar et al., 2021b), I reported the discovery and characterization of the brightest galaxy at redshifts $z > 5$, COOL J1241+2219 (hereafter, CJ1241). CJ1241 was discovered by the COOL-LAMPS collaboration (*ChicagO Optically selected strong Lens - Located At the Margins of Public Surveys*), a new team centered around undergraduate researchers at the University of Chicago. As the lead graduate student and a founding member of COOL-LAMPS (PI: Michael D Gladders), I have played an integral part in the

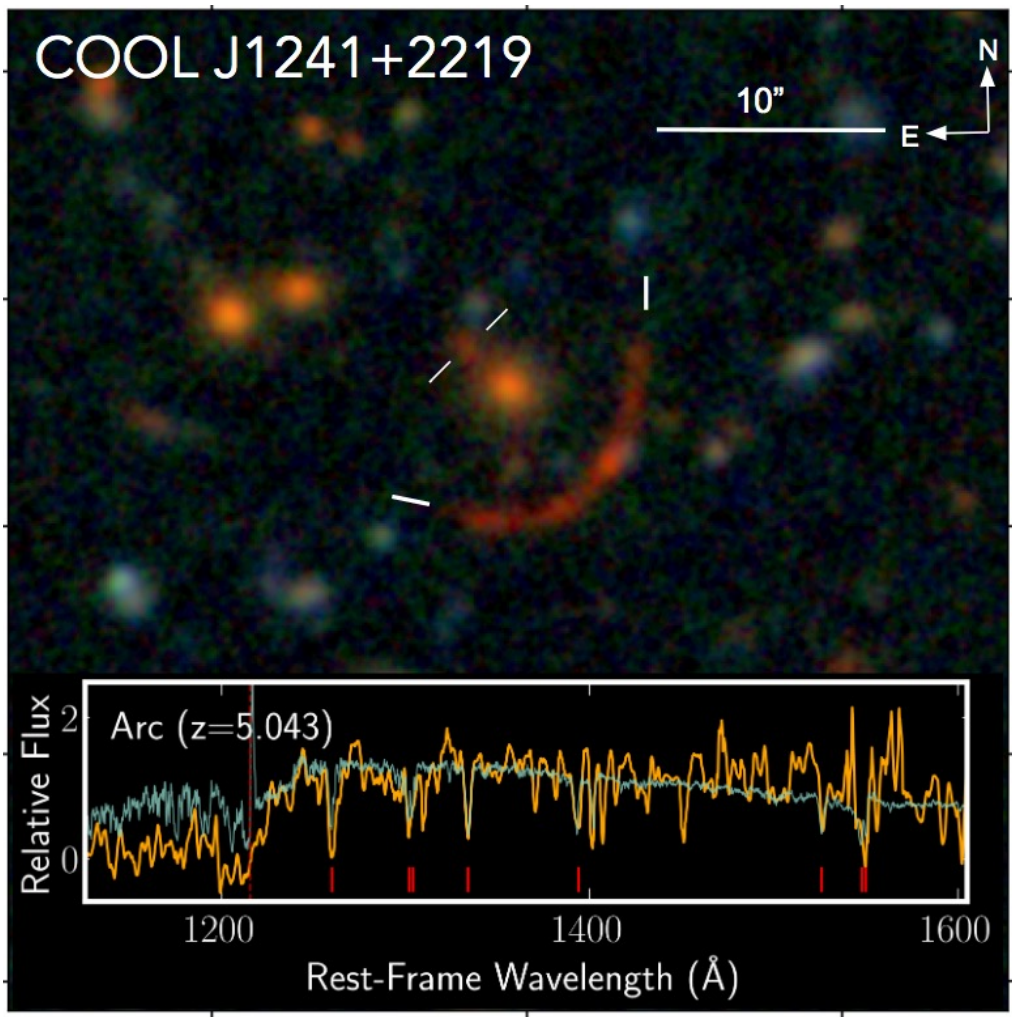

Figure 7.2 Magellan/PISCO g, r and $i + z$ composite image of COOL J1241. The arc and counter image are marked with solid white lines. The lensed arc is at $z = 5.043$, and the foreground lens is at $z = 1.00$. We show the smoothed rest-frame UV spectrum of the arc in the inset panel (without LyA emission; orange), with a reference spectrum (cyan).

collaboration, and have mentored 19 students since 2020.

COOL-LAMPS characterizes rare gravitationally lensed systems at the margins of color-magnitude and color-color space. A focus for followup is bright lensed galaxies that have colors suggestive of high-redshift dropouts. With recent large imaging surveys from 2m-4m class telescopes (e.g., DECaLS, Pan-STARRS, DELVE), our collaboration has inspected 1.1 million lines of sight, and has cataloged $\sim$ 1500 lensing candidates. We discovered CJ1241 in 2020, an extraordinarily bright arc (Figure 2) at $z = 5.04$ and at magnitude $z_{AB} = 20.5$, 5$\times$ brighter than any galaxy discovered at that redshift or higher.

With a detailed study using ground-based *grizJH* imaging and optical spectroscopy with SED fitting and lens modeling analysis, I found that this Lyman-break galaxy (LBG) is remarkably massive ($\log M_* = 10.11^{+0.21}_{-0.26}$) for that epoch, and while still actively star-forming (SFR $= 27^{+13}_{-9}$ $M_\odot$/yr) its spectrum is nearly extinction free (E(B-V) < 0.1). This M_* and SFR place CJ1241 on the high-mass end of the star-forming main sequence (Santini et al. 2017), with an M_* that is within 2-3x of the Milky Way at 1/10th the age of the Universe. CJ1241 is inherently 2-4x more luminous than the characteristic UV luminosity (L_*) at these redshifts with little dust attenuation; this is consistent with sub-mm observations with the NOEMA array (upper limit), indicating only a modest dust mass.

7.2 Future Directions

This thesis is an attempt to contribute to the understanding of how the most massive galaxies evolve across cosmic time, as observed in cluster environments and as gravitationally lensed systems. Here, I explore a few directions that this work may take in the future.

7.2.1 Connecting high and low redshift massive galaxies

The most massive galaxies, which over their lifetime have formed $> 10^{11}$ $M_\odot$ of stars, are extraordinary windows into galaxy formation and evolution. At low redshifts, massive

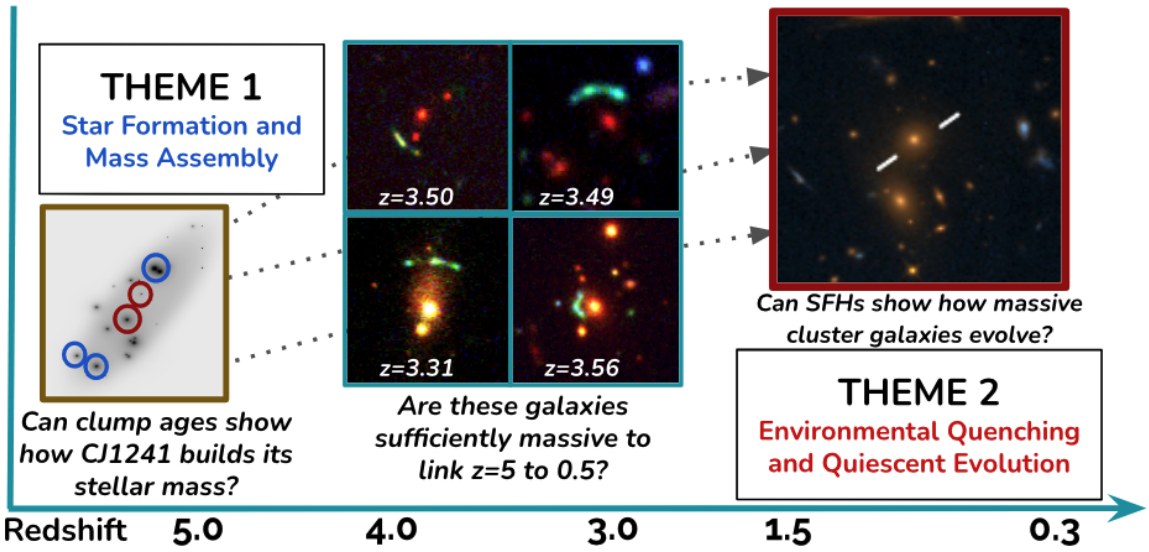

Figure 7.3 Future directions: (Left to Right) (1) Using clump ages to define mass assembly in $z = 5$ galaxies. (2) Measuring SFHs of $z = 3 - 4$ COOL-LAMPS galaxies to explore links between high and low redshift massive objects. (3) Studying the role of environmental quenching in a descendent-antecedent cluster BCG sample.

galaxies are typically giant ellipticals (Kauffmann et al., 2003; Franx et al., 2008) found mostly at the cores of galaxy clusters. These systems formed most of their stars rapidly at early times (Carnall et al., 2019a; Cooke et al., 2019) — hence to understand the entire life cycle of massive galaxies observed at low redshifts, we must observe their antecedents at high redshifts when their stellar mass is building up, i.e., at $z \gtrsim 3$. However, studying the antecedents of these systems at high redshifts is challenging. Instances of gravitationally lensed massive galaxies at $z > 3$ offer the best opportunity for high-resolution spatial and spectral observations that can reveal how these objects form and assemble. With the advent of large-area imaging surveys, we now have access to significant samples of sufficiently distant bright lensed sources, and can probe in detail the formation epoch of massive galaxies.

High-redshift dusty star-forming galaxies are claimed to be the antecedents of massive low-redshift quiescent galaxies (Muzzin et al., 2008; Casey, 2016). However, recent work shows that nearly dust-free massive galaxies at high-redshifts (detected in the UV/optical as Lyman-break galaxies) that have undergone rapid growth could become massive quiescent

galaxies at low redshifts (Ito et al., 2019; Verma et al., 2007). This exciting possibility motivates me to study distant lensed galaxies during their stellar mass build-up phase.

In the next few years, I aim to study mass assembly in high-redshift lensed massive galaxies, as the next scientific step in characterizing these unique systems. I will also connect this early-formed stellar mass to star formation histories (SFHs) in their potential low-redshift descendents.

7.2.2 The Brightest Massive Galaxies at 3<z<5: What is the fate of star-forming clumps?

In high-redshift lensed systems, mass-growth and star formation (SF) is thought to occur in 100 parsec-sized clumps Ceverino et al. (2010). Theory predicts two dramatically different fates of these clumps, linked to mass assembly in these galaxies — a) **outside-in** growth: long-lived clumps gradually migrate to the center and grow the galaxy (Bournaud et al., 2014), or b) **inside-out** evolution: feedback/central starburst activity dissipates clumps into the galaxy on short-timescales (Oklopčić et al., 2017). Only deep spatially resolved spectroscopy achievable by observing strong lenses allows us to measure clump ages at the requisite spatial scales, probing radial age gradients and the existence of long-lived clumps that can differentiate between these scenarios. My discovery of a $z = 5.04$ galaxy CJ1241 illustrates the exciting opportunities for studying mass assembly in distant lensed galaxies. In (Khullar et al., 2021b), I showed that CJ1241 has formed the bulk of its stellar mass during the epoch of reionization. Such a large stellar mass at $z = 5$ is rare (and highly biased relative to the overall mass density distribution), and hence CJ1241 is extremely likely to reside in a larger overdensity in the Universe that will become a galaxy cluster at later times (Cooke et al., 2019).

I will measure SFHs in sub-galactic components of CJ1241 to reveal how this $z = 5$ galaxy assembled its mass. In 2023 (January-June), we will receive *JWST* NIRSpec/IFU

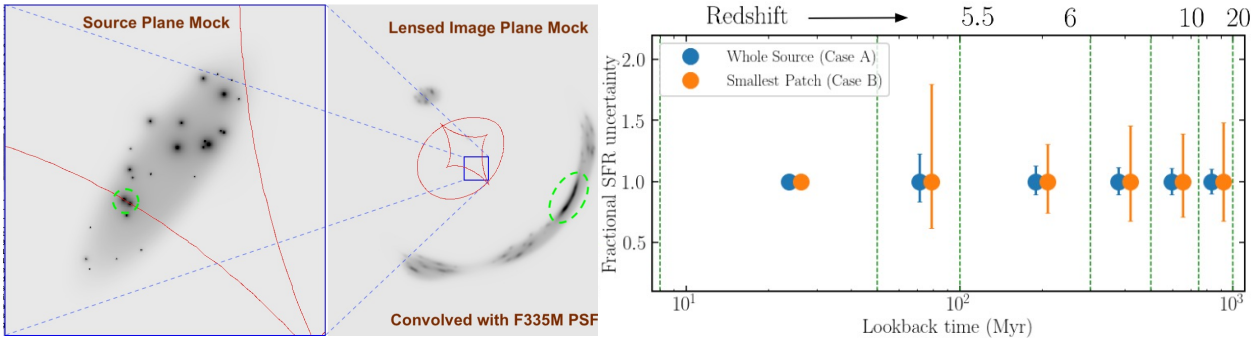

Figure 7.4 (Left) A mock lensed and source image of CJ1241 to illustrate the likely configuration; the magnified bright arc clump (in green) straddles a caustic, and maps to a small region ($< 100pc$). (Right) Expected SFH uncertainty for 6 age bins spanning ages of young (0-100 Myr), intermediate ($\sim$200Myr) and old ($\sim$1Gyr) stellar populations; constraints are shown for the full arc (blue, uncertainty $< 5\%$) and a single clump (orange, uncertainty $< 20\%$).

spectra and NIRCam imaging from my approved Cycle 1 program for CJ1241 (GO 2566, PI: Khullar). These observations will sample all major rest-frame optical emission lines with sufficient signal to spectrally resolve Balmer lines at $\sim 10/\mathrm{kms}^{-1}$. At 2μm, we will be able to spatially resolve clumps at $10\times$ the normal resolution of JWST (as small as $\sim$75pc). I will use SED fitting to characterise the SFH of the entire galaxy ($< 5\%$ level), and on a clump-by-clump basis (at $< 20\%$ level, Figure 7.4); this is unprecedented for non-local galaxies. I will measure age gradients within CJ1241 to confirm an inside-out or outside-in formation pathway (Akhshik et al., 2020). I will also bolster this analysis with upcoming *Chandra* (AGN signatures) and *VLA* (molecular gas) data, and recently collected *HST* imaging (lens modeling+UV continuum).

Inspired by success with CJ1241, COOL-LAMPS has focused significant ground-based resources to study candidate $z > 3$ lensed galaxies. We have doubled the number of confirmed bright $z > 3$ lensed systems with spectroscopy (*Magellan/Gemini*) and photometry (*Magellan/HST*). Current analyses suggest that these brightest galaxies (at $z > 3$) are unusually massive (Manwadkar, Zhang, Khullar et al. 2022 in prep). I will conduct SED studies of the brightest six of these lensed $z >3$ galaxies to describe their mass assembly.

I will use in-hand *Magellan* imaging and spectra to characterize stellar ages and masses, and propose for *HST+JWST* observations on these high-priority targets. As JWST has successfully launched and undergoing commissioning, I look forward to observing spectra of high-redshift COOL-LAMPS targets with this fantastic observatory.

7.2.3 Galaxies in cluster cores: How does environment affect quenching?

To robustly connect massive high-redshift galaxies to low-redshift descendents (most of which are cluster quiescent galaxies, including BCGs), we need to:
(1) Measure the SFHs of low-redshift systems — a galaxy's archaeological record, and
(2) Disentangle the influence of internal (feedback processes) and external (stripping of SF gas, mergers within clusters) factors in quenching star formation (Webb et al., 2020).

For these studies, we require an evolutionarily-linked galaxy cluster sample spanning a wide redshift range. In Khullar et al. (2019), I characterized emission and absorption in a spectroscopic sample of 44 member galaxies (including 3 high-redshift BCGs) in 5 of the most distant clusters in the 2500 deg^2 South Pole Telescope-SZ survey (Bleem et al., 2015b). In Khullar et al. (2021a), I characterized SFHs of member galaxies in 60 galaxy clusters at $0.3 < z < 0.9$.

In Khullar et al. (2021a), I *excluded BCGs*, as (1) BCGs trace unique evolutionary paths relative to other galaxies (Cerulo et al., 2019; Cooke et al., 2019), and (2) we have only recently obtained spectroscopy for a homogeneous BCG sample. Using heterogeneous samples, McDonald et al. (2015); Cooke et al. (2016) suggest that BCG growth may be dominated at early times by SF-gas rich mergers, and at late times by feedback-regulated cooling. These scenarios imprint unique observational signatures on morphology and spectra of BCGs, and can be studied by measuring SF-related timescales, i.e., $t_{\rm age}$, $\tau_{\rm SF}$ and $\tau_{\rm quench}$ (Tacchella et al., 2021). Fast quenching (<0.5 Gyr) times indicate merger activity/feedback (Rodríguez Montero et al., 2019), while slow quenching (>2-4 Gyr) suggests secular evolution.

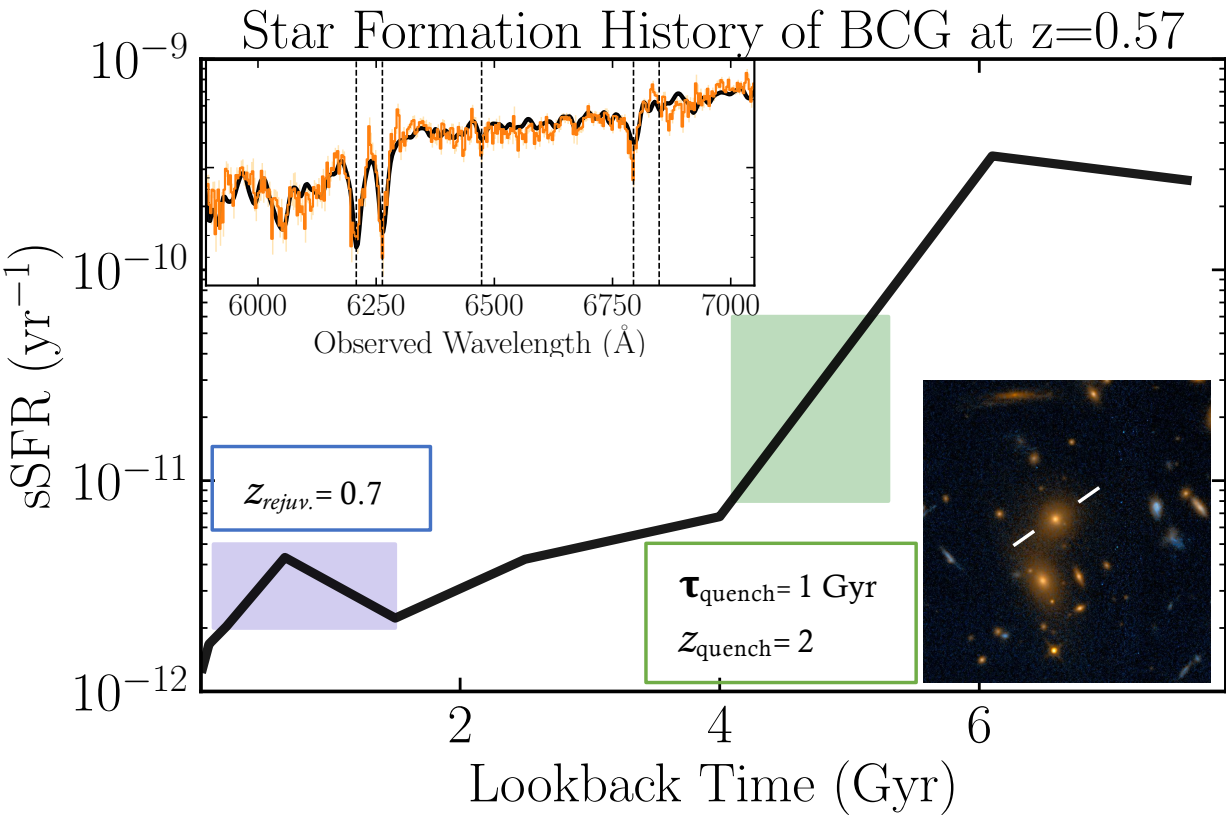

Figure 7.5 Best-Fit BCG SFH for SPT-CLJ0307-6225 ($z = 0.57$). I measure a quenching epoch ($z = 2$, green) and a recent SF epoch ($z = 0.7$, blue) using Bayesian SED fitting to optical spectra (top inset, data in orange, best fit in black), which samples age markers (Hδ, CaH&K absorption). (Bottom inset) HST F200LP+F110W image of cluster core, with marked BCG.

I will conduct the first comprehensive study of $\sim$ 150 BCGs in the SPT antecedent-descendent cluster sample (Bleem et al., 2015b, 2020a). I will use Bayesian SED fitting of spectra and photometry to measure stellar masses, SFHs and timescales in cluster BCGs. I will use existing HST/WFC3 (GO 15307, PI: Gladders, Co-I Khullar) imaging, ground-based multi-band optical/IR imaging, and extensive ground-based spectroscopy to study $\sim$150 cluster BCGs at $0.3 < z < 1.5$. These data sample SFR, age and metallicity indicators for stellar populations (e.g., [O II] $3727, 3729\mathring{A}$, CaH&K, $H\beta$, $H\gamma$, and $H\delta$) that I will use to measure precise SF timescales. A combination of timescale measurements (see example in Fig 7.5) and morphological data (from HST observations) will allow me to (1) characterize quenching mechanisms Belli et al. (2019), and (2) compare these to cluster-infall timescales from simulations Oman et al. (2021) to study the impact of the cluster environment.

Finally, I would like to note the unique time at which this document is presented, with JWST just successfully launched in December 2021; the telescope is currently undergoing an extremely productive commissioning period for the telescope and its instruments. Just like Hubble in the 1990s and Spitzer and Chandra space telescopes in the 200s, JWST promises to revolutionize the field of extragalactic astrophysics (see a thorough treatise on the potential of past and future great observatories in Armus et al. (2021). For studies of both high-redshift lensed galaxies and high-redshift cluster members, JWST is bound to be a revolutionary facility, that I am looking forward to utilizing in the next few years.

CHAPTER 8

REFERENCES

Abbott, T. M. C., Abdalla, F. B., Allam, S., et al. 2018, ApJS, 239, 18, doi: 10.3847/1538-4365/aae9f0

Abraham, R. G., Glazebrook, K., McCarthy, P. J., et al. 2004, AJ, 127, 2455, doi: 10.1086/383557

Abramson, L. E., Gladders, M. D., Dressler, A., et al. 2016, ApJ, 832, 7, doi: 10.3847/0004-637X/832/1/7

Ahumada, R., Allende Prieto, C., Almeida, A., et al. 2020, ApJS, 249, 3, doi: 10.3847/1538-4365/ab929e

Akhshik, M., Whitaker, K. E., Brammer, G., et al. 2020, ApJ, 900, 184, doi: 10.3847/1538-4357/abac62

Alberts, S., Pope, A., Brodwin, M., et al. 2014, MNRAS, 437, 437, doi: 10.1093/mnras/stt1897

—. 2016a, ApJ, 825, 72, doi: 10.3847/0004-637X/825/1/72

—. 2016b, ApJ, 825, 72, doi: 10.3847/0004-637X/825/1/72

Allam, S. S., Tucker, D. L., Lin, H., et al. 2007, ApJ, 662, L51, doi: 10.1086/519520

Andreon, S., Newman, A. B., Trinchieri, G., et al. 2014, A&A, 565, A120, doi: 10.1051/0004-6361/201323077

Armus, L., Megeath, S. T., Corrales, L., et al. 2021, arXiv:2104.00023. https://arxiv.org/abs/2104.00023

Ashby, M. L. N., Stern, D., Brodwin, M., et al. 2009, ApJ, 701, 428, doi: 10.1088/0004-637X/701/1/428

Balogh, M. L., Morris, S. L., Yee, H. K. C., Carlberg, R. G., & Ellingson, E. 1997, ApJ, 488, L75, doi: 10.1086/310927

—. 1999, ApJ, 527, 54, doi: 10.1086/308056

Balogh, M. L., Navarro, J. F., & Morris, S. L. 2000, ApJ, 540, 113, doi: 10.1086/309323

Balogh, M. L., Gilbank, D. G., Muzzin, A., et al. 2017, MNRAS, 470, 4168, doi: 10.1093/mnras/stx1370

Bartalucci, I., Arnaud, M., Pratt, G. W., & Le Brun, A. M. C. 2018a, ArXiv e-prints. https://arxiv.org/abs/1803.07556

—. 2018b, A&A, 617, A64, doi: 10.1051/0004-6361/201732458

Bayliss, M. B., Hennawi, J. F., Gladders, M. D., et al. 2011a, ApJS, 193, 8, doi: 10.1088/0067-0049/193/1/8

—. 2011b, ApJS, 193, 8, doi: 10.1088/0067-0049/193/1/8

Bayliss, M. B., Rigby, J. R., Sharon, K., et al. 2014a, ApJ, 790, 144, doi: 10.1088/0004-637X/790/2/144

Bayliss, M. B., Ashby, M. L. N., Ruel, J., et al. 2014b, ApJ, 794, 12, doi: 10.1088/0004-637X/794/1/12

Bayliss, M. B., Ruel, J., Stubbs, C. W., et al. 2016a, ApJS, 227, 3, doi: 10.3847/0067-0049/227/1/3

—. 2016b, ApJS, 227, 3, doi: 10.3847/0067-0049/227/1/3

Bayliss, M. B., Zengo, K., Ruel, J., et al. 2017a, ApJ, 837, 88, doi: 10.3847/1538-4357/aa607c

—. 2017b, ApJ, 837, 88, doi: 10.3847/1538-4357/aa607c

Beers, T. C., Flynn, K., & Gebhardt, K. 1990, AJ, 100, 32, doi: 10.1086/115487

Belli, S., Newman, A. B., & Ellis, R. S. 2015, ApJ, 799, 206, doi: 10.1088/0004-637X/799/2/206

—. 2019, ApJ, 874, 17, doi: 10.3847/1538-4357/ab07af

Belokurov, V., Evans, N. W., Moiseev, A., et al. 2007, ApJ, 671, L9, doi: 10.1086/524948

Bertin, E., & Arnouts, S. 1996, A&AS, 117, 393, doi: 10.1051/aas:1996164

Bicker, J., & Fritze-v. Alvensleben, U. 2005, A&A, 443, L19, doi: 10.1051/0004-6361:200500194

Blanton, M. R., & Moustakas, J. 2009, ARA&A, 47, 159, doi: 10.1146/annurev-astro-082708-101734

Bleem, L. E., Stalder, B., de Haan, T., et al. 2015a, ApJS, 216, 27, doi: 10.1088/0067-0049/216/2/27

—. 2015b, ApJS, 216, 27, doi: 10.1088/0067-0049/216/2/27

—. 2015c, ApJS, 216, 27, doi: 10.1088/0067-0049/216/2/27

Bleem, L. E., Bocquet, S., Stalder, B., et al. 2020a, ApJS, 247, 25, doi: 10.3847/1538-4365/ab6993

—. 2020b, ApJS, 247, 25, doi: 10.3847/1538-4365/ab6993

Bocquet, S., & Carter, F. W. 2016, The Journal of Open Source Software, 1, doi: 10.21105/joss.00046

Böhringer, H., Chon, G., Collins, C. A., et al. 2013, A&A, 555, A30, doi: 10.1051/0004-6361/201220722

Bouché, N., Dekel, A., Genzel, R., et al. 2010, ApJ, 718, 1001, doi: 10.1088/0004-637X/718/2/1001

Bournaud, F., Perret, V., Renaud, F., et al. 2014, ApJ, 780, 57, doi: 10.1088/0004-637X/780/1/57

Bouwens, R. J., Illingworth, G. D., Oesch, P. A., et al. 2014, ApJ, 793, 115, doi: 10.1088/0004-637X/793/2/115

—. 2015, ApJ, 803, 34, doi: 10.1088/0004-637X/803/1/34

Brinchmann, J., Charlot, S., White, S. D. M., et al. 2004, MNRAS, 351, 1151, doi: 10.1111/j.1365-2966.2004.07881.x

Brodwin, M., McDonald, M., Gonzalez, A. H., et al. 2016, ApJ, 817, 122, doi: 10.3847/0004-637X/817/2/122

Brodwin, M., Brown, M. J. I., Ashby, M. L. N., et al. 2006, ApJ, 651, 791, doi: 10.1086/507838

Brodwin, M., Ruel, J., Ade, P. A. R., et al. 2010a, ApJ, 721, 90, doi: 10.1088/0004-637X/721/1/90

—. 2010b, ApJ, 721, 90, doi: 10.1088/0004-637X/721/1/90

Brodwin, M., Stern, D., Vikhlinin, A., et al. 2011, ApJ, 732, 33, doi: 10.1088/0004-637X/732/1/33

Brodwin, M., Stanford, S. A., Gonzalez, A. H., et al. 2013a, ApJ, 779, 138, doi: 10.1088/0004-637X/779/2/138

—. 2013b, ApJ, 779, 138, doi: 10.1088/0004-637X/779/2/138

Brodwin, M., Greer, C. H., Leitch, E. M., et al. 2015, ApJ, 806, 26, doi: 10.1088/0004-637X/806/1/26

Bruzual, G., & Charlot, S. 2003, MNRAS, 344, 1000, doi: 10.1046/j.1365-8711.2003.06897.x

Bruzual A., G. 1983, ApJ, 273, 105, doi: 10.1086/161352

Bruzual A., G., & Charlot, S. 1993, ApJ, 405, 538, doi: 10.1086/172385

Caldeira, J., & Nord, B. 2020, arXiv e-prints, arXiv:2004.10710. https://arxiv.org/abs/2004.10710

Caldeira, J., Wu, W. L. K., Nord, B., et al. 2019, Astronomy and Computing, 28, 100307, doi: 10.1016/j.ascom.2019.100307

Calzetti, D., Armus, L., Bohlin, R. C., et al. 2000, ApJ, 533, 682, doi: 10.1086/308692

Calzetti, D., Kinney, A. L., & Storchi-Bergmann, T. 1994, ApJ, 429, 582, doi: 10.1086/174346

Carlstrom, J. E., Holder, G. P., & Reese, E. D. 2002a, ARA&A, 40, 643, doi: 10.1146/annurev.astro.40.060401.093803

—. 2002b, ARA&A, 40, 643, doi: 10.1146/annurev.astro.40.060401.093803

Carlstrom, J. E., Ade, P. A. R., Aird, K. A., et al. 2011a, PASP, 123, 568, doi: 10.1086/659879

—. 2011b, PASP, 123, 568, doi: 10.1086/659879

Carnall, A. C. 2017, arXiv e-prints, arXiv:1705.05165. https://arxiv.org/abs/1705.05165

Carnall, A. C., Leja, J., Johnson, B. D., et al. 2019a, ApJ, 873, 44, doi: 10.3847/1538-4357/ab04a2

Carnall, A. C., McLure, R. J., Dunlop, J. S., & Davé, R. 2018, MNRAS, 480, 4379, doi: 10.1093/mnras/sty2169

Carnall, A. C., McLure, R. J., Dunlop, J. S., et al. 2019b, MNRAS, 490, 417, doi: 10.1093/mnras/stz2544

Casey, C. M. 2016, ApJ, 824, 36, doi: 10.3847/0004-637X/824/1/36

Casey, C. M., Narayanan, D., & Cooray, A. 2014, Physics Reports, 541, 45, doi: 10.1016/j.physrep.2014.02.009

Casey, C. M., Zavala, J. A., Aravena, M., et al. 2019, ApJ, 887, 55, doi: 10.3847/1538-4357/ab52ff

Cerulo, P., Orellana, G. A., & Covone, G. 2019, MNRAS, 487, 3759, doi: 10.1093/mnras/stz1495

Ceverino, D., Dekel, A., & Bournaud, F. 2010, MNRAS, 404, 2151, doi: 10.1111/j.1365-2966.2010.16433.x

Ceverino, D., Dekel, A., Tweed, D., & Primack, J. 2015, MNRAS, 447, 3291, doi: 10.1093/mnras/stu2694

Chambers, K. C., Magnier, E. A., Metcalfe, N., et al. 2016, The Pan-STARRS1 Surveys. https://arxiv.org/abs/1612.05560

Chevallard, J., & Charlot, S. 2016, MNRAS, 462, 1415, doi: 10.1093/mnras/stw1756

Choi, J., Conroy, C., Moustakas, J., et al. 2014, ApJ, 792, 95, doi: 10.1088/0004-637X/792/2/95

Choi, J., Dotter, A., Conroy, C., et al. 2016, ApJ, 823, 102, doi: 10.3847/0004-637X/823/2/102

Cimatti, A., Daddi, E., & Renzini, A. 2006, A&A, 453, L29, doi: 10.1051/0004-6361:20065155

Cimatti, A., Daddi, E., Renzini, A., et al. 2004, Nature, 430, 184, doi: 10.1038/nature02668

Coe, D., Salmon, B., Bradač, M., et al. 2019, ApJ, 884, 85, doi: 10.3847/1538-4357/ab412b

Conroy, C. 2013, ARA&A, 51, 393, doi: 10.1146/annurev-astro-082812-141017

Conroy, C., & Gunn, J. E. 2010a, ApJ, 712, 833, doi: 10.1088/0004-637X/712/2/833

—. 2010b, ApJ, 712, 833, doi: 10.1088/0004-637X/712/2/833

Cooke, E. A., Hatch, N. A., Rettura, A., et al. 2015, MNRAS, 452, 2318, doi: 10.1093/mnras/stv1413

Cooke, K. C., Kartaltepe, J. S., Tyler, K. D., et al. 2019, ApJ, 881, 150, doi: 10.3847/1538-4357/ab30c9

Cooke, K. C., O'Dea, C. P., Baum, S. A., et al. 2016, ApJ, 833, 224, doi: 10.3847/1538-4357/833/2/224

Cornachione, M. A., Bolton, A. S., Shu, Y., et al. 2018, ApJ, 853, 148, doi: 10.3847/1538-4357/aaa412

Costantin, L., Pérez-González, P. G., Méndez-Abreu, J., et al. 2021, arXiv e-prints, arXiv:2103.10438. https://arxiv.org/abs/2103.10438

Cowie, L. L., Songaila, A., Hu, E. M., & Cohen, J. G. 1996, AJ, 112, 839, doi: 10.1086/118058

Cranmer, K., Brehmer, J., & Louppe, G. 2019, arXiv e-prints, arXiv:1911.01429. https://arxiv.org/abs/1911.01429

Culverhouse, T. L., Bonamente, M., Bulbul, E., et al. 2010, ApJ, 723, L78, doi: 10.1088/2041-8205/723/1/L78

Daddi, E., Renzini, A., Pirzkal, N., et al. 2005, ApJ, 626, 680, doi: 10.1086/430104

Daddi, E., Dickinson, M., Morrison, G., et al. 2007, ApJ, 670, 156, doi: 10.1086/521818

Davé, R., Anglés-Alcázar, D., Narayanan, D., et al. 2019, MNRAS, 486, 2827, doi: 10.1093/mnras/stz937

Davé, R., Thompson, R., & Hopkins, P. F. 2016, MNRAS, 462, 3265, doi: 10.1093/mnras/stw1862

De Lucia, G., Springel, V., White, S. D. M., Croton, D., & Kauffmann, G. 2006, MNRAS, 366, 499, doi: 10.1111/j.1365-2966.2005.09879.x

de Vaucouleurs, G. 1948, Annales d'Astrophysique, 11, 247

Dekel, A., & Mandelker, N. 2014, MNRAS, 444, 2071, doi: 10.1093/mnras/stu1427

Demarco, R., Wilson, G., Muzzin, A., et al. 2010, ApJ, 711, 1185, doi: 10.1088/0004-637X/711/2/1185

DESI Collaboration, Aghamousa, A., Aguilar, J., et al. 2016, arXiv e-prints, arXiv:1611.00036. https://arxiv.org/abs/1611.00036

Dey, A., Schlegel, D. J., Lang, D., et al. 2019, AJ, 157, 168, doi: 10.3847/1538-3881/ab089d

Diaferio, A., & Geller, M. J. 1997, ApJ, 481, 633, doi: 10.1086/304075

Díaz-García, L. A., Cenarro, A. J., López-Sanjuan, C., et al. 2019, A&A, 631, A156, doi: 10.1051/0004-6361/201832788

Diehl, H. T., Buckley-Geer, E. J., Lindgren, K. A., et al. 2017, The Astrophysical Journal Supplement Series, 232, 15, doi: 10.3847/1538-4365/aa8667

Dodelson, S. 2017, Gravitational Lensing

Domínguez Sánchez, H., Huertas-Company, M., Bernardi, M., Tuccillo, D., & Fischer, J. L. 2018, MNRAS, 476, 3661, doi: 10.1093/mnras/sty338

Dressler, A. 1980, ApJ, 236, 351, doi: 10.1086/157753

Dressler, A., & Gunn, J. E. 1982, ApJ, 263, 533, doi: 10.1086/160524

—. 1983, ApJ, 270, 7, doi: 10.1086/161093

Dressler, A., Oemler, Jr., A., Poggianti, B. M., et al. 2013, ApJ, 770, 62, doi: 10.1088/0004-637X/770/1/62

Dressler, A., Oemler, Augustus, J., Poggianti, B. M., et al. 2013, ApJ, 770, 62, doi: 10.1088/0004-637X/770/1/62

—. 2004, ApJ, 617, 867, doi: 10.1086/424890

Dressler, A., Kelson, D. D., Abramson, L. E., et al. 2016, ApJ, 833, 251, doi: 10.3847/1538-4357/833/2/251

Dreyer, J. L. E. 1895, MmRAS, 51, 185

Drlica-Wagner, A., Ferguson, P. S., Adamów, M., et al. 2022, arXiv e-prints, arXiv:2203.16565. https://arxiv.org/abs/2203.16565

Duffy, A. R., Schaye, J., Kay, S. T., & Dalla Vecchia, C. 2008, MNRAS, 390, L64, doi: 10.1111/j.1745-3933.2008.00537.x

Edge, A. C., Stewart, G. C., Fabian, A. C., & Arnaud, K. A. 1990, MNRAS, 245, 559

Einstein, A. 1936, Science, 84, 506, doi: 10.1126/science.84.2188.506

Eisenhardt, P. R. M., Brodwin, M., Gonzalez, A. H., et al. 2008, ApJ, 684, 905, doi: 10.1086/590105

Elias, J. H., Joyce, R. R., Liang, M., et al. 2006, in Society of Photo-Optical Instrumentation Engineers (SPIE) Conference Series, Vol. 6269, Society of Photo-Optical Instrumentation Engineers (SPIE) Conference Series, 62694C, doi: 10.1117/12.671817

Elíasdóttir, Á., Limousin, M., Richard, J., et al. 2007, arXiv e-prints, arXiv:0710.5636. https://arxiv.org/abs/0710.5636

Ellingson, E., Lin, H., Yee, H. K. C., & Carlberg, R. G. 2001, ApJ, 547, 609, doi: 10.1086/318423

Ellison, S. L., Simard, L., Cowan, N. B., et al. 2009, Monthly Notices of the Royal Astronomical Society, 396, 1257, doi: 10.1111/j.1365-2966.2009.14817.x

Elston, R. J., Gonzalez, A. H., McKenzie, E., et al. 2006, ApJ, 639, 816, doi: 10.1086/499423

Estrada-Carpenter, V., Papovich, C., Momcheva, I., et al. 2020, ApJ, 898, 171, doi: 10.3847/1538-4357/aba004

Fagioli, M., Carollo, C. M., Renzini, A., et al. 2016, ApJ, 831, 173, doi: 10.3847/0004-637X/831/2/173

Fakhouri, O., Ma, C.-P., & Boylan-Kolchin, M. 2010, MNRAS, 406, 2267, doi: 10.1111/j.1365-2966.2010.16859.x

Falcón-Barroso, J., Sánchez-Blázquez, P., Vazdekis, A., et al. 2011, A&A, 532, A95, doi: 10.1051/0004-6361/201116842

Fan, L., Lapi, A., Bressan, A., et al. 2010, ApJ, 718, 1460, doi: 10.1088/0004-637X/718/2/1460

Fassbender, R., Böhringer, H., Nastasi, A., et al. 2011a, New Journal of Physics, 13, 125014, doi: 10.1088/1367-2630/13/12/125014

—. 2011b, New Journal of Physics, 13, 125014, doi: 10.1088/1367-2630/13/12/125014

Feldmann, R., Hopkins, P. F., Quataert, E., Faucher-Giguère, C.-A., & Kereš, D. 2016, MNRAS, 458, L14, doi: 10.1093/mnrasl/slw014

Ferreras, I., Charlot, S., & Silk, J. 1999, ApJ, 521, 81, doi: 10.1086/307513

Finkelstein, S. L., Papovich, C., Salmon, B., et al. 2012, ApJ, 756, 164, doi: 10.1088/0004-637X/756/2/164

Flaugher, B., Diehl, H. T., Honscheid, K., et al. 2015, AJ, 150, 150, doi: 10.1088/0004-6256/150/5/150

Florian, M. K., Rigby, J. R., Acharyya, A., et al. 2020, arXiv e-prints, arXiv:2006.11387. https://arxiv.org/abs/2006.11387

—. 2021, ApJ, 916, 50, doi: 10.3847/1538-4357/ac0257

Foreman-Mackey, D., Hogg, D. W., Lang, D., & Goodman, J. 2013, PASP, 125, 306, doi: 10.1086/670067

Franx, M., Dokkum, P. G. v., Schreiber, N. M. F., et al. 2008, ApJ, 688, 770, doi: 10.1086/592431

Franx, M., Illingworth, G. D., Kelson, D. D., van Dokkum, P. G., & Tran, K.-V. 1997, ApJ, 486, L75, doi: 10.1086/310844

Frye, B., Broadhurst, T., & Benítez, N. 2002, ApJ, 568, 558, doi: 10.1086/338965

Fumagalli, M., Franx, M., van Dokkum, P., et al. 2016, ApJ, 822, 1, doi: 10.3847/0004-637X/822/1/1

Gallazzi, A., Bell, E. F., Zibetti, S., Brinchmann, J., & Kelson, D. D. 2014, ApJ, 788, 72, doi: 10.1088/0004-637X/788/1/72

Gallazzi, A., Charlot, S., Brinchmann, J., White, S. D. M., & Tremonti, C. A. 2005, MNRAS, 362, 41, doi: 10.1111/j.1365-2966.2005.09321.x

Garg, A., Stubbs, C. W., Challis, P., et al. 2007, AJ, 133, 403, doi: 10.1086/510118

Gettings, D. P., Gonzalez, A. H., Stanford, S. A., et al. 2012, ApJ, 759, L23, doi: 10.1088/2041-8205/759/1/L23

Gifford, D., Miller, C., & Kern, N. 2013, ApJ, 773, 116, doi: 10.1088/0004-637X/773/2/116

Gilbank, D. G., Baldry, I. K., Balogh, M. L., Glazebrook, K., & Bower, R. G. 2010, MNRAS, 405, 2594, doi: 10.1111/j.1365-2966.2010.16640.x

Gilda, S., Lower, S., & Narayanan, D. 2021, ApJ, 916, 43, doi: 10.3847/1538-4357/ac0058

Gladders, M. D., Yee, H. K. C., & Ellingson, E. 2002, AJ, 123, 1, doi: 10.1086/324637

Glazebrook, K., & Bland-Hawthorn, J. 2001, PASP, 113, 197, doi: 10.1086/318625

Gobat, R., Rosati, P., Strazzullo, V., et al. 2008, A&A, 488, 853, doi: 10.1051/0004-6361:200809531

Gonzalez, A. H., Decker, B., Brodwin, M., et al. 2015, ApJ, 812, L40, doi: 10.1088/2041-8205/812/2/L40

Greenberg, D. S., Nonnenmacher, M., & Macke, J. H. 2019, arXiv e-prints, arXiv:1905.07488. https://arxiv.org/abs/1905.07488

Gruen, D., Seitz, S., Brimioulle, F., et al. 2014, MNRAS, 442, 1507, doi: 10.1093/mnras/stu949

Guglielmo, V., Poggianti, B. M., Moretti, A., et al. 2015, MNRAS, 450, 2749, doi: 10.1093/mnras/stv757

Gunn, J. E., & Gott, III, J. R. 1972, ApJ, 176, 1, doi: 10.1086/151605

Guo, Q., & White, S. D. M. 2008, MNRAS, 384, 2, doi: 10.1111/j.1365-2966.2007.12619.x

Hahn, C., & Melchior, P. 2022, arXiv e-prints, arXiv:2203.07391. https://arxiv.org/abs/2203.07391

Haines, C. P., Iovino, A., Krywult, J., et al. 2017, A&A, 605, A4, doi: 10.1051/0004-6361/201630118

Hayes, M., Schaerer, D., Östlin, G., et al. 2011, ApJ, 730, 8, doi: 10.1088/0004-637X/730/1/8

Heavens, A. F., Jimenez, R., & Lahav, O. 2000, MNRAS, 317, 965, doi: 10.1046/j.1365-8711.2000.03692.x

Hénon, M. 1964, Annales d'Astrophysique, 27, 83

High, F. W., Stalder, B., Song, J., et al. 2010, ApJ, 723, 1736, doi: 10.1088/0004-637X/723/2/1736

Hilton, M., Stanford, S. A., Stott, J. P., et al. 2009a, ApJ, 697, 436, doi: 10.1088/0004-637X/697/1/436

—. 2009b, ApJ, 697, 436, doi: 10.1088/0004-637X/697/1/436

Hilton, M., Hasselfield, M., Sifón, C., et al. 2017, ArXiv e-prints. https://arxiv.org/abs/1709.05600

Hinshaw, G., Larson, D., Komatsu, E., et al. 2013, ApJS, 208, 19, doi: 10.1088/0067-0049/208/2/19

Hodges, J. L. 1958, Arkiv för Matematik, 3, 469

Holden, B. P., van der Wel, A., Franx, M., et al. 2005a, ApJ, 620, L83, doi: 10.1086/428663

—. 2005b, ApJ, 620, L83, doi: 10.1086/428663

Huang, N., Bleem, L. E., Stalder, B., et al. 2020a, AJ, 159, 110, doi: 10.3847/1538-3881/ab6a96

Huang, X., Storfer, C., Ravi, V., et al. 2020b, ApJ, 894, 78, doi: 10.3847/1538-4357/ab7ffb

Hubble, E. 1929, Proceedings of the National Academy of Science, 15, 168, doi: 10.1073/pnas.15.3.168

—. 1934, ApJ, 79, 8, doi: 10.1086/143517

Hubble, E., & Humason, M. L. 1931, ApJ, 74, 43, doi: 10.1086/143323

Hutchings, J. B., & Edwards, L. 2000, AJ, 119, 1100, doi: 10.1086/301255

Ilbert, O., McCracken, H. J., Le Fèvre, O., et al. 2013, A&A, 556, A55, doi: 10.1051/0004-6361/201321100

Inami, H., Bacon, R., Brinchmann, J., et al. 2017, A&A, 608, A2, doi: 10.1051/0004-6361/201731195

Ishida, E. E. O., Vitenti, S. D. P., Penna-Lima, M., et al. 2015, Astronomy and Computing, 13, 1, doi: 10.1016/j.ascom.2015.09.001

Ito, K., Kashikawa, N., Toshikawa, J., et al. 2019, ApJ, 878, 68, doi: 10.3847/1538-4357/ab1f0c

Ivison, R. J., Richard, J., Biggs, A. D., et al. 2020, Monthly Notices of the Royal Astronomical Society: Letters, 495, L1, doi: 10.1093/mnrasl/slaa046

Iyer, K., & Gawiser, E. 2017, ApJ, 838, 127, doi: 10.3847/1538-4357/aa63f0

Iyer, K. G., Gawiser, E., Faber, S. M., et al. 2019, ApJ, 879, 116, doi: 10.3847/1538-4357/ab2052

Jacobs, C., Collett, T., Glazebrook, K., et al. 2019, The Astrophysical Journal Supplement Series, 243, 17, doi: 10.3847/1538-4365/ab26b6

Jaelani, A. T., More, A., Oguri, M., et al. 2020, MNRAS, 495, 1291, doi: 10.1093/mnras/staa1062

Jafariyazani, M., Newman, A. B., Mobasher, B., et al. 2020, ApJ, 897, L42, doi: 10.3847/2041-8213/aba11c

James, B. L., Pettini, M., Christensen, L., et al. 2014, MNRAS, 440, 1794, doi: 10.1093/mnras/stu287

Jarrett, T. H., Chester, T., Cutri, R., et al. 2000, AJ, 119, 2498, doi: 10.1086/301330

Jee, M. J., Dawson, K. S., Hoekstra, H., et al. 2011, ApJ, 737, 59, doi: 10.1088/0004-637X/737/2/59

Johnson, B., & Leja, J. 2017a, bd-j/prospector: Initial release, doi: 10.5281/zenodo.1116491

—. 2017b, bd-j/prospector: Initial release, doi: 10.5281/zenodo.1116491

Johnson, B. D., Leja, J., Conroy, C., & Speagle, J. S. 2021, ApJS, 254, 22, doi: 10.3847/1538-4365/abef67

Johnson, T. L., Rigby, J. R., Sharon, K., et al. 2017, ApJ, 843, L21, doi: 10.3847/2041-8213/aa7516

Johnson, T. L., Sharon, K., Gladders, M. D., et al. 2017, The Astrophysical Journal, 843, 78, doi: 10.3847/1538-4357/aa7756

Jørgensen, I., & Chiboucas, K. 2013, AJ, 145, 77, doi: 10.1088/0004-6256/145/3/77

Jørgensen, I., Chiboucas, K., Berkson, E., et al. 2017, AJ, 154, 251, doi: 10.3847/1538-3881/aa96a3

Jørgensen, I., Chiboucas, K., Flint, K., et al. 2006, ApJ, 639, L9, doi: 10.1086/501348

Jullo, E., Kneib, J. P., Limousin, M., et al. 2007, New Journal of Physics, 9, 447, doi: 10.1088/1367-2630/9/12/447

Juneau, S., Glazebrook, K., Crampton, D., et al. 2005, ApJ, 619, L135, doi: 10.1086/427937

Kahanamoku, S., 'Anolani Alegado, R., Kagawa-Viviani, A., et al. 2020, arXiv e-prints, arXiv:2001.00970. https://arxiv.org/abs/2001.00970

Kaiser, N. 1986, MNRAS, 222, 323, doi: 10.1093/mnras/222.2.323

Kass, R. E., & Raftery, A. E. 1995, Journal of the american statistical association, 90, 773

Kauffmann, G., White, S. D. M., & Guiderdoni, B. 1993, MNRAS, 264, 201, doi: 10.1093/mnras/264.1.201

Kauffmann, G., Heckman, T. M., White, S. D. M., et al. 2003, MNRAS, 341, 33, doi: 10.1046/j.1365-8711.2003.06291.x

Kauffmann, G., Heckman, T. M., White, S. D. M., et al. 2003, MNRAS, 341, 33, doi: 10.1046/j.1365-8711.2003.06291.x

Kelson, D. D. 2003, PASP, 115, 688, doi: 10.1086/375502

Kelson, D. D., Williams, R. J., Dressler, A., et al. 2014, ApJ, 783, 110, doi: 10.1088/0004-637X/783/2/110

Kennicutt, Robert C., J. 1992, ApJ, 388, 310, doi: 10.1086/171154

Kewley, L. J., Geller, M. J., & Jansen, R. A. 2004, AJ, 127, 2002, doi: 10.1086/382723

Khochfar, S., & Silk, J. 2006, ApJ, 648, L21, doi: 10.1086/507768

Khullar, G., Bleem, L. E., Bayliss, M. B., et al. 2019, ApJ, 870, 7, doi: 10.3847/1538-4357/aaeed0

Khullar, G., Bayliss, M. B., Gladders, M. D., et al. 2021a, arXiv e-prints, arXiv:2111.09318. https://arxiv.org/abs/2111.09318

Khullar, G., Gozman, K., Lin, J. J., et al. 2021b, ApJ, 906, 107, doi: 10.3847/1538-4357/abcb86

Kneib, J. P., & Soucail, G. 1996, in Astrophysical Applications of Gravitational Lensing, ed. C. S. Kochanek & J. N. Hewitt (Dordrecht: Springer Netherlands), 113–118

Knuth, D. E. 1997, The Art of Computer Programming, Volume 2 (3rd Ed.): Seminumerical Algorithms (USA: Addison-Wesley Longman Publishing Co., Inc.)

Koester, B. P., Gladders, M. D., Hennawi, J. F., et al. 2010, ApJ, 723, L73, doi: 10.1088/2041-8205/723/1/L73

Kravtsov, A. V., & Borgani, S. 2012, ARA&A, 50, 353, doi: 10.1146/annurev-astro-081811-125502

Kroupa, P. 2001a, MNRAS, 322, 231, doi: 10.1046/j.1365-8711.2001.04022.x

—. 2001b, MNRAS, 322, 231, doi: 10.1046/j.1365-8711.2001.04022.x

Kubo, J. M., Allam, S. S., Drabek, E., et al. 2010, ApJ, 724, L137, doi: 10.1088/2041-8205/724/2/L137

Kurtz, M. J., & Mink, D. J. 1998, PASP, 110, 934, doi: 10.1086/316207

Lahav, O., Edge, A. C., Fabian, A. C., & Putney, A. 1989, MNRAS, 238, 881, doi: 10.1093/mnras/238.3.881

Larson, R. B., Tinsley, B. M., & Caldwell, C. N. 1980, ApJ, 237, 692, doi: 10.1086/157917

Leethochawalit, N., Kirby, E. N., Moran, S. M., Ellis, R. S., & Treu, T. 2018, ApJ, 856, 15, doi: 10.3847/1538-4357/aab26a

Leja, J., Carnall, A. C., Johnson, B. D., Conroy, C., & Speagle, J. S. 2019a, ApJ, 876, 3, doi: 10.3847/1538-4357/ab133c

—. 2019b, ApJ, 876, 3, doi: 10.3847/1538-4357/ab133c

Leja, J., Johnson, B. D., Conroy, C., van Dokkum, P. G., & Byler, N. 2017a, ApJ, 837, 170, doi: 10.3847/1538-4357/aa5ffe

—. 2017b, ApJ, 837, 170, doi: 10.3847/1538-4357/aa5ffe

Leja, J., Johnson, B. D., Conroy, C., et al. 2019c, ApJ, 877, 140, doi: 10.3847/1538-4357/ab1d5a

Lemaître, G. 1927, Annales de la Société Scientifique de Bruxelles, 47, 49

Licquia, T. C., & Newman, J. A. 2015, ApJ, 806, 96, doi: 10.1088/0004-637X/806/1/96

Lilly, S. J., Carollo, C. M., Pipino, A., Renzini, A., & Peng, Y. 2013, ApJ, 772, 119, doi: 10.1088/0004-637X/772/2/119

Livermore, R. C., Jones, T. A., Richard, J., et al. 2015, MNRAS, 450, 1812, doi: 10.1093/mnras/stv686

Lotz, J. M., Koekemoer, A., Coe, D., et al. 2017, ApJ, 837, 97, doi: 10.3847/1538-4357/837/1/97

Lovell, C. C., Acquaviva, V., Thomas, P. A., et al. 2019, MNRAS, 490, 5503, doi: 10.1093/mnras/stz2851

Lower, S., Narayanan, D., Leja, J., et al. 2020a, ApJ, 904, 33, doi: 10.3847/1538-4357/abbfa7

—. 2020b, ApJ, 904, 33, doi: 10.3847/1538-4357/abbfa7

Madau, P., & Dickinson, M. 2014, ARA&A, 52, 415, doi: 10.1146/annurev-astro-081811-125615

Mamon, G. A., Biviano, A., & Murante, G. 2010, A&A, 520, A30, doi: 10.1051/0004-6361/200913948

Mancone, C. L., Gonzalez, A. H., Brodwin, M., et al. 2010a, ApJ, 720, 284, doi: 10.1088/0004-637X/720/1/284

—. 2010b, ApJ, 720, 284, doi: 10.1088/0004-637X/720/1/284

Mancone, C. L., Baker, T., Gonzalez, A. H., et al. 2012a, ApJ, 761, 141, doi: 10.1088/0004-637X/761/2/141

—. 2012b, ApJ, 761, 141, doi: 10.1088/0004-637X/761/2/141

Mantz, A. B., Allen, S. W., Morris, R. G., et al. 2020, MNRAS, 496, 1554, doi: 10.1093/mnras/staa1581

Mantz, A. B., Abdulla, Z., Allen, S. W., et al. 2017, ArXiv e-prints. https://arxiv.org/abs/1703.08221

Marchesini, D., Muzzin, A., Stefanon, M., et al. 2014, ApJ, 794, 65, doi: 10.1088/0004-637X/794/1/65

Marriage, T. A., Acquaviva, V., Ade, P. A. R., et al. 2011, ApJ, 737, 61, doi: 10.1088/0004-637X/737/2/61

Matharu, J., Muzzin, A., Brammer, G. B., et al. 2020, MNRAS, 493, 6011, doi: 10.1093/mnras/staa610

McDonald, M., Benson, B. A., Vikhlinin, A., et al. 2013a, ApJ, 774, 23, doi: 10.1088/0004-637X/774/1/23

—. 2013b, ApJ, 774, 23, doi: 10.1088/0004-637X/774/1/23

McDonald, M., McNamara, B. R., van Weeren, R. J., et al. 2015, ApJ, 811, 111, doi: 10.1088/0004-637X/811/2/111

McDonald, M., Stalder, B., Bayliss, M., et al. 2016, ApJ, 817, 86, doi: 10.3847/0004-637X/817/2/86

McDonald, M., Allen, S. W., Bayliss, M., et al. 2017a, ArXiv e-prints. https://arxiv.org/abs/1702.05094

—. 2017b, ApJ, 843, 28, doi: 10.3847/1538-4357/aa7740

McDonald, M., Allen, S. W., Hlavacek-Larrondo, J., et al. 2019, ApJ, 870, 85, doi: 10.3847/1538-4357/aaf394

Mei, S., Holden, B. P., Blakeslee, J. P., et al. 2006a, ApJ, 644, 759, doi: 10.1086/503826

—. 2006b, ApJ, 644, 759, doi: 10.1086/503826

Messier, C. 1781, Catalogue des Nébuleuses et des Amas d'Étoiles (Catalog of Nebulae and Star Clusters), Connoissance des Temps ou des Mouvements Célestes, for 1784, p. 227-267

Miknaitis, G., Pignata, G., Rest, A., et al. 2007, ApJ, 666, 674, doi: 10.1086/519986

Mitchell, P. D., Lacey, C. G., Cole, S., & Baugh, C. M. 2014, MNRAS, 444, 2637, doi: 10.1093/mnras/stu1639

Mobasher, B., Dickinson, M., Ferguson, H. C., et al. 2005, ApJ, 635, 832, doi: 10.1086/497626

Moore, B., Lake, G., & Katz, N. 1998, ApJ, 495, 139, doi: 10.1086/305264

Moresco, M., Pozzetti, L., Cimatti, A., et al. 2010, A&A, 524, A67, doi: 10.1051/0004-6361/201014044

—. 2013, A&A, 558, A61, doi: 10.1051/0004-6361/201321797

Moutard, T., Sawicki, M., Arnouts, S., et al. 2018, ArXiv e-prints. https://arxiv.org/abs/1802.07628

Mullis, C. R., Rosati, P., Lamer, G., et al. 2005, ApJ, 623, L85, doi: 10.1086/429801

Muzzin, A., Wilson, G., Lacy, M., Yee, H. K. C., & Stanford, S. A. 2008, ApJ, 686, 966, doi: 10.1086/591542

Muzzin, A., Wilson, G., Yee, H. K. C., et al. 2009, ApJ, 698, 1934, doi: 10.1088/0004-637X/698/2/1934

—. 2012, ApJ, 746, 188, doi: 10.1088/0004-637X/746/2/188

Muzzin, A., Marchesini, D., Stefanon, M., et al. 2013, ApJ, 777, 18, doi: 10.1088/0004-637X/777/1/18

Nantais, J. B., van der Burg, R. F. J., Lidman, C., et al. 2016, A&A, 592, A161, doi: 10.1051/0004-6361/201628663

Nelson, D., Pillepich, A., Springel, V., et al. 2019, ArXiv e-prints. https://arxiv.org/abs/1902.05554

Newman, A. B., Belli, S., Ellis, R. S., & Patel, S. G. 2018a, ApJ, 862, 125, doi: 10.3847/1538-4357/aacd4d

—. 2018b, ApJ, 862, 126, doi: 10.3847/1538-4357/aacd4f

Newman, A. B., Ellis, R. S., Bundy, K., & Treu, T. 2012, ApJ, 746, 162, doi: 10.1088/0004-637X/746/2/162

Noble, A. G., Webb, T. M. A., Muzzin, A., et al. 2013, ApJ, 768, 118, doi: 10.1088/0004-637X/768/2/118

Noble, A. G., Webb, T. M. A., Yee, H. K. C., et al. 2016, ApJ, 816, 48, doi: 10.3847/0004-637X/816/2/48

Noeske, K. G., Weiner, B. J., Faber, S. M., et al. 2007a, ApJ, 660, L43, doi: 10.1086/517926

Noeske, K. G., Faber, S. M., Weiner, B. J., et al. 2007b, ApJ, 660, L47, doi: 10.1086/517927

Oemler, Jr., A. 1974, ApJ, 194, 1, doi: 10.1086/153216

Oklopčić, A., Hopkins, P. F., Feldmann, R., et al. 2017, MNRAS, 465, 952, doi: 10.1093/mnras/stw2754

Oldham, L., Auger, M. W., Fassnacht, C. D., et al. 2017, MNRAS, 465, 3185, doi: 10.1093/mnras/stw2832

Oman, K. A., Bahé, Y. M., Healy, J., et al. 2021, MNRAS, 501, 5073, doi: 10.1093/mnras/staa3845

Onodera, M., Renzini, A., Carollo, M., et al. 2012, ApJ, 755, 26, doi: 10.1088/0004-637X/755/1/26

Onodera, M., Carollo, C. M., Renzini, A., et al. 2015, ApJ, 808, 161, doi: 10.1088/0004-637X/808/2/161

Oser, L., Ostriker, J. P., Naab, T., Johansson, P. H., & Burkert, A. 2010, ApJ, 725, 2312, doi: 10.1088/0004-637X/725/2/2312

Pacifici, C., Kassin, S. A., Weiner, B. J., et al. 2016, ApJ, 832, 79, doi: 10.3847/0004-637X/832/1/79

Pallero, D., Gómez, F. A., Padilla, N. D., et al. 2019, MNRAS, 488, 847, doi: 10.1093/mnras/stz1745

Papamakarios, G., & Murray, I. 2016, in Advances in Neural Information Processing Systems, ed. D. Lee, M. Sugiyama, U. Luxburg, I. Guyon, & R. Garnett, Vol. 29 (Curran Associates, Inc.). https://proceedings.neurips.cc/paper/2016/file/6aca97005c68f1206823815f66102863-Paper.pdf

Papovich, C., Momcheva, I., Willmer, C. N. A., et al. 2010, ApJ, 716, 1503, doi: 10.1088/0004-637X/716/2/1503

Pasquali, A., Smith, R., Gallazzi, A., et al. 2019, MNRAS, 484, 1702, doi: 10.1093/mnras/sty3530

Paterno-Mahler, R., Blanton, E. L., Brodwin, M., et al. 2017, ApJ, 844, 78, doi: 10.3847/1538-4357/aa7b89

Peebles, P. J. E. 1970, AJ, 75, 13, doi: 10.1086/110933

Peng, C. Y., Ho, L. C., Impey, C. D., & Rix, H.-W. 2002, AJ, 124, 266, doi: 10.1086/340952

—. 2010, AJ, 139, 2097, doi: 10.1088/0004-6256/139/6/2097

Peng, Y., Maiolino, R., & Cochrane, R. 2015, Nature, 521, 192, doi: 10.1038/nature14439

Persson, S. E., Barkhouser, R., Birk, C., et al. 2008, in Society of Photo-Optical Instrumentation Engineers (SPIE) Conference Series, Vol. 7014, Ground-based and Airborne Instrumentation for Astronomy II, 70142V, doi: 10.1117/12.790015

Petrillo, C. E., Tortora, C., Vernardos, G., et al. 2019, MNRAS, 484, 3879, doi: 10.1093/mnras/stz189

Pettini, M., Steidel, C. C., Adelberger, K. L., Dickinson, M., & Giavalisco, M. 2000, ApJ, 528, 96, doi: 10.1086/308176

Pillepich, A., Nelson, D., Hernquist, L., et al. 2018, MNRAS, 475, 648, doi: 10.1093/mnras/stx3112

Pintos-Castro, I., Yee, H. K. C., Muzzin, A., Old, L., & Wilson, G. 2019, ApJ, 876, 40, doi: 10.3847/1538-4357/ab14ee

Planck Collaboration, Ade, P. A. R., Aghanim, N., et al. 2011, A&A, 536, A8, doi: 10.1051/0004-6361/201116459

—. 2014, A&A, 571, A20, doi: 10.1051/0004-6361/201321521

Prescod-Weinstein, C., Walkowicz, L. M., Tuttle, S., Nord, B., & Neilson, H. R. 2020, arXiv e-prints, arXiv:2001.00674. https://arxiv.org/abs/2001.00674

Quintana, H., Carrasco, E. R., & Reisenegger, A. 2000, AJ, 120, 511, doi: 10.1086/301476

Raichoor, A., Mei, S., Nakata, F., et al. 2011, ApJ, 732, 12, doi: 10.1088/0004-637X/732/1/12

Rawle, T. D., Edge, A. C., Egami, E., et al. 2012, ApJ, 747, 29, doi: 10.1088/0004-637X/747/1/29

Reichardt, C. L., Stalder, B., Bleem, L. E., et al. 2013, ApJ, 763, 127, doi: 10.1088/0004-637X/763/2/127

Rest, A., Stubbs, C., Becker, A. C., et al. 2005, ApJ, 634, 1103, doi: 10.1086/497060

Rhee, J., Smith, R., Choi, H., et al. 2017, ApJ, 843, 128, doi: 10.3847/1538-4357/aa6d6c

Richard, J., Smith, G. P., Kneib, J.-P., et al. 2010, MNRAS, 404, 325, doi: 10.1111/j.1365-2966.2009.16274.x

Riechers, D. A., Bradford, C. M., Clements, D. L., et al. 2013, Nature, 496, 329, doi: 10.1038/nature12050

Rigby, J. R., Bayliss, M. B., Chisholm, J., et al. 2018a, ApJ, 853, 87, doi: 10.3847/1538-4357/aaa2fc

Rigby, J. R., Bayliss, M. B., Sharon, K., et al. 2018b, AJ, 155, 104, doi: 10.3847/1538-3881/aaa2ff

Rivera-Thorsen, T. E., Dahle, H., Chisholm, J., et al. 2019, Science, 366, 738, doi: 10.1126/science.aaw0978

Rodighiero, G., Daddi, E., Baronchelli, I., et al. 2011, ApJ, 739, L40, doi: 10.1088/2041-8205/739/2/L40

Rodriguez-Gomez, V., Pillepich, A., Sales, L. V., et al. 2016, MNRAS, 458, 2371, doi: 10.1093/mnras/stw456

Rodríguez Montero, F., Davé, R., Wild, V., Anglés-Alcázar, D., & Narayanan, D. 2019, MNRAS, 490, 2139, doi: 10.1093/mnras/stz2580

Roman-Duval, J., Proffitt, C. R., Taylor, J. M., et al. 2020, Research Notes of the American Astronomical Society, 4, 205, doi: 10.3847/2515-5172/abca2f

Rong, Y., Li, H., Wang, J., et al. 2018, MNRAS, 477, 230, doi: 10.1093/mnras/sty697

Rosa-González, D., Terlevich, E., & Terlevich, R. 2002, MNRAS, 332, 283, doi: 10.1046/j.1365-8711.2002.05285.x

Rosati, P., Della Ceca, R., Norman, C., & Giacconi, R. 1998, ApJ, 492, L21, doi: 10.1086/311085

Rosati, P., Tozzi, P., Ettori, S., et al. 2004, AJ, 127, 230, doi: 10.1086/379857

Rosati, P., Tozzi, P., Gobat, R., et al. 2009, A&A, 508, 583, doi: 10.1051/0004-6361/200913099

Ruel, J., Bazin, G., Bayliss, M., et al. 2014a, ApJ, 792, 45, doi: 10.1088/0004-637X/792/1/45

—. 2014b, ApJ, 792, 45, doi: 10.1088/0004-637X/792/1/45

Salmon, B., Coe, D., Bradley, L., et al. 2020, ApJ, 889, 189, doi: 10.3847/1538-4357/ab5a8b

Sánchez-Blázquez, P., Jablonka, P., Noll, S., et al. 2009, A&A, 499, 47, doi: 10.1051/0004-6361/200811355

Santini, P., Fontana, A., Castellano, M., et al. 2017, ApJ, 847, 76, doi: 10.3847/1538-4357/aa8874

Santos, J. S., Tozzi, P., & Rosati, P. 2011, Memorie della Societa Astronomica Italiana Supplementi, 17, 66. https://arxiv.org/abs/1012.1151

Saracco, P., Gargiulo, A., La Barbera, F., Annunziatella, M., & Marchesini, D. 2020, MNRAS, 491, 1777, doi: 10.1093/mnras/stz3109

Saracco, P., Longhetti, M., & Andreon, S. 2009, MNRAS, 392, 718, doi: 10.1111/j.1365-2966.2008.14085.x

Saro, A., Mohr, J. J., Bazin, G., & Dolag, K. 2013, ApJ, 772, 47, doi: 10.1088/0004-637X/772/1/47

Schechter, P. 1976, ApJ, 203, 297, doi: 10.1086/154079

Sérsic, J. L. 1963, Boletin de la Asociacion Argentina de Astronomia La Plata Argentina, 6, 41

Shanks, T., Ansarinejad, B., Bielby, R. M., et al. 2021, MNRAS, 505, 1509, doi: 10.1093/mnras/stab1226

Shapley, A. E., Steidel, C. C., Pettini, M., & Adelberger, K. L. 2003, ApJ, 588, 65, doi: 10.1086/373922

Shapley, H., & Curtis, H. D. 1921, Bulletin of the National Research Council, 2, 171

Sharon, K., Bayliss, M. B., Dahle, H., et al. 2020, VizieR Online Data Catalog, J/ApJS/247/12

Sifón, C., Battaglia, N., Hasselfield, M., et al. 2016a, MNRAS, 461, 248, doi: 10.1093/mnras/stw1284

—. 2016b, MNRAS, 461, 248, doi: 10.1093/mnras/stw1284

Snyder, G. F., Brodwin, M., Mancone, C. M., et al. 2012a, ApJ, 756, 114, doi: 10.1088/0004-637X/756/2/114

—. 2012b, ApJ, 756, 114, doi: 10.1088/0004-637X/756/2/114

Soifer, B. T., Neugebauer, G., Franx, M., Matthews, K., & Illingworth, G. D. 1998, ApJ, 501, L171, doi: 10.1086/311462

Song, J., Zenteno, A., Stalder, B., et al. 2012a, ApJ, 761, 22, doi: 10.1088/0004-637X/761/1/22

—. 2012b, ApJ, 761, 22, doi: 10.1088/0004-637X/761/1/22

Soucail, G., Mellier, Y., Fort, B., Mathez, G., & Cailloux, M. 1988, A&A, 191, L19

Spinrad, H., & Taylor, B. J. 1971, ApJS, 22, 445, doi: 10.1086/190232

Springel, V., Di Matteo, T., & Hernquist, L. 2005, MNRAS, 361, 776, doi: 10.1111/j.1365-2966.2005.09238.x

Stalder, B., Stark, A. A., Amato, S. M., et al. 2014a, in Proc. SPIE, Vol. 9147, Ground-based and Airborne Instrumentation for Astronomy V, 91473Y, doi: 10.1117/12.2054933

Stalder, B., Stark, A. A., Amato, S. M., et al. 2014b, in Proc. SPIE, Vol. 9147, Ground-based and Airborne Instrumentation for Astronomy V, 91473Y, doi: 10.1117/12.2054933

Stalder, B., Stark, A. A., Amato, S. M., et al. 2014c, in Society of Photo-Optical Instrumentation Engineers (SPIE) Conference Series, Vol. 9147, Ground-based and Airborne Instrumentation for Astronomy V, 91473Y, doi: 10.1117/12.2054933

Stalder, B., Ruel, J., Šuhada, R., et al. 2013a, ApJ, 763, 93, doi: 10.1088/0004-637X/763/2/93

Stalder, B., Ruel, J., Šuhada, R., et al. 2013b, ApJ, 763, 93, doi: 10.1088/0004-637X/763/2/93

Stanford, S. A., Eisenhardt, P. R., & Dickinson, M. 1998a, ApJ, 492, 461, doi: 10.1086/305050

—. 1998b, ApJ, 492, 461, doi: 10.1086/305050

Stanford, S. A., Gonzalez, A. H., Brodwin, M., et al. 2014, ApJS, 213, 25, doi: 10.1088/0067-0049/213/2/25

Stanford, S. A., Eisenhardt, P. R., Brodwin, M., et al. 2005a, ApJ, 634, L129, doi: 10.1086/499045

—. 2005b, ApJ, 634, L129, doi: 10.1086/499045

Stanford, S. A., Romer, A. K., Sabirli, K., et al. 2006, ApJ, 646, L13, doi: 10.1086/506449

Stanford, S. A., Brodwin, M., Gonzalez, A. H., et al. 2012, ApJ, 753, 164, doi: 10.1088/0004-637X/753/2/164

Staniszewski, Z., Ade, P. A. R., Aird, K. A., et al. 2009, ApJ, 701, 32, doi: 10.1088/0004-637X/701/1/32

Stark, D. P., Auger, M., Belokurov, V., et al. 2013, MNRAS, 436, 1040, doi: 10.1093/mnras/stt1624

Steidel, C. C., Strom, A. L., Pettini, M., et al. 2016, ApJ, 826, 159, doi: 10.3847/0004-637X/826/2/159

Stott, J. P., Collins, C. A., Sahlén, M., et al. 2010, ApJ, 718, 23, doi: 10.1088/0004-637X/718/1/23

Strandet, M. L., Weiss, A., De Breuck, C., et al. 2017, ApJ, 842, L15, doi: 10.3847/2041-8213/aa74b0

Strazzullo, V., Pannella, M., Mohr, J. J., et al. 2019, A&A, 622, A117, doi: 10.1051/0004-6361/201833944

Sukay, E., Khullar, G., Gladders, M. D., et al. 2022, arXiv e-prints, arXiv:2203.11957. https://arxiv.org/abs/2203.11957

Sunyaev, R. A., & Zeldovich, Y. B. 1972, Comments on Astrophysics and Space Physics, 4, 173

Tacchella, S., Bose, S., Conroy, C., Eisenstein, D. J., & Johnson, B. D. 2018, ApJ, 868, 92, doi: 10.3847/1538-4357/aae8e0

Tacchella, S., Conroy, C., Faber, S. M., et al. 2021, arXiv e-prints, arXiv:2102.12494. https://arxiv.org/abs/2102.12494

Tejero-Cantero, A., Boelts, J., Deistler, M., et al. 2020, Journal of Open Source Software, 5, 2505, doi: 10.21105/joss.02505

Tinsley, B. M. 1980, Fund. Cosmic Phys., 5, 287, doi: 10.48550/arXiv.2203.02041

Tinsley, B. M., & Gunn, J. E. 1976, ApJ, 203, 52, doi: 10.1086/154046

Tonry, J., & Davis, M. 1979, AJ, 84, 1511, doi: 10.1086/112569

Tran, K.-V. H., Papovich, C., Saintonge, A., et al. 2010a, ApJ, 719, L126, doi: 10.1088/2041-8205/719/2/L126

—. 2010b, ApJ, 719, L126, doi: 10.1088/2041-8205/719/2/L126

Tran, K.-V. H., Nanayakkara, T., Yuan, T., et al. 2015, ApJ, 811, 28, doi: 10.1088/0004-637X/811/1/28

Trujillo, I., Conselice, C. J., Bundy, K., et al. 2007, MNRAS, 382, 109, doi: 10.1111/j.1365-2966.2007.12388.x

van Dokkum, P. G., & Franx, M. 2001, ApJ, 553, 90, doi: 10.1086/320645

van Dokkum, P. G., Franx, M., Kelson, D. D., & Illingworth, G. D. 1998, ApJ, 504, L17, doi: 10.1086/311567

van Dokkum, P. G., Franx, M., Kriek, M., et al. 2008, ApJ, 677, L5, doi: 10.1086/587874

Vanderlinde, K., Crawford, T. M., de Haan, T., et al. 2010, ApJ, 722, 1180, doi: 10.1088/0004-637X/722/2/1180

Verdugo, T., Motta, V., Muñoz, R. P., et al. 2011, A&A, 527, A124, doi: 10.1051/0004-6361/201014965

Verma, A., Lehnert, M. D., Förster Schreiber, N. M., Bremer, M. N., & Douglas, L. 2007, MNRAS, 377, 1024, doi: 10.1111/j.1365-2966.2007.11455.x

von Hoerner, S. 1963, ZAp, 57, 47

Wang, T., Elbaz, D., Daddi, E., et al. 2016, ApJ, 828, 56, doi: 10.3847/0004-637X/828/1/56

Webb, K., Balogh, M. L., Leja, J., et al. 2020, MNRAS, 498, 5317, doi: 10.1093/mnras/staa2752

Webb, T. M. A., Muzzin, A., Noble, A., et al. 2015, ApJ, 814, 96, doi: 10.1088/0004-637X/814/2/96

Wellons, S., Torrey, P., Ma, C.-P., et al. 2015, MNRAS, 449, 361, doi: 10.1093/mnras/stv303

Wetzel, A. R., Tinker, J. L., & Conroy, C. 2012, MNRAS, 424, 232, doi: 10.1111/j.1365-2966.2012.21188.x

Wetzel, A. R., Tinker, J. L., Conroy, C., & van den Bosch, F. C. 2013, MNRAS, 432, 336, doi: 10.1093/mnras/stt469

Whitaker, K. E., van Dokkum, P. G., Brammer, G., & Franx, M. 2012, ApJ, 754, L29, doi: 10.1088/2041-8205/754/2/L29

Whitaker, K. E., van Dokkum, P. G., Brammer, G., et al. 2013, ApJ, 770, L39, doi: 10.1088/2041-8205/770/2/L39

White, M., Cohn, J. D., & Smit, R. 2010, MNRAS, 408, 1818, doi: 10.1111/j.1365-2966.2010.17248.x

Wiklind, T., Dickinson, M., Ferguson, H. C., et al. 2008, ApJ, 676, 781, doi: 10.1086/524919

Williamson, R., Benson, B. A., High, F. W., et al. 2011, ApJ, 738, 139, doi: 10.1088/0004-637X/738/2/139

Wilson, G., Muzzin, A., Lacy, M., et al. 2006, ArXiv Astrophysics e-prints

Woodrum, C., Jørgensen, I., Fisher, R. S., et al. 2017, ApJ, 847, 20, doi: 10.3847/1538-4357/aa8871

Worthey, G. 1994, ApJS, 95, 107, doi: 10.1086/192096

Worthey, G. 1999, in Astronomical Society of the Pacific Conference Series, Vol. 192, Spectrophotometric Dating of Stars and Galaxies, ed. I. Hubeny, S. Heap, & R. Cornett, 283

Yuan, T., Nanayakkara, T., Kacprzak, G. G., et al. 2014, ApJ, 795, L20, doi: 10.1088/2041-8205/795/1/L20

Zabludoff, A. I., & Mulchaey, J. S. 1998, ApJ, 496, 39, doi: 10.1086/305355

Zeimann, G. R., Stanford, S. A., Brodwin, M., et al. 2012, ApJ, 756, 115, doi: 10.1088/0004-637X/756/2/115

Zwicky, F. 1951, PASP, 63, 61, doi: 10.1086/126318